PAUL SCHERRER INSTITUT

PSI

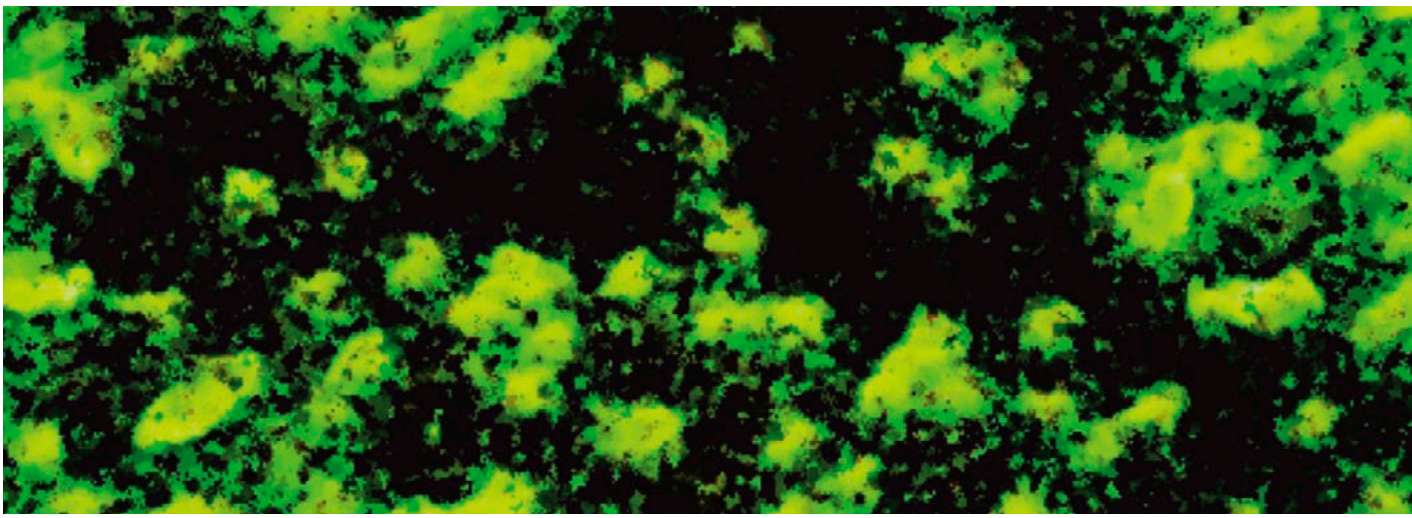

Annual Report 2016

Electrochemistry Laboratory

Cover
Elemental mapping of the surface of a proton conducting fuel cell membrane prepared by swift heavy ion beam irradiation and grafting. Green areas (sulfur) indicate ion conducting domains (diameter around 1 micron), black areas (fluorine) the insulating matrix.

PAUL SCHERRER INSTITUT

Annual Report 2016

Electrochemistry Laboratory

Paul Scherrer Institut
Electrochemistry Laboratory
5232 Villigen PSI
Switzerland

Secretary
Phone +41 56 310 29 19
Fax +41 56 310 44 15

Hardcopies of this report are available from

Cordelia Gloor
cordelia.gloor@psi.ch
Paul Scherrer Institut
5232 Villigen PSI
Switzerland

A full version of this report is also available on the web
http://www.psi.ch/lec

Publisher
Electrochemistry Laboratory
Paul Scherrer Institut
5232 Villigen PSI
Switzerland

Editorial Team
Cordelia Gloor / Peter Lutz
Lorenz Gubler
Thomas J. Schmidt

Printing
Paul Scherrer Institut

ISSN 1661-5379
DOI: 10.3929/ethz-a-007047464
PSI Electrochemistry Laboratory :: Annual Report 2016

CONTENTS

Electrocatalysis & Interfaces

93 The Electrochemistry Laboratory

Facts & Figures

EDITORIAL

PSI's Electrochemistry Laboratory is the leading center for electrochemical research in Switzerland, which manifests itself in the great variety of different ongoing projects. We can proudly claim that our approach of bridging fundamental electrochemical science with applied electrochemical engineering is even unique on international standards as it always allows us to keep a systemic view even when we are addressing basic scientific questions. Significant parts of our groups are partners within the Swiss Competence Centers for Energy Research (SCCERs) *Mobility* and *Heat & Electricity Storage*, respectively. These centers have been inaugurated in 2014 and are multi-year programs addressing the challenges of the Swiss Energy Strategy. In the past year, both competence centers could successfully secure their assets for the funding period 2017–2020, an important step for all participating partners to transition their research from the first three years of operation into more applied development of new technologies and increase their technological readiness levels.

One major project within PSI's Energy & Environment Division over the last two years has been the design and construction of the Energy System Integration (ESI) Platform, a container-based flexible energy storage platform on the 100 kW level in which all laboratories of the division are collaborating. The ESI Platform was officially inaugurated in fall 2016. Within the demonstrator, the Electrochemistry Laboratory is responsible for the so-called Hydrogen Pathway, in which a 100 kW electrolyzer is operated to produce pressurized H_2 and O_2 using fluctuating renewable power. Both gases are stored for later re-electrification purposes using highly-efficient H_2-O_2 Polymer Electrolyte Fuel Cells developed and built in collaboration with our industrial partner Swiss Hydrogen SA.

In this Annual Report 2016, you will not only find details on PSI's Electrochemistry Laboratory and the SCCER *Heat & Electricity Storage*, but also some short insights into ongoing projects and activities, summarized in more than 43 short reports authored by our researchers demonstrating some of our contributions to the grand challenge of electrochemical energy storage and conversion. In addition, some key facts and figures from 2016 are given, including a full list of our more than 62 publications and numerous talks demonstrating the leading role PSI's Electrochemistry Laboratory is playing internationally.

In April 2016, we could again attract world-class scientists as speakers for our annual international PSI Electrochemistry Symposium whose topic was «Electrolytes – The Underestimated Player in Electrochemical Processes» attracting an audience of more than 120 participants. The internationally well-known speakers (T. Norby, University of Oslo, Norway; K.D. Kreuer, MPI für Festkörperforschung Stuttgart, Germany; W. Wieczorek, Warsaw University of Technology, Poland; T. Abe, University of Kyoto, Japan; T.A. Zawodzinksi, University of Tennessee, USA) certainly helped to attract this interested audience; details of this event you will find also in this annual report on page 106.

2016 was also a successful year for 13 of our PhD students who successfully defended their theses. I am happy that all of the new PhDs were able to directly continue their careers either in an academic or industrial environment.

At this point it needs to be mentioned that all our projects and results could not have been achieved without the funding we received over the years from industrial partners and the different funding agencies in Switzerland and abroad. We, therefore, would like to take this opportunity to thank all our funding sources hoping to continue our successful collaborations in the years to come.

Thomas J. Schmidt

THE ELECTROCHEMISTRY LABORATORY AT A GLANCE

Our Mission

Advancement of electrochemical energy storage and conversion by

- **developing novel electrochemical materials, cells and devices;**
- **providing insights into electrochemical materials, cells and device properties.**

PSI's Electrochemistry Laboratory is Switzerland's largest Center for Electrochemical Research with around 70 employees. Our mission is to advance the scientific and technological understanding of electrochemical energy storage and conversion specifically in the context of a sustainable energy system, in which renewable energy is required to be stored in secondary batteries or chemicals (as e.g., hydrogen) and (re-)converted into electricity. Our applied fundamental R&D, hence, is focused on devices like secondary batteries – specifically Li- and Na-based systems –, polymer electrolyte fuel cells and electrolyzers, as well as redox flow cells, respectively.

As a research institute's laboratory we are bridging the gap between fundamental science and applied engineering by combining both academically as well as industrially relevant questions. For all outlined devices we not only develop fundamental understanding of materials on atomic and molecular level (electrochemical materials sciences and electrocatalysis), but also on the applied development of technical cells and devices, e.g., fuel cell systems.

On all technical complexity levels, we are developing and utilizing advanced *in situ* and *operando* diagnostic tools to gain insights in properties and processes from the nanometer to the centimeter scale, respectively, often making use of PSI's unique large scale facilities such as the Swiss Light Source (SLS) and the Swiss Neutron Spallation Source (SINQ).

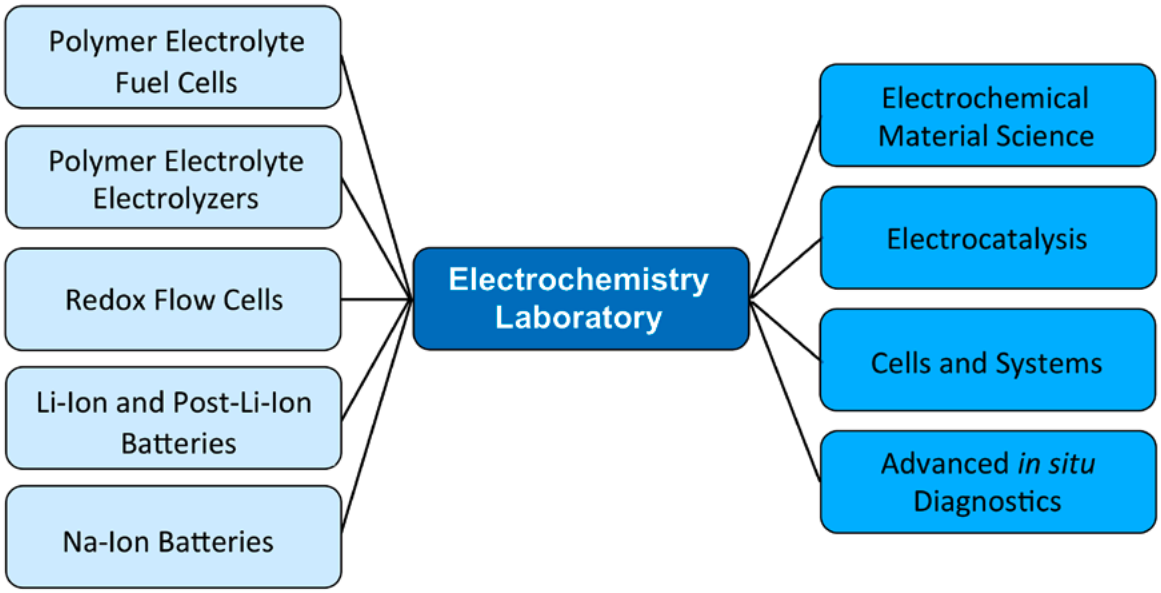

Electrochemical energy storage

The vision of the Electrochemical Energy Storage Section is the development of the best energy storage system.

We work on rechargeable batteries which are mainly lithium and sodium based. The scientific goal is a profound understanding of electrochemical processes in complex non-aqueous systems. In particular, of utmost scientific interest are the numerous interactions of all components of electrochemical energy storage systems (batteries, supercapacitors, and hybrids) determining the safety and life time of such systems.

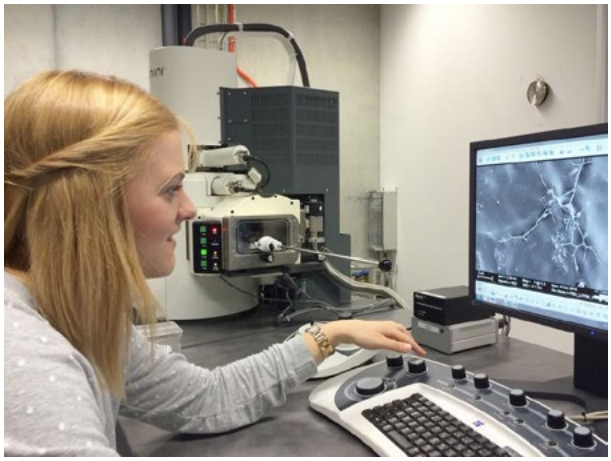

SEM/EDX technique to probe morphology of battery components.

The work equally considers the synthesis of novel materials for electrochemical energy storage, the modification of known materials (e.g., carbon) and material characterization, keeping in mind the entire span from basic science to industrial applications. To answer the scientific questions, we develop various sophisticated *in situ* and *operando* methods for use in the field of non-aqueous solid-state electrochemistry and investigate the physical and electrochemical properties of insertion materials and electrochemical interfaces *in situ*. Also, we do electrochemical engineering work on three-dimensional electrodes and characterize industrial batteries.

Electrochemical energy conversion

The Electrochemical Energy Conversion Section is focused on the development and in-depth understanding of materials, processes and devices for the conversion of renewable energy into electricity or chemical energy carriers. Especially in the context of a sustainable energy system utilizing hydrogen as an energy carrier, its electrochemical energy conversion is of particular importance.

In this topical context our goal is the in-depth understanding of technologies like Polymer Electrolyte Fuel Cells (PEFC), Polymer Electrolyte Water Electrolyzers (PEWE) for water electrolysis and processes like the co-electrolysis of CO_2 and water, respectively. In addition, we are focusing on materials development for Redox Flow Cell systems.

The R&D strategy involves activities on four pathways:

- system, stack and cell engineering;
- membrane development based on PSI's own radiation-grafting technology and the development of cell components;
- research in electrocatalysis and the reaction kinetics of the important reactions (e.g., the oxygen electrode reactions) for improved understanding of intrinsically limiting factors; and
- the development and application of advanced *in situ* and *operando* diagnostic tools on stack, cell and component levels including analyses of the electrode-electrolyte interface.

Fuel cell system testing. Experimental set-up for advanced start/stop investigation.

ENERGY STORAGE RESEARCH IN SWITZERLAND

The SCCER Heat & Electricity Storage highlights of Phase I

Thomas J. Schmidt, Jörg Roth

The SCCER Heat and Electricity Storage (HaE) is dedicated to energy storage research, the first three years were completed successfully and the second funding period till 2020 has begun. It is about time now to report some highlights from the different fields of research of the SCCER.

The energy turnaround, replacing fossil and nuclear by renewable sources, is facilitated if energy storage solutions become available in line with the progress of the transition towards renewable energy sources.

During Phase I (2014–2016) of the SCCER Heat and Electricity Storage a variety of storage technologies were investigated. Among the different research projects, the following examples show extraordinary potential to become relevant within the scope of ES 2050 [1] and therefore selected as highlights of Phase I of the SCCER HaE.

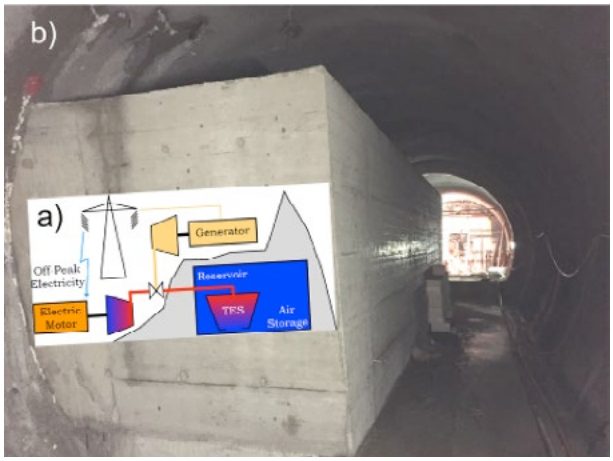

Figure 1. *a) Working principle of AA-CAES*
b) TES container inside the demonstration plant.

Adiabatic compressed air energy storage

Andreas Haselbacher, ETHZ
Sophia Haussener, EPFL
Maurizio Barbato, SUPSI
ALACAES, Biasca

The growing share of fluctuating renewable energy sources like wind and solar requires short- and long-term energy storage to guarantee the power supply. Pumped hydro storage is at present the main option for large-scale storage.

Pumped hydro storage is available since little more than 100 years and the massive capacity build up started in the 1970's. Therefore the best locations for such installations are already explored. One promising alternative to pumped hydro storage is advanced adiabatic compressed air energy storage (AA-CAES). The working principle is depicted in Figure 1a. In contrast to the diabatic form of CAES, which has been proven for several decades at the industrial scale with the plants in Huntorf (Germany) and McIntosh (USA), AA-CAES stores the heat generated during air compression in a thermal energy storage (TES). During expansion, the heat is recovered from the TES by the air, leading to an increase of potential round-trip efficiencies from around 45–50 % to more than 70 %. Compared to diabatic CAES, AA-CAES has the additional advantage of not requiring the burning of fossil fuels; during operations, AA-CAES does not emit CO_2. In Phase I, the basic concepts were investigated on lab scale and at the end a demonstration plant was commissioned (Figure 1b). In Phase II, the plant will be operated producing real life data for further systemic investigations. The close collaboration of three research groups and the industrial partner enabled the fast progress, supported by project funding from the CTI SCCER- and the NRP 70 programme. [2–4]

Sodium ion batteries

Claire Villevieille, PSI
Maksym Kovalenko, ETHZ/ Empa

Batteries are the most energy efficient way to store electricity since no transition between energy carriers take place. Electrical charge in, electrical charge stored, electrical charge out. Therefore it is the first storage option when it comes to store surplus electricity. From a high level perspective, the drawbacks are solely of economical nature.

From a technical point of view, the economic argument splits to safety, durability, performance and bills of material questions needed to be optimized for the specific application.

For stationary use, weight and volume constraints on batteries are less demanding than for mobile applications, therefore a reduced/lower power density is acceptable if there is a cost advantage associated.

Due to the abundance of sodium in the Earth's crust, sodium ion (Na-ion) batteries could be a more economical alternative to lithium-ion (Li-ion) batteries. Early in Phase I of the SCCER, the straightforward approach to use materials which are well known from Li-ion batteries and replace the active material only proved not feasible. Alternative electrode binders and electrodes for anodes and cathodes were developed. At the end of Phase I of the SCCER HaE, a Na-ion battery, composed of novel anode material based on bio-waste material (almond shells) and P2-$Na_{0.67}(Mn_{0.6}Fe_{0.25}Co_{0.15})O_2$ cathode demonstrates the achievements (Figure 2).

It can be seen that the cycle stability gives room for improvement, which is one of the aims for Phase II of the SCCER. [5, 6]

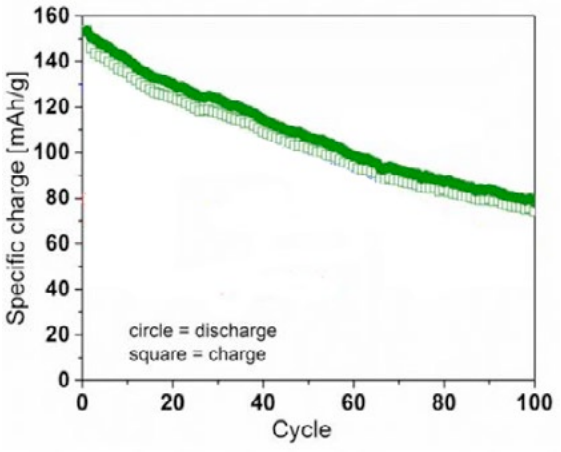

Figure 2. *Cycle stability of Na-ion battery at end of SCCER Phase I, electrodes pre-conditioned.*

Hydrogen production via redox flow battery

Hubert Girault, EPFL

Storing energy in the context of renewable electricity is a multi-time-scale topic. It is necessary to account for short term shading effects of passing clouds on solar panels (seconds/minutes) up to periods of overcast sky, fog and absence of wind (days/weeks). Not to forget day and night load balancing. Redox flow batteries (RFB) offer a solution for such challenges since due to its principle, power and storage capacity are decoupled, other than in regular batteries having «built in fuel» electrodes.

Like in fuel cells, the redox flow cell is supplied with external fuel (electrolyte). Like an accumulator the process is fully reversible in one device. Since the electrolytes are in liquid phase, storing them is straightforward (plastic containers can do the job). However, the downside of RFB is a low energy density and the relatively low energy efficiency of (80–85 %) compared to other batteries. This limits the use of RFB to niche applications so far, but makes them interesting for research.

During Phase I of the SCCER HaE, an idea was formulated: If the redox couple were Cerium (III/IV) combined with Vanadium (II/III) as electrolytes, a parallel catalytic reaction can produce hydrogen and oxygen, thus the cell can do electrolysis once the electrolyte is fully charged (see Figure 3a). This is interesting for processes which require a continuous stream of hydrogen, like biogas-upgrading at waste water treatment plants.

A commercially available Vanadium (IV/V) Vanadium (II/III) flow cell was installed at the Martigny waste water treatment plant in the beginning of Phase I. Along with the installation, the hydrogen formation process based on a Molybdenum Carbide catalyst was investigated. A reactor for hydrogen formation was designed and tested. The hydrogen production rate of the current design is about 20 g/hr but can easily be scaled-up.

While during Phase I the hydrogen production reaction has come from the idea to a prototype system, the Cerium (III/IV) to oxygen idea could not be realized in straightforward manner due to material incompatibilities within the flow cell. Several ideas for the design of the Vanadium (IV/V) discharge process exist and the process development is subject for Phase II of the SCCER HaE.

Not only the flow cell as large technical installation exists in Martingy but also a hydrogen fueling station and a 50 kW electrolyzer was installed (see also the highlight of demonstrators within SCCER HaE). [7]

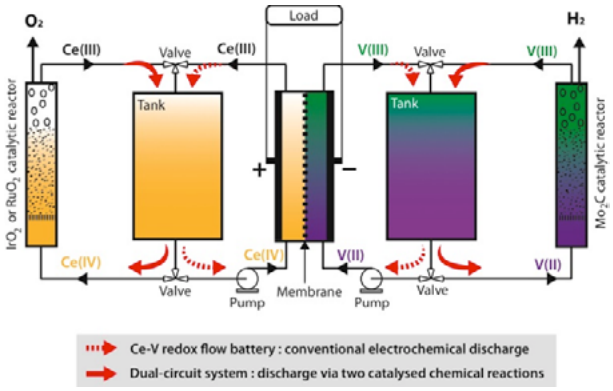

Figure 3. *RFB concept with hydrogen /oxygen production.*

Elecrochemical CO_2 conversion

Thomas J. Schmidt, PSI
Christophe Copéret, ETHZ
Peter Broekmann, Uni Bern

In terms of grid scale storage options, the question remains how to deal with surplus electricity (once all the available high efficiency storage options are exhausted). Can one afford to allow for curtailment, shall the energy be stored in a chemical compound at lower cycle efficiency but for long time scales?

The latter becomes an interesting option if seasonal or transportation aspects are considered. Also organic chemistry, not relying on fossil feedstock, becomes an option if the conversion process of CO_2 and H_2O to CH_4 or other low molecular hydrocarbons (e.g. methanol or formic acid) is mastered in an efficient manner.

Syngas reaction (Sabatier Process) is known for a long time, but the harsh conditions of this process in terms of pressure and temperature and the need for a separate upstream hydrogen generation are the drawbacks of the state of the art systems for producing CH_4.

Alternatively, electrochemical processes producing selectively certain organic compounds based on CO_2 and H_2O in one device are envisioned (Figure 4). In Phase I of the SCCER, this concept was evaluated on all scales. Work was done on theoretical modeling of reaction mechanisms, synthesis and characterization of selective catalysts, design of electrodes and characterization in an electrochemical cell. Copper and gold were investigated as electrode material of choice and it was found that the surface morphology is key for the selectivity of the reaction. In terms of electrochemical performance of the cell, first experiences were gained and the specific requirements on the cell design and components like membrane and gas distributors were gained. Figure 4b depicts the products gained in the electrochemical test at different current densities.

The proof of principle was presented during Phase I, including economic considerations for identifying the best product (formic acid and methanol were found to be economically most interesting as well as CO). In Phase II the focus is set on electrochemical CO_2 reduction with the aim to come up with a 1 kW co-electrolyzer. [8, 9]

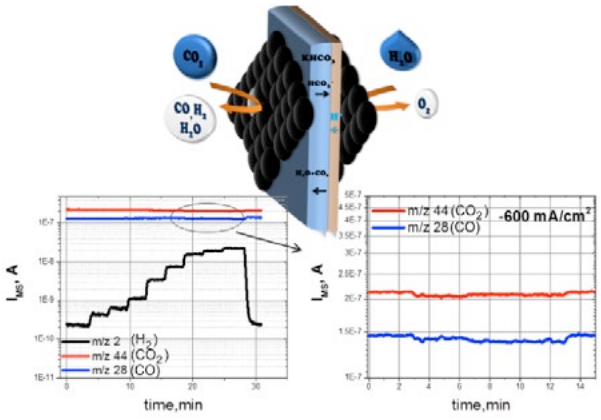

Figure 4. *Scheme and results of CO electrolysis cell.*

Assessment of energy storage in Switzerland

Martin Patel, UniGenf
Christan Bauer, PSI
Jörg Worlitschek, HSLU

Besides all the technical solutions for energy storage, whether they are state of the art or exist only in concepts, the economic, regulatory/legal and environmental aspects are key for future implementation of storage in the energy grid.

At beginning of Phase I the system assessment group (a collaboration of three institutes) developed the tools necessary to conduct studies on economic and environmental scenarios around energy storage technology. The tools were further developed and a comprehensive study on different storage options in terms of their costs and greenhouse gas emissions are the highlight of Phase I. A ranking for storage options, depending on cycle time is given. At a system size of 1 MW for short (<1 min) term storage, battery systems are most economic and associates with the least green-house gas emissions, while for medium term storage (day), battery is still advantageous in terms of cost, but not in terms of greenhouse gas emissions. Batteries fall behind pumped hydro and adiabatic air storage (see Figure 5). Also a closer look at the economics of power to gas was taken. Here the key message was that methane or even hydrogen production is economically viable only if additional services can be provided.

In Phase II, the assessment of technologies developed within the SCCER, like thermal energy storage and the demonstrators will be included on technological, energy system and national economic level. [10]

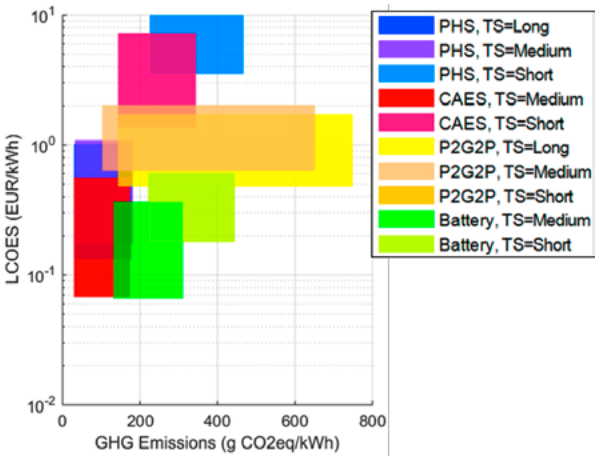

Figure 5. *Cost and greenhouse gas footprint of different storage options at a system size of 1 MW.*

Demonstrators within SCCER HaE

Markus Friedl, HSR
Peter Jansohn, PSI
Hubert Girault, EPFL

Many concepts for energy storage exist on paper, on material level and lab scale devices. The assessment of the concepts in terms of their suitability for everyday use can be done only on demonstrators of power and capacities of about 1/100 to 1/10 below the dimensions of the real application.

Two such demonstrators are described in separate highlights (AA-CAES and RFB) with hydrogen production and the hydrogen filling station (Figure 6a, b). Within the SCCER, three more demonstrator projects can be reported. Already at the beginning of Phase I the 25 KW power to gas plant at the HSR in Rapperswil was put into operation and over two years experience with this plant was gathered. One year of operation was dedicated to study the interaction with a gas powered vehicle. While the second year dealt with gas grid injection. Another variable of this system was the CO_2 source. Captured CO_2 from air (Climeworks), raw biogas and compressed CO_2 were used. The main results of the operation are summarized in a balance of plant (Figure 6c).

The energy system integration platform (ESI), an installation with increased complexity was commissioned in Phase I of the SCCER (Figure 6d). Here, the interplay of different conversion type storage systems is explored on a 100 kW scale. Here energy storage via hydrogen and methane, also in combination of biogenic carbon sources like wet and dry biomass, is investigated. The modular layout of the ESI comprises a 200 kW PEM electrolyzer, gas purification, 100 kW PEM fuel cell, a container-based system for methanation of dry and wet biomass and a gas storage facility. The system is (virtually) coupled with a PV installation to provide realistic operating conditions for the electrolyzer. In Phase I the ESI was mainly designed and erected. Most systems were installed by end of 2016. In early 2017, the most components installed on the platform will be available for experiments.

Figure 6. *a) top left: Hydrogen filling station.*
b) top right: Site of the RFB at Martigny.
c) lower left: Power to gas unit Rapperswil.
d) lower right: Energy system integration platform at PSI.

It is planned that the ESI will be part of a demonstrator network together with NEST and MOVE, both at Empa allowing for the exchange of load profiles and response feedback. It is expected that by the end of Phase II the ESI platform will generate the data needed for detailed economic assessment of the different storage paths. [7, 11, 12]

Acknowledgement

We kindly acknowledge the CTI Energy Program for the SCCER HaE support, the SNF, BFE and CCEM for supporting the activities of the SCCER HaE.

References

[1] Energy Strategy 2050, http://www.bfe.admin.ch/energiestrategie2050/index.html?lang=de, Accessed April 20, 2017.
[2] L. Geissbühler, V. Becattini, G. Zanganeh, A. Haselbacher, A. Steinfeld, *SCCER HaE Storage – Annual Activity Report 2016*, 5 (2016).
[3] S. Zavattoni, M. Barbato, L. Geissbühler, A. Haselbacher, G. Zanganeh, A. Steinfeld, *SCCER HaE Storage – Annual Activity Report 2016*, 7 (2016).
[4] I. Ortega-Fernández, S. Zavattoni, J. Rodríguez-Aseguinolaza, M. Barbato, B. D'Aguanno, *SCCER HaE Storage – Annual Activity Report 2016*, 9 (2016).
[5] M.V. Kovalenko, *SCCER HaE Storage – Annual Activity Report 2016*, 22 (2016).
[6] J. Cabañero, C. Marino, C. Villevieille, *SCCER HaE Storage – Annual Activity Report 2016*, 24 (2016).
[7] V. Amstutz, C. Dennison, H. Vrubel, E. Zanzola, A. Battistel, H.H. Girault, *SCCER HaE Storage – Annual Activity Report 2016*, 37 (2016).
[8] A. Dutta, A. Kuzume, M. Rahaman, V. Kaliginedi, A. Zanetti, N. Luedi, M. Mohos, P. Broekmann, *SCCER HaE Storage – Annual Activity Report 2016*, 53 (2016).
[9] A. Pătru, T.J. Schmidt, SCCER HaE Storage – Annual Activity Report 2016, 55 (2016).
[10] D. Parra, M.K. Patel, X. Zhang, C. Bauer, A. Abdon, J. Worlitschek, *SCCER HaE Storage – Annual Activity Report 2016*, 59 (2016).
[11] M. Friedl, B. Meier, E. Frank, *SCCER HaE Storage – Annual Activity Report 2016*, 63 (2016).
[12] P. Jansohn, M. Hofer, T. Schildhauer, *SCCER HaE Storage – Annual Activity Report 2016*, 65 (2016).

SCIENTIFIC ACHIEVEMENTS 2016

Fuel Cells & Electrolysis –

Materials & Diagnostics

Comonomer selection for radiation-grafted membranes in water electrolyzer cells

A. Albert, U. Babic, T.J. Schmidt, L. Gubler
phone: +41 56 310 4539, e-mail: albert.albert@psi.ch

Polymer electrolyte membranes in a water electrolyzer fulfil the function of a proton conductor, gas separator, and electric insulator. In addition to these primary functions, the membrane is expected to be physically robust, chemically stable, and of low cost.

Thick perfluorosulfonic acid (PFSA) membranes, such as Nafion N115 and N117 with a dry thickness of 125 and 180 µm, respectively, are commonly used in polymer electrolyte water electrolyzers (PEWEs). These thick membranes are relatively stable, and have acceptable gas barrier and mechanical properties. However, thick membranes create relatively large ohmic resistances, which become the dominant loss term at high current densities. Cost is also one of the main disadvantages of these perfluorinated materials. In addition, these membranes are not suited for temperatures above 90 °C due to loss of mechanical integrity. Therefore, further research is required to improve the membranes or find alternative materials.

Polymer electrolyte membranes prepared by radiation-induced grafting are another promising option. Advantages of the radiation-induced grafting method are its versatility and a potentially low-cost fabrication process. The properties of radiation-grafted membranes can be readily modified by varying the composition and architecture of the graft copolymer. An adequate monomer/comonomer selection or combination can be chosen to obtain a membrane with desired properties.

Radiation grafted-membranes which contain a monomer with α-protected position, such as α-methylstyrene (AMS), are known to be more stable during the thermal stress test than those that contain a monomer without α-protected position, such as styrene (St). In addition, the AMS-based radiation-grafted membranes exhibit lower hydrogen crossover and area resistance than Nafion N115 and N117 membranes [1].

In this work, focused on improving the radiation-grafted membranes, an alternative comonomer which readily copolymerizes with AMS is sought. Isoprene, isobutylene, methyl methacrylate, butyl acrylate, styrene, acrylonitrile, methacrylonitrile, divinylbenzene, are known to be able to copolymerize with AMS [1–8]. The polymerization of AMS with itself is known to be difficult due to the low ceiling temperature of around 61 °C [9].

Experimental

Various comonomers are tested in a similar grafting condition to that of the preparation of AMS/AN radiation-grafted membranes with a 5 kGy preirradiated 50 µm poly(ethylene-co-tetrafluoroethylene) (ETFE) base film. The preparation conditions are described elsewhere [1]. Instead of acrylonitrile (AN), other monomers are used to assess their readiness to copolymerize with AMS. A monomer is categorized as suitable for the copolymerization with AMS if the obtained graft level is more than 5 % after 24 h under the used preparation conditions.

The reaction time and conditions were adjusted accordingly to obtain a given target graft level with the new comonomer. The membranes containing the new comonomer were evaluated in a water electrolyzer and fuel cell, and compared with the N117 membrane and membranes containing acrylonitrile (AN) comonomer.

Results

In search of another suitable comonomer for AMS, following criteria are used. The monomer should be commercially available and of low cost. It should have a protected α-position as in AMS or have additional functionality, e.g. a nitrile functional group to improve the gas barrier property of the membrane. Table 1 shows the chemical structure of selected co-monomers and their readiness to copolymerize with AMS.

Comonomer	Chemical structure	Readiness
Acrlyonitrile		yes
2-Methyleneglutaronitrile	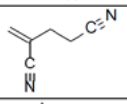	yes
2-Methyl-2-butenenitrile	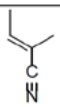	no
Methacrylamide		no
Isopropenyl acetate	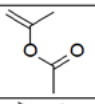	no
3-Chloro-2-methyl-1-propene		no
Propargyl alcohol		no

Table 1. *Chemical structure of selected comonomers and their readiness to copolymerize with AMS.*

Only 2-methyleneglutaronitrile (MGN) has been identified in this work in addition to AN as a suitable comonomer for AMS under the used preparation conditions. However, it needs to be pointed out that the other comonomers might also be able to copolymerize with AMS if the reaction conditions favor the reaction or other polymerization methods are utilized.

In order to obtain the desired graft level, adjustments in irradiation dose to 100 kGy, solvent to dichloromethane, and reaction temperature to 50 °C have to be made for the membrane preparations containing MGN comonomer. The desired graft level of 50 % is reached after a reaction time of around 28 h for AMS/MGN and 47 h for AMS/MGN/DiPB membranes under the adjusted preparation condition. Figure 1 shows the structure of radiation-grafted membranes with MGN and AN comonomers.

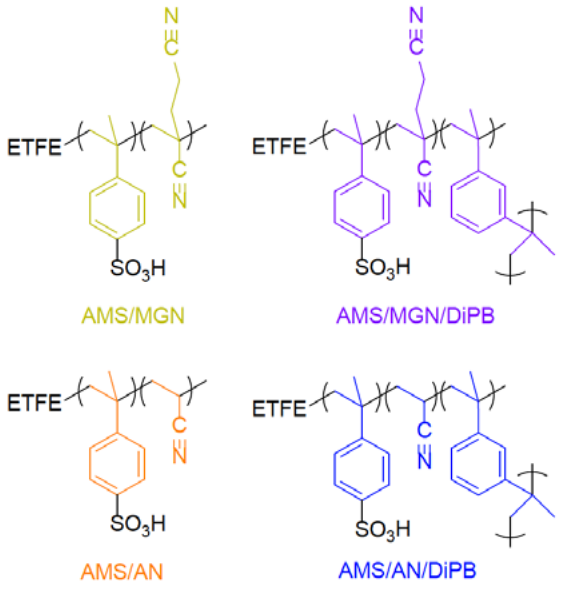

Figure 1. *Chemical structure of radiation-grafted membranes with MGN and AN comonomers.*

Figure 2 shows the polarization curve of catalyst coated membranes (CCMs) made from Nafion N117 and radiation-grafted membranes. The radiation-grafted membranes show a better performance than N117. The membranes with the new MGN comonomer, which are based on ETFE 25 µm base film, have a better performance than the membranes with the AN comonomer, which are based on ETFE 50 µm base film. The addition of 1,3-diisopropenylbenzene (DiPB) crosslinker lowers the performance of the radiation-grafted membranes. However, the crosslinker is known to increase the stability of membranes [1].

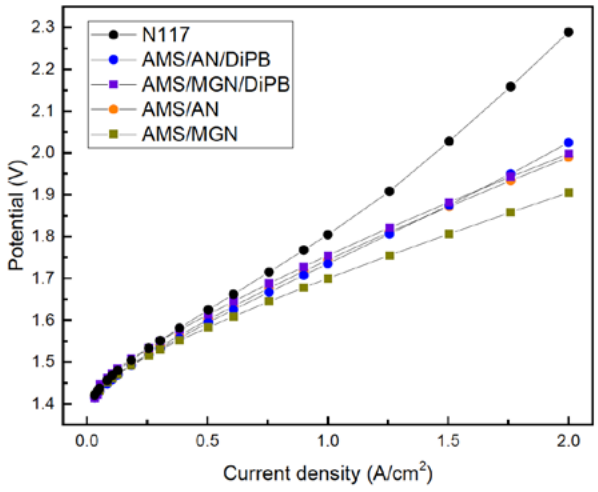

Figure 2. *Polarization curve of CCMs made from various membranes in a water eletrolyzer at 60 °C and 1 bar pressure.*

Figure 3 shows the hydrogen crossover vs. area resistance (property map) of various membranes obtained in a water electrolyzer and fuel cell configuration (inset). The radiation-grafted membranes exhibit lower hydrogen crossover values than the N117 membrane in both water electrolyzer and fuel cell tests.

The membranes with MGN comonomer show lower hydrogen crossover than the membranes with AN comonomer, although with a dry thickness of around 40 µm they are thinner than the membranes with AN comonomer with a dry thickness of around 65 µm. Two nitrile groups in MGN instead of one as in AN improve the gas barrier properties of the membranes.

The area resistance of the radiation-grafted membranes is lower than that of the N117 membrane in the fuel cell tests (inset). In the electrolyzer tests, the membranes containing MGN monomer have similar resistance to N117 membrane, and higher than the membranes with AN comonomer. This is in contrast with the membrane's performance in the water electrolyzer tests. The additional area resistance might come from the contact resistance of the extra porous carbon layer, which is added to compensate for the thickness difference of the membranes in the cell.

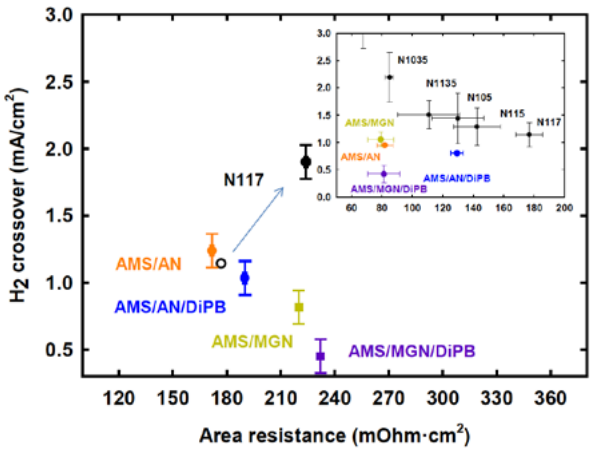

Figure 3. *Property map of various membranes in water eletrolyzer and fuel cell (inset) tests.*

The membranes with MGN monomer, which show better performance, lower hydrogen crossover, and lower/similar area resistance than Nafion N117 membrane and the membranes with AN monomer, are promising alternative membranes for the water electrolyzer application.

Acknowledgement

The research leading to these results has received funding from the European Union's Seventh Framework Programme (FP7/2007-2013) for the Fuel Cells and Hydrogen Joint Technology Initiative under grant agreement n°303484 (NOVEL).

References

[1] A. Albert, T. Lochner, T.J. Schmidt, L. Gubler, *ACS Appl. Mater. Interfaces* **8** (24), 15297–15306 (2016).
[2] F.A. Bovey, *J. Polym. Sci.* **62**, 197–209 (1962).
[3] L.J. Fetters, M. Morton, *Macromolecules* **2**, 453–458 (1969).
[4] A. Rudin, M.C. Samanta, *J. Appl. Polym. Sci.* **24**, 1665–1689 (1979).
[5] D. Li, R. Faust, *Macromolecules* **28**, 4893–4898 (1995).
[6] N.T. McManus, A. Penlidis, M.A. Dube, *Polymer* **43**, 1607–1614 (2002).
[7] J.Y. Li, F. Muto, T. Miura, A. Oshima, M. Washio, S. Ikeda, M. Iida, Y. Tabata, C. Matsuura, Y. Katsumura, *Eur. Polym. J.* **42**, 1222–1228 (2006).
[8] L. Gubler, M. Slaski, A. Wokaun, G.G. Scherer, *Electrochem. Commun.* **8**, 1215–1219 (2006).
[9] H.W. McCormick, *J. Polym. Sci.* **25**, 488–490 (1957).

Polymer electrolyte water electrolyzer degradation: Effects of variable operating conditions on the performance and gas purity

U. Babic, S. Koch, T.J. Schmidt, L. Gubler
phone: +41 56 310 5629, e-mail: ugljesa.babic@psi.ch

Polymer electrolyte water electrolysis (PEWE) is a promising energy conversion technology to valorize excess electricity from fluctuating renewable sources in the form of hydrogen. If the PEWE is to be deployed to serve as an energy storage technology in the grid, the potential challenges related to the component durability need to be understood and addressed. The PEWE industry has demonstrated several systems operating over 30,000 hours with degradation rates in the range of 2–4 µV/h [1, 2, 3]. Systems with a lower content of precious metals in terms of protective coatings and catalysts show degradation rates ranging from 30–600 µV/h [4, 5], with significantly shorter lifetimes. Moreover, the effect of variable operating conditions on the component degradation is still not very well understood.

New materials development towards less expensive and durable PEWE components would greatly benefit from the systematic understanding of failure modes and enable establishing accelerated stress-tests (ASTs) to trigger and promote specific degradation mechanisms.

Experimental

In this work, we present the effect of current on/off cycling over 100 h on the cell performance and gas purity. The current was cycled stepwise between 0.032 A/cm^2 and 2 A/cm^2, in 30 second intervals. A square 25 cm^2 cell was used, with titanium (Ti) sintered porous transport layers (PTLs) with thickness of 1 mm and average porosity of 10 µm. Water was fed to both anode and cathode cell compartments at 300 ml/min flow rate to ensure that the catalyst coated membrane (CCM) remains hydrated. Two CCMs with Nafion 115 (N115, dry thickness 125 µm) and Nafion 117 (N117, 175 µm) were stored for 24 h in 18 MΩ water before the assembly. The cell with the assembled CCM was heated up to 60 °C and held at this temperature until the minimum of area resistance (measured at 1 kHz with AC milliohm meter) was observed. The current was cycled between 1 and 2 A/cm^2 with 5 minute holding time until the cell voltage stabilized at the respective operating point. After this conditioning, polarization curves were measured galvanostatically, with measurement times of 5 minutes per point.

Results

Under the testing conditions explained before, the N117 and N115 based CCMs exhibited degradation rates of 350 µV/h and 880 µV/h at 1 A/cm^2, respectively. Based on the fact that the thicker CCM showed less performance decay (Figure 1), it is most likely that the degradation is coming from the cationic contamination of the proton-exchange sulfonic acid group sites in the membrane and the catalyst layer ionomer. The conductivity of the water from the cathodic loop increased from 1.3 µS/cm to 4.6 µS/cm after 100 h. Metal cations accumulate in the water over time. Because of the difference of concentrations in the water and membrane and the applied electric potential, metal cations diffuse and migrate through the membrane, occupying the proton-exchange sites and reduce the ionic conductivity of the CCM. The area resistance increases from 215 to 221 and 164 to 187 mΩ·cm^2 for N117 and N115, respectively.

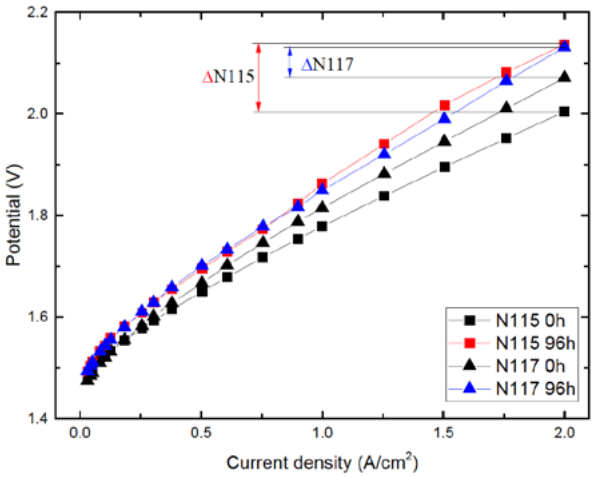

Figure 1. *Polarization curves of N115 and N117 based CCMs before and after 100 h of start-stop cycling, at 60 °C, 1 bar.*

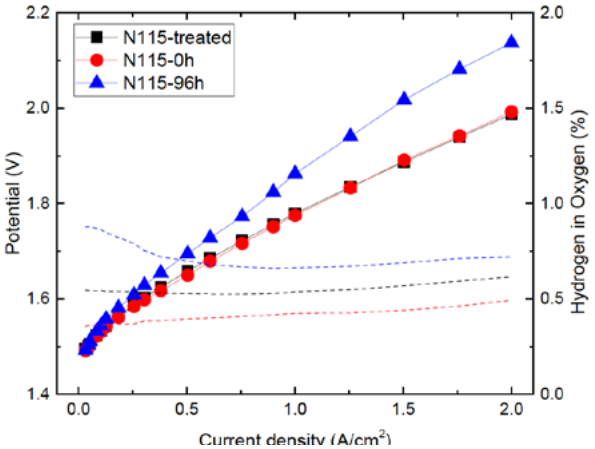

Figure 2. *Polarization curves of a N115 based CCM at BOL (●), after 100 h of start-stop (▲), and after regeneration in 0.5 M H_2SO_4(■). Dashed lines show the H_2 in O_2 measured during the polarization curves.*

The more heavily degraded N115 CCM was re-protonated in 0.5 M H_2SO_4 for 2 hours, and rinsed with 18 MΩ water before re-assembly using the same PTLs and BPPs as in the initial experiment. Polarization curves indicate that the degradation is mostly reversible, and is attributed to cationic contamination (Figure 2). The initial (0 h) polarization curve exhibits slightly higher potentials at low current densities compared to the one from the regenerated CCM, indicating that the catalytic properties might have changed during the start-stop cycling procedure. It also shows lower potentials at current densities above 1 A/cm^2, indicating lower ohmic losses.

It also shows lower potentials at current densities above 1 A/cm^2, indicating lower ohmic losses. The CCM could have been initially contaminated to a certain extent, and the contamination level was reduced below the initial one after re-protonation. Interestingly, the hydrogen crossover has increased during 100 h of testing. The increase of the hydrogen crossover over time can be attributed either to the loss of material through the chemical decomposition of the membrane, or the local thinning through the creep of material into the PTL pores.

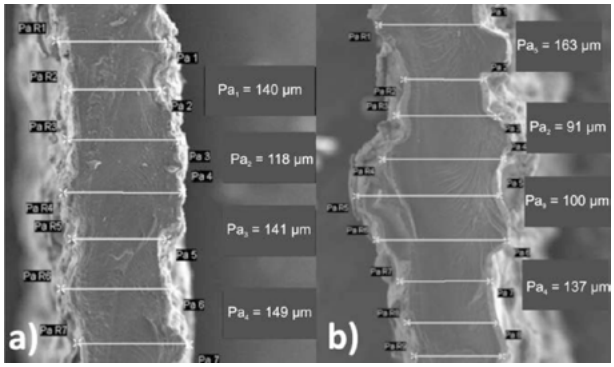

Figure 3. *Cross section of a N115 CCM after a) 1 hour of testing, b) 100 h of start-stop cycling.*

A pristine N115 based CCM was assembled in the cell, conditioned, operated for 1 hour, and analyzed under the scanning electron microscope (SEM) to investigate whether the operating conditions have an influence on the creep of the material (Figure 3a). The CCM was used in the electrolyzer for 1 h shows a much more even thickness profile compared to the CCM that had undergone start-stop operation (Figure 3b). By taking distance measurements at different positions of the two CCMs, we observe that the membrane has thinned during operation. The tails of the thickness distribution in the histogram (Figure 4) of the CCM operated for 100 h are more pronounced, indicating material creep into the PTL pores over time, assumedly under prolonged exposure to higher temperatures.

Additionally, as the current is cycled between on and off states in short intervals, the temperature of the CCM is cycled due to excess heat produced. The average thickness is also lower, indicating an overall thinning of 19 µm. The thinning would be further promoted by iron or copper cation contaminating the CCM, as they catalyze the decomposition of H_2O_2 into radicals, which attack the membrane polymer and cause chain scission [2].

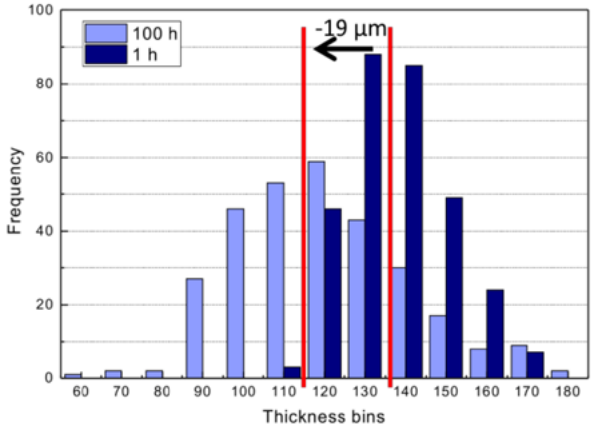

Figure 4. *Histogram of thickness of the N115 based CCMs after 1 h of testing and 100 h of start-stop cycling, respectively. Red lines indicate the average thickness.*

Conclusion and outlook

Without an ion exchanger in the water recirculation loop, the contamination of the CCM with metal cations seems to be the prevailing mechanism of performance deterioration of the PEWE. A voltage increase of of 880 µV/h at 1 A/cm^2 was observed for the N115 based CCM during 100 h of start-stop cycling. The performance is largely restored after re-protonation of the CCM in 0.5 M H_2SO_4. More research is required to diagnose whether some other degradation stressors play a role together with metal cations to affect the performance decay.

The gas purity is affected as well, as the hydrogen crossover has irreversibly increased over the duration of the experiment. It is difficult to conclude at this stage whether membrane material has been lost as a result of chemical degradation, or only local thinning has occurred through creep. Furthermore detailed investigations are aimed at deconvoluting relevant aging mechanisms and establishing corresponding accelerated stress tests.

Acknowledgment

Funding by the Swiss Federal Office of Energy (SFOE) is gratefully acknowledged.

References

[1] K.E. Ayers, E.B. Anderson, C.B. Capuano, B.D. Carter, L.T. Dalton, G. Hanlon, J. Manco, M. Niedzwiecki, *ECS Trans.* **33** (3), 3–15 (2010).

[2] A.B. LaConti, H. Liu, C. Mittelsteadt, R.C. McDonald, *ECS Trans.* **1** (8), 199–219 (2006).

[3] E. Anderson, oral presentation at the *2nd International Workshop on Durability and Degradation Issues in PEM Electrolysis Cells and its Components*, Freiburg, Germany, February 16–17 (2016).

[4] C. Rakousky, U. Reimer, K. Wippermann, M. Carmo, W. Lueke, D. Stolten, *J. Power Sources* **326**, 120–128 (2016) .

[5] S. Sun, Z. Shao, H. Yu, G. Li and B. Yi, *J. Power Sources* **267**, 515–520 (2014).

Water cluster connectivity in PEFC gas diffusion layers

J. Eller, J. Roth, F. Marone, M. Stampanoni, F.N. Büchi
phone: +41 56 310 2396, e-mail: jens.eller@psi.ch

Automotive fuel cells with state of the art materials and cell structures reach today more than 1 W/cm^2 with current densities up to 3 A/cm^2 [1]. At such high current densities water management becomes more and more important and has to be properly designed on various scales from the system level to nanoscale structures, including all cell components as flow field plates, gas diffusion layers (GDL), the polymer membrane and the catalyst layer (CL). In order to minimize the ohmic losses, the polymer membrane needs to be well humidified [2], however at high current densities performance losses from increased gas transport limitations should be avoided. The accumulation of liquid water in the porous gas diffusion layers, especially under the flow field ribs, results in performance drops due to increased gas transport resistance in particular at the cathode [3–6]. The structure of the liquid water in the GDL is thus the result of the subtle balance between capillary water transport, heat transport, evaporation and condensation in the complex gradients of humidity and temperature in the porous structure.

For optimizing materials and operation strategies, the effects of local water saturation needs to be understood and ultimately controlled. Therfore water cluster connectivity and size are determined by X-ray tomographic mictroscopy (XTM) in cells operating at 80 °C, with current densities up to 3 A/cm^2 for two different gas humidities and for two flow field geometries (rib widths). Further analysis and results can be found in the original publication [7].

Experimental

A specially designed two-channel (0.8 mm width, 0.3 mm depth, 10 mm length) PEFC with graphitic flow fields (Sigracet BMA5 from Eisenhuth GmbH, Germany) was used for the XTM experiments. Two different flow field designs, differing only in the rib width (0.8 and 1.6 mm) were used. As electrochemical components, catalyst coated membranes (H200) from Solvicore (Hanau, D) based on 50 µm dry thickness Nafion membranes were used in combination with Toray TGP-H-060 gas diffusion electrodes (hydrophobized with PTFE, about 10 %) with a hydrophobic microporous layer (Solvicore H200 cathode GDL/MPL). Between the ribs of the flow field, the membrane-electrode assemblies (MEA) were compressed to 450 µm, corresponding to a compression of the GDLs to about 75 % of their initial thickness. The catalyzed domain of the MEA was 16 mm^2 (4.5 mm x 3.6 mm) and fitted completely into the X-ray beam during the XTM scans. Cells were operated at 80 °C cell temperature with H_2/Air at undersaturated (78 % rH; An2) and oversaturated (108 % rH; An3) feed gas humidity at a fixed current density of 0.75 A/cm^2, whereas cells operated with H_2/O_2 were operated at 78 % rH at current densities between 1.5 to 3 A/cm^2 (O2 – O4).

Operando XTM scans in absorption contrast mode were performed at the TOMCAT beamline of the Swiss Light Source (SLS) using a fast, CMOS technology based camera (pco.Dimax, Germany), that allows even ultra fast sub-second XTM scans [8, 9]. The camera was mounted on a microscope (ELYA

Figure 1. *Sketch of the different cluster types that can be found in the GDL domain; blue: full connected water clusters (FC); green: top connected (TC); red: bottom connected (BC); purple: non connected (NC); rib domain and GDL fibers are shown in black, catalyst layer and membrane are shown in gray. Reproduced from [7] published under CC BY-NC-ND (http://creativecommons.org/licenses/by/4.0/).*

solutions, Czech Republic) providing a pixel size of 2.9 x 2.9 µm^2, about 5.8 x 5.8 mm^2 field of view and 2.44 x 10^{-17} m^3 voxel size (2.44 x 10^{-2} pL) at full chip readout (2016 x 2016 pixels). The exposure time per projection was 10 ms, so rotating the cell 180 ° while taking 1001 radiographic projections led to a total X-ray exposure of 10 s per scan.

All XTM data sets have been segmented for void, liquid and solid phase. The individual water clusters within the analyzed GDL domain were assigned to different connection type cluster categories. It is distinguished between full connected (FC) water clusters, that provide a percolation path in TP-direction from bottom to the top of the GDL, bottom connected (BC) and top connected (TC) water clusters that are only connected to the top or the bottom of the GDL domain, respectively, and isolated, non-connected (NC) water clusters (see Figure 1).

Results

The majority of the liquid water belongs to the category of FC-type clusters (see Figure 2). Under the ribs in average 96 % of the water volume is fully connected in just 1 to 3 % of the water clusters, independent of operating conditions or flow field width. A similarly high average FC volume fraction of 82 % was found in the channel GDL domains of the oversaturated conditions A03 and A13, where about one out of ten clusters is FC connected. BC and TC type water makes up 25 to 45 % of the clusters under the ribs, but with negligible 1 to 5 % of the liquid volume. In the channel domains however, there is a clear difference between BC and TC type clusters, where the majority of about 50 % water clusters are of BC type occupying in average 14 % of the water volume and much fewer TC type clusters (5 to 8 %) within no more than to 2 % of the water volume. The volume fraction of NC type clusters is negligible under the ribs (~1 %) and only slightly higher in the channel domains (3 %). Interestingly, the volume fraction of BC and FC type clusters of the channel GDL domains sums up to the FC type volume fraction under the ribs providing evidence that water transport is mainly due to capillary forces driven flow of

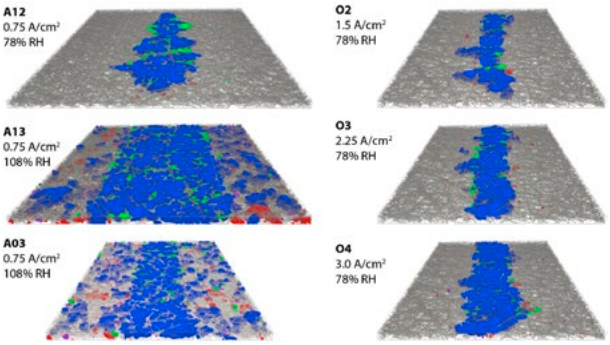

Figure 2. *3D rendering of the different cluster types for all conditions with water saturation above 1 % using same color coding as in Figure 1. Reproduced from [7] published under CC BY-NC-ND (http://creativecommons.org/licenses/by/4.0/).*

liquid water from the MPL to the gas channel as diffusive vapor transport is negligible at oversaturated conditions. Since the available XTM scans are only temporal snapshots of the local saturation distribution, it seems possible that BC-type clusters grown into FC type or FC clusters may shrink after droplet detachment and temporarily convert into BC type.

The amount of water clusters under the ribs scales with saturation for variations of feed gas humidity as well as for increasing current density with the highest values found at oversaturated conditions. Under the channels the water clusters can drain directly into the channel and do not grow above 10 nL as they remain isolated, whereas water clusters with volumes of up to ~130 nL are found under the ribs. Here, the GDL-rib interface seems to act as a barrier that forces the TP-transport clusters to join – may it be due to capillary forces driven in-plane growth or condensation under the ribs. Figure 3 shows a 3D visualization of the liquid water, where the 10 largest clusters of each domain are colored differently than the smaller clusters. Under the ribs, the majority of the saturation seems to be collected by at maximum 5 clusters for all conditions. Conditions O3 and O4 are even dominated by a single cluster that spans over the entire field of view in the along-the-channel direction. For the oversaturated conditions the largest clusters under the ribs seem even to expand into the channel GDL domains. There, the ten largest clusters are of similar size and cover only about 50 % of the water volume.

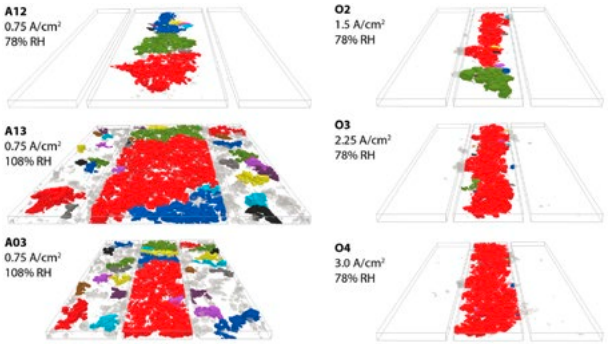

Figure 3. *3D rendering water saturation of the individual channel and rib domains for all conditions with water saturation above 1 %. The 10 largest clusters are colored individually. Reproduced from [7] published under CC BY-NC-ND (http://creativecommons.org/licenses/by/4.0/).*

Acknowledgement

Financial support from the Swiss Federal Office of Energy under grant no. 153708, precise machining work by M. Hottiger, software and electronic support by T. Gloor, as well as support during the measuring campaign at the TOMCAT beamline by S. Irvine, R. Gaudenzi, S. Kreitmeier and M. Zurbrügg are gratefully acknowledged.

References

[1] O. Gröger, H.A. Gasteiger, J.-P. Suchsland. *J. Electrochem. Soc.* **162** (14), A2605 (2015).
[2] T.E. Springer, T.A. Zawodzinski, S. Gottesfeld. *J. Electrochem. Soc.* **138** (8), 2334 (1991).
[3] D.R. Baker, C. Wieser, K.C. Neyerlin, M.W. Murphy. *ECS Trans.* **3** (1), 989 (2006).
[4] M.F. Mathias, J. Roth, J. Fleming, W. Lehnert. In *Handbook of Fuel Cells*. John Wiley & Sons, Ltd (2010).
[5] P. Boillat, P. Oberholzer, A. Kaestner, R. Siegrist, E.H. Lehmann, G.G. Scherer, A. Wokaun, *J. Electrochem. Soc.* **159** (7), F210 (2012).
[6] P. Oberholzer, P. Boillat, A. Kaestner, E.H. Lehmann, G.G. Scherer, T.J. Schmidt, A. Wokaun., *J. Electrochem. Soc.* **160** (6), F659 (2013).
[7] J. Eller, J. Roth, F. Marone, M. Stampanoni, F.N. Büchi, *J. Electrochem. Soc.* **164** (2), F115 (2017).
[8] R. Mokso, F. Marone, D. Haberthür, J.C. Schittny, G. Mikuljan, A. Isenegger, M. Stampanoni, *AIP Conf. Proc.* **1365** (1), 38 (2011).
[9] J. Eller, F. Marone, F.N. Büchi, *ECS Trans.* **69** (17), 523 (2015).

Fuel cell membranes based on hydrocarbon ionomers: Approaches for stabilization against radical induced degradation: a modeling study

L. Gubler

phone: +41 56 310 2673, e-mail: lorenz.gubler@psi.ch

Perfluoroalkylsulfonic acid (PFSA) ionomers are commonly used as electrolyte membrane in low temperature fuel cells. The quest for alternative, non-PFSA membranes has, however, not subsided and hydrocarbon or partially fluorinated membranes continue to be of interest for fuel cells and other applications, such as water electrolyzers or redox flow batteries. On the one hand, they may be of lower cost. On the other hand, the versatility of their chemistry allows the synthesis of tailor-made materials for given target applications and operating conditions. Yet non-PFSA membranes are generally and intrinsically more susceptible to radical induced attack and degradation [1]. In particular, aromatic units present in most of these polymers react readily and rapidly with hydroxyl radicals ($HO^{\bullet}$), which triggers chain scission and polymer decomposition.

Simulation

In a previous study, a simulation framework for radical formation and polymer attack in membrane electrode assemblies of fuel cells has been established including comparison to experimental findings [2]. In a subsequent study, the catalytic antioxidant functionality of Ce and Mn ions has been analyzed and explained [3]. Here, the attack of $HO^{\bullet}$ on poly(styrenesulfonic acid) (PSSA), a model compound for aromatic hydrocarbon ionomers, and potential approaches to prevent chain degradation is studied based on an adapted kinetic simulation.

$HO^{\bullet}$ is the radical with the highest oxidative strength in the fuel cell environment. Here, we assume a constant formation rate of $HO^{\bullet}$ based on literature data of $r_{HO\bullet} = 10^{-7}$ M·s^{-1}. $HO^{\bullet}$ attacks the polymer R, which, via intermediates, can lead to chain scission:

$$R + HO^{\bullet} \rightarrow \text{intermediates} \rightarrow \text{chain scission} \quad (1)$$

For PSSA of high molecular weight in water, the rate constant is given in Table 1. The concentration of aromatic units [R] in the membrane is assumed to be 1 M.

Radical scavenging using antioxidants

In analogy to PFSA membranes, we consider that an additive is incorporated into the membrane, which acts as an antioxidant and reacts with (i.e., scavenges) $HO^{\bullet}$. Owing to the high reactivity of $HO^{\bullet}$ with PSSA and the corresponding short lifetime of $HO^{\bullet}$ of around 1 ns, it is clear that cerium is not a suitable scavenger, since the reaction rate of $HO^{\bullet}$ with Ce^{3+} ($3 \cdot 10^7$ M^{-1}s^{-1}) is too slow to allow scavenging significant fractions of $HO^{\bullet}$. Therefore, we consider antioxidants of the H-donor type:

$$AH + HO^{\bullet} \rightarrow A^{\bullet} + H_2O \quad (2)$$

These show rate constants for the reaction with $HO^{\bullet}$ near the diffusion limit, i.e. around 10^{10} M^{-1}s^{-1} (Table 1). The antioxidant is thereby oxidized to $A^{\bullet}$. Representative compounds are hindered phenols. The fraction of $HO^{\bullet}$ scavenged f($HO^{\bullet}$) can be calculated according to:

$$f(HO^{\bullet}) = \frac{k_2 \cdot [A]}{k_1 \cdot [P] + k_2 \cdot [A]} \quad (3)$$

Therefore, to scavenge a significant fraction of hydroxyl radicals, say, more than 90 %, the antioxidant concentration needs to be higher than 0.4 M, which corresponds to 40 % of the concentration of SSA units. Hence, scavenging $HO^{\bullet}$ in an environment with an aromatic hydrocarbon polyelectrolyte is a challenging task. At a concentration of 1 M, 96 % of $HO^{\bullet}$ are scavenged by the antioxidant AH.

Reaction	Rate constant	Unit	Reference
1	$4 \cdot 10^8$	$M^{-1}s^{-1}$	4
2	10^{10}	$M^{-1}s^{-1}$	3

Table 1. *Rate constants for the reaction of $HO^{\bullet}$ with PSSA (1) and a hypothetical phenol type antioxidant (2).*

Many of the antioxidants used in technical plastics, such as hindered phenols, are not self-regenerating and are used up over time. In the case here, at a concentration of 0.4 M, the antioxidant would be depleted after 51 days in the cell. For sustained antioxidant action, it needs to be regenerated, in analogy to the cerium ions added to PFSA ionomers, in which case H_2O_2 present in the MEA at a concentration of around 0.5 mM reduces Ce^{4+} to Ce^{3+} [3]. Here, we assume a similar reaction to take place to restore the antioxidant:

$$A^{\bullet} + H_2O_2 \rightarrow AH + HOO^{\bullet} \quad (4)$$

with a rate constant k_4. For this reaction to take place, the redox potential of the antioxidant needs to be higher than that of the $HOO^{\bullet}$,H^+/H_2O_2 couple, which is 1.46 V at pH 0. In this case, the compound can undergo cyclic oxidation / reduction reactions and thereby act as a catalytic antioxidant:

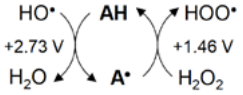

The concentration of the ‹active› antioxidant, i.e. AH, is influenced by the magnitude of the rate constants k_2 and k_4. Since k_2 is assumed to be a constant, near diffusion-limited rate constant, the effect of the radical scavenging properties and protection against radical attack of the polymer is studied as a function of k_4 and the concentration of the additive AH (Figure 1).

The results show that the rate constant k_4 to restore the $HO^{\bullet}$ scavenger does not need to be very high, i.e., > 0.05 M^{-1}s^{-1}, to ensure a sufficiently high population of the reduced oxidation state of the additive. The challenge is rather to find a suitable couple $A^{\bullet}$,H^+/AH with a redox potential of 1.5 V or higher. The redox potential of the phenol/phenoxyl radical is only around 1.4 V at pH 0. With electron withdrawing substituents, this value could be increased, yet with this the risk increases that the oxidized version of the additive may itself attack the polymer.

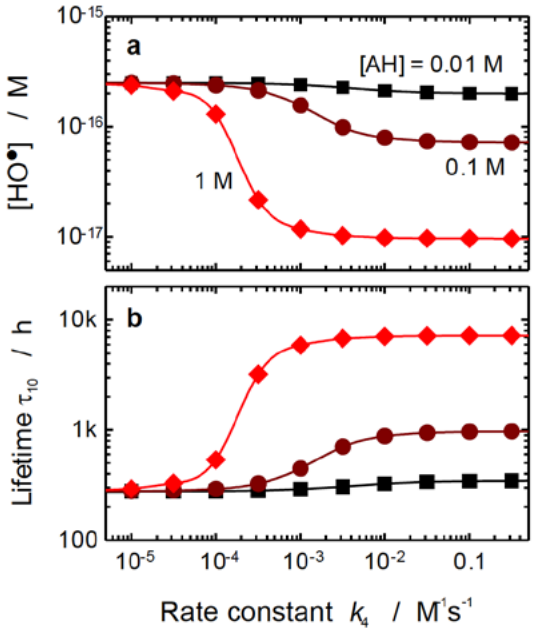

Figure 1. Effect of the rate constant k_4 for the regeneration of the antioxidant AH on the resulting concentration of HO• (a) and the increase in the lifetime t_{10} of the membrane (b), corresponding to the loss of 10 % of the membrane polymer constituents.

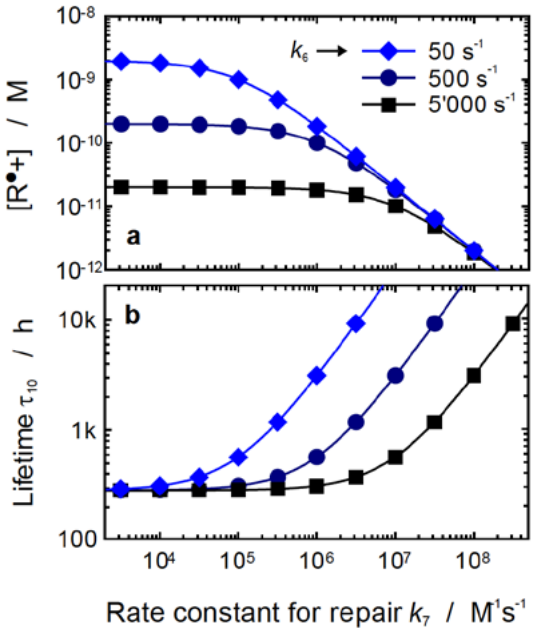

Figure 2. Scenario for the repair of the polymer via the reduction of the aromatic radical cation, $R^{\bullet+}$, an intermediate of the polymer degradation process prior to chain scission, to restore the original polymer (reaction 7) for different values of the rate constant for chain scission k_6. Concentration of radical cation (a) and improvement of lifetime t (b).

Repair Mechanism

An alternative to radical scavenging is to stabilize intermediates of the polymer formed upon radical attack. If an intermediate has a sufficiently long lifetime, suitable repair mechanisms may be invoked to restore the polymer. In the case of the adduct •R-OH formed upon attack of HO• on PSSA, or derivatives thereof, acid catalyzed water elimination yields the radical cation $R^{\bullet+}$:

$$R + HO^{\bullet} \rightarrow {}^{\bullet}R\text{-}OH \rightarrow \ldots \rightarrow R^{\bullet+} \quad (5)$$

The radical cation can induce chain scission reactions, which irreversibly damages the polymer:

$$R^{\bullet+} \rightarrow \text{chain degradation} \quad (6)$$

In case of PSSA, the lifetime of the radical cation is below 1 µs, whereas in the case of poly(α-methylstyrene sulfonic acid), its lifetime is in the millisecond range [5]. The repair mechanism considered in the following is the reaction of the radical cation with H_2O_2, which restores the original polymer:

$$R^{\bullet+} + H_2O_2 \rightarrow R + H^{+} + HOO^{\bullet} \quad (7)$$

In the simulation, the concentration of the radical cation and the lifetime of the polymer is calculated as a function of k_6, the first order rate constant for chain scission from the radical cation, and k_7, the rate constant for the repair reaction involving H_2O_2 (Figure 2).

Evidently, the slower the chain scission process and, correspondingly, the longer the lifetime of the radical cation $R^{\bullet+}$, the more effective the repair reaction will be. However, the required rate constant for, say, an increase of membrane lifetime by a factor of ten, is in the range of 10^6 to 10^8 $M^{-1}s^{-1}$. Experimental values for these reaction rates are currently not available and future work must aim at establishing these in a suitable kinetic study.

Conclusion

For the protection of hydrocarbon or partially fluorinated membranes against radical induced degradation in the fuel cell, additives incorporated into the polymer as antioxidants need to effectively scavenge HO•, i.e., show a high rate constant in the range of 10^{10} $M^{-1}s^{-1}$. In addition, regeneration of the antioxidant is required to provide sustained scavenger functionality over thousands of hours.

A fraction of radicals inevitably attacks the ionomer. To mitigate irreversible chain scission, it is conceivable to design the polymer such that upon attack of a radical, the intermediate(s) formed can undergo some sort of repair reaction before chain scission occurs.

A combination of radical scavenging and polymer repair mechanism may evidently provide the most promising approach to minimize irreversible degradation of the polymer chain. A detailed experimental investigation is called for to determine whether these ideas can be implemented into an actual membrane design.

References

[1] V.A. Sethuraman, J.W. Weidner, A.T. Haug, L.V. Protsailo, *J. Electrochem. Soc.* **155**, B119–B124 (2008).
[2] L. Gubler, S.M. Dockheer, W.H. Koppenol, *J. Electrochem. Soc.* **158**, B755–B769 (2011).
[3] L. Gubler, W.H. Koppenol, *J. Electrochem. Soc.* **159**, B211–B218 (2012).
[4] Y.K. Bhardwaj, H. Mohan, S. Sabharwal, T. Mukherjee, *Radiat. Phys. Chem.* **62**, 229–242 (2001).
[5] L. Gubler, W.H. Koppenol, in: *The chemistry of membranes used in fuel cells: degradation and stabilization*. S. Schlick (Ed.), Wiley, in press (2017).

Radiation grafted membranes in high-temperature electrochemical H_2 pumping

T. Rojek, T.J. Schmidt, L. Gubler
phone: +41 56 310 4188, e-mail: tomasz.rojek@psi.ch

Electrochemical hydrogen pumping is a method of hydrogen separation and compression which may be particularly suited for extraction of hydrogen from low concentration streams, treatment of which by established technologies (pressure swing adsorption, membrane separation) is energy extensive. Moreover, high-temperature polymer electrolyte systems offer the possibility to treat gases contaminated with known catalyst poisons (CO, H_2S) and do not require extensive humidification.

Membranes play a central role in high-temperature polymer electrolyte cells. The polymer matrix acts as host for phosphoric acid, which in turn provides protonic conductivity even under dry conditions. Hereunder we explore membrane materials prepared by radiation grafting as candidates for high-temperature electrochemical hydrogen pumping.

Experimental

Radiation grafted membranes were prepared by immersing pre-irradiated (100 kGy, electron beam) poly(ethylene-co-tetrafluoroethylene) (ETFE) films (DuPont, 25 µm) in a reaction mixture composed of solvent (isopropanol or water) and monomer (4-vinyl pyridine or 1-vinyl imidazole) at 60 °C for 24 h in order to achieve high grafting levels and a corresponding nitrogen site density of 5–6 mmol/g. Subsequently, imbibition with electrolyte was performed by immersing grafted films in phosphoric acid (85 %) for 5 days at room temperature (Scheme 1).

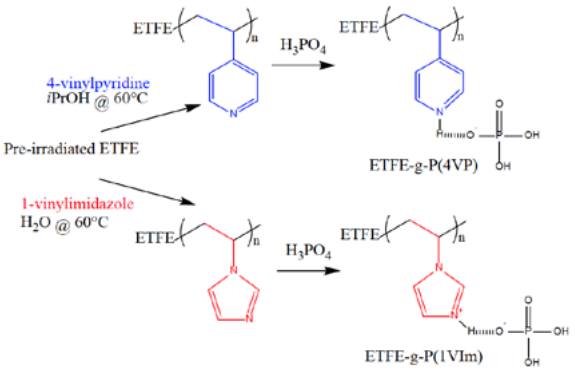

Scheme 1. *Synthesis route involving e-beam irradiation, grafting of suitable monomers and phosphoric acid doping.*

Acid uptake was determined by means of ion chromatography (Metrohm 882 Compact IC Plus) after leaching and ion exchange in 0.1 M HCl.

Hydrogen pumping experiments were carried out with a membrane electrode assembly comprising gas diffusion electrodes (SGL 38 GDL with Pt/Vulcan XC-72 catalyst, 1 mg Pt/cm^2) and the tested membrane with an active area of 45.15 cm^2. The cell was fed with hydrogen humidified at room temperature, which corresponds to relative humidity of 1.5 % and 0.9 % at 120 °C and 140 °C, respectively.

Electrochemical impedance spectroscopy (EIS) was performed using a Biologic SP-300 potentiostat with a perturbation signal of 10 mV. The obtained spectra were fitted with a modified Randles circuit using ZView software (Scriber Associates).

Results

The cell voltage as a function of current density is presented in Figure 1. For both types of grafted membranes an almost linear behaviour is observed and a high current density of 1.0 A/cm^2 can be reached.

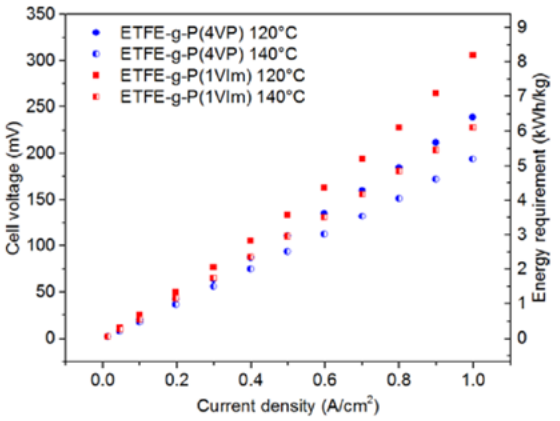

Figure 1. *Polarization curves and corresponding energy requirement of cells with radiation grafted membranes.*

Further insight into the voltage losses in a hydrogen pumping cell may be gained by means of EIS. The losses associated with reaction kinetics are expected to be rather low due to the high exchange current density for hydrogen oxidation and reduction reactions on platinum [1]. Hence, losses represented by the semi-circle in the Nyquist plot (Figure 2) can most likely be attributed to the polarization resistance of the electrode/electrolyte interface.

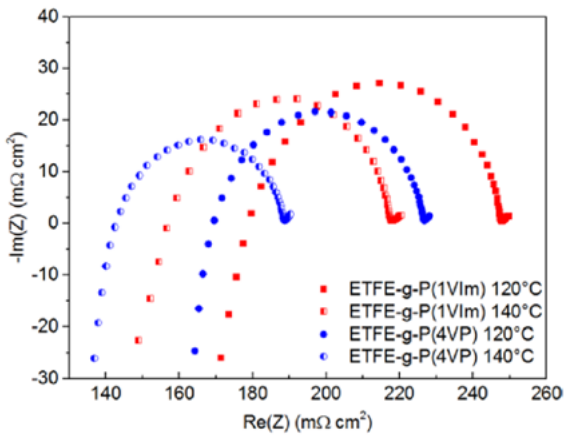

Figure 2. *Electrochemical impedance spectra recorded at open circuit voltage.*

Based on the results presented in Figure 3 it can be concluded that the majority of the voltage losses may be attributed to ohmic losses dominated by the ionic resistance of the membrane.

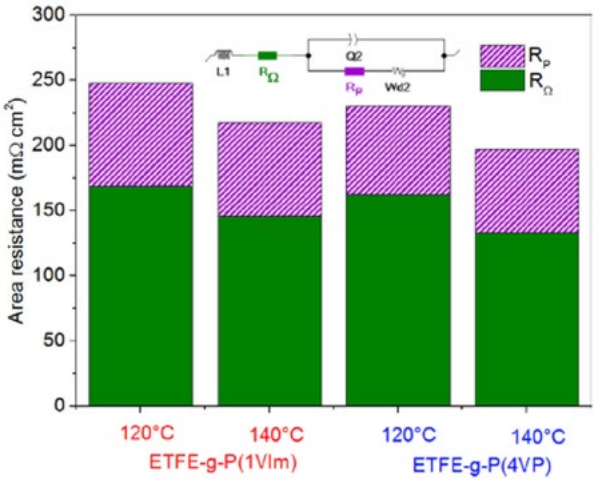

Figure 3. *Resistance loss terms in the hydrogen pump cell. Rp: polarization resistance, RΩ: ohmic resistance.*

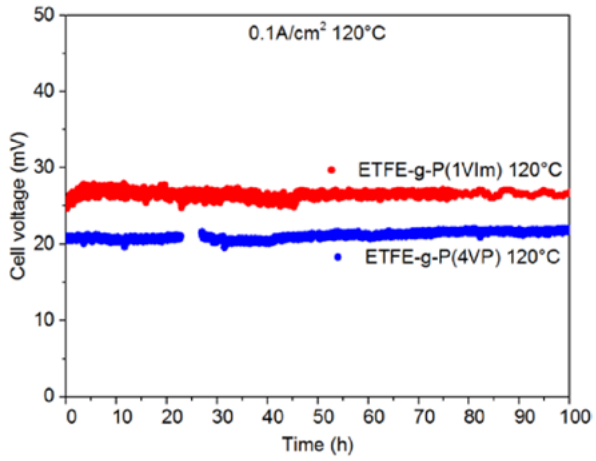

Figure 4. *Cell voltage as function of time at 120 °C.*

Stability of the synthesised membranes was assessed in constant current tests (Figure 4 and Figure 5). As Figure 4 demonstrates, both types of membranes exhibited stable performance for 100 h at 120 °C. At higher temperatures, however, ETFE-g-P(1VIm) shows superior stability over ETFE-g-P(4VP), the performance of which gradually deteriorates (Figure 5). Temporary restoration of performance was possible by means of cyclic voltammetry (0.15–1.0 V) suggesting contamination of the platinum catalyst by degradation products.

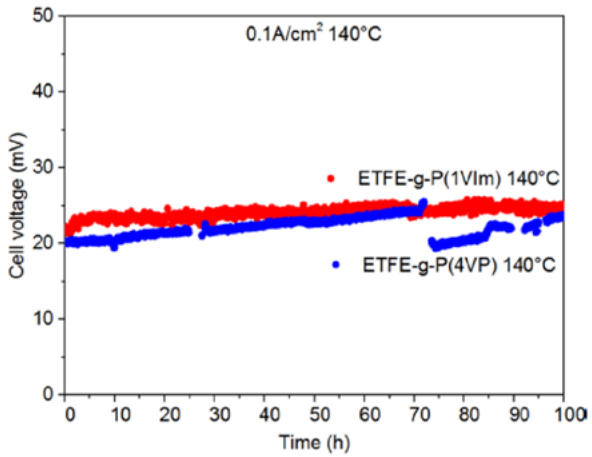

Figure 5. *Cell voltage as function of time at 140 °C.*

Conclusions

The ETFE-g-P(1VIm) membrane obtained via radiation grafting followed by phosphoric acid doping is able to operate effectively as proton conductor in low humidity conditions (relative humidity < 1.5 %). Voltage losses in hydrogen pumping cell can be mostly attributed to the ionic resistance of the membranes, yet non-ohmic losses are still non-negligible.

The ETFE-g-P(4VP) membrane has limited stability at temperatures higher than 120 °C. Improvement in this area remains to be explored by polymer modification methods such as cross-linking.

Further improvements in hydrogen pumping efficiency should be pursued by increasing phosphoric acid content of the membranes, improving membrane/electrode interface and increasing operating temperature.

Acknowledgement

The authors gratefully acknowledge the Swiss National Science Foundation for the financial support (grant no. 156604).

References

[1] J. Durst, A. Siebel, C. Simon, F. Hasche, J. Herranz, H.A. Gasteiger, *Energy Environ. Sc.* **7**, 2255–2260 (2014).

Swift heavy ion induced structuring of radiation grafted membranes: indirect approach

V. Sproll, T.J. Schmidt, L. Gubler
phone: +41 56 310 2673, e-mail: lorenz.gubler@psi.ch

Radiation grafting is a versatile, cost efficient and potentially easily up-scalable tool to tailor and improve membrane characteristics, rendering these membranes promising alternatives in fuel cell applications [1]. The synthesis of these membranes comprises two different steps, the activation of the base film (usually by electron or γ-irradiation) and the modification involving the grafting of the activated film using selected monomers and subsequent sulfonation. Investigations applying the well-defined model system of (sulfonated) polystyrene base ethylene-alt-tetrafluoroethylene (ETFE, ETFE-g-PS(SA)) showed the impact of polymer architecture on membrane properties such as proton conductivity and fuel cell performance [2, 3].

Recently, it was shown that proton conducting channels aligned in the direction of proton transport in a fuel cell could be formed using swift heavy ion (SHI) irradiation [4]. The obtained structure is in strong contrast to the structure of common radiation grafted membranes. Electron or γ-radiation induced grafting represents a statistical process leading to the formation of a random morphology with phase-separated hydrophilic / hydrophobic domain structure. The inherent limitation caused by the tortuosity of the aqueous phase in this kind of membrane could be reduced in SHI grafted membranes and resulted in superior proton conductivity and fuel cell performance.

This work represents an extension to the concept of SHI induced structuring. An approach is presented to separate track density – and thus the degree of base film structuring – and the applied dose by introducing a recombination step for the radicals created upon SHI irradiation followed by a second irradiation step with electrons to homogenously activate the base film (Figure 1, *indirect approach,* compared to *direct approach* where the radicals created upon SHI irradiation are directly used for grafting). This concept might also be of interest when monomers are used that require a high radical concentration to reach high grafting levels while at the same time only a low degree of base film structuring is desired. Apart from this special case, another advantage of this two-step process might be the homogenous distribution of radicals introduced with the second irradiation step throughout the bulk of the base film.

Experimental

The membrane synthesis was conducted in similar manner to what has been reported in our earlier work [4, 5], and films and membranes were compared at a grafting level (GL) of 25 %. For the SHI structuring $^{84}Kr^{16+}$ was used with ion densities of $100 \cdot 10^6$ ions cm^{-2}, $320 \cdot 10^6$ ions cm^{-2}, $960 \cdot 10^6$ ions cm^{-2} and $2560 \cdot 106$ ions cm^{-2}, which will be abbreviated following the notation Kxy (= $xy \cdot 10^6$ ions cm^{-2}). The SHI irradiation of the ETFE base films was conducted by Oxyphen AG (Wetzikon, Switzerland). After SHI irradiation the films were subjected to a radical elimination step as described below in order to quench the generated radicals. Afterwards, the films were pre-irradiated under an air atmosphere with electrons using a MeV class accelerator and a dose of 5 kGy. For comparison purposes, untreated ETFE base films were electron irradiated under the same conditions. All films were stored at –80 °C until used.

Results

For the indirect approach and its high degree of freedom in design the SHI irradiated base film was subjected to different conditions under which a recombination of the created radicals was facilitated in order to find the most suitable process. These conditions comprise a heat-treatment in air at 60 °C for 6 weeks as well as in vacuum for 3 weeks, in order to eliminate the possible influence of oxygen on the quenching process. Furthermore, a recombination at room temperature (in air, 6 weeks and 3 weeks) was investigated. After this treatment, it was assumed that all radicals formed upon ion beam irradiation were quenched while the structure of the track in the base polymer was retained. The films were subsequently irradiated with electrons. Reaction times to yield a grafting degree of ~ 25 % did not vary from the unmodified standard system that was electron irradiated with the same deposited dose but without prior SHI irradiation, thereby confirming that the quenching of SHI radicals was successful. It was presumed that the heat-treatment under vacuum would lead to some extent of cross-linking of the «track walls». This was expected to stabilize the track structure as well as have a decelerating effect on the grafting kinetics with increasing fluence.

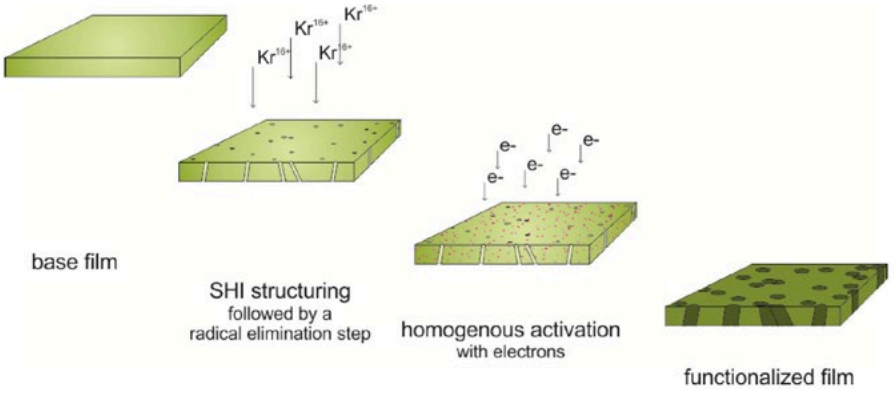

Figure 1. *Schematic representation of the indirect approach in SHI induced structuring of radiation grafted membranes.*

Neither of this could be observed. The grafting times were the same for all ion densities.

As a tool to investigate the success of SHI induced structuring energy dispersive X-ray (EDX) spectroscopic analysis of the cross-section was performed. The grafting of polystyrene into ETFE is a diffusion controlled process as the monomer solubility in the base film is extremely low. Therefore, grafting starts in the surface region and slowly propagates towards the center of the film with the incorporated polystyrene «opening» the structure of the base film and thereby increasing its accessibility for the styrene monomer. In the standard electron irradiated system (5 kGy, Std.e-) this results in an inhomogenous through-plane distribution of grafts (Figure 2a–b).

EDX is an extremely valuable tool to track graft propagation via sulfur mappings as the sulfur atom has only been introduced to the grafted film upon sulfonation and reflects the graft distribution within the film. The irradiation with SHI leads to straight tracks of reduced material density and should therefore result in an increased diffusion of monomer through these tracks and from there into the bulk of the film. This would lead to a facilitated grafting in through-plane direction and should be reflected in the sulfur mappings showing increased through-plane homogeneity.

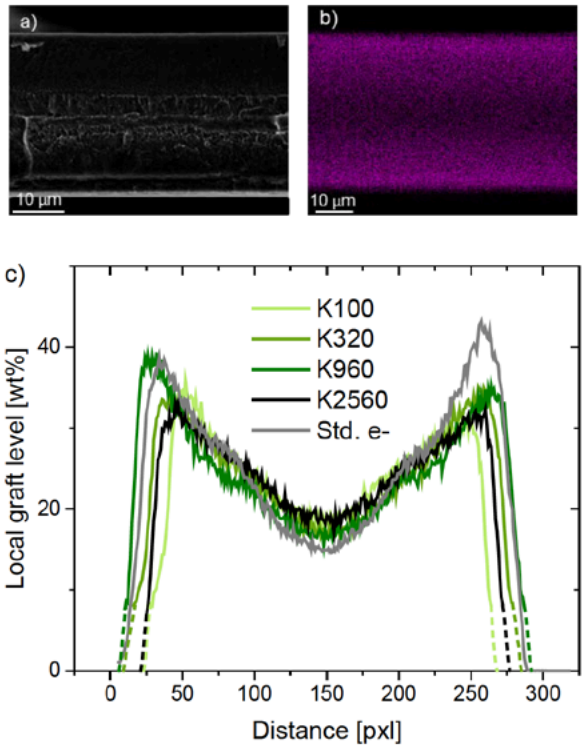

Figure 2. *SEM (a) and EDX sulfur mapping (b) of the cross-section of the standard electron irradiated membrane at ~ 25 % GL. Panel (c) shows the overlaid sulfur distribution profiles (through-plane) of all investigated SHI densities and the standard electron irradiated membrane normalized to 25.0 % GL.*

However, under the tested conditions, no influence of the SHI irradiation on the through-plane homogeneity of the grafts could be observed (Figure 2c), no matter which recombination conditions were tested. It is not clear whether the track structure is erased during the «recombination phase» or upon the grafting procedure itself. A temperature up to 60 °C should not be high enough to activate sufficient chain mobility to erase the track structure (Tg = 110 °C [1]). Therefore, it might also be possible that the swelling of the film due to the incorporation of monomers is the reason. Though the diffusion into the tracks is most reasonably enhanced compared to the unmodified bulk material, after electron irradiation radicals are distributed homogenously and grafting starts over the complete surface of the film proceeding inwards. At this first stage the expansion of the surrounding material might close the open structure of the SHI tracks. A final explanation for the different results compared to the work of Maekawa et al. [6] cannot be given, as the reason for the track erasure under the tested conditions is not clear but might lie in the different ion used ($^{129}Xe^{23+}$ instead of $^{84}Kr^{16+}$) or the different type of irradiation in the second step (γ- instead e-irradiation).

Acknowledgement

Funding by the PSI within the CROSS-framework (cross-division projects) is gratefully acknowledged.

References

[1] L. Gubler, *Adv. Energy Mater.* **4** (3), 1300827 (2014).
[2] V. Sproll, G. Nagy, U. Gasser, J.P. Embs, M. Obiols-Rabasa, T.J. Schmidt, L. Gubler, S. Balog, *Macromolecules* **49** (11), 4253–4264 (2016).
[3] V. Sproll, T.J. Schmidt, L. Gubler, *Polym. Int.* **65** (2), 174–180 (2016).
[4] V. Sproll, M. Handl, R. Hiesgen, K.A. Friedrich, T.J. Schmidt, L. Gubler, *ACS Appl. Mater. Interfaces* (2016), submitted.
[5] H. Ben youcef, S. Alkan-Gürsel, A. Buisson, L. Gubler, A. Wokaun, *Fuel Cells* **10** (3), 401–410 (2010).
[6] Y. Kimura, J. Chen, M. Asano, Y. Maekawa, R. Katakai, M. Yoshida, *Nucl. Instrum. Meth. B* **263** (2), 463–467 (2007).

Phosphoric acid injection experiments into gas diffusion layers

J. Halter, A. Lamibrac, T.J. Schmidt, F.N. Büchi
phone: +41 56 310 4131, e-mail: jonathan.halter@psi.ch

High temperature polymer electrolyte fuel cells (HT-PEFC) are based on phosphoric acid imbibed polyben-zimidazole membranes and operate at temperatures between 160 °C and 200 °C. Only a fraction of PA interacts with the base polymer; therefore, PA is free to move and redistribute within the membrane electrode assembly (MEA). At high current densities, PA migrates towards the anode and can enter the gas diffusion layer (GDL) [1]. This flooding of the anode GDL can lead to loss of electrolyte and is therefore a major factor limiting the lifetime of HT-PEFCs. In recent work, X-ray tomographic microscopy (XTM) has been applied as a novel method to investigate the interaction of the porous structure of the GDL and PA [1], as it allows visualizing the flow of PA into and through the GDL. In order to further understand the wetting behaviour of the GDL with PA, an *ex situ* XTM method was developed to analyse the relation of capillary pressure and PA saturation in the GDL at steady state.

Experimental

In Figure 1, the setup used is shown. The GDL is placed between an acid reservoir at the bottom and a hydrophobic membrane at the top for well-defined boundary conditions. In a first step, the dry GDL structure is determined by XTM.

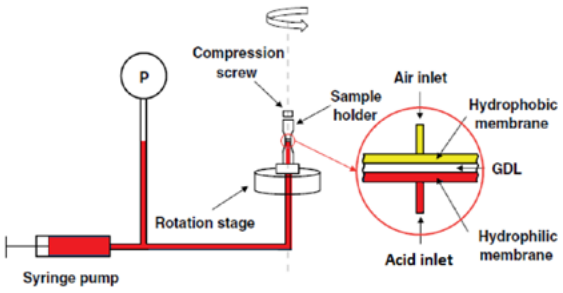

Figure 1. *Experimental setup used for the imbibition imaging inside μ-CT [2].*

Then, PA is injected from the bottom and the capillary pressure, which is the difference of the pressure of PA and atmospheric pressure, is measured using a pressure sensor. For each further step, PA is injected up to the desired capillary pressure and the PA saturation is determined by performing an XTM scan. All experiments were made with Toray TGH-H60 GDL with 20 w% PTFE and were carried out at room temperature.

Results

When comparing the capillary pressure-saturation curve for PA and water (Figure 2), similar trends are observed. Both fluids do not wet the GDL at 0 mbar, both have a breakthrough point at about 40 mbar and reach the maximal saturation around 80 mbar.

The breakthrough point is the capillary pressure at which the fluid reaches the opposite side of the GDL. When plotting the saturation at different capillary pressures vs. the thickness of the GDL, a PA breakthrough at 40 mbar is observed (Figure 3).

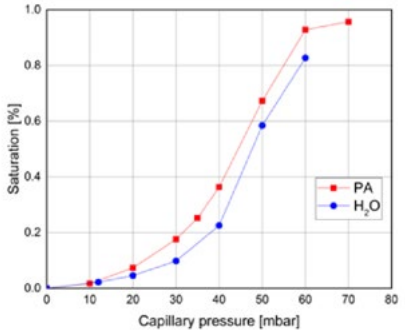

Figure 2. *Capillary pressure-saturation curve for the imbibition of PA and water [2] into the GDL.*

A major difference between the PA and water invasion experiments is the context in which these experiments are made. In LT-PEFCs, liquid water is produced at the cathode catalyst layer and needs to be removed through the cathode GDL. To do so, the breakthrough pressure needs to be overcome in an operating LT-PEFC. However, in HT-PEFC, PA serves as the electrolyte and PA movement into the GDL is not desired for the cell operation. Therefore, the breakthrough pressure should not be reached in operating HT-PEFCs.

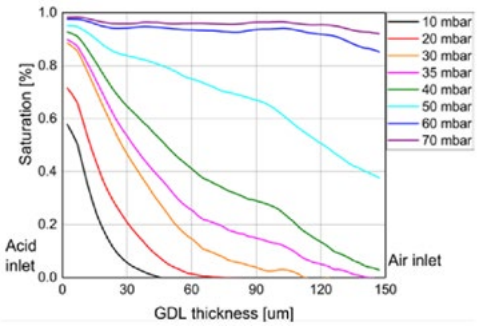

Figure 3. *PA saturation vs. GDL thickness.*

Conclusion

For the first time, a setup for measuring PA invasion into GDLs was developed and capillary pressure-PA saturation curves were measured. When comparing PA with water invasion, a similar wetting behaviour is observed for the two fluids.

Acknowledgement

Financial support from the CCEM project ADMIST, including funding contributions from the Swiss Federal Office of Energy (BFE), the Swiss Electric Research fund (SER) and BASF SE is gratefully acknowledged.

References

[1] S.H. Eberhardt, M. Toulec, F. Marone, M. Stampanoni, F.N. Büchi, T.J. Schmidt, *J. Electrochem. Soc.* **162**, F310–F316 (2015).
[2] A. Lamibrac, J. Toth, M. Toulec, F. Matone, M. Stampanoni, F.N. Büchi, *J. Electrochem. Soc.***163**, F202–F209 (2016).

Binder contribution to mass and charge transports in gas diffusion layers

A. Lamibrac, J. Eller, F.N. Büchi
phone: +41 56 310 5768, e-mail: adrien.lamibrac@psi.ch

To achieve high fuel cell efficiency, the gas diffusion layers (GDL) in polymer electrolyte fuel cells (PEFC) must offer the least possible resistance to the gas being supplied or removed to/from the catalyst layer. GDLs are made from carbon fibres and in some cases a carbonaceous binder is necessary to provide mechanical stability.

The contribution of porous binders to the overall gas transport through GDLs is poorly understood because of the difficulties of the experimental identification of this contribution. The combination of X-ray tomographic microscopic (XTM) imaging with simulation allows for deducing the transport resistances of GDLs from their structure. However the 3D reconstructed images usually do not distinguish between fibres and (porous) binder even though their transport properties may be different. As a result, simulated and experimental transport properties may not match [1].

In order to properly simulate the different transport properties of GDLs, a segmentation procedure, which enables the distinction of binder and fibres in 3D images, has been developed. The image acquisition and post-processing is first described and results of the simulations are then presented.

Experimental

SGL 24BA gas diffusion layer material from SGL (SGL Carbon, Meitingen, D) is an example of a GDL comprising porous binder (Figure 1). This material was investigated with a CT scanner nanotom m (General Electric). 3D reconstructed images of a 6 mm diameter sample were obtained using 2500 projections with X-ray tube voltage and current set to 60 kV and 200 µA, respectively. A voxel edge length of 2.2 µm was achieved. The complete sample did fit into the field of view.

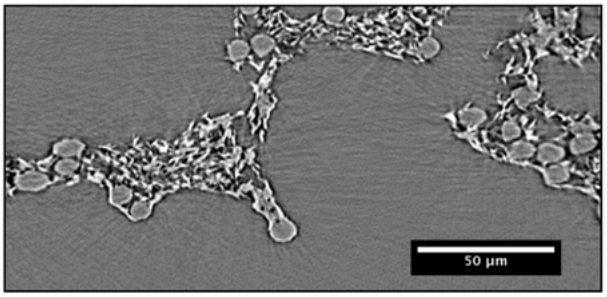

Figure 1. *Slice of a 24BA GDL, imaged at the Tomcat beamline of the Swiss Light Source. Voxel edge length: 0.16 µm. Binder exhibits flake like shapes.*

Image Processing

The result of the tomographic scan is a 3D grayscale reconstructed image. A slice of such an image is shown in Figure 2a. At this stage no quantitative information can be extracted. To do so, each voxel is labelled as void or solid (Figure 2b) by thresholding. However, as the solid consists of fibres and binder, further segmentation is required. This additional segmentation starts with thresholding of the solid domain. As the grayscale distributions of binder and fibres are overlapping, some fibres are labelled as binder and vice-versa. Identification of the artefacts and their reallocation to the proper phase is required.

Fibres are connected in a large network. As a consequence, small fibre clusters disconnected from the main fibre structure are identified as artefacts and reallocated to binder. As the edges of the fibres just cover a part of the detector pixels, their corresponding voxels appear lighter and form a thin layer around the fibres. An erosion of the binder phase eliminates these artefacts. The remaining binder is dilated. The resulting final ternary segmented image (void, binder, fibres) is shown in Figure 2c.

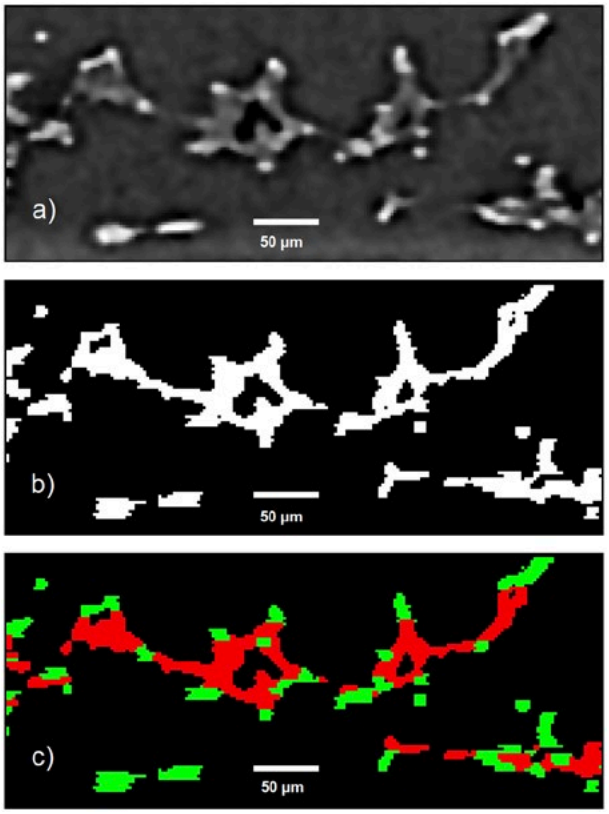

Figure 2. *Through-plane slice of SGL 24BA;*
a) 3D reconstructed image.
b) binary segmented image void/solid.
c) ternary segmented image void/binder/fibres. Voxel edge length: 2.2 µm.

Compared to Figure 1, the details of the binder in Figure 2a are not visible due to lower spatial resolution. The porosity of the binder is therefore not accounted for which lowers the overall GDL porosity. Thus the GDL porosity obtained with the image is 77 % (Figure 3) while Rashapov et al. [2] report a porosity of 85 %. This value is obtained if a 53 % porosity is applied to the binder phase.

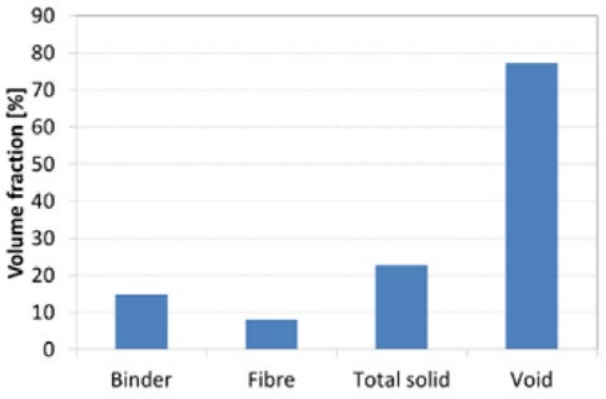

Figure 3. *Volume fractions of a SGL 24BA calculated from the 3D ternary segmented image.*

Results

In SGL 24 BA, based on image evaluation, the binder represents 65 % of the solid volume and its distribution is heterogeneous across the GDL thickness with a lower content in the middle of the GDL. On the contrary, the fibres are well distributed across the GDL thickness.

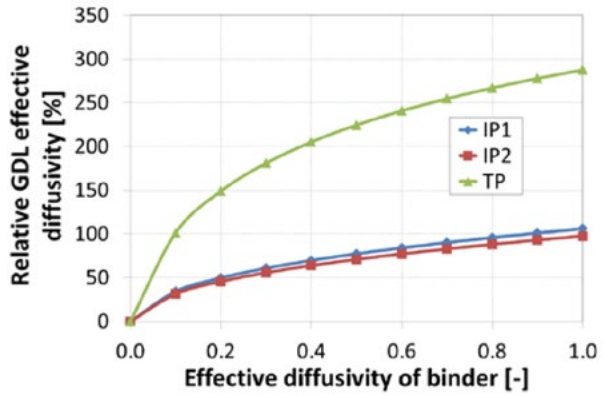

Figure 4. *Increase of relative GDL effective diffusivity as function of binder effective diffusivity; IP1 and IP2 orthogonal in-plane directions, TP through plane direction.*

Numerical diffusion simulations are performed using the ternary segmented 3D structure and the ConductoDict module of the GeoDict® program package (Math2Market, Kaiserslautern, D). Distinct transport coefficients are allocated to the binder and fibres. For example, diffusion can take place in the binder but not in fibres. If non-porous binder (as in Figure 2b) is used for the simulation important underestimation of the GDL diffusivity arises.

A GDL in-plane effective diffusivity of about 0.6 was experimentally measured for uncompressed SGL 24BA GDLs [3]. To match this value using the numerical simulation and the ternary segmented structure, an effective binder diffusivity of 0.2 is needed. Figure 4 shows that the GDL in- and through-plane effective diffusivities are 50 % and 150 % higher at a binder effective diffusivity of 0.2, as compared to a non-porous binder.

Conclusions

The binder represents a significant part of the solid volume in an SGL 24BA GDL. When 3D segmented images and numerical simulations are combined to deduce mass or charge transport coefficients, it is critical to distinguish between fibres and binder since the two components have different transport properties.

For the first time, a new segmentation procedure was implemented to make possible this distinction and influence of the binder on the overall GDL transport properties was quantified. Significant increase of the GDL diffusivity is observed when considering a porous binder. The gas transport through the binder could have important consequences especially at high liquid water saturation in the GDL. Since the capillary pressure required to enter the small pores of the binder is expected to be higher than that of the pores formed by the fibre network, binder pores should remain dry and therefore allow for gas transport in a flooded GDL.

Acknowledgement

The authors thank the Swiss National Science Foundation for financial support (SNSF project no. 407040 153790). M. Hottiger and T. Gloor are gratefully acknowledged for technical assistance and R. Schweiss (SGL Carbon, Meitingen, D) for providing material. This work was performed in the framework of the Swiss Comptence Center for Energy Research (SCCER) mobility.

References

[1] J. Becker, R. Flückiger, M. Reum, F.N. Büchi, F. Marone, M. Stampanoni, *J. Electrochem. Soc.* **156**, B1175 (2009).
[2] R.R. Rashapov, J. Unno, J.T. Gostick, *J. Electrochem. Soc.* **162**, F603–F612 (2015).
[3] R.R. Rashapov, J.T. Gostick, *Transp. Por. Med.* **115**, 411–433 (2016).

Characterization of porous transport layers for polymer electrolyte water electrolyzers by X-ray tomography

T. Schuler, K. Takanohashi[1], M. Suermann , T.J. Schmidt, F.N. Büchi
phone: +41 56 310 5147, e-mail: tobias.schuler@psi.ch

Due to high power densities and dynamic operation, polymer electrolyte water electrolysis (PEWE) is a promising technology for hydrogen production. Water is split by electrochemical reactions into H_2 and O_2. Similar to fuel cells the individual components make different contributions to the high frequency, kinetic and mass transport losses in PEWE [1].

Characterization of the porous transport layers (PTL) is required for the fundamental understanding of the transport losses, PTLs need to have sufficient electric and thermal conductivity and electrochemical stability at potentials above 1.2 V for electrolysis operation. Therefore, for the anode Ti is chosen as material and commercial PTLs are often made from sintered Ti-powder.

On the one hand water stream has to be distributed homogenously towards the catalyst layer, on the other hand the gaseous product has to be removed from the catalyst layer. As a consequence a two phase flow is induced in the porous materials. X-ray tomographic microscopy (XTM) is used to investigate the dry structure of titanium sintered PTLs.

Experimental

Tomographic microcopy of commercially available Ti powder sintered materials was performed with a CT-scanner nanotom m (General Elelctric). A X-ray energy of 120 kV and acquisition times for single projections of 1000 ms were used. The voxel cube length was chosen to be 1 µm. Furthermore a 0.1 mm Cu filter was used in addition to prevent beam hardening effects.

Three different types of Ti sinter were characterized T5, T10 and T20, featuring three different particle size distributions. Samples of 1 x 2 x 20 mm samples were fixed on a PEEK sample holder and images were acquired at ambient conditions. The reconstructed data was segmented by thresholding using the software Fiji.

Results

Figure 1 shows the 3D reconstruction of the bulk phase of PTL T10. The sintered Ti particles are represented in grey.

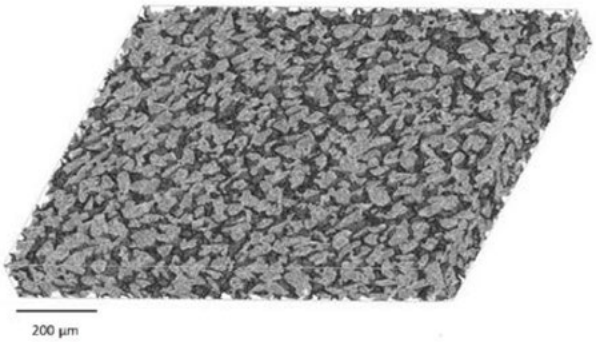

Figure 1. *3D reconstruction of titanium sintered porous transport layer T10 obtained from XTM.*

The reconstruction of the dry PTL scans enabled the characterization of the material morphology and properties due to the characteristic high contrast between solid Ti phase and air. The 3D reconstruction was used for determination of the effective porosity and Ti particle sizes. The particle size distribution of the PTLs was measured by local thickness analysis. The local thickness is defined as the maximum diameter of a sphere which is completely inside a structure at a given point of the structure. Figure 2 exemplifies the characteristic morphology of Ti sintered PTLs. The size distribution is visualized by different colors in image A). The distribution is shown in plot B).

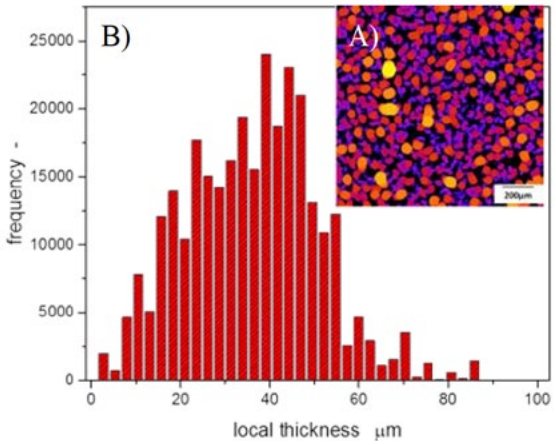

Figure 2. *Image A) shows the local thickness distribution of Ti sintered porous transport layer. Plot B) shows the local thickness distribution.*

The mean particle diameter for T5, T10 and T20 was estimated to be 56 µm, 58 µm and 96 µm respectively. In analogy to the particle size analysis the pore size was estimated. The mean pore size diameters were estimated to be 30 µm, 36 µm and 57 µm. The bulk phase of the PTLs featured similar porosities of 30 %, 35 % and 33 %.

An analysis of in and through plane of local thickness showed an isotropic structure of the PTLs by identical distributions.

Conclusion and outlook

The high contrast in XTM between solid and non-solid phases allows for an accurate estimation of the PTL morphology. Based on the 3D structure, transport parameters such as permeability can also be determined.

Acknowledgement

Financial support by Swiss Federal Office of Energy (SFOE) is gratefully acknowledged.

Reference

[1] M. Suermann, T.J. Schmidt, F.N. Büchi, *Electrochim. Acta* **211**, 989–997 (2016).

[1] visiting from Yamanashi University, Kofu, Japan

Polymer electrolyte water electrolysis: differential vs. balanced pressure

M. Suermann, T.J. Schmidt, F.N. Büchi
phone: +41 56 310 5763, e-mail: michel.suermann@psi.ch

Polymer electrolyte water electrolysis (PEWE) is used to convert electrical (excess) energy into chemical energy by splitting water into hydrogen and oxygen. Depending on the application, the gases need to be compressed, e.g. for mobility, hydrogen pressures in the order of 1000 bar have to be provided. Conventionally, gases are compressed mechanically. However, the electrochemical compression, i.e. pressurized PEWE, has potentially lower efforts/costs for compression and/or drying [1]. With respect to the PEWE pressure operation, either differential or balanced pressure is possible. For differential pressure only hydrogen is compressed and oxygen is kept close to ambient pressure. Contrary, for balanced pressure operation, both gases are produced at the same pressure. In this work the differences between these two pressure strategies are discussed in terms of performance and compression losses due to polarization and gas crossover on the cell level.

Experimental, measurement methods and theory

Experiments were performed using a differential cell with an active area of 4 cm^2. For the single cell a commercial catalyst coated membrane (CCM) based on Nafion 117 (Greenerity® E400, Solvicore, DE) is sandwiched between two porous transport layers (PTL) made of sintered titanium powder (GKN Sinter Metals Filters, DE).

Galvanostatic current/voltage characteristics (i/E-curves) are recorded between 1 and 4000 mA/cm^2. Furthermore the high frequency resistance (HFR) is measured at 25 kHz to determine the ohmic overpotential to calculate the iR-free cell voltage.

Theoretically an increase in the (iR-free) cell voltage is expected according to the change in the thermodynamic cell voltage which can be calculated by the Nernst's law:

$$E^0_{cell}(p,T) = E^0(T) + \frac{R \cdot T}{2 \cdot F} \ln\left(\frac{a(H_2) \cdot \sqrt{a(O_2)}}{a(H_2O)}\right), \quad (1)$$

where α is the activity. When assuming an activity of liquid water of unity and ideal gas behaviour the thermodynamic cell voltage at 50 °C for ambient pressure, 10 bar differential and balanced pressure is 1.208 V, 1.240 V and 1.256 V, respectively.

Results

Since the ohmic overpotential is independent of pressure, only the iR-free cell voltage is further processed. In Figure 1 the iR-free cell voltage at 50 °C for ambient pressure, 10 bar differential and balanced pressure are compared. According to equation 1, when increasing hydrogen and/or oxygen pressure(s), an increase in the cell voltage is expected due to the increasing thermodynamic cell voltage. This holds largely true for the differential pressure operation, i.e. isothermal compression behaviour is confirmed. Contrary, as the current density increases, the cell voltage for 10 bar balanced pressure converges to the ambient pressure voltage. This trend is well in line with previous findings and can be related with improved oxygen evolution reaction (OER) kinetics among other effects [2, 3].

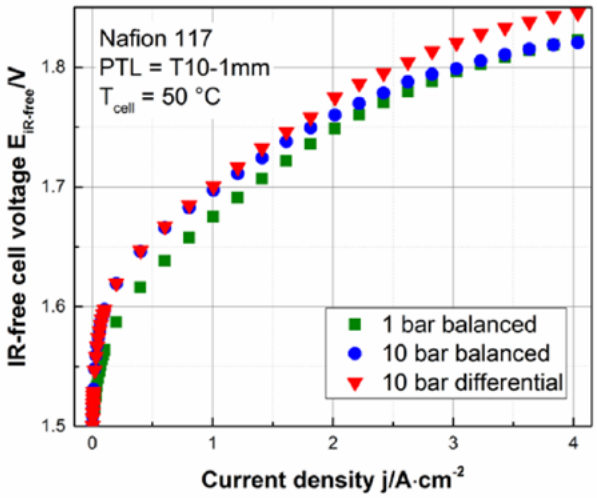

Figure 1. *IR-free cell voltage at 50 °C for ambient, 10 bar differential and balanced pressure.*

Besides the performance related compression losses, additional losses due to gas crossover have to be considered. For the differential pressure operation only the hydrogen gas crossover needs to be taken into account. Contrary, for the balanced pressure operation also the oxygen gas crossover, which is about half of that of hydrogen, has to be considered [4]. By assuming that all oxygen is recombined at the cathode (Pt-based catalyst) with hydrogen back to water, the total loss at balanced pressure due to gas crossover corresponds to about twice of the hydrogen crossover loss.

For Nafion 117 the loss due to hydrogen gas crossover can be expressed as an equivalent current density, normalized to the partial pressure, which is about 0.3 mA·cm^{-2}·bar^{-1} at 55 °C [4]. For extrapolation towards higher pressures, a gas crossover behaviour following Fick's law is assumed.

In the following the cell voltage increase due to pressurization is merged together with the losses due to gas crossover resulting in the overall compression loss, normalized to the lower heating value (LHV) of hydrogen (240 kJ/mol). Assuming the experimental findings from Figure 1 can be extrapolated towards lower and higher pressures, the overall compression loss for differential and balanced pressure operation are calculated as a function of the current density (1 and 2 A/cm^2) and of the final hydrogen pressure up to 1000 bar. Results are shown in Figure 2. Here only the produced hydrogen is of interest, but still the loss due to oxygen gas crossover is considered for the balanced pressure operation. In Table 1 the actual difference in the iR-free cell voltage between the pressurized and the ambient pressure operation (data from Figure 1) and their ratio with respect to the theoretical thermodynamic cell voltage increase for differential pressure operation of (ΔE0cell(p,T) = 32 mV) are summarized.

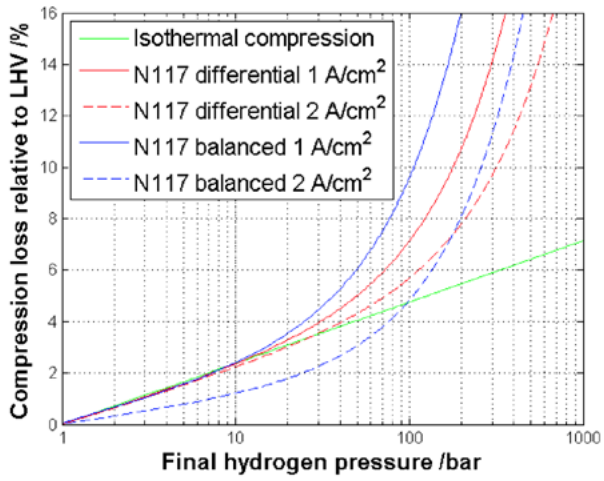

Figure 2. *Compression loss relative to the LHV of hydrogen for differential and balanced pressure PEWE operation at 50 °C using Nafion 117. The solid and dashed lines correspond to an applied current density of 1 and 2 A/cm², respectively.*

Based on the data in Figure 2 several observations can be made for electrolysis based on Nafion 117:

- At pressures below about 10 bar, curves are linear because the crossover is negligible and losses are dominated by isothermal compression.
- Above about 10 bar, the shape of the curves changes from linear to exponential (in the semi-logarithmic plot) because losses due to the gas crossover become more and more dominant.
- Because the differential pressure follows isothermal compression behaviour more closely, the difference between 1 and 2 A/cm² is smaller than for balanced pressure.
- At small current densities (here 1 A/cm²), the overall compression losses are lower for differential pressure operation.
- At high current densities (here 2 A/cm²), balanced pressure operation is preferable up to pressures of about 150 bar, because the pressure induced beneficial OER processes compensate for the doubled gas crossover loss. However, for higher hydrogen pressures differential pressure operation becomes more advantageous.

	$\Delta E_{iR\text{-}free}$ wrt 1bar	wrt $\Delta E^0(p,T)$	$\Delta E_{iR\text{-}free}$ wrt 1 bar	wrt $\Delta E^0(p,T)$
	at 1 A/cm²		at 2 A/cm²	
10 bar differential	25.6 mV	80%	26.0 mV	81%
10 bar balanced	22.4 mV	70%	11.4 mV	36%

Table 1. *Difference in the iR-free cell voltage between pressurized and ambient pressure operation and their ratios with respect to (wrt) the theoretical thermodynamic voltage increase for differential pressure operation (ΔE0(p,T) = 32 mV).*

So far the two pressure concepts were discussed only from an energetic point of view considering the compression losses due to electrochemical performance and gas crossover for a specific material and operating conditions. For real PEWE systems however, even more parameters have to be considered, e.g. gas purity, dew-point of the gases, capex vs. opex, asf. This would be a study on its own.

Conclusions

The differences between differential and balanced pressure PEWE operation are discussed by comparing the (iR-free) cell voltage and the gas crossover for Nafi-on 117 based cells at 50 °C. Based on this, the overall compression loss is discussed as a function of the final hydrogen pressure and the current density.

At lower operating pressures and for small current densities, both pressure strategies are dominated by the isothermal compression behaviour. With increasing operating pressure the loss due to gas crossover becomes more dominant. Thus at small current densities (here 1 A/cm²) the overall compression loss is less for differential pressure operations above 10 bar compared to balanced pressure. Contrary, because of the beneficial OER processes at balanced pressure operation, especially at higher current densities (here 2 A/cm²), the overall compression loss is less compared to differential pressure operation up to about 150 bar.

Even if this work can't discuss the entire complexity of real applications, it shows the potential of optimizing pressure strategies.

Acknowledgement

Funding by the Swiss Federal Office of Energy (SFOE), Belenos Clean Power Holding Ltd. and the Energy System Integration (ESI) platform at PSI, and technical support by Martin Ammann and Thomas Gloor (both PSI) are gratefully acknowledged. TJS thanks the Commission for Technology and Innovation Switzerland and the Swiss Competence Center for Energy Research Heat & Electricity Storage.

References

[1] B. Bensmann, R. Hanke-Rauschenbach, G. Müller-Syring, M. Henel, K. Sundmacher, *Applied Energy* **167**, 107–124 (2016).
[2] S.A. Grigoriev, M.M. Khaliullin, N.V. Kuleshov, V.N. Fateev, *Russ. J. Electrochem.* **37**, 819–822 (2001).
[3] M. Suermann, T.J. Schmidt, F.N. Büchi, *Electrochim. Acta* **211**, 989–997 (2016).
[4] M. Schalenbach, T. Hoefner, P. Paciok, M. Carmo, W. Lueke, D. Stolten, *J. Phys. Chem. C* **119**, 25145–25155 (2015).

Effect of electron energy on radiation grafting of PEFC gas diffusion layers

A. Forner-Cuenca, V. Manzi-Orezzoli, L. Gubler, P.M. Kristiansen, T.J. Schmidt, P. Boillat
phone: +41 56 310 2743, e-mail: antoni.forner@psi.ch

Polymer electrolyte fuel cells (PEFCs) are already available on the market; however they suffer from reduced performance under operation at high current densities due to a complex water-gas management in the cells. To tackle this issue, we developed a novel type of gas diffusion layer (GDL) with patterned wettability using the electron radiation grafting method [1,2]. The PSI is now in the forefront of advanced porous materials for PEFCs as the use of modified GDLs has proven to significantly improve fuel cell performance thanks to a new water distribution and reduced mass transport [2,3].

However, there is still room for improvement. The synthetic procedure of a second generation of modified GDLs should also tallow for selectively controlling the penetration depth. This would permit modifications of specific layers in bi-layer materials, such as the ones composed of microporous layers and GDLs. Other important aspects relate to the effect that electron energy has on the two-dimensional distribution of the absorbed dose. In this report, we present a combination of experiments and numerical simulations to study the effect of electron energy on the pattern resolution. It should be noted that other fields, such as microfluidics, can benefit from the presented approach.

Experimental

Toray TPG-H 060 carbon paper was in-house coated with 70 %wt fluoroethylene propylene (FEP) using the dipping method [4]. Samples were electron beamed using various energies at a fix dose of 50 kGy. In the 0–200 keV range, an EBLab 200 sealed laboratory emitter system from Comet AG (Flamatt, Switzerland) was used. For the high energy, a linear accelerator was used at LEONI Studer (Däniken, Switzerland). A 2 mm thick steel mask with 500 µm width openings spaced 930 µm was employed.

Acrylic acid (Sigma Aldrich 99 %) at 15 %wt in water was used as monomer solution to graft the hydrophilic polyacrylic acid onto the FEP coating. After treatment, an ionic replacement was carried out for characterization purposes. The treated GDLs were immersed into 0.025 M NaOH solution in order to replace the protons (from the acrylic group) by sodium cations (Na^+).

Energy dispersive X-ray (EDX) analysis was performed on the top and bottom surfaces of the modified GDLs using an FE-SEM Ultra 55 (Carl Zeiss, Oberkochen, Germany) with a compatible accessory (EDAX TSL, AMETEK). Elemental mappings were obtained for carbon (C), fluorine (F), oxygen (O) and sodium (Na). Fibers and, in less extent, the fluoropolymeric coating contribute to carbon signal, while fluorine is only coming from the coating. Sodium should be exclusively present in the sodium polyacrylate molecules resulting from the H^+-Na^+ exchange in polyacrylic acid. The elemental mappings were processed to obtain graphical quantitative information and to be able to compare different mappings. As the coating content and distribution is not the exact same between different samples, we normalize the measured Na intensity to the measured F intensity.

Simulations

The code system PENELOPE (Penetration and Energy Loss of Positrons and Electrons) was used for the simulations presented in this report [5,6]. The geometry used for the simulations, shown in Figure 1, consists of a combination of bodies of different materials (PET protective layer, steel mask, GDL) and a rectangular mono-directional electron beam source. To obtaining a sufficient statistical population, a shower of 10^7 electrons was used in every case.

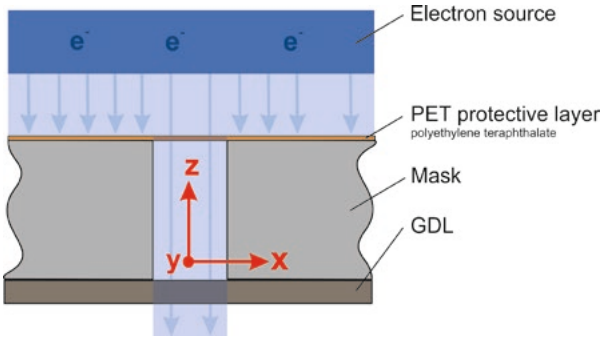

Figure 1. *Illustration of the geometry considered (not to scale) as simulation space.*

Results

The experimental results of EDX mappings (Figure 2) show that, at least, an electron energy of 160 keV is needed to penetrate throughout the complete material thickness. Additionally, the relative concentration of Na seems to be lower at the bottom interface at 160 and 180 keV.

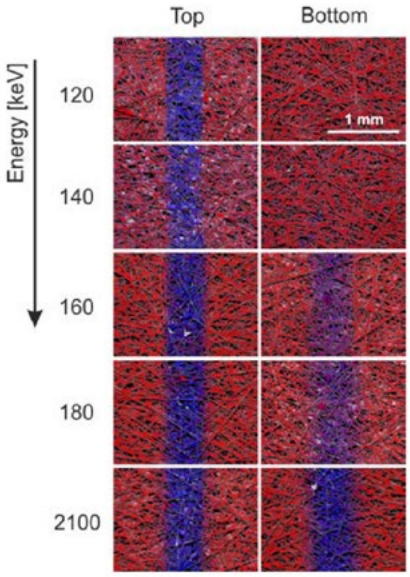

Figure 2. *Processed EDX mapping showing Na/F signal (in blue) and C signal (in red) for different electron energies. Top and bottom GDL interfaces are compared.*

As a result of the Monte Carlo simulations, the two-dimensional dose distribution over the GDL cross sections at different energies is shown in Figure 3. It can be seen that maximum absorbed doses are obtained in the centre while broadening and blurring occurs notably in the 140–200 keV energy range, due to scattering events. This effect is strongly reduced at larger energies (> 300 keV) as the dose absorbed follows a much shaper profile over the cross section.

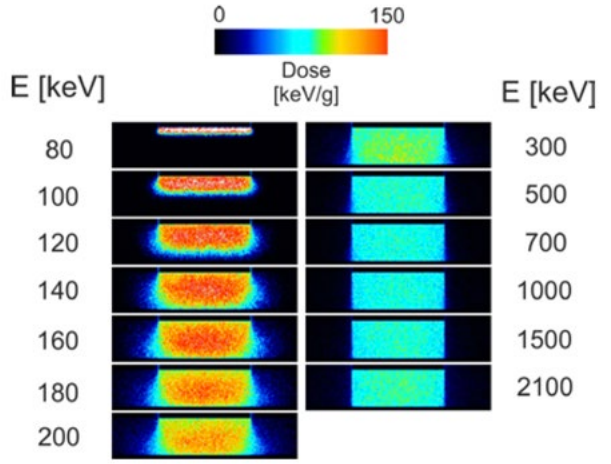

Figure 3. *Simulation results of 2D dose distribution at the GDL for different values of electron energy.*

In order to compare experimental results (Figure 2) with numerical simulations (Figure 3), we calculated Na/F and dose average (over y-coordinate) profiles, respectively, of top and bottom surfaces and compare them in Figure 4. Differences between both are notable, especially at 140 keV, in which simulated results overestimate the penetration of the electron beam. These differences could be explained by the actual PET protective layer thickness and the real air gap between electron source and irradiated substrate.

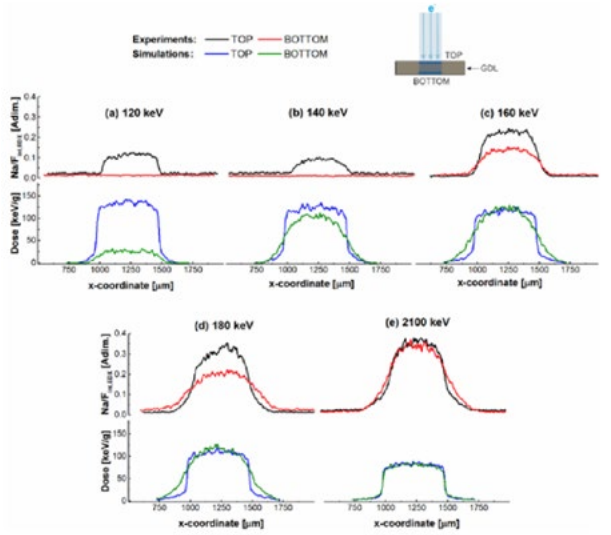

Figure 4. *Comparison of experimental and simulation results of top and bottom of the GDL.*

The general trend considering experimental results shows that broadening of the modified regions as energy increases for the top surface. The simulation captures well this trend and fairly similar pattern widths are obtained, though additional broadening is seen in the experimental results. We speculate that these differences are due to deviations of beam monodirectionality, which could not be captured by simulations. This effect could also explain the blurring of the edge-regions as compared to the sharp edges obtained with simulations.

Regarding the bottom surfaces, a similar trend is observed but larger in magnitude than that of the top surfaces (up to 180 keV). This corresponds well to the simulation results predicting a difference in width and sharpness between the top and bottom surfaces. Interestingly, at the highest energy (2100 keV), both top and bottom surfaces have nearly the same pattern, as predicted by numerical simulations. The slight differences can be due to backscattering from the metallic holder.

There are two other notable contributions to the quality of the patterns that have not been discussed in this report:

(1) the distance between the mask and the substrates significantly influences the resolution, especially at low electron energies;
(2) the bodies underneath the substrate backscatter radiation which can strongly decrease the achievable resolution. This is studied and discussed in further detail in Ref. [7].

Conclusion

It has been shown that electron energies larger than 140 keV are needed to modify 200 µm thick porous GDLs. The experimental results are in good agreement with the Monte Carlo simulations. Additionally, the simulations predict that the edges of the irradiated regions are increasingly blurred as energy increases. This trend peaks up around 180–200 keV and the effect is strongly reduced at 300 keV. Due to a theoretically superior resolution, this value of electron energy should be chosen for future monolayer GDL production.

Acknowledgement

Funding from the Swiss National Science Foundation (project n° 143432) is gratefully acknowledged.

References

[1] P. Boillat, A. Forner-Cuenca, L. Gubler, C. Padeste, F.N. Büchi, *EP 2996184 A1*, Priority date: 9.09.2014.
[2] A. Forner-Cuenca, J. Biesdorf, L. Gubler, P.M. Kristiansen, T.J. Schmidt, P. Boillat, *Adv. Mater.* **27**(41), 6317–6322 (2015).
[3] A. Forner-Cuenca, J. Biesdorf, V. Manzi-Orezzoli, L. Gubler, T.J. Schmidt, P. Boillat, *J. Electrochem. Soc.* **163** (10), F1389–F1398 (2016).
[4] A. Forner-Cuenca, V. Manzi-Orezzoli, J. Biesdorf, M. El Kazzi, D. Streich, L. Gubler, T.J. Schmidt, P. Boillat, *J. Electrochem. Soc.* **163** (8), F788–F801 (2016).
[5] F. Salvat, J. Fernandez-Vera, J. Sempau, *OECS/NEA Data Bank* (2006).
[6] J. Sempau, E. Acosta, J. Baro, J. Fernandez-Vera, F. Salvat, *Nucl. Instrum. Methods Phys. Res. B* **132** (3), 377–390 (1997).
[7] A. Forner-Cuenca, V. Manzi-Orezzoli, L. Gubler, P.M. Kristiansen, T.J. Schmidt, P. Boillat, *Radiat. Phys. Chem.* **135**, 135–141 (2016).

Neutron imaging characterization of an evaporation cooling system for a polymer electrolyte fuel cell (PEFC)

M. Cochet, A. Forner-Cuenca, V. Manzi, M. Siegwart, D. Scheuble, P. Boillat
phone: +41 56 310 5256, e-mail: magali.cochet@psi.ch

Polymer electrolyte fuel cells (PEFC), although a promising technology for carbon-free production of electricity, are penalized by system complexity, partly due to cooling and humidifying systems. These systems are necessary to avoid the heating up and drying of the membrane, which stop the electrochemical reaction. Here we present an novel evaporative cooling concept for PEFCs. Unlike other concepts, our approach does not require any additional layer in the cell structure. Water flows through dedicated flowfield channels, parallel to the gas channels, and is distributed over the cell area with the help of a modified gas diffusion layer (GDL). A synthetic method developed at PSI [1, 2] transforms some portions of the GDL into hydrophilic lines, which are used to wick the water from the supply channels at low capillary pressure. These lines, parallel and equally spaced, define pathways for liquid water separate from the gases, so as to avoid flooding (see Figure 1). In this report, we look at the evaporation rates that can be achieved and how they are linked to gas mass flow rates.

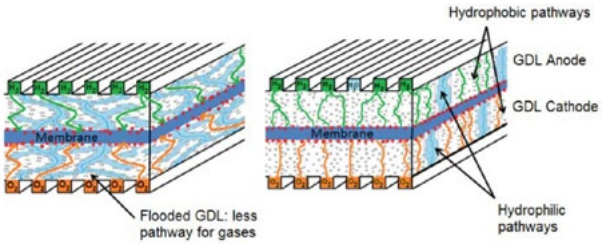

Figure 1. *Comparison between a cell with classic hydrophobic GDL and a cell with modified GDL.*

Experimental setup

In order to investigate the evaporation rates, a new test bench was built which allows to measure the heat fluxes going through the cell, transports the water to the GDL and is suitable for Neutron Radiography (NR). NR allows the detection of very small amounts of liquid water even behind dense materials such as aluminum. Therefore it can give information on the water distribution in our test PEFC.

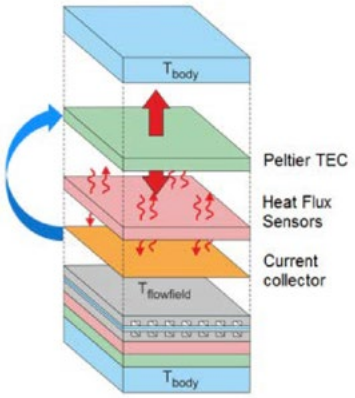

Figure 2. *Diagram of the thermal test cell.*

Three current collectors (CC) are placed in direct contact with the flowfields on each side (anode and cathode) of our test cell. They are equipped with resistive thermometers which measure the flow field temperature. This temperature is used as a feedback for three PID regulated Peltier thermo-electric coolers (TEC). Three tangential gradient heat flux sensors (HFS) are placed between the TEC and the CC, and deliver a voltage proportional to the net incident heat flux. The HFS measured values were corrected for heat losses using a measurement without gas flows. Figure 2 shows how all these elements are assembled between an aluminum compression body and the cell itself. Liquid water is brought into the cell on the anode side only by a special flow field, with one channel in the center dedicated to the liquid water and 5 gas channels on each side. All channels are 1 mm large and 0.5 mm deep. Since the cooling water is only brought on the anode side, the patterned GDL is placed also only on the anode. It has a thickness of 250 µm and a content of FEP of 70 % in weight. The hydrophilic lines are 500 µm wide and the separation between two lines is 950 µm. A home-made Micro-Porous Layer (MPL) based on Carbel is used between this GDL and the catalyst coated membrane (CCM). The GDL on the cathode side is a commercial SGL 24BC GDL with an integrated MPL. Since only the evaporation is studied here, the gases flown are H_2 on the anode and N_2 on the cathode. Flow field temperatures and inlet temperatures for the gases and for the cooling water are 80 °C. Pressures are equal to 2 bars, and the gases inlet relative humidity is 0 %.

Results

Figure 3 shows the influence of the gas mass flow rates on the heat fluxes.

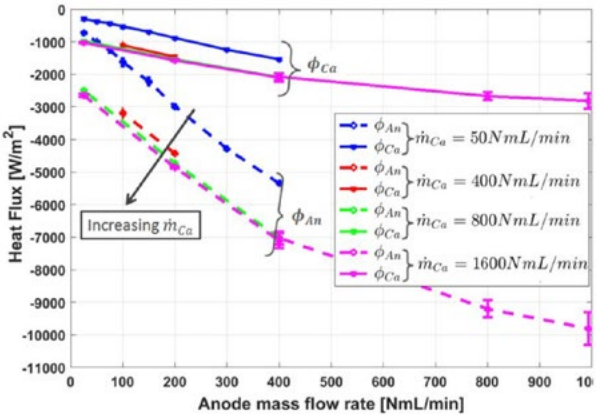

Figure 3. *Anode and cathode heat flux versus anode mass flow rate for several cathode mass flow rates.*

For all cases, the heat flux is higher in absolute value on the anode than on the cathode, but the behaviors with respect to gas mass flow rates are similar. For small values of the anode flow rate (up to 400 NmL/min), the heat fluxes increase linearly, and deviate from this trend for higher flow rates. The linear part corresponds to cases where the anode flow is small enough

to be fully saturated with water vapor. On the other hand, for higher values of the mass flow rate, the flow leaves the active area without being fully saturated, and the heat fluxes do not reach the maximal possible value. The behavior with respect to cathode mass flow rate is similar; however the linear increase stops at much lower values, around 50 NmL/min.

A simple 1D model was made based on the assumptions that the evaporation takes place on both sides, and that the total heat flux is linked to the evaporation rate $\dot{m}_{evap}$:

$$\phi_{total} = \phi_a + \phi_n = \dot{m}_{evap} \times L_{Lv}/S$$

where L_{Lv} is the latent heat of vaporization and S the HFS surface.

We also assume that the evaporation on the anode side is controlled by the convection from the anode gas flow only, and is not influenced by the cathode gas flow. The evaporation on the cathode side is more complex: the water vapor diffuses through all the layers (GDLs, MPLs and membrane) before reaching the gas channels on the cathode side and being carried away by the cathode gas flow. Figure 5 sums up our 1D model assumptions:

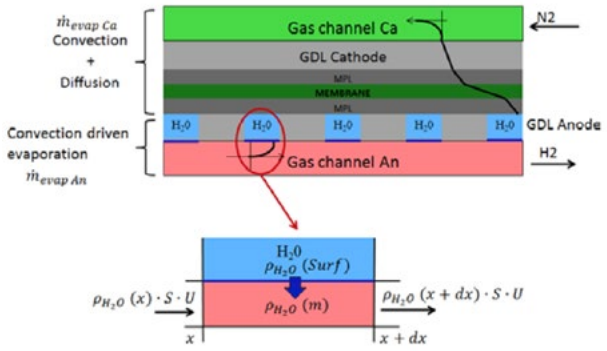

Figure 4. *1D model assumptions for the evaporation taking place in the test cell.*

The species conservation on a small element of an anode gas channel gives us:

$$U \cdot S \cdot \left(\rho_{H_2O}(x+dx) - \rho_{H_2O}(x)\right) = Surf \cdot MTC \cdot \left(\rho_{H_2O}(Surf) - \rho_{H_2O}(m)\right)$$

When this equation is integrated, we find:

$$\dot{\phi}_{evap} = \dot{m}_{gas\ An} \cdot Y_{sat} \cdot \left[1 - exp\left(-\frac{\overline{MTC} \cdot \rho_{H_2} \cdot Surf}{\dot{m}_{gas\ An}}\right)\right] \cdot L_{LV}(80°C)$$

where $\dot{m}_{gas\ An}$ is the anode gas mass flow rate, Y_{sat} the mass fraction of water vapour at saturation, ρ_{H_2} the density of incoming H_2, $\overline{MTC}$ the average mass transfer coefficient and $Surf$ the surface of the water-filled hydrophilic lines in contact to the anode gas flow. This last parameter cannot be predicted; however it can be extracted from the NR images. Figure 5 left shows an example of a post-processed NR image of the active area of our fuel cell. The dark line in the center is the cooling water channel; the small lines perpendicular to it are the hydrophilic regions of the GDL filled with water. First, the graylevel images are binarized, and the resulting image is inverted so that the pixels representing the water have a value of 1. This image is then multiplied by a binary image representing the flowfields ribs and channels: the ribs and the water channel have a value of 0, the gas channels a value of 1. Last, the pixels of the final image are added and multiplied to the area of one pixel to obtain the contact surface $Surf$.

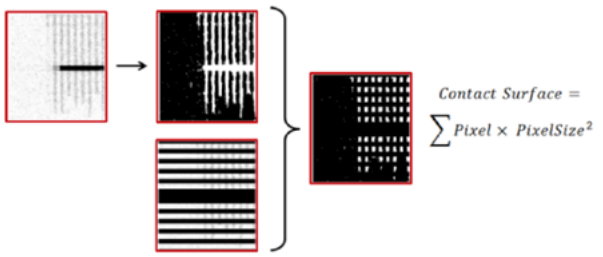

Figure 5. *Left: NR image of the active area of the test cell with evaporation cooling scheme. Right: Detection algorithm to determine the surface of the water filled hydrophilic lines in contact with the gas flow.*

Once $Surf$ is known, the heat flux due to the evaporation on the anode side can be computed and compared to the total measured heat flux. There is a good qualitative agreement between the 1D model and the measurements. In fact, the difference between measured and model heat fluxes is an offset that does not depend on the anode mass flow rate. We consider that this offset is the heat due to the evaporation on the cathode side. Once the offset is taken into account, the 1D model is in very good agreement with the measurements for all cathode mass flow rates, as can be seen on Figure 6.

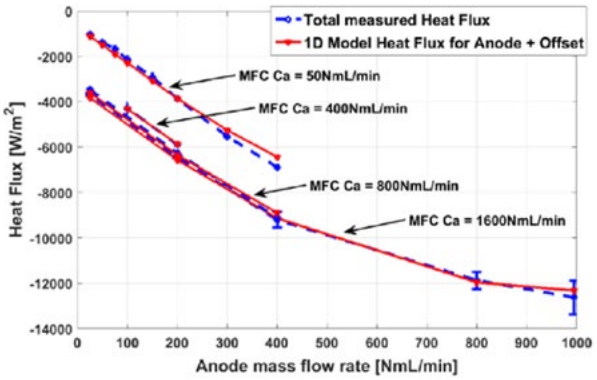

Figure 6. *Comparison of the total measured heat fluxes and the 1D model.*

Conclusions

A thermal test bench has been built to characterize the evaporation of an evaporative cooling scheme for PEFC. Using a simple 1D model based on pure convection, we can reliably calculate the evaporation rate on the anode side.

Acknowledgement

The authors would like to thank the SCCER Mobility and the Swiss National Science Foundation (project n° 142432) for their financial support.

References

[1] P. Boillat, A. Forner-Cuenca, L. Gubler, C. Padeste, F.N. Büchi, *EP 2996184 A1*, Priority date: 9.09.2014.

[2] A. Forner-Cuenca, J. Biesdorf, L. Gubler, P.M. Kristiansen, T.J. Schmidt, P. Boillat, *Adv. Mater.* **27** (41), 6317–6322 (2015).

Gas diffusion media with patterned wettability: MPL synthesis

V. Manzi-Orezzoli, A. Forner-Cuenca, L. Gubler, T.J. Schmidt, P. Boillat
phone: +41 56 310 4447, e-mail: victoria.manzi@psi.ch

Water management in polymer electrolyte fuel cells (PEFCs) is one of the key features to consider in order to have a high performing and efficient PEFC. The water management, as well as the gaseous fuel feed, mainly takes place through the gas diffusion media (GDM); which is a composite consisting on a gas diffusion layer (GDL) and a microporous layer (MPL).

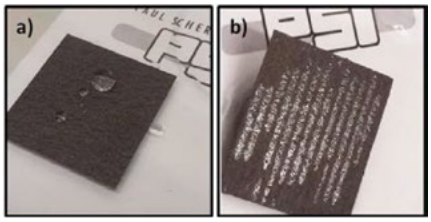

Figure 1. *Images of GDLs Toray H060: a) with a plain hydrophobic treatment and b) with patterned wettability.*

Within our group, a GDL with selected modified regions [1] providing preferential water pathways which help to improve the water management [2] was developed, with first *in situ* tests realized using a separate self-standing MPL. Work is now undertaken to integrate the MPL in the synthesis process of our GDM. Here we present first results about the synthesis of a FEP based MPL compatible with our process.

Experimental

The MPL ink was prepared by adding 0.58 g of acetylene black carbon (Alfa Aesar 99.9 %, 50 % compressed), 55 mL of miliQ water, 47 mL of isopropanol (PROLABO, VWR) and 0.35 g of fluorinated ethylene propylene (FEP) dispersion (FEPD121 DuPont 55 % solids). The dispersion was sonicated for 30 min, and 5 min again before application. The MPLs were spray coated onto the GDL substrates with a load ratio of 0.3 mL/cm^2 and then sintered at 270 °C.

Characterization:
The electron microscopy images were obtained with a FESEM Ultra 55 FE-SEM Ultra 55 (Carl Zeiss, Oberkochen, Germany). The *in situ* experiments were performed by recording polarization curves at 70 °C at 100 % relative humidity with a H_2/Air feedstock at 2 bars and a gas flow of 2000 NmL/min for both anode and cathode in a cell with 15.77 cm^2 active area. Each step was held for 15 minutes and the average of the last minute was calculated. This value was taken as the potential at certain current density value. For the MEA construction catalysts coated membrane (Primea 5710, Gore) with a GDL SGL 24BC on the anode side were used. The cathode side was varied for each different experiment.

Results and discussion

We compare the home-made (HM) MPLs with our benchmark material, SGL 24BC, to be sure that the base material for our modification is competitive to commercially available GDMs. The HM MPLs are thinner than the commercial, 25 ± 10 µm against 40 µm, but they have similar contact angles, 146 ± 4° for HM and 152 ± 3° for SGL 24BC.

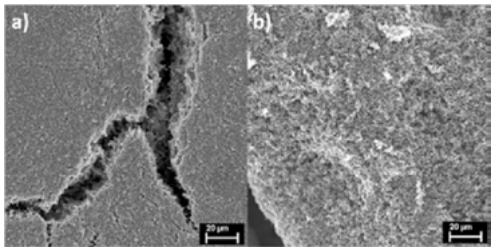

Figure 2. *SEM images of MPLs: a) Commercially available MPL SGL 24BC. b) Home-made casted MPL on a SGL 24BA GDL substrate.*

The topology of the two MPLs is quite different. As can be seen in Figure 2a, the commercial MPL has a more compact structure where the layer is covered by large cracks distributed along the MPL. The HM MPL has a less compact and apparently more porous structure (Figure 2b), also the HM MPL recovers the fibers of the GDL rather than forming a continuous layer on top of it.

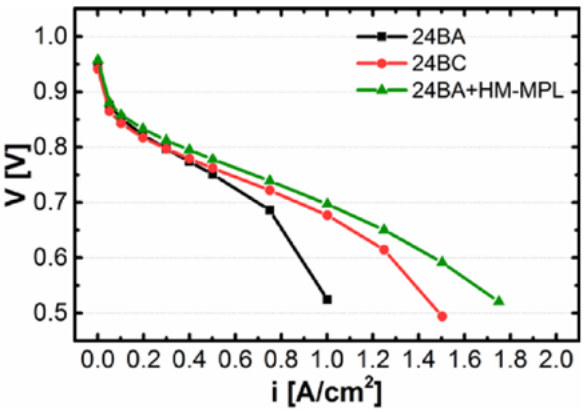

Figure 3. *Polarization curve comparison for three different materials used on the cathode side.*

Performance wise the incorporation of the HM MPL largely improve the performance of the GDL, being as good, even slightly better than the commercial SGL 24BC. These results provide us with a promising base material for the incorporation of our patterned wettability design.

Acknowledgement

The authors would like to acknowledge Dr. Alexandra Patrû and Muriel Siegwart for scientific discussion and technical support.

References

[1] A. Forner-Cuenca, V. Manzi-Orezzoli, J. Biesdorf, M. El Kazzi, D. Streich, L. Gubler, T.J. Schmidt, P. Boillat, *J. Electrochem. Soc.* **163**, F788–F801 (2016)
[2] A. Forner-Cuenca, J. Biesdorf, V. Manzi-Orezzoli, L. Gubler, T.J. Schmidt, P. Boillat, *J. Electrochem. Soc.* **163**, F1389–F13988 (2016).

Time-of-flight neutron imaging for distinction of water and ice

M. Siegwart, R. Woracek[1], V. Manzi-Orezzoli, A. Tremsin[2], M. Strobl[1], T.J. Schmidt, P. Boillat
phone: +41 56 310 5772, e-mail: muriel.siegwart@psi.ch

Start-up at sub-zero temperatures is a great challenge for polymer-electrolyte fuel cells (PEFC). Therefore, advanced characterisation methods need to be developed which provide insight into freezing mechanisms in order to optimize fuel cell design and components. As the water produced by the PEFC is of high purity it can be present at sub-zero temperatures in its super-cooled state, which means it is liquid even if the temperature is below its melting temperature. How long the water is present in its super-cooled state is dependent on several parameters such as cluster volume size, hydrophobicity of the surface or presence of freezing nucleus.

For studying the phase change of water during *in situ* fuel cell experiments, imaging methods need to be developed which allow determining the phase state of water with high time resolution.

Time-of-flight (TOF) neutron imaging is a neutron wavelength resolved method that allows measurements of transmission spectra in every pixel of the image by evaluating the velocity (which can be converted to wave-length) of each detected neutron. The velocity is measured by the time it takes the neutron to travel from the chopper disk to the detector over a known path length. The neutron attenuation between liquid water and ice differs at long wavelengths ($\gtrsim$ 4Å).

By using TOF or other wavelength selective neutron imaging techniques (e.g. dual spectrum method with beryllium filter [1]) the aggregate state of water can be determined. By applying the dual spectrum neutron imaging method for investigating a fuel cell with 50 cm² active area, it was demonstrated that the first freezing events occur close to the gas outlets [2]. However, the contrast of neutron cross section between liquid water and ice with the dual spectrum method is rather low (1.6 %) and a reliable distinction is not possible for a small water thickness.

We performed TOF neutron imaging experiments at the test beam line for ESS at the Helmholtz Zentrum Berlin (HZB) [3] to prove that with a reasonably short exposure time (5–10 min) and a low wavelength resolution enough neutron statistics can be collected and contrast is high enough to reliably distinguish between liquid water and ice.

Experimental

Water scale: The device used to perform the experiments was a simple water scale made of aluminium. The bottom part of the water scale is depicted in Figure 1. It accommodates four different water/ice thicknesses: 125, 250, 500 and 1000 µm.

Chopper system for time of flight: In order to measure with a high duty cycle of 29 % the Band Chopper Discs 1 and 2 of the ESS test beam line were used [3]. The frequency of the chopper discs was set to 21 Hz. With these settings, a slit opening time (pulse duration) of 14 ms and a period of 47 ms were achieved. With a distance from the chopper disc to the detector of 16.3 m, a small pulse overlap of 6 ms was produced.

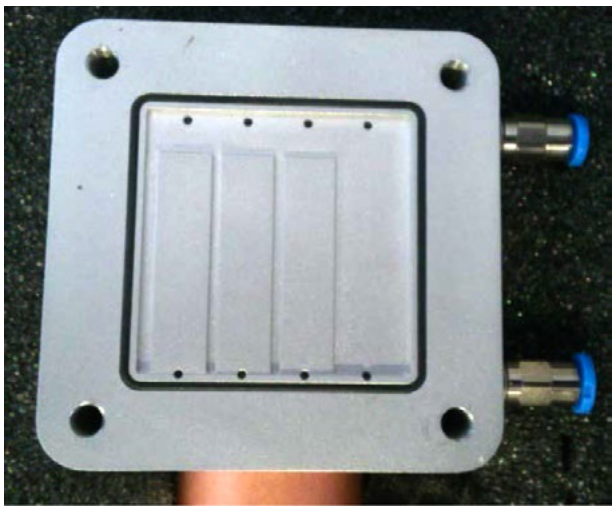

Figure 1. *Water scale that accommodates liquid water or ice with thicknesses of 125, 250, 500 and 1000 µm.*

The water scale was filled with water through a channel behind the four holes at the bottom, while the holes on top of the water scale, which are connected through a channel to an outlet pipe, allowed the air to escape. For drying, pressurized air was connected first to the top channel and later to the bottom channel. The water scale was not filled completely with water in order to leave room for volume expansion during the phase change to ice. The total sealed area inside the O-ring is 3 x 3 cm² and slightly larger than the field of view of the detector. Borated aluminium plates with a width of 3 mm and thickness of 5 mm were placed at the backside of the depicted bottom part in Figure 1. Borated aluminium absorbs neutrons, and the neutron counts measured in the area behind it are used for scattering correction.

«Climate chamber»: The water scale was placed into an aluminum box which was continuously flushed with pressurized air to avoid condensation of water on the lid of the scale. Peltier elements and a temperature controller (KSV) were used to control the temperature of the water scale. After filling the scale with water it was cooled down to 6 °C and images of liquid water were taken. Then, the temperature was decreased to –2 °C in order to take images of super-cooled water. Finally, the scale was cooled to –13 °C to produce ice and then the temperature was increased slowly to –2 °C where images of ice were taken.

Neutron Detector: The TOF neutron imaging experiments were performed with a neutron sensitive Micro Channel Plate (MCP) detector with 512 x 512 pixel and 55 µm pixel pitch [4]. The field of view was 2.8 x 2.8 cm².

[1] European Spallation Source ESS AB, Lund, Sweden
[2] University of California at Berkeley, Berkeley, CA, USA

Image processing: For calculating the attenuation coefficient and the cross section of liquid water and ice, all images underwent the following processing:

1. Intensity correction for fluctuation of neutron reactor output and detector efficiency;
2. Correction for scattered neutron (with measured intensity behind borated aluminium);
3. Referencing by a dry image.

Results and Discussion

Figure 2 shows the cross section of liquid water and ice with a thickness of 1 mm in beam direction. The measured cross section is averaged over a pixel area of 2 mm² and compared to theoretical calculations of the effective cross section that take the spectrum of the beamline and the pulse duration into account. The measurement was performed with a very low wavelength resolution ($\Delta\lambda = 3.5$ Å). The exposure time was approximately 7 minutes.

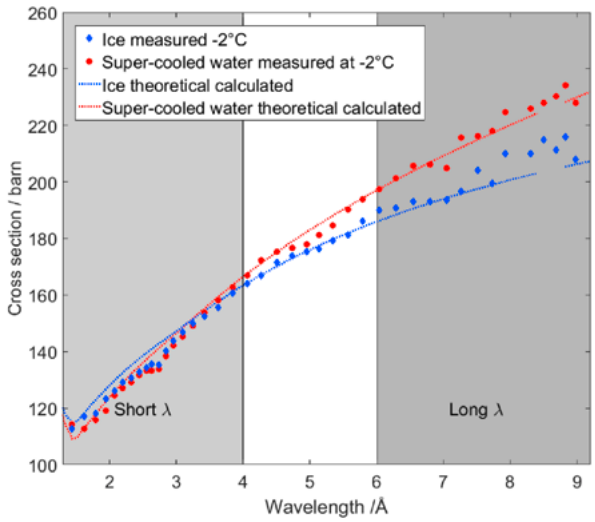

Figure 2. *Measured neutron cross-section averaged over 2 mm² pixel area of super-cooled water at –2 °C (red) and ice at –2 °C (blue)) compared to theoretical calculated cross section as a function of neutron wavelength. The x-axes shows the weighted average of the wavelength* ($\Delta\lambda = 3.5$ Å).

The cross section (σ) is calculated by inverting the Beer-Labert law:

$$\sigma_x = \frac{-log\left(\frac{I_x}{I_{dry}}\right)}{N_x * \delta_x}$$

with x being the substance (liquid water or ice), I_x the neutron intensity measured behind the sample filled with water/ice, I_{dry} the intensity of the dry sample, N the atomic number density (taking into account the differences of atomic densities of liquid water and ice) and δ the thickness. The ratio $\frac{I_x}{I_{dry}}$ is the transmission, while $-log\left(\frac{I_x}{I_{dry}}\right)$ is called attenuation (Δ_x) of the water content. The average attenuation is calculated for the two wavelength regions shown in Figure 2. In the short wavelength region, the attenuation for ice and water is approximately the same, while for long wavelengths it is lower for ice than for water. The contrast between liquid water and ice is quantified by calculating relative attenuation coefficients, $\alpha_{,rel,ice}$ and $\alpha_{,rel,liquid}$, which are, in case the water thickness is small, very little dependent on the water/ice thickness. $\alpha_{,rel}$ is the ratio of the attenuation at long neutron wavelengths (LW) over the attenuation at short wavelengths (SW): $\alpha_{,rel} = \frac{\Delta_{LW}}{\Delta_{SW}}$. The regions of wavelengths that were considered short respectively long are marked grey in Figure 2 and labelled accordingly. Based on these wavelength regions a contrast of 8.3 % (± 0.5 %) between super-cooled water and ice at –2 °C is calculated. This contrast is approximately 5 times higher than the one obtained with the dual spectrum method.

Acknowledgement

Dirk Scheuble is gratefully acknowledged for building the experimental setup and for his support during experiments.

References

[1] J. Biesdorf, P. Oberholzer, F. Bernauer, A. Kaestner, P. Vontobel, E.H. Lehmann, T.J. Schmidt, P. Boillat, *Phys. Rev. Lett.* **112** (24), 248301 (2014).

[2] P. Stahl, J. Biesdorf, P. Boillat, K.A. Friedrich, *J. Electrochem. Soc.* **163** (14), F1535–F1542 (2016).

[2] R. Woracek, T. Hofmann, M. Bulat, M. Sales, K. Habicht, K. Andersen, M. Strobl, *Nucl. Instr. and Meth. A.* **839**, 102–116 (2016).

[4] A. Tremsin, V. Dangendorf, K. Tittelmeier, B. Schillinger, M. Schulz, M. Lerche, W. Feller, *Nucl. Instr. and Meth. A* **787**, 20–25 (2015).

SCIENTIFIC ACHIEVEMENTS 2016

Batteries –

Materials

Effective conductivity of electrolyte in lithium-sulfur cells

J.M. Conder, C. Villevieille, S. Trabesinger, P. Novák, L. Gubler, R. Bouchet[1]
phone: +41 56 310 2120, e-mail: joanna.conder@psi.ch

Asymmetric separators with polysulfide barrier properties and Li^+ exchange sites, consisting of porous polypropylene (PP) grafted with styrene sulfonate (SS), PP-g-PLiSS, were developed and investigated as an alternative for Celgard, the state-of-the-art separator for the lithium–sulfur (Li–S) battery. These asymmetric separators were thoroughly characterized in Li–S cells to assess their practical applicability and to determine the threshold amount of cation-exchange groups (SS) that can be introduced into the PP base polymer without sacrificing the separator's asymmetry and other properties crucial for a well-functioning Li–S cell [1, 2]. The latter includes transport properties of the PP-g-PLiSS, in particular the effective ionic conductivity through the separator.

Herein, we discuss the influence of the cation-exchange groups located at and near the surface of the PP base polymer on the resistance of both the electrolyte (swelling of the SS) and the lithium electrode/electrolyte interface.

Experimental

Electrochemical impedance spectroscopy (EIS) measurements were carried out using a standard coin-type cell, in which a separator was placed between two identical lithium metal electrodes (thickness: 0.75 mm, ø = 13 mm, Alfa Aesar). The PP-g-PLiSS separators with two distinct graft levels (GL), i.e., 8 and 30 % GL, were chosen for this study as representative asymmetric separators with low and high amounts of cation-exchange groups, respectively. Prior to cell assembly, each grafted separator was pre-soaked in the electrolyte, 1 M lithium bis(trifluoromethane) sulfonimide (LiTFSI) in a mixture of dimethoxyethane (DME) and 1,3-dioxolane (Diox) (2 : 1 by weight, BASF), to ensure complete wetting. Once placed in the cell, it was additionally wetted with 30 µl of electrolyte. Celgard 2400 (Celgard®, USA), used as a reference separator, was not pre-soaked in the electrolyte. Instead, it was directly wetted with 50 µl of electrolyte during the cell assembly.

The measurements were performed at open circuit potential (OCP) using a VMP3 multichannel potentiostat (Bio-Logic Science Instruments). A sinusoidal perturbation of 10 mV was applied over the frequency range from 1 MHz to 50 mHz. All spectra were first deconvoluted using an equivalent circuit and subsequently fitted with ZView software (Scribner Associates Inc.). The resistance values were normalized to the geometrical area of the electrode.

The effective conductivity through the separator, σ_{eff}, was calculated as follows:

$$\sigma_{eff} = \frac{L}{A \cdot R_{el}} \cdot \frac{1}{\varepsilon}$$

where L is the thickness of the separator, A is the geometrical area of the electrode (1.3 cm^2), and R_{el} is the ohmic resistance of the electrolyte ($R_{el} + R_{swell}$ in the case of the 30 % grafted separator). The values were corrected by taking into account the porosity (ε) of the separator. In the case of Celgard, this parameter was taken from the specifications, whereas in case of the grafted separators, the porosity was quantified based on the FIB/SEM analysis followed by 3D reconstruction of the polymer microstructure [3]. All values used for quantification are listed in Table 1.

	R_{el} (Ω cm^2)	L (µm)	ε (%)
Celgard 2400	2.8	25.0	40
8% grafted PP-*g*-PLiSS	4.8	26.6	36
30% grafted PP-*g*-PLiSS	76	29.8	16

Table 1. *Summary of the electrolyte resistance, thickness and porosity for the three different separators.*

Results

In the case of the reference cell with Celgard, the diameter of the middle-frequency (MF) semicircle ascribed to the resistance of the Li electrode/electrolyte interface, R_{int}, increases gradually as a function of time.

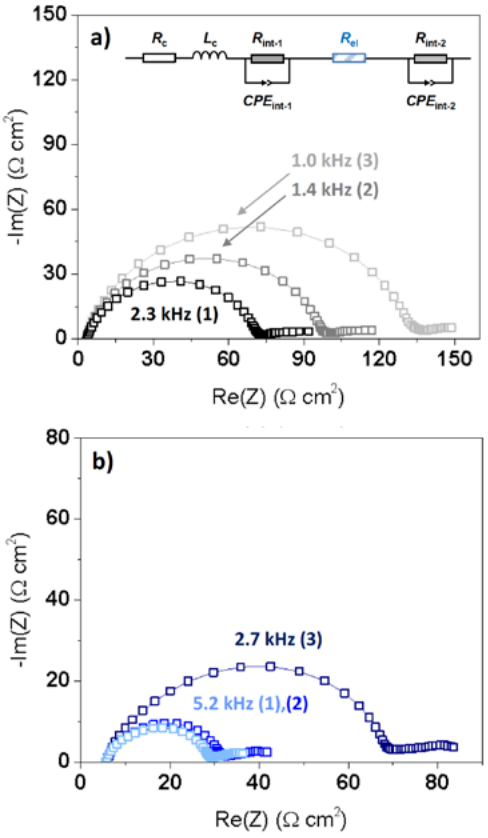

Figure 1. *Evolution of the impedance response of symmetric Li/Li cells with (a) Celgard and (b) 8 % grafted PP-g-PLiSS separator as a function of time: after cell assembly (1), after 10 min (2) and after 4 h (3). The equivalent circuit used for fitting the EIS spectra is shown in the inset of panel (a).*

[1] Université de Grenoble Alpes, LEPMI, Grenoble, France

This phenomenon is due to the formation and growth of the passivation layer, solid/electrolyte interphase (SEI), on the Li electrode surface [4, 5]. Initially, R_{int} was equal to 60 Ω cm², and this value nearly doubled within the next 4 h (Figure 1a). The characteristic frequency, however, decreased over the measured time range from initially 2.3 kHz to finally 1.0 kHz indicating that the growth and/or rearrangement of the SEI gets slower with time. A decrease was also observed for the electrolyte resistance, R_{el}, which started at ca. 3.1 Ω cm² and gradually declined, reaching a quasi-stable value of 2.8 Ω cm² after 1 h.

With the 8 % grafted PP-g-PLiSS (Figure 1b), the general trend of R_{int} was similar to that seen for the reference cell, however, the absolute values of the Li electrode/electrolyte interfacial resistance were on average ca. 50 Ω cm² lower than that of the reference cell. Besides, the characteristic frequency of the MF semicircle was higher by almost a factor of three, reflecting the fast dynamics of the reactions taking place at the Li electrode/electrolyte interface. The latter originated most probably from the presence of cation-exchange groups at and near the surface of the separator. However, the concentration of SS groups therein was yet too low to result in a separate impedance contribution, unlike in the case of the 30 % grafted PP-g-PLiSS (Figure 2).

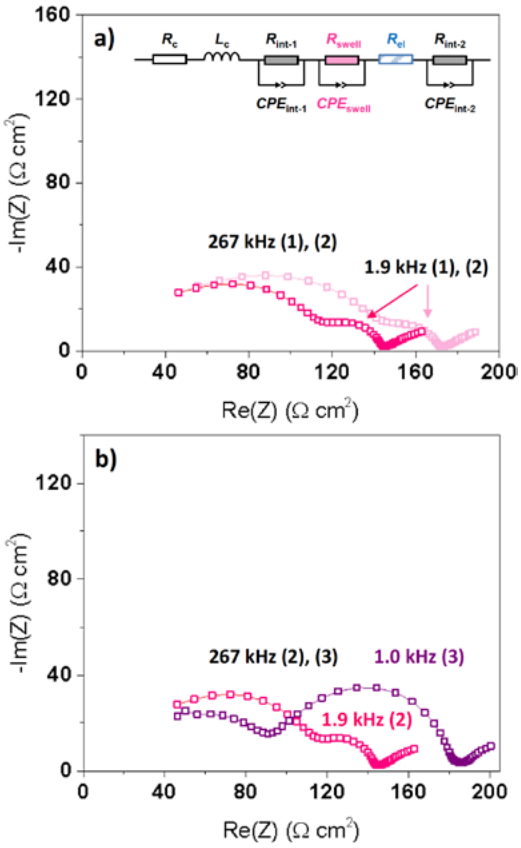

Figure 2. *Evolution of the impedance response of a symmetric Li/Li cell with 30 % grafted PP-g-PLiSS separator as a function of time. For clarity, only the spectra recorded (a) after cell assembly (1) and after 10 min (2), and (b) after 10 min (2) and 4 h (3) are presented. The equivalent circuit used for fitting the EIS spectra is shown in the inset of panel (a).*

The increase in the number of SS groups at and near the surface of the PP base polymer changed the impedance response of the symmetric cell significantly. With the highly grafted separator (GL of 30 %), a new contribution appeared in the high-frequency (HF) to MF region (Figure 2). This new contribution was ascribed to a combination of the electrolyte resistance, R_{el} and the swelling of the cation-exchange layer (R_{swell} || CPE_{swell}) in the electrolyte.

Initially, $R_{el} + R_{swell}$ of the cell with the 30 % grafted separator was as high as 100 Ω cm², indicating the difficulty to readily swell the asymmetric separator when the porosity is significantly reduced (Table 1). Over time, it continuously decreased, reflecting the improvement of the swelling of the cation-exchange layer in the electrolyte. $R_{el} + R_{swell}$ leveled off at around 70 Ω cm² after roughly 80 min, once the swelling equilibrium was attained. The trend was opposite for R_{int}. The amplitude of the MF semicircle gradually increased as a function of time, from initially 27 Ω cm² to finally 80 Ω cm². The characteristic frequency of this loop was comparable to that seen previously for the reference cell with Celgard (Figure 1a).

Next, we calculated the effective conductivity through Celgard and PP-g-PLiSS separators. Although the effective conductivity through the 8 % grafted separator is very close to the one through Celgard (1.2 and 1.7 mS cm^{-1}, respectively) the values are not identical. The slightly lower conductivity through the 8 % grafted separator reflects the kinetic hindrance to Li-ion transfer introduced at and near the surface of the separator by the grafted SS groups. This drop is, as expected, more pronounced with the 30 % grafted PP-g-PLiSS separator, whose effective conductivity is almost one order of magnitude lower (0.2 mS cm^{-1}) than that of Celgard. This further confirms the change in the ion mobility within the two different layers of the asymmetric PP-g-PLiSS separator, as already hypothesized in our previous reports [1, 2].

Conclusions

The EIS study on symmetric Li/Li cells showed that the chemistry of the separator has a strong influence on the transport properties of the electrochemical system. In the present case, it was essential to balance the amount of the SS groups at and near the surface of the PP base polymer to substantially decrease the Li electrode/electrolyte interfacial resistance, while maintaining a practical effective conductivity through the asymmetric separator.

Acknowledgement

The authors thank the Swiss National Science Foundation (project n° 200021_144292) for financial support.

References

[1] J. Conder, S. Urbonaite, D. Streich, P. Novák, L. Gubler, *RSC Adv.* **5**, 79654–79660 (2015).
[2] J. Conder, A. Forner-Cuenca, E. Müller, L. Gubler, P. Novák, S. Trabesinger, *ACS Appl. Mater. Interfaces* **8**, 18822–18831 (2016).
[3] J. Conder, *PhD Thesis No. 23786*, ETH Zürich, 2016.
[4] C. Daniel, J.O. Besenhard, *Handbook of Battery Materials*, Wiley (2012).
[5] D. Herbert, J. Ulam, *Electric dry cells and storage batteries*, US Patent 3,043,896 A (1962).

Chemical decomposition of tristrimethylsilylphosphite (TMSPi) in lithium ion batteries

C. Bolli, A. Guéguen, E.J. Berg
phone: +41 56 310 5091, e-mail: christoph.bolli@psi.ch

Electrolytes for lithium ion batteries (LIB) normally consist of a mixture of a linear carbonate (e.g. diethyl carbonate (DEC)), a cyclic carbonate (e.g. ethylene carbonate (EC)) and a salt (typically $LiPF_6$). Commercial electrolyte mixtures often also contain additives, which may act as redox-shuttles to improve battery safety, as layer forming compounds to protect the electrode surfaces, or as scavengers of electrochemically formed side products in order to improve LIB performance. [1, 2]

The additive Tris(trimethyl)silylphosphite (TMSPi) has gained significant interest in the recent years. Choi et al. have shown that TMSPi reduces the amount of detrimental HF and that cells containing TMSPi showed decreased capacity fading. [3] However, Winter et al. have shown that TMSPi also reacts with $LiPF_6$ leading to decomposition of the additive and to formation of gaseous side products such as Me_3SiF. [4] The aim of this report is to investigate the lifetime of TMSPi in commercially available battery electrolyte using online electrochemical mass spectrometry (OEMS) to detect gaseous side products.

Experimental

Positive electrodes were prepared by coating a slurry based on HENCM (89 %), PVDF (5 %), SC65 (4.64 %), SFG6L (1.36 %) in NMP on Celgard 2400® (Celgard) monolayer polypropylene (PP). Graphite electrodes were prepared by coating a slurry based on SFG6 (95.7 %), CMC (3.8 %), SC65 (0.5 %) in H_2O on Cu foil. After punching circular discs as electrodes (Ø: 15 mm (HENCM), 20 mm (graphite)) these were heated, dried under vacuum and inserted in an Ar filled glovebox.

LP47 (EC/DEC 3 : 7, 1 M $LiPF_6$, BASF SE) and TMSPi (98 % Alfa Aesar) were used as received. LP47 solutions containing 1 %wt TMSPi were freshly prepared. Detailed descriptions of the construction and assembling of OEMS cells as well as calibration and technical information regarding the OEMS setup can be found in previous works. [5] HENCM/SFG6 full cells with differently aged LP47 electrolytes containing 1 %wt TMSPi were cycled at C/10 rate.

Results

Figure 1A shows the potential profile for the 1st charge and the corresponding evolution of Me_3SiF (m/z = 77) for fresh, two and four days aged LP47 electrolyte containing 1 %wt TMSPi. The Me_3SiF evolution for freshly prepared electrolyte is mainly potential dependent as a result of reactions between TMSPi and electrochemically formed side-products as HF. Two and four days aged electrolytes show the maximum evolution of Me_3SiF at the beginning of the measurement, from when the evolution rate decays exponentially as result of dilution.

The observed gas was formed in the electrolyte during the storage time by a chemical reaction of TMSPi with $LiPF_6$. For the aged electrolytes no Me_3SiF is formed during cycling, showing that already short storage times diminish the ability of TMSPi to act as scavenger.

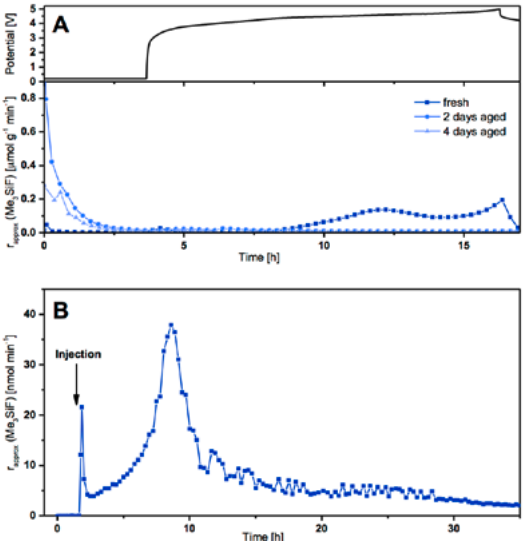

Figure 1. *A: Potential profile (top) and evolution-rate of Me_3SiF (bottom) for a HENCM/SFG6 full cells (120 ul LP47 + 1 %wt TMSPi, C/10 cycling, 5 V cut-off). B: Evolution rate of Me_3SiF after injecting 3 %wt TMSPi in DEC into LP47 electrolyte.*

To investigate the rate of the reaction, a modified cell was designed, which allows the injection of liquids into an OEMS cell and to monitor the gas-evolution. To simplify the experiment, the cell contained solely LP47 electrolyte and a solution of TMSPi in DEC was injected. Figure 1B shows an immediate reaction between TMSPi and $LiPF_6$ and formation of Me_3SiF directly after mixing. The maximum evolution rate for Me_3SiF is observed at about 9 h after the injection. Afterwards the rate decreases until a constant level is reached at about 20 h.

Conclusions

In carbonate solvents the reaction of TMSPi with $LiPF_6$ salt is very fast and reduces the ability of the additive to act as HF scavenger during cycling. Effective scavenging can only be achieved if TMSPi containing electrolytes are freshly prepared.

Acknowledgement

Financial support from BASF SE is kindly acknowledged.

References

[1] S.S. Zhang, *J. Power. Sources* **104**, 1379–1374 (2006).
[2] A.M. Haregewoin, A.S. Wotango, B.-J. Hwang, A. Didion, *Energ. Environ. Sci.* **9**, 1955–1988 (2016).
[3] J.-G. Han, S.J. Lee, J. Lee, J.-S. Kim, K.T. Lee, N.-S. Choi, *ACS Appl. Mater. Interfaces* **7**, 8319–8329 (2015).
[4] X. Qi, L. Tao, H. Hahn, C. Schultz, D.R. Gallus, X. Cao, S. Nowak, S. Röser, J. Li, I. Cekic-Laskovic, B. Rezaei Rad, M. Winter, *RSC Adv.* **6**, 38342–38349 (2016).
[5] A. Guéguen, D. Streich, M. He, M. Mendez, F.F. Chesneau, P. Novák, E.J. Berg, *J. Electrochem. Soc.* **163**, A1095–A1100 (2016).

Sodiated nickel manganese spinel as cathode materials for Na-ion batteries

L. Boulet-Roblin, A. Gerlitz, C. Villevieille
phone: +41 56 310 2115, e-mail: lucien.boulet@psi.ch

Renewable energies are the solution to greenhouse emission; however storage abilities are limited which lower their efficiency. Li-ion battery (LIB) is one of the most promising technologies in term of storage solutions but they are too expensive for this market. Alternative battery systems need to be investigated in order to decrease such costs. Recently, sodium-ion batteries (NIBs) attracted a lot of attention due to their working principle similar to the LIBs. The Na abundance and the usage of only Al current collector are expected to reduce battery costs to ca. 25 % compared to Li-ion battery for slightly lower energy density [1, 2].

In order to improve the NIBs performance, novel cathode materials with high operating voltage are targeted. Based on our researches in disordered LiNi0.5Mn1.5O4 spinel materials (named hereafter LNMO), a concept based on Li/Na substitution led to the development of NaNMO ($NaNi_{0.5}Mn_{1.5}O_4$) material for NIBs [3]. By analogy to LNMO, we expect that NaNMO spinel would allow 3D sodium-diffusion high-voltage cathode for Na-ion batteries.

In order to obtain NaNMO material, an electrochemical delithiation and then sodiation was used as proof of concept. Structural and electrochemical performance were also investigated.

Experimental

Electrodes were prepared by casting a mixture of 90 wt.% d-LNMO (provided by SAFT), 5 wt.% Super-P carbon and 5 wt.% PVDF binder suspended in NMP solution. The casted slurry was dried at 80 °C under vacuum overnight. All the cells were assembled in an Argon-filled glove box. Metallic lithium and sodium foil were used as counter electrode and a glass fiber sheet as separator soaked with LP30 electrolyte (EC : DMC 1 : 1 %wt 1 M $LiPF_6$) and 1 M $NaClO_4$ dissolved in propylene carbonate (PC), respectively. The cells were cycled galvanostatically between 3.5–5.0 V vs. Li^+/Li or 2.5 V and 4.3 V vs. Na^+/Na at C/20 rate (based on a theoretical specific charge of 147 mAh/g) at room temperature using Bat-small from Astrol Electronics AG.

NaNMO electrodes were obtained through electrochemical delithiation of LNMO electrode by charging them vs. Li/Li^+. Afterwards, these delithiated LNMO electrodes were rinsed with DMC and assembled in a cell vs. Na/Na^+.

XRD measurements were performed using a PANalytical Empyrean diffractometer with Cu-Kα radiation. The XRD patterns were refined using the Rietveld method.

Results

Figure 1 shows the galvanostatic profiles of the LNMO first (de) lithiation and NaNMO first (de)sodiation. When lithium is replaced by sodium in the spinel, the electrochemical plateaus attributed to $Ni^{4+/3+/2+}$ redox couples are replaced by a sloping potential profile. Unfortunately, the working potential window of NaNMO (2.5–4.3 V vs. Na^+/Na) is much lower than in the case of the lithiated spinel. A specific charge higher than 130 mAh/g is usually obtained during the first sodiation.

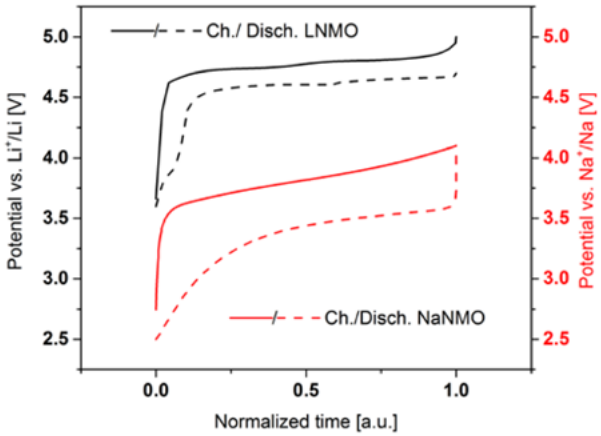

Figure 1. *Galvanostatic curves of electrochemical delithiation of d-LNMO and electrochemical sodiation of NaNMO.*

Figure 2 presents the Rietveld refinement of NaNMO after the first sodiation. The disordered cubic structure of d-LNMO (Fd-3m) is kept, meaning that Ni and Mn are statistically distributed on the 16d, Na on the 8a and O on the 32e Wyckoff positions. However, the lattice parameters of NaNMO are larger than the ones of LNMO (a = b = c = 8.45 Å instead of 8.17 Å) most probably due to the larger radius size of sodium ions than lithium ones. The relatively high background contribution until 40 ° is due to carbon Super-P in the electrode. Since the spinel structure is kept, NaNMO is potentially a 3-D lithium diffusion material.

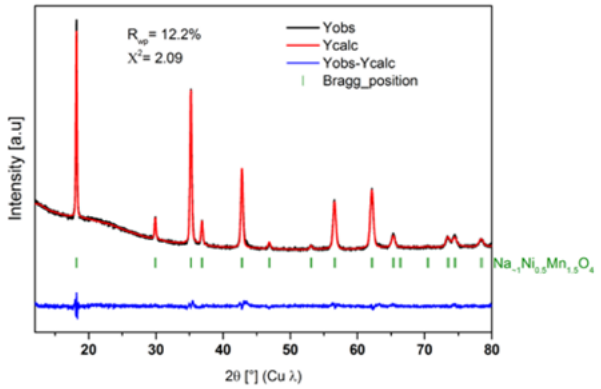

Figure 2. *Rietveld refinement of NaNMO XRD pattern after the first sodiation.*

Figure 3 shows the evolution of the specific charge during cycling of NaNMO vs. metallic sodium. As one can see during the first sodiation, the theoretical charge is almost obtained (i.e. 135 mAh/g for 1 Na^+ exchanged per mole, supposedly).

However, only ca. 70 mAh/g is obtained during the first desodiation. On subsequent cycle, the fading is more drastic and the electrochemical performance reached 40 mAh/g after 20 cycles. During the first three cycles, higher specific charges are obtained during sodiation than desodiation, meaning that more sodium can be inserted in the NaNMO that can be afterward extracted. Surprisingly, the Na intercalation/extraction is nicely reproducible after 20 cycles with almost no lost between charge/discharge, indicating most probably an insertion reaction mechanism with stable structural changes.

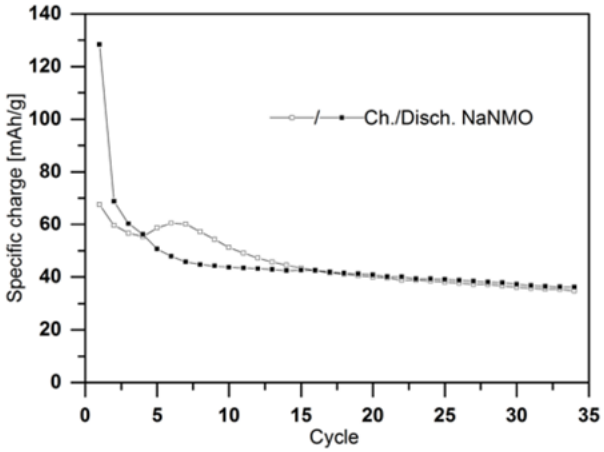

Figure 3. *Specific charge of NaNMO vs. Na^+/Na at C/20 rate.*

As one can see after 35 cycles, the pattern of the spinel structure after the first sodiation (Figure 4, black curve) matches the one obtained after 35 cycles (red curve), confirming the stability of the spinel structure during (de)sodiation. However, a slightly larger lattice parameter is found with a = b = c = 8.46 Å instead of 8.45 Å. It indicates that more sodium was inserted after the first sodiation as the irreversible specific charge suggested it during the first three cycles.

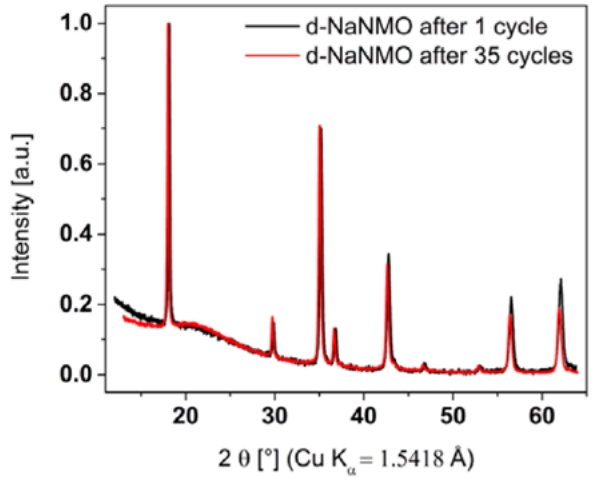

Figure 4. *XRD patterns of sodiated NaNMO after the first and 35th cycles (desodiation and sodiation).*

Conclusions

The NaNMO spinel was successfully obtained via electrochemical delithiation of LNMO and then electrochemical sodiation. Electrochemical tests showed that the performance of NaNMO is rather poor compared to its Li counterpart but proves the possible use of sodium nickel manganese spinel as positive material for Na-ion battery. The electrochemical performance are rather low but could be attributed to a change of electronic conductivity, smaller sodium diffusion coefficient than the lithium one, possible structural degradations upon cycling because of the large sodium ion radius. The NaNMO structure is kept during numerous cycles, which shows that this material could be promising in Na-ion batteries, even if the potential range has to be increased and specific charge fading during cycling has to be stabilized (i.e. with doping).

Acknowledgement

The authors are grateful to SAFT for the financial support.

References

[1] N. Yabuuchi, M. Kajiyama, J. Iwatate, H. Nishikawa, S. Hitomi R. Okuyama, R. Usui, Y. Yamada, S. Komaba, *Nat. Mater.* **11**, (6), 512–517 (2012).
[2] X. Xiang, K. Zhang, J. Chen, *Adv. Mat.* **27** (36), 5343–5364 (2015).
[3] D. Liu, W. Zhu, J. Trottier, C. Gagnon, F. Barray, A. Guerfi, A. Mauger, H. Groult, C.M. Julien, J.B. Goodenough, K. Zaghib, *RSC Adv.* **4** (1), 154–167 (2014).
[4] P. Delichère, S. Joiret, A. Hugot-le Goff, K. Bange, B. Hetz, *J. Electrochem. Soc.* **135** (7), 1856–1857 (1988).

Almond shell-derived carbonaceous materials as anodes for Na-ion batteries

J. Cabañero, C. Marino, C. Villevieille
phone: +41 56 310 3699, e-mail: joel.cabanero@psi.ch

Due to the abundance of sodium in the Earth's crust, Na-ion batteries could be a relatively cheaper alternative to lithium-ion batteries. However, the lower energy density of this technology limits their application to stationary energy storage. While there's a wide array of choice for cathode materials, the choice for a stable anode material is limited to disordered carbons [1] as graphite is not suitable to the sodium-ion system.

Disordered carbon materials are generally synthesized out of industrial products such as sucrose and polyacrylonitrile [2]. These compounds, however, can be replaced by bio-waste materials which present the advantage of further decreasing the cost of the electrode materials.

In this study, shells from almonds were used as a source of carbonaceous materials and used as negative electrode for sodium-ion batteries. Various atmospheres were used for the synthesis and the impact on the carbon properties was investigated by means of galvanostatic cycling, X-ray diffraction (XRD), scanning electron microscopy (SEM), Raman spectroscopy and specific surface area measurement (Brunauer-Emmett-Teller Theory, BET).

Experimental

Almond shells were first ground using mortar and pestle and then soaked in 10 % (v/v) H_2SO_4 solution for 24 h. Removal of the acid was subsequently done by washing with deionized water until reaching neutral pH. The shells were dried at 80 °C for 12 h prior to size reduction using ball milling. Carbonization was then operated in a tubular oven at 1000 °C under different atmospheres [Ar, N_2, Ar + 5 vol % H_2].

Finally, the resulting carbonaceous samples were named as Ar, N_2, and AW_5. Galvanostatic cycling was performed in a half-cell with sodium metal as counter electrode and 1 M $NaClO_4$ in PC used as the electrolyte. The electrode has 85 : 5 : 10 %wt (active material: Super C65: CMC) composition.

Results

The SEM images (Figure 1) reveal similar morphological features among the carbonaceous samples independent of the atmospheres used. The primary particles are very small below the micrometre range even if some of them can be very large with several microns as can be seen in the case of N_2 sample. As expected from the ball milling procedure, the particle size distribution is also very broad. We noticed that the particles tend to form big agglomerates of several tens of micrometres.

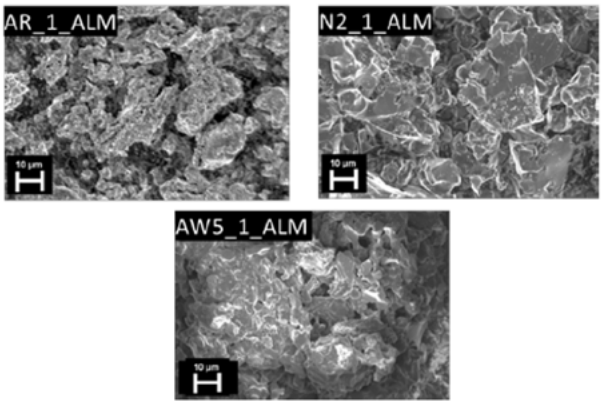

Figure 1. *SEM images of the carbonaceous samples.*

In Figure 2, the XRD patterns of the carbonized samples reveal characteristic broad peaks at 2θ values ca. 22° and 44° corresponding to the (002) and (100) peaks, respectively. A minor impurity (CaS) was detected at 32° and 45° in the patterns of the carbonaceous materials and originated most probably from the calcination of $CaSO_4$ present in the almond shell.

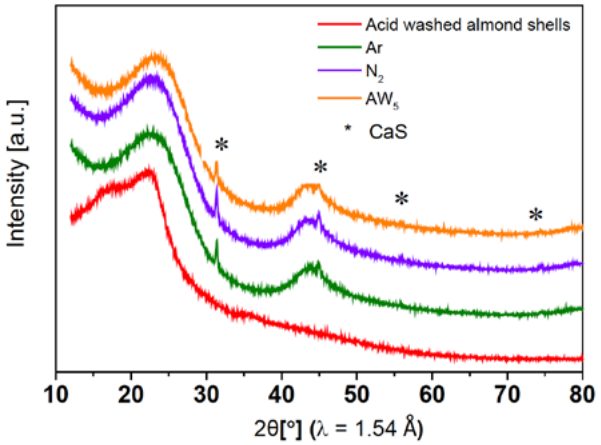

Figure 2. *XRD patterns of the pristine acid washed almond shells and the carbonaceous samples.*

Raman spectroscopy was performed in order to check the level of graphitization of the materials. A typical Raman spectrum of disordered carbons is composed of the G (~ 1600 cm^{-1}) and D (~ 1330 cm^{-1}) bands which correspond to the E_{2g} graphitic and A_{1g} defect-induced modes, respectively. The Raman shifts of these two bands are summarized in Table 1. While the Raman shifts of the samples Ar and N_2 are similar with values at 1600 cm^{-1} (G-band) and 1331 cm^{-1} (D-band), the D band of AW_5 has a lower shift at 1328 cm^{-1} indicating a higher defect level.

Furthermore, the ID/IG ratio, which gives an insight into the degree of graphitization of the carbon samples, was found to be the highest at 1.38 for Ar and the lowest at 1.29 for AW_5,

meaning that the sample synthesized under AW_5 has the highest degree of graphitization. Interestingly, the ratio of N_2 shows an intermediate value at 1.34.

Sample	Raman shift (cm^{-1})		I_D/I_G ratio
	G band	D Band	
Ar	1600	1331	1.38
N_2	1600	1331	1.34
AW_5	1600	1328	1.29

Table 1. *Raman shifts of the D and G bands and degree of graphitization (ID/IG ratio) of the carbonaceous samples.*

Similar specific surface areas (4 m^2/g) were found for the materials synthesized under Ar and N_2 atmospheres. Figure 3 shows the pore size distribution of the carbon samples which lies in the range of 15 to 53 Å, indicating that the synthesized carbons are mesoporous. The measurement of the AW_5 is in progress.

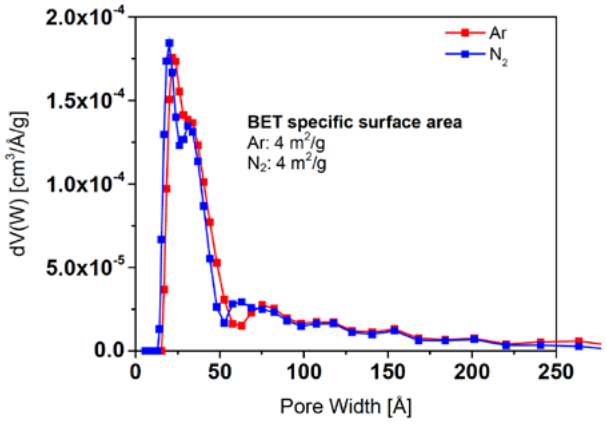

Figure 3. *Pore size distribution and BET specific surface area of the carbonaceous samples.*

The cycling performance of the different materials is shown in Figure 4. Initially, both Ar and N_2 have specific charge values at ca. 325 mAh/g with a Coulombic efficiency of ca. 70 % for the first cycle. The sample AW_5 exhibits the lowest specific charge at ca. 200 mAh/g for the first cycle and the lowest Coulombic efficiency ca. 50 %. On succeeding cycles, the samples synthesized under Ar and N_2 present stable specific charge values at ca. 265 mAh/g whereas the one synthesized under AW5 delivers only 100 mAh/g. The relative low electrochemical performance obtained for AW_5 could be linked to the higher level of graphitization obtained from Raman spectroscopy analysis. Surprisingly, the specific charge of N_2 sample increases accompanied by a decrease in Coulombic efficiency. This may be attributed to the electrolyte decomposition upon cycling. Further optimizations are ongoing to verify the electrochemical performance.

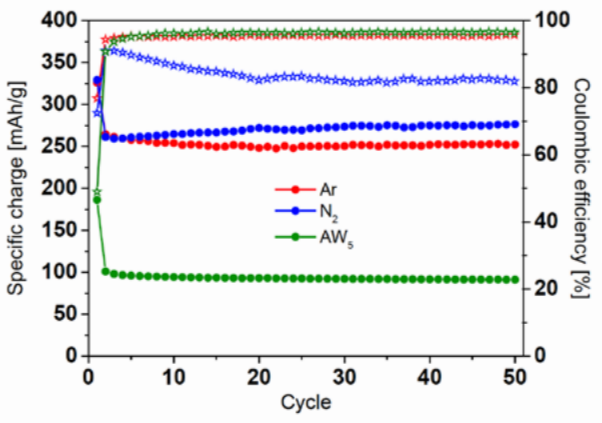

Figure 4. *Electrochemical performance of the carbonaceous samples cycled at C/10 rate*

Conclusion

Disordered carbons have been successfully synthesized using biowaste materials i.e. almond shells. The inert atmosphere used during synthesis has a significant impact on the physical and electrochemical performance of the disordered carbons. Carbons synthesized out of Ar and N_2 have similar specific surface area, pore size distribution and electrochemical performance despite a probable different surface composition. Meanwhile, carbons synthesized under a reducing atmosphere (AW_5) resulted to poorer electrochemical performance compared to the ones synthesized under an inert atmosphere.

Acknowledgement

This work is performed through the Swiss Competence Center for Energy Research Heat and Electricity Storage. Prof. Dr. Petr Novák is acknowledged for fruitful discussions.

References

[1] E. Irisarri, A. Ponrouch, M.R. Palacin, *J. Electrochem. Soc.* **162** (14), A2476–A2482 (2015).
[2] D.A. Stevens, J.R. Dahn, *J. Elect. Soc.* **147**, 1271–1273 (2000).
[3] M.M. Doeff, Y.Q. Hu, F. McLarnon, R. Kostecki, *Electrochem. Solid-State Lett.* **6**, A207–A209 (2003).

Electrochemical performance of Sn nanoparticles as anode material in all-solid-state Li-ion battery based on LLZO:Ta garnet electrolyte

G. Ferraresi, C.L. Tsai[1], S. Uhlenbruck[1], M. El Kazzi, P. Novák, C. Villevieille
phone: +41 56 310 4542, e-mail: giulio.ferraresi @psi.ch

Solid electrolytes are envisaged as alternative to organic electrolytes since they can improve the safety of the battery. Among the already discovered inorganic Li-ion conductors, the garnet material with a cubic structure, Ta-doped $Li_7La_3Zr_2O_{12}$ (LLZO:Ta), offers both acceptable ionic conductivity at room temperature and stability in contact with Li metal. [1]

Although the solid garnet electrolyte (LLZO:Ta) was considered to be stable in the potential range from zero to six volt vs. Li^+/Li, recent studies point out that the stability window could be drastically limited down to 2.9 V vs. Li^+/Li. [2]

Here, we report the possibility to use alloy-based Sn nanoparticles as negative electrode in combination with Ta-doped LLZO solid electrolyte to build all-solid-state Li cells. The electrode, prepared as a conventional slurry mixture and coated directly on the surface of the solid electrolyte pellet, shows during the lithiation step an electrochemical activity comparable to the one obtained with Sn in conventional liquid counterpart (LP30 electrolyte). The lithiation of Sn is confirmed by post-mortem X-ray photoelectron spectroscopy (XPS).

Experimental

LLZO:Ta pellets (600 µm thickness) were used as solid electrolyte for the deposition of a Sn-based electrode mixture on the surface. A blend of Sn nanoparticles (100 nm), LLZO solid electrolyte, conductive carbon (Super P) and binder (PVdF) in the ratio 40 : 40 : 10 : 10 were homogeneously dispersed in N-methyl Pyrrolidone (NMP) solvent under Argon atmosphere and thoroughly coated on the surface of the LLZO pellet. The stack was dried at 80 °C under dynamic vacuum to evaporate the solvent before being isostatically pressed on the surface. Ion-milling tool coupled with scanning electron microscopy (SEM) helped to reveal the cross-section of the as-coated samples.

Galvanostatic cycle was carried out by building half-cell vs. Li metal applying a current of 10 µA and 80 µA for the LLZO and LP30 half-cells, respectively. Along this report all the potential will be given using Li^+/Li as a reference. Post-mortem XPS was performed on pristine and lithiated electrodes to investigate the surface reactions on the Sn-electrodes.

Results

The morphological composition of the as prepared LLZO:Ta solid electrolyte and the electrode mixture are initially investigated. The solid electrolyte layers were showing relative density values ranging from 88–96 % measured by geometrical parameters. Morphological investigation of the prepared stack was carried out by ion-milling coupled with scanning electron microscopy (SEM) images.

In Figure 1, the cross-section of the final stack is shown. The lower part of the image is attributed to the LLZO:Ta solid electrolyte where defined grains of different sizes appear to be properly sintered together. The space between the grains is found to be Al-rich, since 2.5 mol % α-Al_2O_3 was used in the initial mixture as sintering additive, but a slight open porosity can also be noticed in the lower part of the image that seems to be randomly present within the solid electrolyte, which limits the relative density but it is not expected to cause the short-circuit of the cell due to the random distribution.

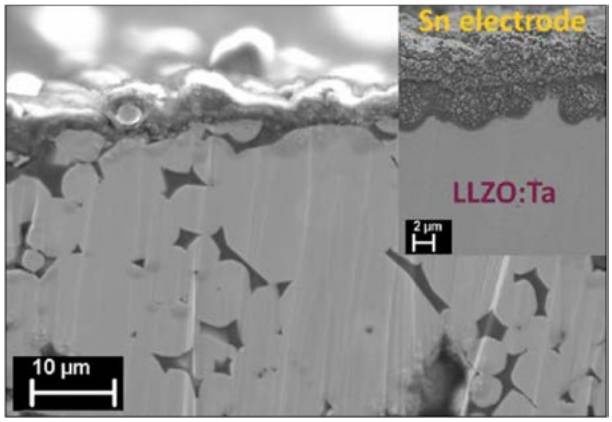

Figure 1. *Cross-section SEM of the Sn/LLZO:Ta stack. Inset: detailed image of the Sn/LLZO:Ta interface.*

The top layer in Figure 1 is attributed to the electrode mixture deposited on the solid electrolyte, as better envisaged in the inset graph. The adhesion of the two layers is crucial for the electrochemical measurement since the solid/solid interface resistance plays a key role during cycling of solid-state batteries. From this morphological analysis, we can see that the electrode mixture is homogeneously coated on the surface of LLZO:Ta. Additionally, an intimate contact between LLZO:Ta and Sn nanoparticles is guaranteed both by the 1 : 1 %wt ratio mixture of the solid electrolyte with Sn nanoparticles in the electrode formulation and by further isostatic pressing after deposition.

After assessment of a proper interfacial contact, the stack was then investigated electrochemically in half-cell configuration by pressing a Li foil layer on the other side of the LLZO:Ta solid electrolyte. The cell was maintaind at 100 °C to limit the resistivity of the bulk electrolyte during operation. For comparison, the same electrode mixture is deposited on a copper current collector and cycled in a half-cell configuration with LP30 liquid electrolyte (EC : DMC 1 : 1 ratio + 1 M $LiPF_6$ salt) in the same potential range. The derivative curves of the first lithiation in the two configurations are reported in Figure 2 between the open circuit potential and 0.2 V.

[1] Forschungszentrum Jülich GmbH, Institute of Energy and Climate Research, Materials Synthesis and Processing, Jülich, Germany

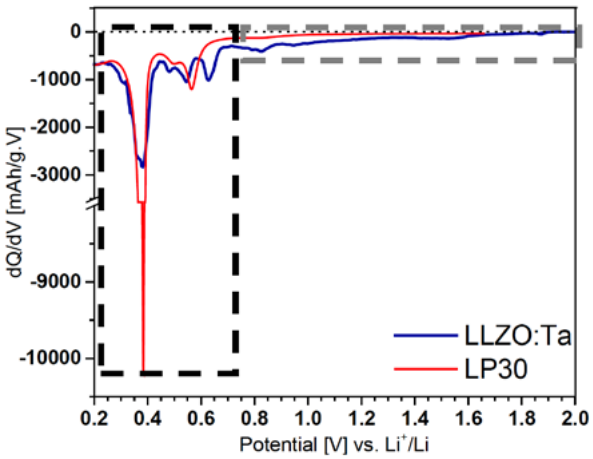

Figure 2. *Derivative curve of the first lithiation of nano-Sn electrodes cycled in conventional liquid electrolyte (LP30) and solid electrolyte (LLZO:Ta).*

Two regions can be distinguished:

a) From 2 V down to 0.8 V, Sn is not electrochemically active with lithium, therefore no peaks are detected in the LP30 half-cell, whereas the LLZO:Ta half-cell shows little activity at 1.5 V and 0.9 V. This process is under investigation but it could be related to the reaction of SnO_2 at the surface of Sn particles.

b) From 0.8 V down to 0.2 V three defined peaks at 0.63 V, 0.52 V and 0.39 V are observed for both samples. These peaks are related to the different Li-Sn alloys formed. [3]

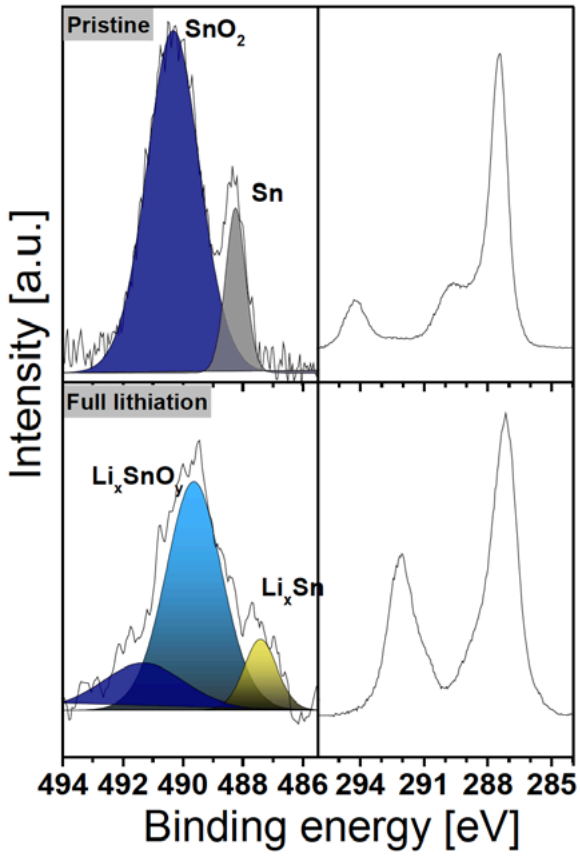

Figure 3. *Peak area ratio between Sn3d and C1s levels along first lithiation.*

The post-mortem XPS investigation endorses the lithiation of the Sn nanoparticles forming Li-Sn alloys (Figure 3), as confirmed by the noticeable shift to lower binding energy of the peaks related to the Sn3d core level. The C1s core level shows a completely different composition than for the pristine, which needs further investigation for a correct understanding, but it could be related to possible degradation of LLZO:Ta interacting with the binder present in the electrode mixture.

Conclusion

For the first time, we prove the possibility to reversibly lithiate Sn nanoparticles in combination with LLZO:Ta solid electrolyte. We have demonstrated that in terms of potential profile the reaction mechanism of Sn nanoparticles is similar in LP30 liquid electrolyte and in LLZO:Ta solid electrolyte and this achievement opens up the possibility to implement alloy-based materials as anodes for all-solid-state Li-ion batteries.

Acknowledgement

Competence Center Energy and Mobility (CCEM) and the Swiss Electric Research (SER) are acknowledged for financial support.

References

[1] R. Murugan, V. Thangadurai, W. Weppner, *Angew. Chem. Int. Ed.* **46**, 7778–7781, (2007).

[2] F. Han, Y. Zhu, X. He, Y. Mo, C. Wang, *Adv. Energy Mater.* **6**, 1501590-n/a, (2016).

[3] M. Winter, J.O. Besenhard, *Electrochim. Acta* **45**, 31–50, (1999).

Tris(trimethylsilyl)phosphate, an efficient fluoride scavenger for FEC/DEC-based Li-ion battery electrolytes

A. Guéguen, C. Bolli, E.J. Berg
phone: +41 56 310 2176, e-mail: aurelie.gueguen@psi.ch

Commercial Li-ion batteries use electrolytes composed of a mixture of cyclic (mostly ethylene carbonate, EC) and linear carbonates (dimethyl/diethyl carbonate DMC/DEC) dissolving the $LiPF_6$ salt. Such electrolytes offer till now the best compromise with respect to Li^+ conductivity, viscosity, electrochemical and thermal stability. Carbonates are however not electrochemically stable > 4.2 V vs. Li^+/Li. One economic way to solve that issue is the use of electrolyte additives. Addition of tris(trimethylsilyl)phosphate (TMSPa) to carbonate electrolytes was reported to improve the cycle life of Li-ion cells through the formation of protective solid permeable interface (SPI) on the cathode [1]. Such layer should stabilize the electrode/electrolyte interface, thus minimizing electrolyte degradation and the amount of gas released during cell operation. Recently we demonstrated that online electrochemical mass spectrometry (OEMS) is a powerful technique to follow the O_2, CO_2 and POF_3 evolution during operation of Li-rich nickel-cobalt-manganese oxide (HE-NCM)-based half cells [2]. In the present report we evaluate the impact of adding TMSPa to carbonate electrolytes on gas evolution of HE-NCM full cells.

Experimental

HE-NCM electrodes were prepared by coating Celgard 2400® polypoplylene sheet with a mixture of 89 %wt HE-NCM (BASF SE), 4.64 %wt conductive carbon Super C65 (Imerys Graphite & Carbon), 1.36 %wt SFG6L (Imerys Graphite & Carbon) and 5 %wt PVdF (polyvinyl-idene fluoride) dispersed in N-methylpyrrolidone (NMP, Sigma-Aldrich). Graphite electrodes were prepared by coating Cu foil with a mixture of 95.7 %wt graphite SFG6 (Imerys Graphite & Carbon), 0.5 %wt conductive carbon Super C65 and 3.8 %wt carboxymethyl cellulose (CMC) binder in water. Electrodes were further punched from HE-NCM (15 mm diameter) and graphite (20 mm diameter) sheets and subsequently dried at 80 and 120 °C, respectively.

The OEMS experiments were performed in a custom-made electrochemical cell (Annual Report 2012, p. 47). HE-NCM full cells were cycled between 0 and 4.7 V (all potentials in the report are given vs. Li^+/Li) at C/10 rate. The electrolyte containing 1 %wt TMSPa (Sigma-Aldrich, purity > 98 %) was prepared just before assembling the cell by adding appropriate amount of TMSPa to 1 M $LiPF_6$ FEC : DEC (12 : 88) electrolyte. No calibration gas was used for POF_3 and Me_3SiF, thus the evolution rates reported for these gases are semiquantitative.

Results

Figure 1 shows the electrochemical data and O_2, CO_2, POF_3 evolution rate profiles for HE-NCM full cells with electrolyte containing 0 or 1 %wt TMSPa. No influence on O_2 and CO_2 evolution profile was observed for the electrolyte containing TMSPa compared to the reference electrolyte. This seems to indicate that TMSPa does not impact significantly the interface layer formed on the HE-NCM electrode. POF_3 evolution rate strongly decreases when TMSPa is present in the electrolyte during the 1st and 2nd charge. Furthermore fragments with m/z 77 and 78 also evolved during cycling (for clarity only fragment 77 is shown here). These fragments belong to Me_3SiF which was previously reported to result from reactions between tris(trimethylsilyl)phosphite and HF [3]. This confirms that TMSPa scavenges agressive fluoride containing species. Me_3SiF starts evolving since the beginning of charge, thus indicating formation of such fluoride species since the very beginning of charge.

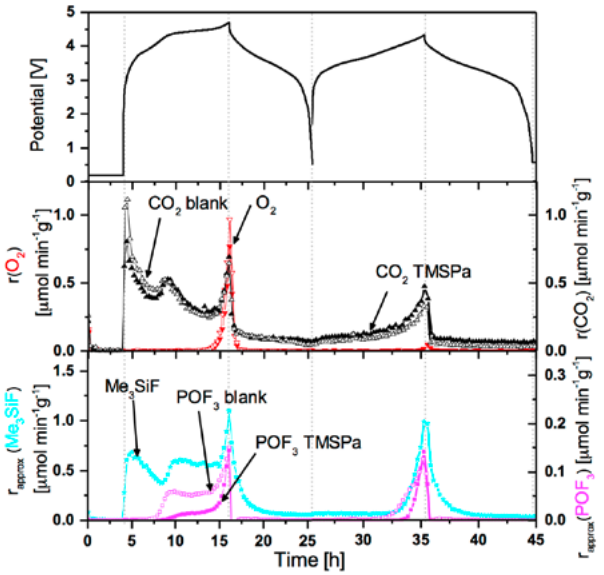

Figure 1. *Potential profile and O_2, CO_2, POF_3 and Me_3SiF evolution rate profiles for HE-NCM full cells with reference electrolyte (empty symbols) and electrolytes containing TMSPa (full symbols).*

Conclusions

Our operando OEMS study further confirmed the fluoride scavenging effect of TMSPa, which thus results in a strong decrease of POF_3 evolution. As POF_3 is a product of $LiPF_6$ salt decomposition, addition of TMSPa minimizes the salt degradation. TMSPa seems to be only chemically active, as no extra oxidation/reduction peak was observed in cyclic voltammetry experiments.

Acknowledgement

The authors thank BASF SE for fruitful discussion and financial support.

References

[1] J. Zhang, J. Wang, J. Yang, Y. NuLi, *Electrochim. Acta* **117**, 99–104 (2014).
[2] A. Guéguen, D. Streich, M. He, M. Mendez, F. Chesneau, P. Novák, E.J. Berg, *J. Electrochem. Soc.* **163**, A1095–1100 (2016).
[3] G. Han, S.J. Lee, J. Lee, J.S. Kim, K.T. Lee, N.S. Choi, *ACS Appl. Mater. Interfaces* **7**, 8319–590 (2015).

Insertion of Li in $Li_{1+x}V_{0.9}O_2$ anodes for Li-ion batteries

L. Castillo Iracheta, P. Novák, R. Robert
phone: +41 56 310 5426, e-mail: rosa.robert@psi.ch

Negative electrode materials in current commercial batteries are carbonaceous, mostly of graphitic carbon, LiC_6, with 372 Ah/kg and 975 Ah/L gravimetric and volumetric capacity. Carbon displays many problems such as solvent co-intercalation in propoylene-carbonate-based electrolytes and limited gravimetric and volumetric capacity.

Insertion oxides as host materials for lithium theoretically offer up to twice the energy density and thus the double the volumetric energy density compared to graphite which is vital for future electronic applications. However, the number of alternative insertion negative electrodes is relatively limited. Working systems are based on titanium (insertion potential between 1.5 V and 2 V versus lithium metal) and the system's energy density is low. In this project we want to explore the possibility of switching to insertion of Li in $Li_{1+x}VO_2$ oxide hosts [1] at a potential where usually conversion/displacement reaction dominates, i.e in the lithium-rich vanadium oxides.

Experimental

$Li_{1+x}V_{0.9}O_2$ (LVO) was prepared by solid state synthesis route using stoichiometric amounts of lithium carbonate Li_2CO_3 (Aldrich, 99 %) and vanadium oxide V_2O_3 (Aldrich, 99 %) as reagents:

$$0.45\ V_2O_3 + 0.555\ Li_2CO_3 \rightarrow Li_{1.11}V_{0.9}O_2 \quad (1)$$

The reactants were mixed and ground using an agate mortar. The resultant mixtures were calcined in a tubular oven at 800 °C under reductive atmosphere $Ar:H_2$ 95 %:5 %.

X-ray powder diffraction studies were done using a PANalytical Empyrean diffractometer equipped with a linear detector (X'Celerator) and Cu-Kα radiation. Measurements were performed either in reflection or transmission geometry. The patterns were recorded continuously by step scanning (with a step size of 0.017°) over the 2Theta range of 10–70°.

The working electrode was prepared by mixing 80 % of the active material, 10 % of carbon black (Super P, Imerys Graphite & Carbon, Switzerland), and 10 % of polyvinylidene fluoride (PVDF) binder. Cell preparation and electrochemical tests were performed as reported in [2].

Results

The X-ray diffraction (XRD) pattern of the as prepared $Li_{1+x}V_{0.9}O_2$ ceramic powders is displayed in Figure 1. The XRD pattern is characteristic of a highly crystalline sample, commonly observed for materials prepared by the ceramic route. The analysis of the observed Bragg reflections indicated the presence of two distinctive phases. The major phase (~ 76 %wt) corresponds to the layer of $LiV_{0.9}O_2$ with space group *R-3m*, crystal system rhombohedral and lattice parameters of a,b ~ 2.8373 Å, and c ~ 14.7734 Å. The minor secondary phase (~ 24 %wt) corresponds to the orthorhombic Li_3VO_4, space group *Pnm21*, and lattice parameters of a ~ 5.4471 Å, b ~ 6.3272 Å and c ~ 4.9483 Å.

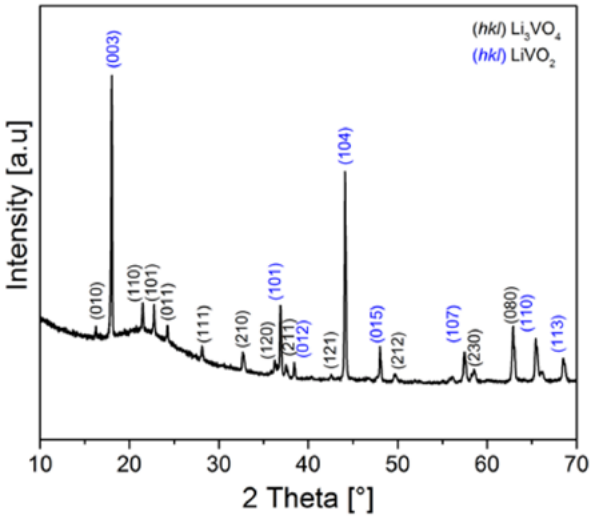

Figure 1. *X-ray diffraction pattern of $Li_{1+x}V_{0.9}O_2$.*

Charge-discharge profile for the first cycle LVO electrode cycled at C/30 (I = 10 mA) vs. Li metal in the potential window of 2.6 V – 0.005 V is shown in Figure 2 above.

During the first lithiation of the LVO electrode we obtain a specific charge of about 260 Ah/kg, which is slightly below the theoretical specific charge of 298 Ah/kg considering 1 e^- transfer. The first delithiation has a specific charge of 150 Ah/kg. The large irreversible charge «loss» between the first lithiation and the first delithiation corresponds to a value of 110 Ah/kg. After the first cycle the irreversible charge loss becomes very small and is almost negligible in the following cycles.

The potential profile (Figure 3, above) on lithiation shows several processes. The first visible process happening from 0.83 V to 0.63 V can be attributed to the formation of the SEI. The second process between 0.61 V and 0.09 V leads to a specific charge consumption of about 60 Ah/kg (0.2 Li insertion). The third process occurs at a large potential plateau from 0.08 V to 0.05 V with a specific charge consumption of about 175 Ah/kg (0.58 Li insertion).

On oxidation, the delithiation of LVO is mainly dominated by the process occurring in the plateau region and a little specific charge is recovered in the sloping region. The voltage profile asymmetry between the reduction and oxidation processes, in the plateau region, corresponds to about 0.22 V, value characteristic of an insertion process at the given rate.

Ex situ X-ray diffraction measurements of the LVO samples at fully discharged state (5 mV) and fully charged to 2.6 V after one full cycle together with the XRD of the as prepared LVO sample are shown in Figure 3 below. The color code of the XRD patterns corresponds to the assigned full circles in the galvanostatic plot.

As was mentioned above, the first lithiation of LVO occurs via two main processes [3]. The overall reaction of LVO with lithium progresses via a two phase reaction mechanism with a structural phase transformation from $Li_{1+x}VO_2$, S.G. *R-3m*, to $Li_2V_{0.9}O_2$, S.G. *P-3m*$_1$, as the following reaction shows (Figure 2):

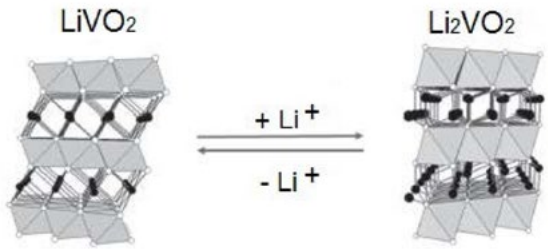

Figure 2. *Schematic representation of the reaction mechanism and phase transformation.*

The *ex situ* sample collected at 5 mV was very prone to relax to a more stable state about 400 mV, thus, this data may not be fully reflective of the discharge state to 5 mV. Indeed, at full discharge we can clearly observe the Bragg reflections of the newly formed $Li_2V_{0.9}O_2$ phase and still a large amount of «unreacted» $LiV_{0.9}O_2$. Based on what we stated above, the observed large amount of $LiV_{0.9}O_2$ will rather indicate a state, assigned by the second full red circle in Figure 3 above, in which the reconversion, i.e. the deintercalation of lithium is already happening.

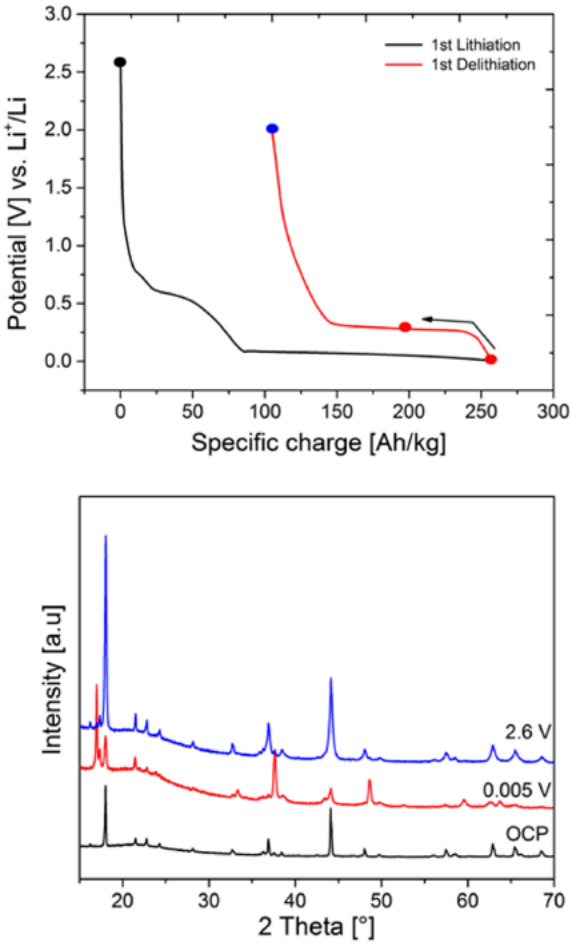

Figure 3. *Galvanostatic plot of LVO electrode cycled at C/30 rate between the potential window of 2.6 V – 0.005 V vs. Li metal (above), and ex situ X-ray diffraction patterns of LVO as prepared, on full discharge and on full charge.*

Overall, the *ex situ* XRD results clearly suggest an intercalation process at a very low potential of ~ 0.1 V vs. Li metal, unusual for oxides, which is enabled via a two phase reaction mechanism.

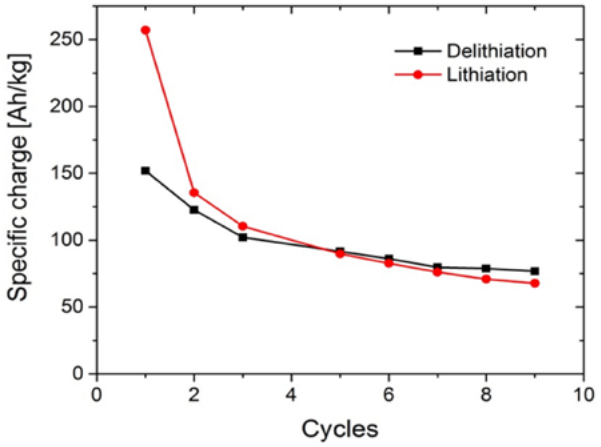

Figure 4. *Cycle performance of LVO electrode cycled vs. Li$^+$/Li at C/30.*

Figure 4 shows the large irreversible charge «loss» between the first lithiation and the first delithiation, which has a value of 110 Ah/kg. The specific charge values at first lithiation and delithiation are 260 Ah/kg and 150 Ah/kg, respectively. After the first cycle the irreversible charge «loss» becomes very small and is almost negligible in the following cycles. At cycle 7 onwards the specific charge is quite stable with a value of 78 Ah/kg.

References

[1] S.-S. Kim, Y. Nitta, N. Tatiana I., J.-C. Lee, Samsung Sdi Co., Ltd. Patent US20060088766 A1, 2006.
[2] R. Robert, Ch. Bünzli, E.J. Berg, P. Novák, *Chem. Mater.* **27**, 526–536 (2015).
[3] A.R. Armstrong, C. Lyness, P.M. Pancmatia, M.S. Islam, P.G. Bruce, *Nat. Mater.* **10**, 223–229 (2011).

XPEEM investigation of Mn, Ni and Co oxidation states at the surface of HE-NMC electrodes cycled to 5 V

D. Leanza, C.A.F. Vaz, P. Novák, M. El Kazzi
phone: +41 56 310 2797, e-mail: daniela.leanza@psi.ch

Li-rich layered oxides with the general formula $Li_{1+x}(NiaCo_bMn_{1-a-b})_{1-x}O_2$ stand out for their promising electrochemical performance and the exceptional high specific charge compared to the traditional cathodes used in Li-ion batteries such as $LiCoO_2$,$LiNi_xMn_yAl_zO_2$ (NCA) and $Li_{1-x}Ni_{1/3}Mn_{1/3}Co_{1/3}O_2$ (NCM111) [1]. However, their commercial use is still hampered by several major challenges related to their voltage instability and capacity fading especially at high-voltage operation, which suggest the need for a deep understanding of the parameters causing cell failure.

The surface structural change upon cycling, from the initial layered structure to a spinel or rock-salt structure together with transition metals dissolution, are considered among the key parameters responsible for the capacity fading and the impedance rise [2, 3]. To have a better insight into the surface reaction mechanisms and the impact of the voltage, the reactivity at the electrode/electrolyte interface has to be considered. For this purpose it is indispensable to explore new surface characterization techniques with good lateral resolution in order to be able to localize separately the different particles composing the electrodes and simultaneously capable of probing the surface evolution of transition metals (TMs) and species deriving from electrolyte decomposition.

In this context, we carried out X-ray PhotoEmission Electron Microscopy (XPEEM) measurements at the SIM beamline at the SLS to monitor the oxidation states of the TMs by X-ray Absorption Spectroscopy (XAS) at the L-edges. The combination of high lateral resolution with a surface sensitivity of 2 to 3 nm makes the XPEEM a suitable technique to accomplish our objective.

We investigated two commercial-like electrodes, $Li_4Ti_5O_{12}$ (LTO) and Li-rich layered oxide (hereafter called HE-NMC) as the anode and cathode respectively. The positive electrode is cycled galvanostatically up to 5.1 V vs. Li^+/Li (Figure 1), well above the thermodynamic stability limit of the electrolyte*, whereas the LTO is cycled along its plateau at 1.55 V vs. Li^+/Li, where the electrolyte is expected to be stable. Positive and negative electrodes are analyzed with XPEEM at the end of the first charge and discharge (circles in Figure 1). The evolution of the transition metals Mn, Ni and Co oxidation states is investigated for both the cathode and the anode.

Results

Element-specific XPEEM contrast images at the Mn L-edge/pre-edge (641.6 eV / 635 eV) and C K-edge/pre-edge (285.6 eV / 275 eV) are reported in Figure 2 A and B, respectively. Regions of the conductive carbon and the HE-NCM active material can be found by following the bright spots delimited by the red square and blue circle, respectively. The local XAS spectra present in this report are measured only on a single particle of HE-NMC (blue circle).

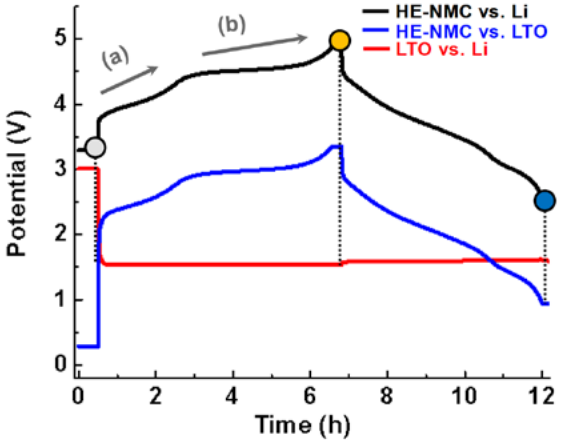

Figure 1. *Galvanostatic curve for the first full cycle performed in 3-electrodes arrangement cell. HE-NMC is cycled vs. LTO with LC30 electrolyte at room temperature and using metallic Li as a reference electrode. During the first delithiation two main plateaus are visible, described in equation (a) and (b).*

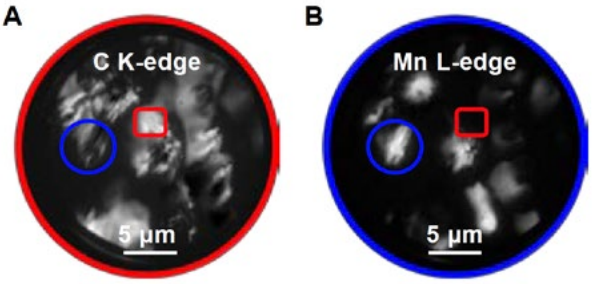

Figure 2. *Element-specific XPEEM images carried out on HE-NCM pristine electrode at the (A) C K-, (B) Mn L-edge reveal the surface distribution of carbon (red square) and active material (blue circle) particles.*

The oxidation states of the transition metals on the pristine electrode are determined to be +4, +3 and +2 for Mn, Co and Ni, respectively. However, significant variations are recorded after the first charge (delithiation). Firstly, the Mn L-edge shows an evolution towards lower energy as a signature of reduced species. This result is unexpected, since the Mn should not be electrochemical active during the first delithiation (charge), based on previous XANES and EXAFS studies [4] performed in transmission mode with bulk sensitivity, as described in the following equations:

$$Li\,[Ni^{+2},Co^{+3},Mn^{+4}]O_2 \leftrightarrow Li_{1-x}\,[Ni^{+4},Co^{+4},Mn^{+4}]O_2 + xLi^+ - xe^- \quad (a)$$

$$Li_2Mn + 4\,O_3 \leftrightarrow Mn + 4\,O_2 + 2\,Li^+ + O + 2\,e^-\ (O_2\ release) \quad (b)$$

Similarly, the presence of reduced Co is detected from the low-energy shoulder of the L-edge (Figure 3, B) together with

* LC30: 1 M $LiClO_4$ in DMC : EC, 1 : 1

oxidized Co species denoted from the evolution of the L-edge at 783 eV. Finally the Ni L-edge shows a slight variation of the shoulder at 855 eV suggesting a partial oxidation to a +4 state. The detection of Mn and Co in lower oxidation states at full delithiation is at variance from equation (a) and (b). This result proves the strong influence of the electrolyte/electrode interaction on the surface electronic changes that the electrode experiences at high potential. After the first discharge (lithiation) (blue curve in Figure 3) one can notice that Ni^{4+} and Co^{4+} revert to the pristine reduced states, as expected. However the Mn and Co L-edge show a strong decrease of the low-energy shoulder, which suggests a depletion of the reduced species at the surface of the HE-NMC that are believed to be dissolved in the electrolyte.

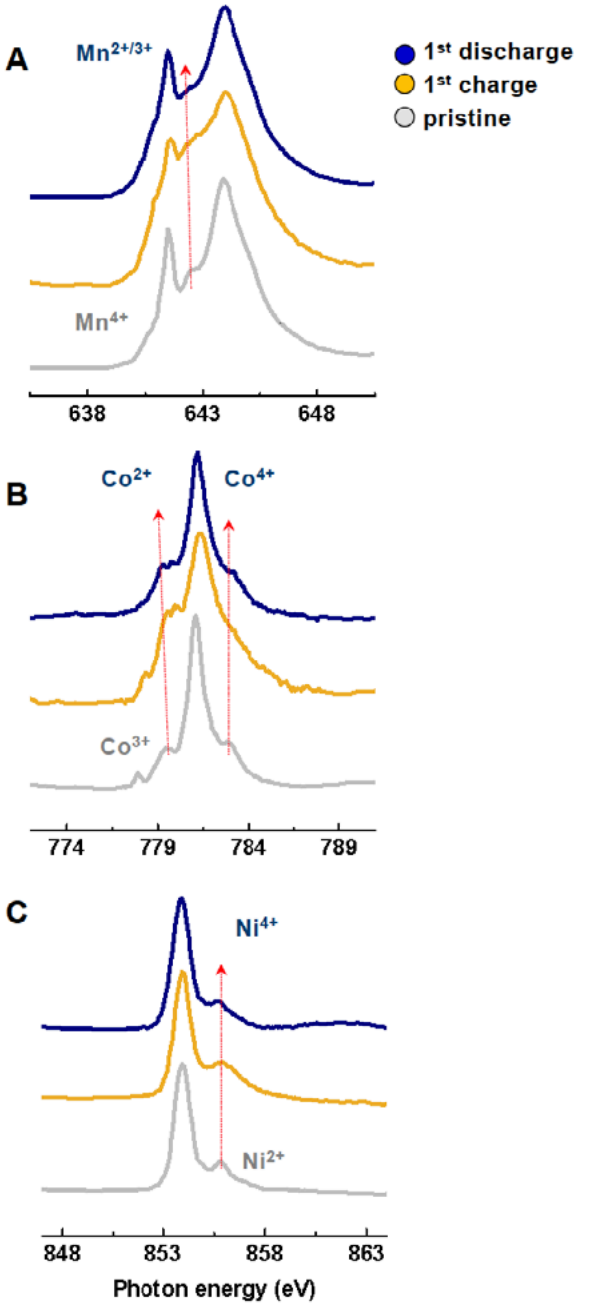

Figure 3. *Local XAS at the Mn (A), Co (B) and Ni (C) L-edges acquired on single particles of HE-NMC on pristine (grey) electrode and at the end of the first charge (yellow) and discharge (blue).*

Indeed, the local XAS acquired on the surface of the negative electrode (LTO) after the first discharge shows the presence of Mn that homogeneously covers the anode on both carbon and LTO particles (Figure 4). The presence of transition metal on the negative electrode evidences diffusion/migration from the cathode through the electrolyte and corroborates the strong electronic modification occurring on the surface of the cathode.

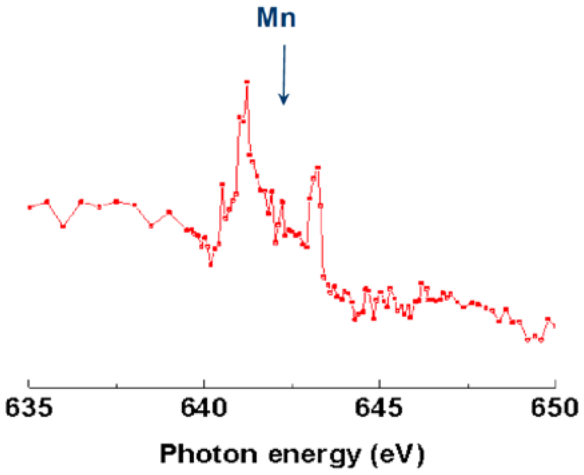

Figure 4. *Mn detected on the surface of LTO negative electrode after the first discharge, as a result of diffusion/migration from the HE-NMC (positive electrode).*

Conclusions

We demonstrate by using XPEEM that the surface of Li-rich material (HE-NMC) suffers from severe structural changes when cycled to high potential (5.1 V vs. Li^+/Li). The presence of reduced transition metals is observed at the end of the first charge, as a result of a strong interaction at the electrolyte/electrode interface. We cannot exclude as well the contribution of the irreversible process of the O_2 release at the end of the delithiation (charge). Moreover, we proved that migration/diffusion of species from the cathode to the anode starts immediately in the first cycle, as confirmed by the detection of Mn on the LTO surface, which can explain the rapid surface structural degradation.

References

[1] J.H. Kim, C.W. Park, Y.K. Sun, *Solid State Ionics* **164**, 43–49 (2003).
[2] F. Lin, I.M. Markus, D. Nordlund, T.-C. Weng, M.D. Asta, H.L. Xin, M.M. Doeff, *Nat. Commun.* **5**, 1–6 (2014).
[3] F. Lin, D. Nordlund, T. Pan, I.M. Markus, T.-C. Weng, H.L. Xin, M.M. Doeff, *J. Mater. Chem. A* **2**, 19833–19840 (2014).
[4] H. Koga, L. Croguennec, M. Ménétrier, P. Mannessiez, F. Weill, C. Delmas, *J. Power Sources* **236**, 250–258 (2013).

XPS analysis of Li-ion battery electrodes: surface complexity and spectra interpretation

D. Leanza, M. Mirolo, P. Novák, M. El Kazzi
phone: +41 56 310 5149, e-mail: mario.el-kazzi@psi.ch

The surface layer developed on cathode and anode materials upon cycling in Li-ion batteries has a direct impact on the battery safety and electrochemical performance. This surface layer has a thickness that varies from few angstroms to tens of nanometers and is composed of organic and inorganic species generated by the strong electrolyte/electrode interaction. The stability of the carbonate based electrolyte* towards the surface of the electrodes is directly linked to the applied voltage across the battery. Therefore, understanding the different reaction mechanisms taking place at the interface electrolyte/electrode is indispensable to engineer and design appropriate solutions for the safe and optimum operation of a battery. However, investigating the surface morphology of Li-ion battery electrodes is very challenging due to the complexity of the electrode composition. A mixture of active material, conductive carbon, and organic binder** result in a porous electrode with high surface roughness (Figure 1). Additionally the different reactivity of each component in respect to the electrolyte and the applied voltage makes the surface analysis even more complicated.

Figure 1. *SEM image of a $Li_xNi_aMn_bCo_cO_2$ (NCM) pristine electrode showing the surface morphology and particle distribution.*

To this purpose, X-ray photoemission spectroscopy (XPS) is considered to be a suitable surface characterization technique to study the surface evolution occurring on cycled electrodes. One of the advantages of XPS is the surface sensitivity that ranges around 10 nm by using a conventional X-ray AlKα (1486.6 eV) source. It also provides direct information about the by-product species related to the electrolyte reduction, e.g. the aprotic solvents EC/DMC, the Li-salt, and the binder, by acquiring the C1s, O1s, and F1s core levels. Finally, by probing the transition metals (TMs) of the active materials, XPS offers indication concerning the potential dependency of their oxidation states. However, despite all the mentioned benefits, XPS still suffers from some intrinsic limitations related to the electrode morphology which makes the spectra deconvolution and interpretation quite complicated and misleading.

In this context, the following report highlights the various phenomena taking place on the surface of Li-ion battery electrodes when XPS is performed. Their origin and impact on the data interpretation will be evidenced.

Results

As mentioned above, the complexity of the Li-ion battery electrode affects strongly and locally the kinetic energy of the photoelectrons generated after X-ray exposure, caused by a non-homogeneous charge distribution on the surface of the different particles. As a result, three uncommon phenomena were identified.

The 1st phenomenon is related to the «negative charge trapping» within the PVDF binder which is generally observed on cathode materials (e.g. NCM, NCA, etc.) after full delithiation at potential above 4 V vs. Li^+/Li. This behavior manifests with a shift of 1.6 V to lower binding energy (BE) of the F1s and C1s (CH_2 and CF_2) components, originated from the PVDF in respect to the C-C component of the conductive carbon or the peaks of the TMs. (Figure 2 a)

The 2nd phenomenon is associated with local «positive charging effect» on the organic and inorganic species generated after the electrolyte reduction on anode materials (e.g. LTO, graphite, Si etc.). The by-products of the decomposed electrolyte are mainly non-conductive oligomers or polymers and they have a thickness between 1 to 10th of nm. Such charging effect causes a shift of the C1s components to higher BE by about ~ 1 eV. (Figure 2 b)

The 3rd phenomenon is related to a small shift of about ± 0.35 eV in the C1s component originating from the conductive carbon (C-C) (Figure 2). This shift is observed often upon cycling and most likely originates from the sample grounding on the sample holder. Recently the shift to lower BE was explained with a build-up of an electric potential gradient at the buried interface between the bulk of the electrode and the surface layer. [1]

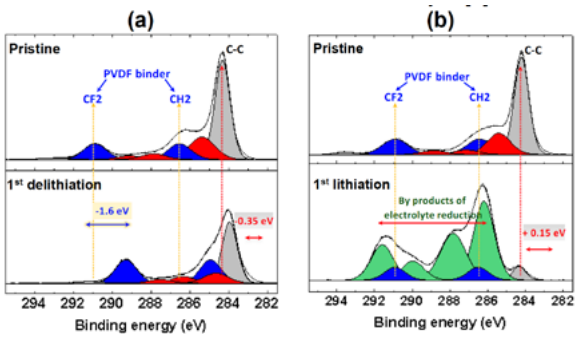

Figure 2. *C1s XPS core level acquired on (a) NCM pristine electrode and after 1st delithiation at 5 V vs. Li^+/Li. (b) on LTO pristine electrode and after full lithiation at 1.55 V.*

Conclusions

The three phenomena presented above make the deconvolution of the core levels peaks very challenging and can lead to a misleading interpretation of the different reaction mechanisms taking place at the interface electrolyte/electrode. To overcome these limitations the electrode needs to be simplified and redesigned using e.g. binder free or thin films model electrodes.

References

[1] J. Maibach, F. Lindgren, H. Eriksson, K. Edstrom, M. Hahlim, *J. Phys. Chem. Lett.* **7**, 1775–1780 (2016).

* 1 M of $LiClO_4$ or $LiPF_6$ dissolved in solvents like DMC, EC, etc.
** PVDF $(-CH_2-CF_2-)n$ is common binder used in Li-ion batteries.

Impact of water based binder on P2-$Na_{0.67}Mn_{0.6}Fe_{0.25}Co_{0.15}O_2$ cathode material for Na-ion batteries

C. Marino, S. Park, C. Villevieille
phone: +41 56 310 5304, e-mail: cyril.marino@psi.ch

The requirement for storing renewable energy generated from sun and wind has caused an increase in the demand for energy storage systems. Due to high cost of lithium-ion batteries (LiBs) in this purpose, cheaper alternatives are required. Sodium is an attractive alternative even though its theoretical energy density is lower than that of lithium. Thus, efforts to improve Na-ion batteries (NaBs) are mainly based on reducing the overall battery costs while maintaining reliable electrochemical performance for long-term cycling.

Polyvinylidene fluoride (PVDF) is the most commonly used binder in electrodes. However, despite its electrochemical stability in LiBs, it is only soluble in the toxic and expensive solvent N-methyl-2-pyrrolidone (NMP). Thus, in this study, we propose to use the eco-friendly carboxymethyl cellulose (CMC) binder, soluble in water, to prepare electrodes of P2-$Na_{0.67}(Mn_{0.6}Fe_{0.25}Co_{0.15})O_2$ (NaMFC) cathode material [1]. As layered oxide materials are water/moisture sensitive, we investigated the stability of the material in water by means of microscopy (SEM) and X-ray diffraction (XRD), and then, we evaluated its electrochemical performance.

Experimental

NaMFC material was synthesized via a high temperature solid-state route. Stoichiometric amounts of acetate precursors (sodium, manganese and cobalt) and iron acetylacetonate were mixed in a water/ethanol solution (3/1) and heated at 100 °C until evaporation. The obtained powder was dried overnight at 100 °C and then grinded. This process was followed by calcination for 3 h at 400 °C in a muffle oven followed by an annealing for 12 h at 900 °C. The stability of NaMFC in the water was assessed using three approaches:

i) soaking NaMFC powder in water for 5 min,
ii) mixing the powder 5 min in the water or
iii) soaking the powder 1 day in the water.

Then, the powders were dried overnight under vacuum at 80 °C. Electrodes were prepared by casting a mixture of 80 %wt active material, 10 %wt carbon black Super C65 (CB, Imerys), 10 %wt CMC in deionized water (called water/CMC) or 10 %wt PVDF in NMP (called NMP/PVDF) onto aluminium foil. After a first drying at ambient temperature for water/CMC or at 80 °C under vacuum for NMP/PVDF, electrodes were punched out and dried overnight at 120 °C under vacuum. Electrochemical cells were assembled in an argon filled glove box using sodi-um metal as counter electrode and 1 M $NaClO_4$ in PC as electrolyte. Cells were cycled in galvanostatic mode at 25 °C at 0.1 C rate.

Results

SEM pictures (Figure 1) reveal that both the reference samples and the samples prepared in water exhibit platelet shape particles of 1–3 µm in length and 300 nm thickness, similarly to the description in the literature [2]. The impact of the water seems to not affect the morphology of the particles. Round shape particles of ca. 100 nm are distinguishable in all samples and might be attributed to the presence of an impurity.

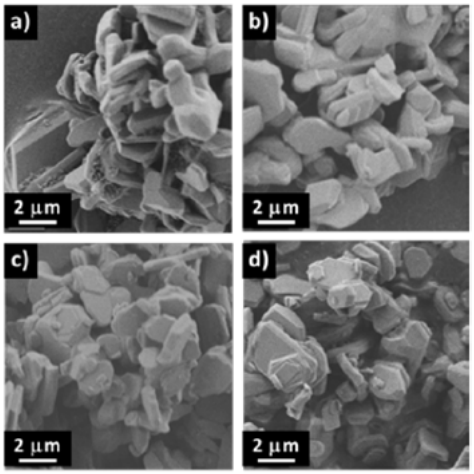

Figure 1. *SEM pictures of NaMFC a) reference, b) soaked in H_2O for 5min, c) stirred in H_2O for 5 min and d) soaked in H_2O for 1 day.*

The XRD patterns of the samples (Figure 2) reveal similar and intense Bragg peaks which can be indexed to a phase close to P2-$Na_{0.67}(Mn_{0.5}Fe_{0.25}Co_{0.25})O_2$ [2]. A closer look at the peak at 32° shows a shift to lower angles when the material is in contact with water. The most important shift (-0.21°) is obtained for the material mixed in water for 5 min in comparison with the material soaked in water for 5 min and 1 day, characterized by a shift of –0.11° and –0.13° respectively. Similar experiments with NMP were performed and a shift lower than –0.1° was obtained (not shown). According to the study of De Boisse et al. [3] on P2-$Na_{0.67}Mn_{0.5}Fe_{0.5}O_2$, a shift to lower angles of the peak at 32° is linked to the desodiation of the material.

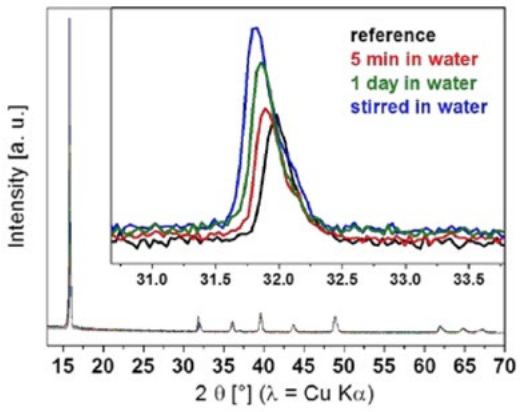

Figure 2. *XRD patterns of various NaMFC samples.*

In order to confirm a partial desodiation of the materials, we measured the pH of the water after the introduction of the NaMFC which jumps from 7 to 12. A titration of the obtained water solution was performed with an acid solution (HCl). Considering a proton exchange Na^+/H^+, we estimated the desodiation level at 13 %at (± 2 %).

The electrodes prepared in water and NMP were char-acterized by SEM (Figure 3). The NMP/PVDF electrode (Figure 3 a) shows a homogeneous distribution of the active material and the carbon particles/binder whereas in the case of CMC/water electrode, the active material is only visible through the cracks (Figure 3 b). The cross section image (Figure 3 c) of the water/CMC electrode reveals an agglomeration of the carbon particles/binder at the top of the electrode which could result in a bad electronic percolation.

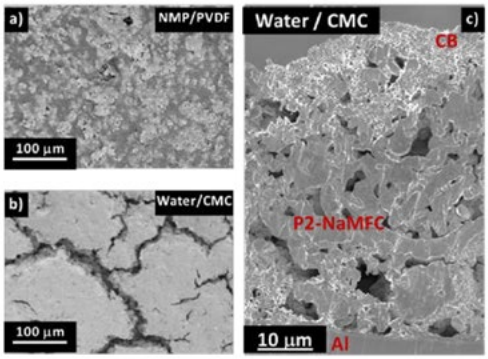

Figure 3. *SEM pictures of NaMFC electrodes prepared in a) NMP/PVDF and b), c) water/CMC.*

The electrochemical performance of the NMP/PVDF and water/CMC electrodes are presented in Figure 4. Due to desodiation level observed for water-based electrode, the first desodiation of water/CMC exhibits a specific charge of 83 mAh/g whereas it reaches 124 mAh/g for NMP/PVDF electrode. Based on our estimation, a specific charge of 108 mAh/g could be reached for water/CMC electrode. Thus, an optimization of the electrode preparation is mandatory to reach higher specific charge. Interestingly, along the first sodiation, the specific charge rises to 101 mAh/g and 143 mAh/g for water/CMC and NMP/PVDF respectively, which indicates that the materials can insert until Na = 0.88 instead of Na = 0.67 for the pristine compound [2]. The protons in NaMFC seem to be detrimental for the electrochemical performance since the specific charge of the water/CMC electrode does not reach the value of NMP/PVDF.

After 80 cycles and during sodiation, specific charges of 115 mAh/g and 88 mAh/g are obtained for NMP/PVDF electrode and water/CMC electrode, respectively.

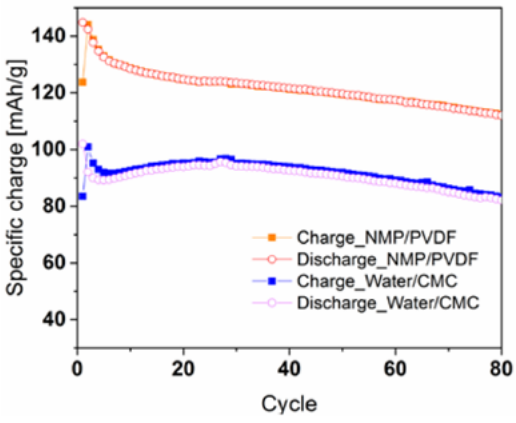

Figure 4. *Electrochemical performance of the NMP/PVDF and water/CMC NaMFC electrodes at 0.1 C.*

The galvanostatic curves of the NMP/PVDF and water/CMC electrodes for the 1st and the 80th cycles are shown in Figure 5.

The 1st desodiation curve of NMP/PVDF is characterized by a sloping region between 3 V to 4.1 V followed by a potential plateau at 4.2 V. Interestingly, the potential plateau cannot be detected in the curve of the water/CMC electrode. Its absence leads to losing the Fe^{4+}/Fe^{3+} redox activity leading to lower specific charge [4]. A similar behaviour is seen for the 1st sodiation curve of NMP/PVDF with a potential plateau at an average potential of 3.8 V, which is not visible in the curve of the water/CMC electrode. After 80 cycles, the desodiation and the sodiation curves are the same independently of electrodes preparation. A higher polarization is observed during sodiation for the water/CMC electrode.

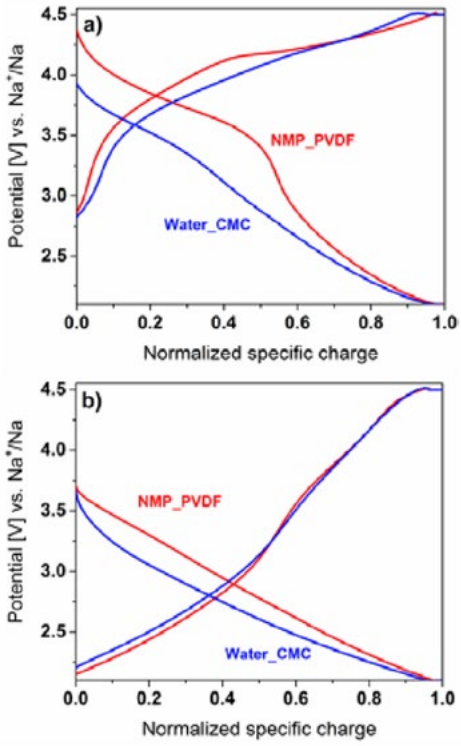

Figure 5. *Galvanostatic curves of the NMP/PVDF and water/CMC NaMFC electrodes for a) the 1st cycle and b) the 80th cycle.*

Conclusion

A water-based electrode using NaMFC as active materials was prepared with the CMC binder and characterized by SEM, XRD prior to electrochemical tests. During the immersion in water, a part estimated at 13 %at of the Na ions are substituted by protons which leads to lower the practical specific charge compared to the standard NMP/PVDF electrode.

Acknowledgement

This work was performed within the Swiss Competence Center for Heat and Electricity Storage framework.

References

[1] C. Marino, E. Marelli, C. Villevieille, *RSC Adv.* **7**, 13851–13857 (2017).
[2] L. Liu, X. Li, S. Bo, Y. Wang, H. Chen, N. Twu, D. Wu, G. Ceder, *Adv. Energy Mater.* **5**, 1500944 (2015).
[3] B. de Boisse, D. Carlier, M. Guignard, L. Bourgeois, C. Delmas, *Inorg. Chem.* **53**, 11197 (2014).
[4] N. Yabuuchi, M. Kajiyama, J. Iwatate, H. Nishikawa, S. Hitomi, R. Okuyama, R. Usui, Y. Yamada, S. Komaba, *Nat. Mat.* **11**, 512 (2012).

Operando XRD study of $LiInP_2O_7$ and $Li_2CuP_2O_7$ electroactive materials for Li-ion batteries

M. Reichardt, S. Sallard, P. Novák, C. Villevieille
phone: +41 56 310 5850, e-mail: martin.reichardt@psi.ch

The actual market of mobile devices (smartphones, laptop…) requiring energy is dominated by Li-ion batteries. The need for higher energy density and higher rate Li-ion cells is growing due to the predicted end of the fossil fuels and the development of electric vehicles [1–3]. One of the main limiting factors for future high energy batteries are the cathode electroactive materials, since their specific charge is much lower than the one of graphite, the common anode material [4]. In this context, polyanion structures are promising electroactive materials [5–7], especially since the discovery of $LiFePO_4$ [8] as a high rate and stable cathode material.

In our previous studies, $LiCrP_2O_7$ [9] and $Li_3Cr_2(PO_4)_3$ [contribution in annual report 2015] have been investigated as cathode model materials with the objective to cycle multiple redox couples (e.g. Cr^{4+}/Cr^{3+} and Cr^{3+}/Cr^{2+}) in order to extend the specific charge. In this work, the electrochemically characterizations of two lithium metal pyrophosphate materials are presented, namely the $Li_2CuP_2O_7$ [10] and $LiInP_2O_7$ [11]. The goal is to extend the concept of multiple redox systems to other active elements and investigate their electrochemical properties. In contrast to other $Li_xMP_2O_7$ materials with the common monoclinic P21 phase, the $Li_2CuP_2O_7$ exists in the monoclinic I2a phase, a layered structure with lithium in the zigzag formed interspace (see Figure 1).

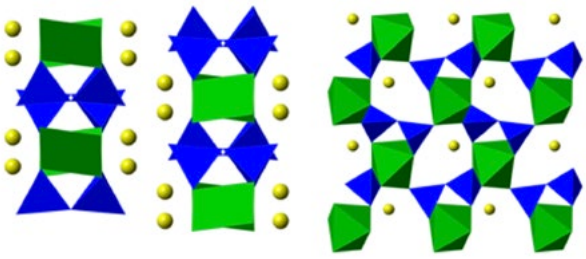

Figure 1. *(left) The $Li_2CuP_2O_7$ structure (I2a) in the projection of the c-axis. CuO_4 (square planar) is represented in green, the PO_4 groups in blue, lithium ions in yellow.*
(right) The structure of monoclinic $LiInP_2O_7$ (P21 phase) in the projection of the c-axis with InO_6 octahedrons represented in green.

Experimental

The solid state synthesis route for $Li_2CuP_2O_7$ was adapted from Spirlet et al. [10]: A stoichiometric mixture of Li_2CO_3 (Sigma-Aldrich), $NH_4H_2PO_4$ (Alfa Aesar) and $CuCl_2$ dihydrate (Sigma Aldrich) was ground carefully in a mortar. The final blue-green product was obtained by calcination in a muffle oven at 700 °C. The $LiInP_2O_7$/C material was made using an in-house solid state carbon coated synthesis route. The precursors Li_2CO_3 (Sigma-Aldrich), $InCl_33$ (Alfa Aesar), $(NH_4)_2HPO_4$ (Fluka) and citric acid were mixed in stoichiometric ratio and ground carefully. The final product was obtained by calcination in a tubular oven under argon atmosphere at 700 °C. X-ray diffraction (XRD) experiments were performed with a PANalytical Empyrean diffractometer using Cu-Kα radiation. All measurements were performed with glass fibres separator soaked with LP30 electrolyte (1 M $LiPF_6$ in EC : DMC 1 : 1 ratio). Along this report, all the potentials will be given versus the Li^+/Li reference.

Results

The crystalline $Li_2CuP_2O_7$ and $LiInP_2O_7$/C materials were characterized by XRD measurements (data not shown). In case of $Li_2CuP_2O_7$, the profile matching refinement confirmed the existence of the monoclinic I2a phase [10]. For $LiInP_2O_7$/C, the materials was found to crystalize in the monoclinic P21 phase [11]. In both cases, the lattice parameters are in good accordance with the literature.

The electrochemical characterization was conducted with the non-carbon coated $Li_2CuP_2O_7$ compound, and with the carbon coated for $LiInP_2O_77$/C.

$Li_2CuP_2O_7$

In Figure 2, the cyclic voltammogram of $Li_2CuP_2O_7$ is presented, and compared to the carbon additive Super C65. In the first reduction, cathodic peaks at 0.75 and 2.0 V are observed. The first one is attributed to the formation of the solid electrode interphase (SEI) at potentials below 1 V. The peak at 2.0 V is irreversible and not yet attributed. In the subsequent cycles, no significant electrochemical activity was observed, apart from the electrochemical activity caused by the carbon additive for potentials below 1.5 V. It has to be noted, that cycling the material to potentials above 4.0 V leads only to irreversible oxidation reactions, which are attributed to electrolyte decomposition.

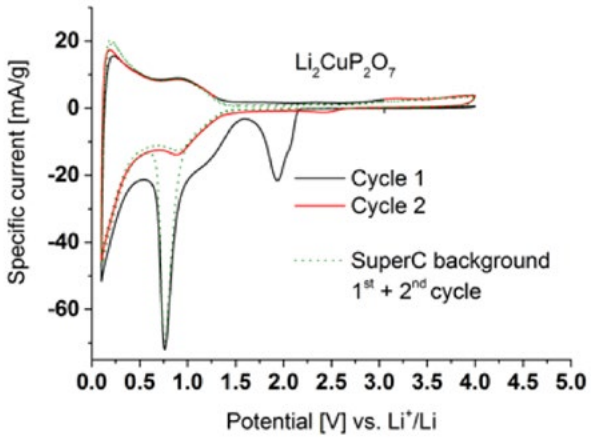

Figure 2. *Cyclic voltammogram of the $Li_2CuP_2O_7$ compound. Cycling conditions: 20 μV/s, 0.1–4.0 V.*

In order to enlighten the cause for this irreversible reaction and the proximate decay in the electrochemical performance, an operando XRD experiment was conducted (Figure 3). Small fluctuations of the peak intensities, especially the main peak

at 2θ = 12.4°, are observed at the beginning of the 1st reduction from the XRD pattern. However, once reaching a potential below 1.50 V, a decrease in intensity for all peaks is observed. Subsequent cycling of the electrode leads to no structural changes in the XRD pattern, in agreement with the CV results where no relevant electrochemical activity is observed.

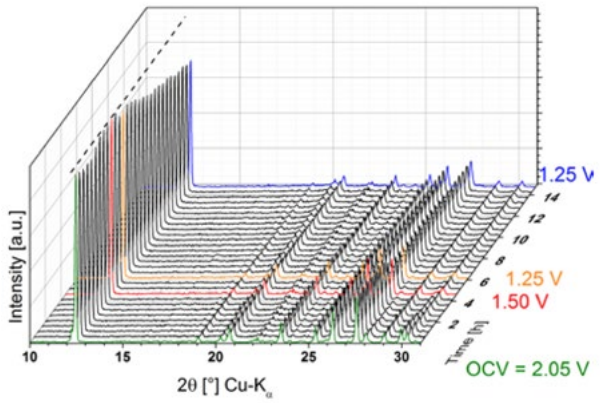

Figure 3. *Waterfall plot of operando XRD measurement of $Li_2CuP_2O_7$ material. Cycling conditions: 10.6 mA/g rate, 1.25–4.0 V.*

$LiInP_2O_7$/C

In Figure 4, the cyclic voltammogram of a $LiInP_2O_7$/C is shown, compared to the carbon Super C65. Over cycling two reversible reactions could be detected with a reduction and oxidation peak at 0.4–0.6 V and 2.0–2.4 V. The cathodic peak at 0.8 V in the first cycle is attributed only partially to the SEI formation on the Super C65 carbon additive, since its specific current value exceeds by far the one of the reference measurement of the carbon additive.

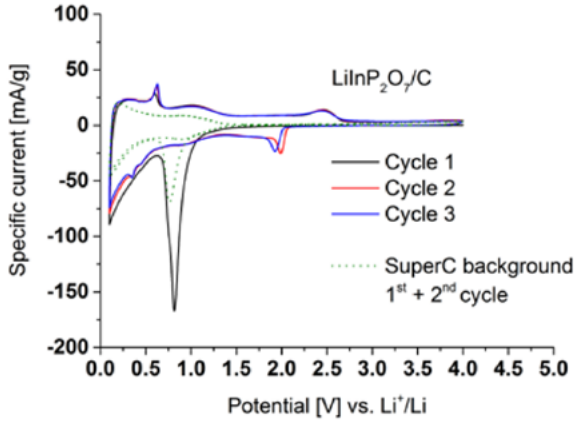

Figure 4. *Cyclic voltammogram of the $LiInP_2O_7$ compound. Cycling conditions: 20 μV/s, 0.1–4.0 V.*

With the motivation to elucidate the reaction mechanism of the $LiInP_2O_7$/C material, an XRD operando measurement was conducted over 1.5 cycles (Figure 5). It can be clearly seen, that in the first 3 hours of the lithiation (potential > 1.0 V), the pristine pattern remains unchanged. However, during the reduction at 1.0 V, a constant diminishing of the intensity of all peaks of the XRD pattern is observed. When the potential reaches a value < 1.0 V (at the end of the potential plateau) the original $LiInP_2O_7$ (P21) turns amorphous. Interestingly, for potentials < 0.4 V during reduction and < 0.6 V during oxidation, a broad peak between 2θ = 20–24° is present. At potentials superior to 2 V, a very diffuse transitory peak in the range from 2θ = 19–26° is also present. Both peaks are indicated with red circles in Figure 5.

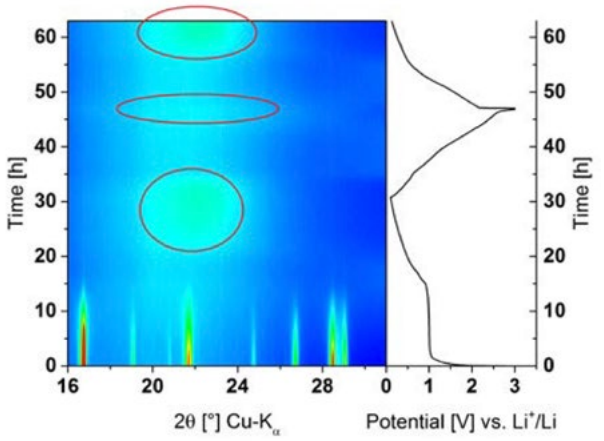

Figure 5. *Contour plot of operando XRD measurement of $LiInP_2O_7$ material. Cycling conditions: 23.8 mA/g rate, 0.1–3.0 V vs. Li^+/Li potential range.*

A reasonable hypothesis to explain the formation of the peak at 20–24° at low potentials could be the reversible formation of Li_xIn_y-alloys. The comparison of the main Bragg peaks of the Li_2In, $Li_{13}In_3$, Li_3In_2 and LiIn phases (data not shown) show good overlap with the new peaks in the acquired pattern, supporting a possible alloying mechanism behind the reversible cycling.

Conclusion

The $Li_2CuP_2O_7$ and $LiInP_2O_7$/C materials were both synthesized via solid-state routes. In case of $Li_2CuP_2O_7$, only an irreversible reduction at 2.0 V is recorded. For the $LiInP_2O_7$/C material, reversible cycling based on two redox couples is reported. Operando XRD studies support the hypothesis of an alloying mechanism with a possible formation of Li-In alloys upon cycling. In summary, these results are a promising starting point in the search for new polyanion-based electroactive materials in future Li-ion cells with $LiInP_2O_7$/C as a proof of concept using multiple redox reactions.

References

[1] M. Armand, J.-M. Tarascon, *Nature 2008* **451**, 652–657.
[2] N. Nitta, F. Wu, J.T. Lee, G. Yushin, *Mater. Today* **18**, 252–264 (2015)
[3] D. Larcher, J.-M. Tarascon, *Nat. Chem.* **7**, 19–29 (2015).
[4] C. Pillot, *5th Isr. Power Sources Conf.* **33**, 1–39 (2015).
[5] P. Barpanda, S. Nishimura, A. Yamada, *Adv. Energy Mater.* **2**, 841–859 (2012).
[6] P. Barpanda, M. Ati, B.C. Melot, G. Rousse, J.-N. Chotard, M.-L. Doublet, M.T. Sougrati, S.A. Corr, J.-C. Jumas, J.-M. Tarascon, *Nat. Mater.* **10**, 772–779 (2011).
[7] M. Tamaru, S.C. Chung, D. Shimizu, S. Nishimura, A. Yamada, *Chem. Mater.* **25**, 2538–2543 (2013).
[8] A.K. Padhi, K.S. Nanjundaswamy, J.B. Goodenough, *J. Electrochem. Soc.* **144**, 1188–1194 (1997).
[9] M. Reichardt, S. Sallard, P. Novák, C. Villevieille, *Acta Crystallogr. Sect. B* **71**, 661–667 (2015).
[10] M.R. Spirlet, J. Rebizant, M. Liegeois-Duyckaerts, *Acta Crystallogr. Sect. C* **49**, 209–211 (1993).
[11] D. Tran Qui, S. Hamdoune, Y. Le Page, *Acta Crystallogr. Sect. C* **43**, 201–202 (1987).

Electrode engineering of silicon-containing graphite electrodes

T. Schott, P. Novák, S. Trabesinger
phone: +41 56 310 3792, e-mail: tiphaine.poux@psi.ch

Graphite, due to its low reaction potential and its performance stability, is the most common negative electrode material in current lithium-ion batteries. However, limits of its theoretical specific charge (372 mAh/g) have already been reached and, therefore, it is impossible to further increase the energy density of the battery using graphite alone.

Silicon is a promising candidate to partially replace graphite due to its relatively low potential window and its very high specific charge (3579 mAh/g), about 10 times higher than that of graphite. However, silicon-based electrodes suffer from strong performance fading upon cycling due to significant volume changes of silicon during lithiation and delithiation. On the electrolyte level, fluoroethylene carbonate (FEC) is an efficient additive to enhance the cycling stability of Si/graphite-based electrode [1] due to better interfacial properties, while a better maintenance of the electrical contact within the electrode can be achieved by optimizing the graphite type and binder nature [2] or the properties of Si/C composite additives [3]. In the present work, we investigated a possibility to further optimize the electrode composition, which would lead to improved electrochemical performance, namely, higher active material utilization and better stability.

We tested different capacity-enhancing graphite electrode additives: nano-Si and SiO as an alternative silicon source. To lower the surface area of electrodes, we studied the option to prepare electrodes without conductive carbon additive, which has high surface area. And finally, speculative effects of molecular weight of the binder components [4] were clarified.

Experimental

Commercially available particulate Si (Nanostructured and Amorphous Materials) and SiO (Alfa Aesar) materials were used as specific-charge-enhancing additives. Their purity and crystallinity were determined by X-ray diffraction (XRD) employing PANalytical Empyrean diffractometer using Cu-Kα radiation. Diffraction pattern were recorded in the 10–80° 2θ-range, using 0.1°/s step. The powder morphology was studied by scanning electron microscopy (SEM) using a Carl Zeiss UltraTM 55 scanning electron microscope operated at an accelerating voltage of 3 kV in the secondary electron detection mode.

For the electrode preparation, a mixture of carboxymethyl cellulose (CMC) and polyacrylic acid (PAA, 25 %wt sol. in H_2O, average M.W. 240,000) was dissolved in a mixture of water : ethanol (7 : 3). Alternatively, PAA with lower (M.W. 100,000) or higher (M.W. 1,250,000) molecular weight was used. Si or SiO powder was stirred with Super C45 carbon additive (C-NERGY, Imerys Graphite and Carbon) in the binder solution. Finally, KS6L graphite flakes (C-NERGY, Imerys Graphite and Carbon) were added to the mixture and the slurry was stirred until a honey-like texture was obtained. The slurries were cast onto copper foil and heat treated at 150 °C under vacuum for 2 h in order to favor the cross-linking reaction between CMC and PAA [5]. The final composition of the electrodes was: 90 %wt KS6L graphite, 5 %wt Si or SiO, 1 %wt Super C45 carbon additive and 4 %wt CMC/PAA (1 : 1) binder. For comparison, electrodes without Super C45 (91 %wt KS6L) and electrodes without Si source (95 %wt KS6L) were studied.

Electrochemical testing was performed in half-cell configuration with metallic lithium as counter electrode, 1 M $LiPF_6$ in EC : DMC (1 : 1) with 2 %wt FEC as electrolyte, and glass fiber separators. The cycling procedure, after a first cycle at 20 mA/g for the solid electrolyte interphase (SEI) formation, was based on a CC-CV (constant-current – constant-voltage) technique with 50 mA/g for lithiation and 186 mA/g for delithiation for CC step, and with potentials of 5 mV vs. Li^+/Li for lithiation, 1.5 V vs. Li^+/Li for delithiation for CV step. The specific charge is presented per mass of electrode coating.

Results

SEM (Figure 1) and XRD (Figure 2) analysis show that the studied Si material is composed of 30–50 nm-sized spherical nanoparticles, regrouped in loose aggregates and displaying high crystallinity, while both studied SiO materials are composed of amorphous micrometric particles of various sizes.

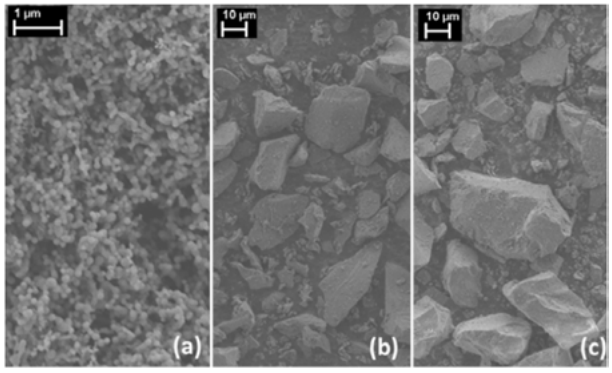

Figure 1. *SEM image of (a) Si, (b) SiO (sample 1), and (c) SiO (sample 2) powders.*

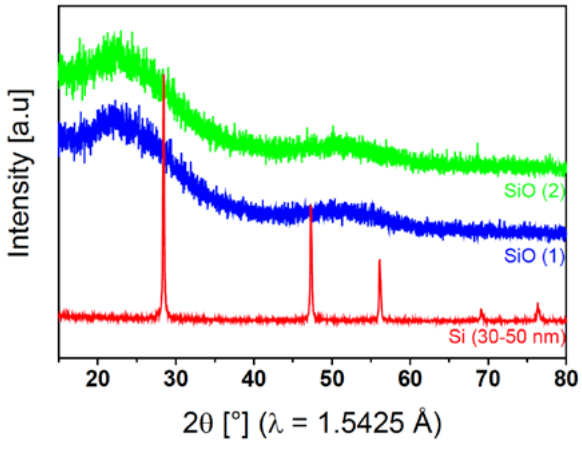

Figure 2. *XRD pattern of Si and SiO powders.*

When the Si nanoparticles were added to graphite electrodes, initially the theoretical specific charge is reached (514 mAh/g, considering 3579 mAh/g for Si and 372 mAh/g for graphite), displaying good cycling stability with high specific charge of ~480 mAh/g after 50 cycles (Figure 3). To the contrary, the specific charge reached for both SiO samples is well below that of Si-based electrodes. Although only 64 %wt Si is available in SiO, a gain of ~100 mAh/g compared to graphite electrode was expected. However, for both SiO samples, the gain is only 50 mAh/g for the first few cycles and it drastically decreases while cycling, leading to a specific charge equal to that of Si-free electrodes after 50 cycles (Figure 3). Moreover, SiO-containing electrodes deliver lower first cycle coulombic efficiency (75 %) than Si nanoparticles (82 %). This is due to the fact that SiO undergoes irreversible conversion during lithiation from SiO to Li_2O and Li-Si alloy. Compared to Si nanoparticles, the performance of SiO-based electrodes is therefore judged as very poor and not of interest for commercial applications.

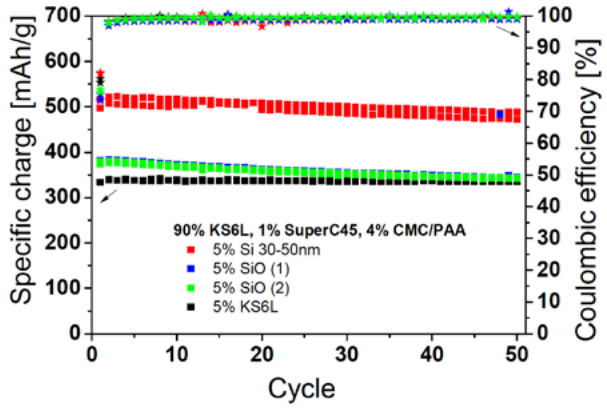

Figure 3. *Electrochemical performance (specific charge: squares, coulombic efficiency: stars) of graphite electrodes containing Si or SiO.*

To reduce the electrode surface area in order to minimize side reactions during the first cycle and consequently to minimize first-cycle inefficiency, some electrodes containing Si nanoparticles were prepared without Super C45. It was observed that the fading rate was similar with and without carbon additive (Figure 4) but the specific charge was slightly lower (by ~20 mAh/g) in the absence of Super C45. This is due to impaired electronic conductivity within electrodes and consequently more difficult utilization of graphite and Si in the absence of interconnecting small carbon particle chains. It was also impossible to improve this result by densifying the electrode through calendering (Figure 4) in order to assure better contact within electrode. Thus, the addition of carbon black, even in small quantities such as of 1 %wt of the total electrode mass, is necessary to allow full utilization of the active material. This amount should however not be increased to avoid a significant increase of the electrode surface area and reduction of active material fraction.

Koo et al. previously demonstrated that the cycling stability of Si-based electrodes can be significantly improved by the cross-linked architecture of the CMC/PAA binder [5]. Thus, we tested CMC/PAA binders with PAA of various molecular weights to check if it affects the mechanical integrity of the electrodes and therefore the cycling stability. As can be seen in Figure 5, the molecular weight of PAA binder has no effect on the electrochemical performance of electrodes containing Si nanoparticles. Therefore, intermediate molecular weight (Mw = 240,000), easy to handle and used for previous experiments, is a good choice for electrode preparation.

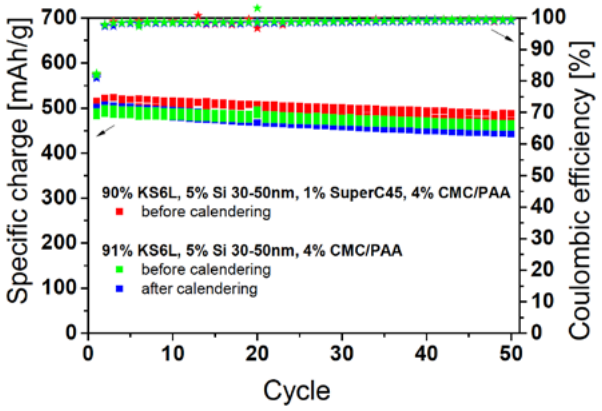

Figure 4. *Electrochemical performance (specific charge: squares, coulombic efficiency: stars) of Si/graphite electrodes with and without Super C45 carbon additive.*

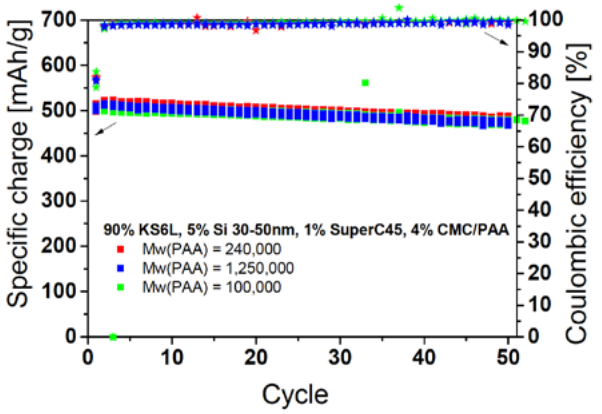

Figure 5. *Electrochemical performance (specific charge: squares, coulombic efficiency: stars) of Si/graphite electrodes with various PAA molecular weights.*

This study demonstrates that replacing silicon by its oxides or reducing the surface area of silicon-containing graphite electrodes cannot be easily achieved without affecting the cycling performance, independently of the binder molecular weight.

Acknowledgement

IMERYS Graphite & Carbon is gratefully acknowledged for financial support and valuable discussions.

References

[1] X. Chen, X. Li, D. Mei, J. Feng, M.Y. Hu, J. Hu, M. Engelhard, J. Zheng, W. Xu, J. Xiao, J. Liu, J.-G. Zhang, *ChemSusChem* **7**, 549–554 (2014).

[2] J.L. Gómez-Cámer, C. Bünzli, M.M. Hantel, T. Poux, P. Novák, *Carbon* **105**, 42–51 (2016).

[3] T. Schott, J.L. Gómez-Cámer, P. Novák, S. Trabesinger, *J. Electrochem. Soc.* **164**, A190–A203 (2017).

[4] H.-K. Park, B.-S. Kong, E.-S. Oh, *Electrochem. Commun.* **13**, 1051–1053 (2011).

[5] B. Koo, H. Kim, Y. Cho, K.T. Lee, N.-S. Choi, J. Cho, *Angew. Chem. Int. Ed.* **51**, 8762–8767 (2012).

Evaluation of lithium plating in Li–Li and Li–Cu cells

T. Schott, S. Trabesinger
phone: +41 56 310 5775, e-mail: sigita.trabesinger@psi.ch

Batteries using metallic lithium as negative electrode suffer from several issues during repeated charge/discharge processes [1]. During normal cycling, lithium deposition and dissolution is continuously occurring. The deposited Li can present various morphologies, such as moss-like, particulate-like or dendritic (needle)-like, depending on the lithium surface and on the current densities applied. The lithium dendrites are more likely to occur at high current densities [2] due to fast lithium deposition, and to be initiated by its surface defects. This is a self-enhancing process because lithium tends to deposit on lithium protuberance, leading to the local volume increase, which in turn causes the cracking of the SEI, which then further aggravates the dendrite growth.

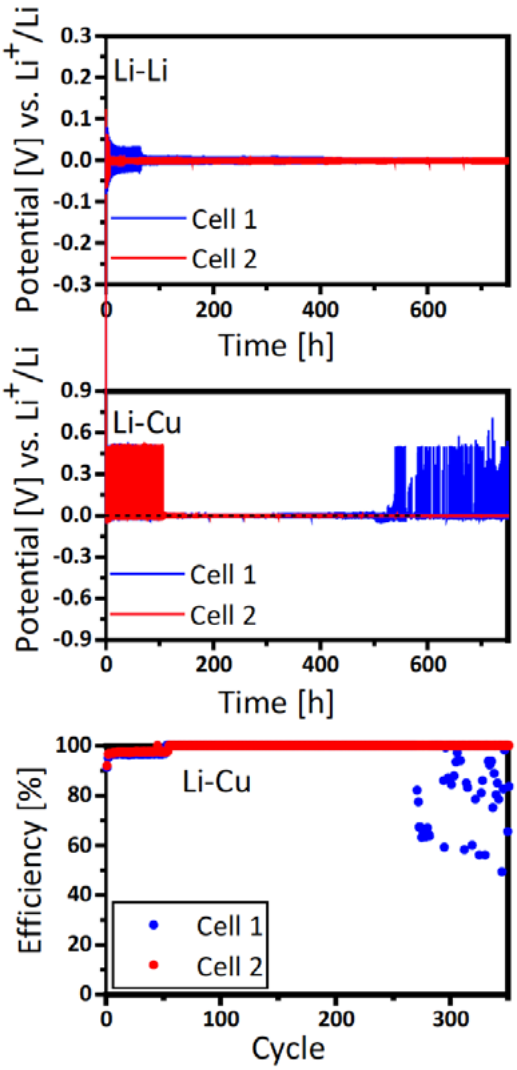

Figure 1. *Top to bottom: potential development in symmetric Li–Li cells; potential development in Li–Cu cells; coulombic efficiency of Li–Cu cells. Cells cycled with 1 separator and 1 M LiTFSI in DME : Diox (2 : 1) with 0.4 M $LiNO_3$ as electrolyte.*

The repeated lithium deposition/stripping processes, which consume both lithium and electrolyte, lead to low coulombic efficiency of the cell. Recently alternative failure mechanisms were proposed [3]. According to the study of Li–NCA cell, the cell failure at high current densities was found to be not due to dendrite growth toward the electrolyte but rather caused by the formation of a highly resistive SEI layer toward the bulk lithium.

Lithium stripping/plating in Li–Li and Li–Cu cells in two different electrolyte environments was investigated to establish testing conditions as well as to identify electrolyte additive sensitivity at high lithium stripping/plating rates.

Experimental

The symmetric Li–Li and asymmetric Li–Cu cells were assembled with different electrolytes (500 µL): LP30 (1 M $LiPF_6$ in EC : DMC (1 : 1)) + 2 % FEC and 1 M LiTFSI in DME : Diox (2 : 1) with 0.4 M $LiNO_3$. Cycling conditions were: for charge and discharge 2.6 mA current was applied for 1 h, corresponding to current density 2 mA/cm^2. Either 1 or 3 glass fibre separators were used in the cell depending on experiment.

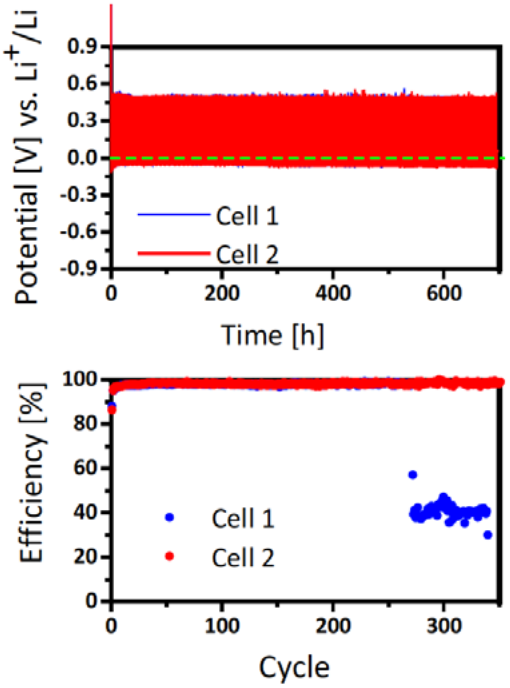

Figure 2. *Top to bottom: potential development of Li–Cu cells and their corresponding efficiency. Cells with 3 separators and 1 M LiTFSI in DME : Diox (2 : 1) with 0.4 M $LiNO_3$ as electrolyte.*

Results

The cycling of Li was first investigated in the standard Li–S electrolyte, namely 1 M LiTFSI in DME : Diox (2 : 1) with 0.4 M $LiNO_3$ additive, which is known to passivate metallic lithium and provide long cycle life. The overpotentials during cycling

in symmetric Li–Li cells were rather low from the start (upper graph in Figure 1). The reproducibility was rather poor, as overpotential of one cell dropped almost to zero already after 10 h, while for the other it stayed at higher value for about 100 hours, before diminishing. Diminishing overpotential is an artefact in Li cycling experiments as the degradation of electrolyte is expected and as a result an increase of overpotential. To clarify this discrepancy, lithium was cycled against copper foil, as then also efficiency of plating and stripping can be assessed. This experimental configuration lead to well reproducible lithium cycling and lead to hypothesis that the drop in overpotential value is correlated to soft short-circuit due to dendrites, resulting in mixed potential response (middle and bottom panels in Figure 1). To confirm this dendritic switch-off of the potential, Li–Cu cells were assembled with 3 separators in order to delay dendrite-caused short-circuit. In Figure 2 it is visible that no sudden drop in overpotential value is occurring during > 600 hours, confirming our hypothesis.

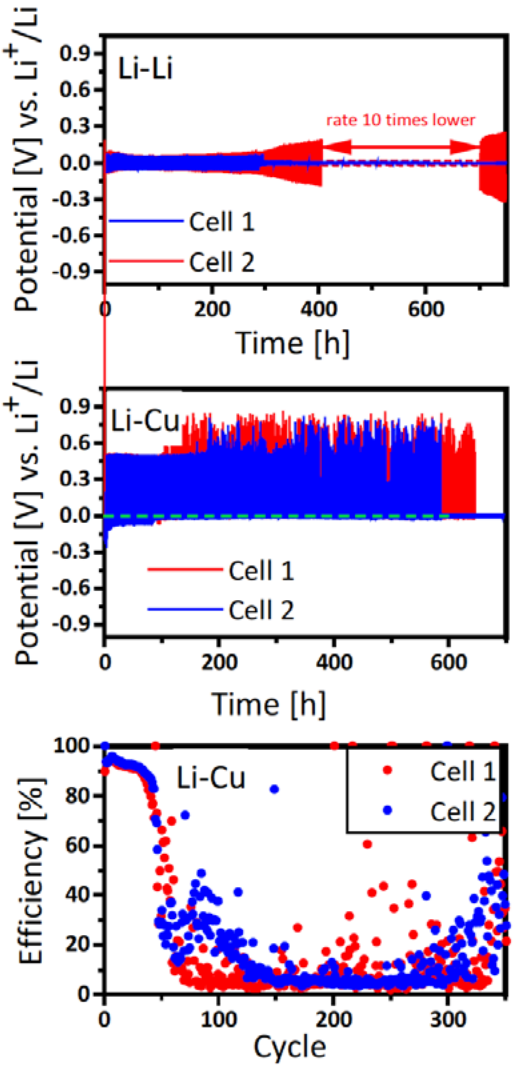

Figure 3. *Top to bottom: potential development in symmetric Li–Li cells; potential development in Li–Cu cells; coulombic efficiency of Li–Cu cells. Cells cycled with 1 separator and LP30 + 2 % FEC as electrolyte.*

The same type of study was performed in carbonate electrolytes containing FEC as an additive (see Figure 3), which is well-known to decompose at low potentials and form high quality SEI on silicon negative electrodes. However, surprisingly here Li–Li cells had longer lifetime (longer time until voltage drop, identified as soft short circuit) than the Li–Cu cells. In Li–Cu after ~ 50 cycles efficiency started dropping and went down to zero. To again confirm the dendritic growth of lithium, 3-separator experiments were performed. However, this time (see Figure 4) larger distance between electrodes did not prolong the life-time of the Li–Cu cells beyond same ~ 50 cycles, deeming our hypothesis of dendrite-induced short-circuit invalid.

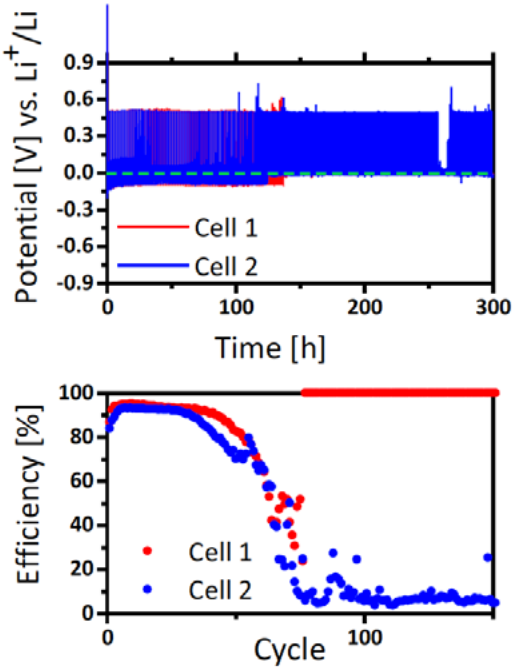

Figure 4. *Top to bottom: potential development of Li–Cu cells and their corresponding efficiency. Cells with 3 separators and LP30 + 2 % FEC as electrolyte.*

Conclusions

It has been found that for studying lithium cyclability it is more advantageous to use asymmetric Li–Cu cells as their cycling reproducibility is much higher and it gives the advantage of plating/stripping efficiency tracking.

Two different electrolyte systems with their most common additives for negative electrodes also showed some unexpected results: dendritic growth in 1 M LiTFSI in DME : Diox (2 : 1) with 0.4 M $LiNO_3$ additive, as well as unknown origin of cell failure with FEC. More experiments are needed to understand the latter, which can be in line with Li–NCA cell [3], caused by resistive SEI formation.

Acknowledgement

BASF SE is acknowledged for financial support within the «BASF Scientific Network for Electrochemistry and Batteries».

References

[1] W. Xu, J. Wang, F. Ding, X. Chen, E. Nasybulin, Y. Zhang, J.-G. Zhang, *Energy Environ. Sci.* **7**, 513–537 (2014).
[2] Y.S. Cohen, Y. Cohen, D. Aurbach, *J. Phys. Chem. B* **104** (51), 12282–12291 (2000).
[3] D. Lu, Y. Shao, T. Lozano, W.D. Bennett, G.L. Graff, B. Polzin, J. Zhang, M.H. Engelhard, N.T. Saenz, W.A. Henderson, P. Bhattacharya, J. Liu, J. Xiao, *Adv. Energy Mat.* **5**, 1400993 (2015).

Influence of the counter electrode on the cycling performance of Li_3PS_4 solid electrolyte

X. Wu, M. El Kazzi, C. Villevieille
phone: +41 56 310 2410, e-mail: claire.villevieille@psi.ch

All-solid-state lithium-ion batteries (SLiB) are an attractive alternative to the Li-ion batteries due to the substitution of the volatile and flammable liquid electrolyte by solid electrolyte. Despite the progress made in the material synthesis of solid electrolytes with high ionic conductivity less is known about their degradation mechanisms particularly at the electrode/electrolyte interfaces. The interfacial reactivity between the solid electrolyte and the electrodes is of vital interest to ensure the long-term cycling of solid-state batteries.

As a starting point, we investigated the electrochemical performance of the $InLi_x|Li_3PS_4|LTO$ cell. Therein, we studied the influence of the counter electrode. Furthermore, the interface between the solid electrolyte and cathode was examined by X-ray photoemission spectroscopy (XPS).

Experimental

The amorphous solid electrolyte Li_3PS_4 was prepared by ball milling using a stoichiometric mixture of the precursors, i.e., Li_2S and P_2S_5. The obtained powder was then pelletized to give dense solid electrolyte. [1]

The solid electrolyte was characterized by X-ray diffraction (XRD) and Raman spectroscopy. X-ray photoemission spectroscopy (XPS) measurements were carried out on the pristine materials as well as on cycled samples. The spectra were normalized by the intensities of the S2p core level in Li_3PS_4. The ionic conductivity of the solid electrolyte pellet was estimated from the resistance measured by AC-electrochemical impedance spectroscopy (EIS) on the symmetric cells using carbon-coated aluminium foil as blocking electrodes. A powder composite cathode consisting of 50 %wt $Li_4Ti_5O_{12}$ (LTO) and 50 %wt Li_3PS_4 was prepared by hand mixing. Finally, the electrochemical cell was assembled using either $InLi_x$ or metallic lithium as counter electrode. The LTO composite electrodes were cycled between 1 and 2 V vs. Li^+/Li. The potential of $InLi_x$ ($x < 1$) is 600 mV vs. Li^+/Li. The voltage window, in which the $In\text{-}Li_x|Li_3PS_4|LTO$ cell was cycled, was then shifted accordingly. The cells were charged and discharged at a current of 17.5 mAh/g_{LTO}. The galvanostatic lithium plating and stripping experiments were conducted using a $In\text{-}Li_x|Li_3PS_4|$stainless steel cell configuration. First, lithium was deposited on the current collector applying a current of –20 µA for 10 h (Q_0). Subsequently, 10 % of Q_0 is stripped (Q_C) and plated (Q_D) in each step to simulate the cycling conditions. The experiment is terminated once the overpotential exceeds 500 mV vs. Li/Li^+. The number of cycles before termination (n) is then used to estimate the lithium electrode cyclic efficiency as described by Equation 1.

$$\eta = \frac{n * Q_c}{n * Q_D + Q_0} \qquad \text{Equation 1}$$

Results

As can be seen from the XRD pattern presented in Figure 1 a, 30 h of active milling were necessary to obtain the amorphous solid electrolyte. Raman spectroscopy reveals the formation of new bonds in a typical PS_4^{3-} tetrahedron as indicated by the peak at 421 cm^{-1} in Figure 2 b. A weak shoulder located at 387 cm^{-1} reveals the formation of $P_2S_6^{4-}$ dimer, a known sulphur-deficient impurity phase that could be created during the ball mill synthesis. [2]

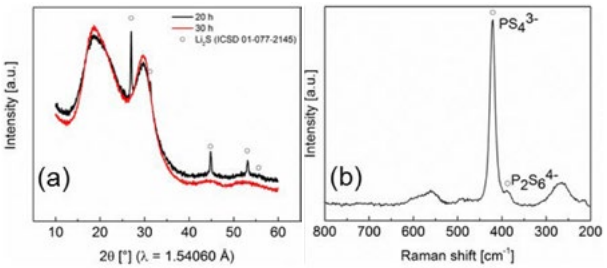

Figure 1. *(a) XRD patterns of Li_3PS_4 milled for 20 and 30 hours, (b) Raman spectrum of the Li_3PS_4 powder after 30 h effective ball milling time.*

The room temperature ionic conductivity of the pelletized Li_3PS_4 was measured around 0.4 mS cm^{-1} and the activation energy was determined to be 0.37 eV. These values confirm this material as a suitable ionic conductor for SLiB.

The use of metallic lithium is attractive due to the high energy density of lithium. However, significant dendrite formation was observed in the lithium plating experiment with Li_3PS_4 as solid electrolyte and metallic lithium as counter electrode (Figure 2 a). Already after three cycles, the formation of dendrite caused the internal short-circuit, and thus failure of the electrochemical cell. Using Equation 1, the cyclic efficiency is estimated to be merely 23 %. By replacing the counter electrode with an $InLi_x$ alloy, the cycling behaviour could be drastically improved up to 60 cycles without short-circuiting (Figure 2 b), which corresponds to 86 % cyclic efficiency. In order to reach higher cyclic efficiency, the parasitic consumption of lithium through reaction with solid electrolyte at the working electrode needs to be further investigated.

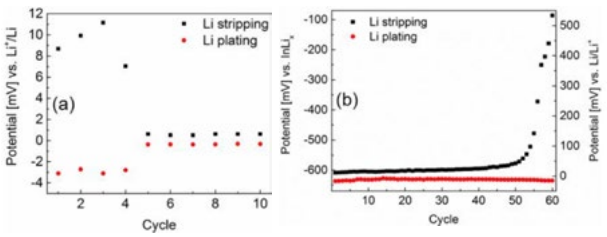

Figure 2. *Li plating and stripping experiments with: (a) metallic lithium and (b) $InLi_x$ counter electrode.*

Electrochemical cells were assembled and cycled in the configuration $InLi_x|Li_3PS_4|$LTO-composite. The cell delivers up to ca. 120 mAh/g_{LTO} with a high cycling stability within 70 cycles. The coulombic efficiency for such a cell exceeds 99 % indicating that a stable and favourable interface between LTO and Li_3PS_4 was obtained.

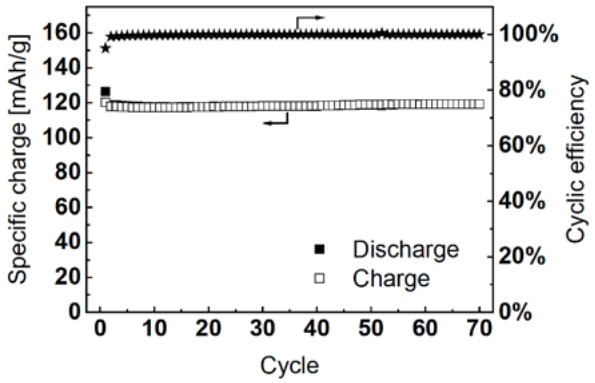

Figure 3. *Specific charge during long-term cycling of an $InLi_x|Li_3PS_4|$LTO-composite cell at a current of 17.5 mAh/g_{LTO}.*

In order to further elucidate the interface between Li_3PS_4 and LTO, post-mortem XPS is performed on the LTO-composite cathode. As shown in Figure 4, the lithiated electrode shows the reduction of Ti^{4+} to Ti^{3+} confirming the electrochemical activity of LTO. After 20 cycles, no significant changes in S2p and P2p core levels from the solid electrolyte have been observed. This indicates the electrochemical stability of the solid electrolyte which is in good agreement with thermodynamic predictions. [3]

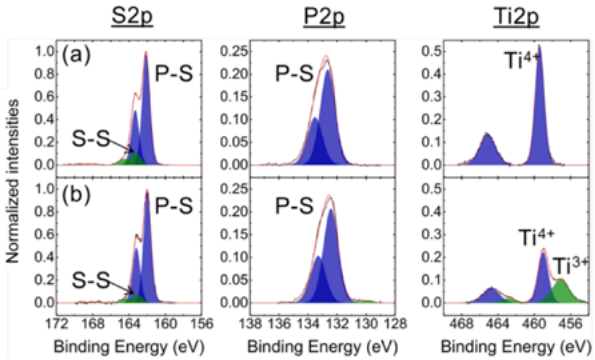

Figure 4. *$S2p_{3/2\text{-}1/2}$, $P2p_{3/2\text{-}1/2}$ and $Ti2p_{3/2\text{-}1/2}$ XPS core levels acquired on LTO-composite cathode:*
a) pristine b) fully lithiated after 20 cycles.

Conclusion

The principle of an all-solid-state lithium ion battery was demonstrated using an in-house designed electrochemical cell. The $InLi_x$ alloy as counter electrode proves to be a critical component to ensure stable cycling and avoid internal short-circuit due to the development of dendrites. Post-mortem XPS measurement confirmed the reduction/oxidation of LTO electrode during cycling and the stable electrode/electrolyte interface. Thus, XPS is the method of choice for tracking the interface between active material and solid electrolyte as well as for direct observation of the electrochemical activity of the active material.

Acknowledgement

This work is supported from the Competence Center Energy and Mobility (CCEM) and the Swiss Electric research initiative (SER). Mr. Marcel Locher is gratefully thanked for the support in the cell design.

References

[1] T. Yamada, S. Ito, R. Omoda, T. Watanabe, Y. Aihara, M. Agostini, U. Ulissi, J. Hassoun, B. Scrosati, *J. Electrochem. Soc.* **162**, A646 (2015).
[2] A. Sakuda, A. Hayashi, M. Tatsumisago, *Sci. Rep.* **3**, 2261 (2013).
[3] Y. Zhu, X. He, Y. Mo, *ACS Appl. Mater. Interfaces* **7**, 23685 (2015).

Functionalized ETFE-*g*-poly(4-vinylpyridine) membranes for all-vanadium redox flow batteries

O. Nibel, T.J. Schmidt, L. Gubler
phone: +41 56 310 2326, e-mail: olga.nibel@psi.ch

All-vanadium redox flow batteries (VRBs) are a promising energy storage technology for the efficient utilization of renewable energy sources such as wind and sunlight. VRBs use the same element, i.e. vanadium, in both half cells, which prevents irreversible cross-contamination of electrolytes and thus reduces the maintenance cost. A VRB consists of a cell or stack of cells where redox reactions occur, two tanks filled with electrolytes, and balance of plant components, such as pumps [1]. A redox flow cell is usually separated in two compartments by an ion exchange membrane (IEM) that avoids cross-mixing of electrolytes and at the same time allows the transport of specific ions across the membrane to maintain charge balance during cell operation. High cross-over of vanadium ions through an IEM results in capacity and efficiency losses and limits its use as energy storage device. Thus, an ideal membrane for the VRB should have low vanadium and water crossover. Moreover, IEMs for VRB applications should have low cost, low area resistance as well as good mechanical and chemical stability [2, 3].

The objective of this study is to design amphoteric IEMs for VRB applications. By introduction of positively charged vinylpyridinium units and a defined extent of crosslinking into new amphoteric IEMs, improved vanadium barrier properties were targeted, whereas the presence of protogenic sulfonic acid groups was expected to reduce their ohmic resistance. The synthesis of amphoteric IEMs started with the preparation of ETFE-*g*-poly(4-vinylpyridine) films by radiation induced graft copolymerization of 4-vinylpyridine (VP) into ethylene tetrafluoroethylene (ETFE) films of 25 µm thickness. Subsequently, grafted films were imparted with desired functionalities according to Scheme 1.

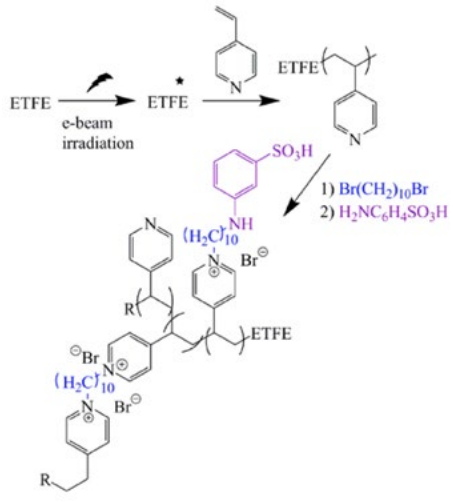

Scheme 1. *Schematic representation of the synthesis of functionalized ETFE-g-poly(VP) membranes.*

Functionalized membranes were analyzed using FT-IR spectroscopy and energy-dispersive X-ray spectroscopy coupled with scanning electron microscopy (EDX-SEM). Moreover, the effect of functionalization on the key properties of the membranes, such as vanadium ion permeability and ohmic resistance, was investigated.

Experimental

Synthesis of grafted films

The ETFE base films (DuPont, 25 µm thickness) were irradiated using an MeV class electron beam in air and stored at –80 °C. The grafting reaction was performed in glass reactors under nitrogen atmosphere. For that, a grafting solution with the following composition was prepared: 50 % (v/v) vinylpyridine + 50 % (v/v) isopropanol. The grafting solution containing irradiated films was bubbled with N_2 for 1 h. Then, the reactor was placed in a thermostatic water bath at 60 °C. After the reaction, grafted films were immersed in isopropanol for 18 h and dried under vacuum at 80 °C.

Functionalization of ETFE-g-poly(VP) films

The first step of functionalization was carried out in a small glass reactor using 0.25 M solution of 1,10-dibromodecane in N-methyl-2-pyrrolidone (NMP). Vinylpyridine grafted films were introduced into the prepared solution and placed in a thermostatic water bath at 45 °C for a given amount of time. Subsequently, the films were removed from the reaction mixture and rinsed with isopropanol.

The second step of functionalization was performed in a small glass reactor using a 0.05 M solution of 3-aminobenzene sulfonic acid in NMP. Grafted films were introduced into the small reactor containing the prepared solution and placed in a thermostatic water bath at 45 °C for 6 hours. Subsequently, functionalized films were immersed in 2 M H_2SO_4 overnight.

Characterization of functionalized membranes

Vanadium ion permeability: Vanadium ion permeability of membranes was determined using self-made diffusion cells consisting of two round bottom flasks separated by the membrane. The left compartment was filled with a 1 M solution of $VOSO_4$ in 2 M H_2SO_4 while the right one was filled with 1 M solution of $MgSO_4$ in 2 M H_2SO_4. The concentration of diffused VO^{2+} ions was determined intermittently via UV-ViS (Cary 4000, Varian).

Determination of membrane area resistance: The area resistance of single redox flow cells containing membranes of interest was measured at fully charged state by means of electrochemical impedance spectroscopy. For these measurements a redox cell test system (Model 857, Scribner Associates) was used. All experiments were carried out with an AC amplitude of 10 mV in a frequency range from 100 kHz to 0.1 Hz at room temperature.

Results and Discussion

The success of the grafting reaction and subsequent functionalization of ETFE-*g*-poly(VP) films was confirmed using FT-IR spectroscopy (Figure 1). In the spectrum of the VP grafted film, the characteristic absorption peak of the pyridine ring

was identified at around 1'600 cm^{-1}. After the first functionalization step the intensity of this peak decreases whereas a new peak characteristic for pyridinium salt appears at around 1'660 cm^{-1}. After the second functionalization step and subsequent rinsing in 2 M H_2SO_4, the peak at 1'600 cm^{-1} disappears completely, suggesting that pyridine units that were not converted to quaternized pyridine were protonated in 2 M H_2SO_4.

Moreover, after the second functionalization step two new peaks appear at 1'500 cm^{-1} and 830 cm^{-1}. The signature at around 1'500 cm^{-1} can be assigned to the N-H deformation vibration of the attached aminobenzene sulfonic acid unit and the peak at 830 cm^{-1} is associated with the presence of the SO^{3-} group. The region between 1'000 and 1'300 cm^{-1} is hidden due to excessive absorption by the ETFE backbone polymer.

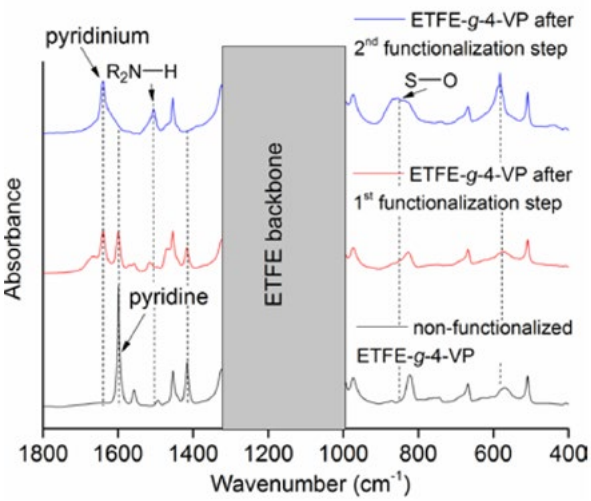

Figure 1. *FT-IR analysis of ETFE-g-poly(VP) membranes in various stages of functionalization. Important vibrational bands are highlighted. FT-IR analysis was performed using membranes with around 43 % graft level (GL). Reaction conditions for functionalization were: 1st step => 24 h, 45 °C and 2nd step => 6 h, 45 °C.*

Elemental distribution in the cross-section of prepared membranes was analyzed by SEM/EDX. If films irradiated with 15 kGy were selected, membranes with a homogenous distribution of grafts in the thickness could be obtained only in case of higher graft levels (GL > 60 %). In contrast, films irradiated with 5 kGy allowed the synthesis of membranes with lower graft levels (GL < 50 %) and homogenous distribution of grafts in the cross-section (Figure 2).

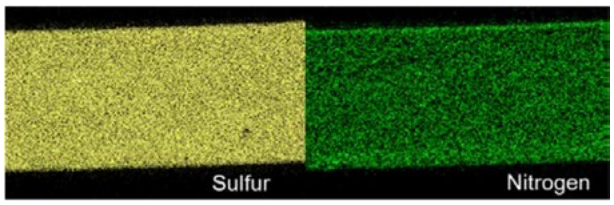

Figure 2. *Cross-sectional analysis of ETFE-g-poly(VP) membrane (43 % GL) that was prepared using ETFE film irradiated with 5 kGy. EDX elemental mappings of sulfur (associated with sulfonic acid) and nitrogen (associated with vinylpyridinium units).*

As can be seen from Figure 3, after the first functionalization step the vanadium permeability of membranes decreases whereas their ohmic resistance increases. The introduction of sulfonic acid groups results, as expected, in a reduced ohmic resistance of membranes and slight increase of their vanadium permeability. In general, functionalization of VP grafted membranes allows considerable improvement of their properties. After complete functionalization, VP grafted membranes exhibit not only lower ohmic resistance but also significantly reduced permeability of vanadium ions. Functionalized membranes have low permeability of VO^{2+} ions and ohmic resistance comparable to that of Nafion 117.

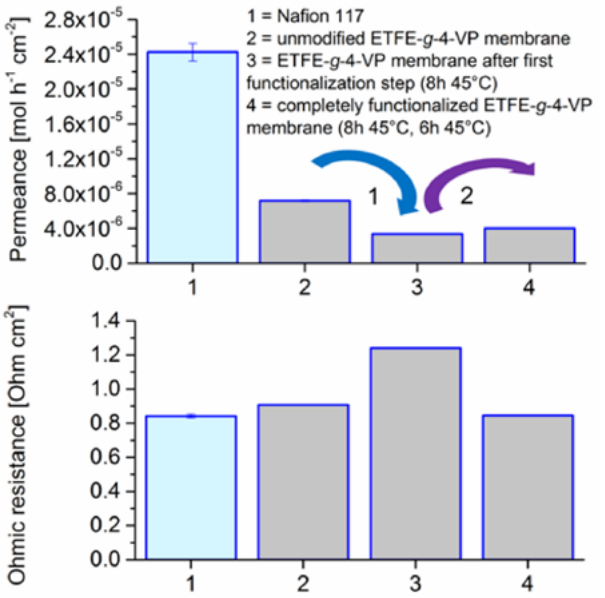

Figure 3. *Key device-relevant properties of membranes (43 ± 2 % GL): permeability of vanadium ions measured ex situ in a diffusion cell and ohmic resistance determined in the device (charged state). Reaction conditions for functionalization were: 1st step => 8 h, 45 °C and 2nd step => 6 h, 45 °C.*

Conclusion

We designed amphoteric ion-conducting membranes for VRB applications by combination of positively charged vinylpyridinium units with protogenic sulfonic acid groups.

The success of the grafting reaction and subsequent functionalization of ETFE-*g*-poly(VP) films was confirmed using IR and EDX spectroscopy. The use of films irradiated with 5 kGy allowed the synthesis of membranes with lower graft levels (GL < 50 %) and homogenous distribution of grafts in the cross-section. Moreover, it was demonstrated that the properties of unmodified ETFE-*g*-poly(VP) films can be tuned by means of functionalization. For instance, in this report we showed membrane functionalization that resulted not only in significantly reduced vanadium permeability of final membranes but also in lower ohmic resistance.

Acknowledgement

Funding by the Swiss National Science Foundation (Sinergia, project REPCOOL) is gratefully acknowledged.

References

[1] T. Shigematsu, *SEI Technical Review* **73**, 4–13 (2011).
[2] X. Li, H. Zhang, Z. Mai, H. Zhang, I. Vankelecom, *Energy Environ. Sci.* **4**, 1147 (2011).
[3] H. Prifti, A. Parasuraman, S. Winardi, T.M. Lim, M. Skyllas-Kazacos, *Membranes* **2**, 275–306 (2012).

Characterization of imbalance effects in vanadium redox flow batteries

F.J. Oldenburg, T.J. Schmidt, L. Gubler
phone: +41 56 310 2920, e-mail: fabio.oldenburg@psi.ch

Redox flow batteries (RFB) receive more and more interest for grid connected and off-grid energy storage applications as they provide independent power and capacity scalability, high storage efficiencies, a low response time and a low environmental impact due to low risk and recyclable electrolytes. To benefit from these advantages, high performance and lifetime of the RFB is required at the same time. This can be achieved by minimizing ohmic, transfer and concentration overpotentials on one side and degradation processes on the other side. Especially the second point is rarely found in the literature since capacity fading due to degradation and electrolyte imbalance effects is a complex problem with many possible origins.

To understand the origin of imbalance effects, analysis of the anolyte and catholyte composition during cell operation is necessary. So far this was approached mainly via semi-theoretical models [1] and via UV/Vis-spectroscopy [2]. The latter method suffers from the complex dimerization behavior of vanadyl ions, as well as the need for low concentration solutions. Park et al. determined average valence states via potentiometric titration and suggested to compensate imbalance effects by asymmetric catholyte/anolyte volumes [3]. Herein, we report a detailed study of electrolyte imbalance effects for two commonly used commercial membranes, i.e. Nafion® NR212 and N117 (DuPont), to gain detailed information on the membrane's influence on capacity fading.

Materials and Methods

Permeance of V(IV) was measured ex situ with in-house made diffusion cells, containing 1 M $VOSO_4$ (Alfar Aesar) on one, and 1 M $MgSO_4$ (Alfa Aesar) on the other side, both in 2 M H_2SO_4. The vanadium diffusion across the membrane was determined with UV/vis-spectroscopy using the absorption of vanadyl ions (VO^{2+}) at 766 nm.

For all cell level experiments, the RFB test system Model 857 from Scribner was used. The electrolyte was self-made from a 1 M $VOSO_4$ (Alfar Aesar) solution in 2 M H_2SO_4 at a flow rate of 40 mL/min and an active cell area of 25 cm^2. At each half cell, a SGL Sigracell® GFD4.6EA carbon felt electrode was used with 20 % compression. The electrode material was heat treated in air at 400 °C for 30 h. The redox flow battery was charged and discharged at 40 mA/cm^2 with a lower and upper potential limit of 0.8 and 1.7 V, respectively.

Results and Discussion

To quantify the contribution of different parameters to capacity fading, 90 cycles of a battery assembled with a Nafion® NR212 membrane were recorded and the total capacity fading of 5'000 As (55 % loss with respect to initial capacity) was nearly completely restored by renewing one after the other the tubings, electrolyte, electrodes and the membrane. Interestingly, the overall capacity loss was dominated by imbalance effects between the anolyte and catholyte (Figure 1). These imbalance effects can result from water evaporation, precipitation of vanadium and cross-contamination effects due to insufficient membrane selectivity.

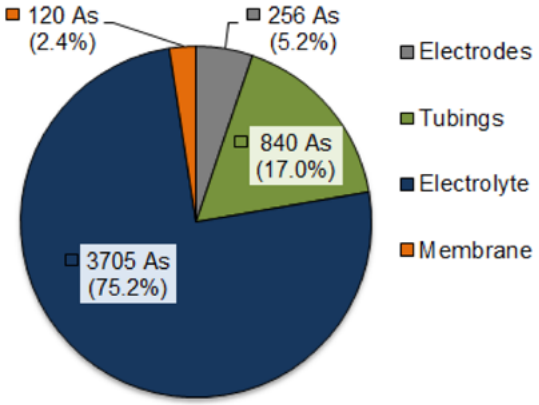

Figure 1. *Contributions to capacity fading for a cell with Nafion® NR212 membrane after 90 cycles at 40 mA/cm².*

To explain this capacity loss on the basis of electrolyte imbalance, the vanadium permeance through the membrane needs to be considered. Figure 2 shows the diffusion of VO^{2+} through a membrane with an area of 3.14 cm^2 in a self-made diffusion cell.

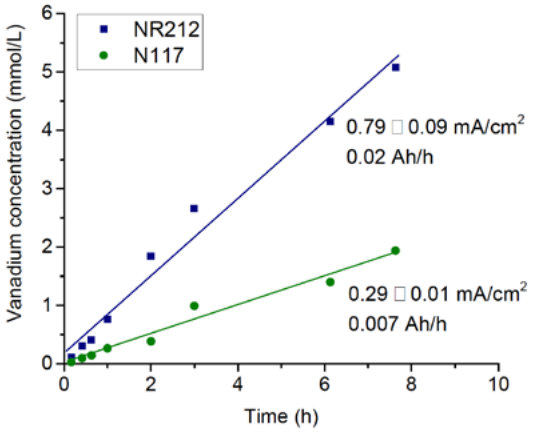

Figure 2. *Ex-situ diffusion of vanadyl ions across Nafion® NR212 and Nafion® N117.*

Permeance $J_{V(IV)}$ values are calculated according to

$$J_{V(IV)} = mF\frac{V}{A}\left[\frac{mA}{cm^2}\right]$$

where *m* is diffusion rate (mol/L·h), *F* the Faraday constant (26.8 Ah/mol), *V* the cell volume and *A* the membrane surface. With the permeance for NR212 and N117 measured *ex situ*, capacity fadings of 0.02 Ah/h and 0.007 Ah/h, respectively, are calculated. When comparing *ex situ* and cell level experiments, it is important to not confuse the parameters given per cycle and per unit of time, since the cycle duration varies between different set-ups and all transport processes are time-dependent. The 80-cycle experiment shown in Figure 1 took

299 h, therefore, *ex situ* diffusion experiments would predict a capacity fading of 21'500 As, which can hardly be correlated with the observed decay. To design vanadium RFBs with low capacity fading, it is important to identify imbalance effects in the cell in order to improve the selectivity of the membrane or to develop mitigation strategies to influence ionic transport processes systematically (asymmetric concentrations, flowrate or charge-discharge current densities). Hence, ion concentrations of all vanadium ions were determined intermittently using potentiometric titration, which is, to the best of our knowledge, a new approach for the experimental detection of all vanadium valence states in one sample. To evaluate the membranes influence on electrolyte imbalance effects, Nafion® N117 and Nafion® NR212 were assembled in identical cells and operated for more than 80 charge-discharge cycles. The thickness of the two membranes are 170 µm and 50 µm in the dry state.

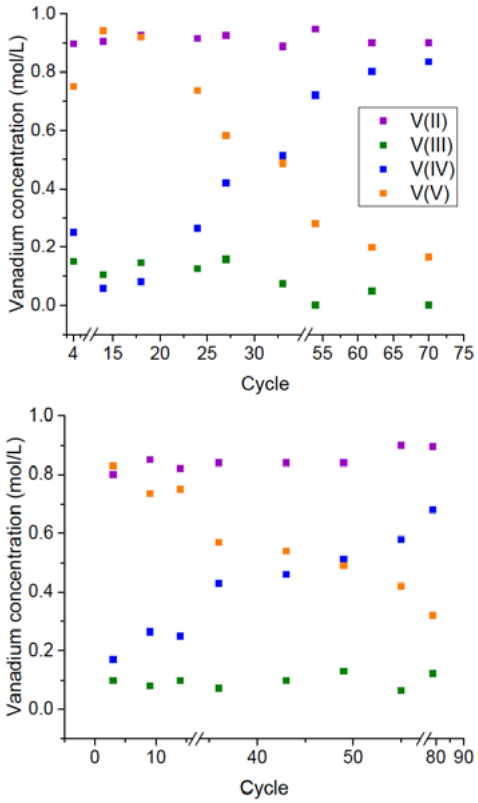

Figure 3. *V(II), V(III), V(IV) and V(V) concentrations determined by potentiometric titration with $KMnO_4$ in extended cycling experiments for Nafion® NR212 (top) and N117 (bottom).*

In accordance with the literature a net vanadium flux from the negative to the positive side is observed, which is expressed by the volume increase on the catholyte and decrease on the anolyte side [2, 3]. Accordingly, the anolyte side limits the cell capacity but, in disagreement with the calculation of Luo et al., V(II) does not accumulate in the anolyte. Prior determinations are based on UV/Vis-measurements of V(IV)-concentrations and the constant valence assumption, which is erroneous, owing to concentration dependent V(IV)/V(V) dimerization reactions and asymmetric transport across the membrane [4]. The increase of V(IV)-concentration in Figure 3 results from the sum of all vanadium transport phenomena (diffusion, migration, convection), which is net directed towards the positive side and induces self-discharge. Hence, the accumulation rate of V(IV) is a result of the permeability of all vanadium species as well as test related contributions of flow rate and electric field for a specific separator with a certain selectivity. For NR212 and N117 rates of V(IV) accumulation in the cell are 2.35 mmol/(h·L) and 1.86 mmol/(h·L), respectively. Both values can be obtained from the linear fit function of the V(IV) concentration (Figure 3). Considering an active area of 25 cm^2 and an electrolyte volume of 60 mL for each side, the measured capacity fading is given in Table 1.

Membrane	Nafion NR212	Nafion N117
Permeance	0.15 mA/cm^2	0.12 mA/cm^2
Capacity fading	3.79 mAh/h	2.99 mAh/h

Table 1. *Permeance and capacity fading caused by in situ vanadium ion transport*

With 3.32 h/cycle (NR212) and 3.65 h/cycle (N117) on average, the capacity loss calculated according to the given capacity loss of the cell for NR212 after 90 cycles is 4`080 As, which is in good agreement with Figure 1. The deviation of 9 % could result from the capacity loss which already appears after the first cycle.

Assuming the same capacity loss of electrodes and tubings, with N117 membrane an electrolyte based capacity loss of 3`330 As (73.2 %) is observed after 80 cycles. According to the permeance for N117 measured in the cell, the calculated loss is 3`143 As and also in good agreement with the observed value (6 % deviation).

Conclusion

Membrane selectivity is a key parameter for improving the performance stability of RFBs. Insufficient selectivity causes electrolyte imbalance effects, which are expressed as capacity fading and loss of practical energy density of the battery. At the same time the system cost increases. So far selectivity was measured by *ex situ* diffusion experiments, often only involving vanadyl ions (VO^{2+}) without considering the effect of an electric field. This only yields the V(IV) diffusion coefficient and correlation to cell tests can hardly be done. To obtain performance stability, membranes need to be synthesized facing the complex problem of electrolyte imbalance. Here, a new parameter is introduced comprising the sum of electro-osmotic, convective and diffusive transport phenomena of all vanadium ions. The vanadyl permeance in the cell was measured using potentiometric titration and could be correlated to the overall electrolyte based capacity fading for Nafion® NR212 and N117 membranes.

In further work, new separator materials should be prepared and characterized using this set-up to obtain more detailed information on the material influence on transport processes. Furthermore, influences of electric field and flow rate need to be quantified.

References

[1] D. You, H. Zhang, C. Sun, X. Ma, *J. Power Sources* **196**, 1578–1585 (2011).
[2] Q. Luo, L. Li, W. Wang, Z. Nie, X. Wei, B. Li, B. Chen, *ChemSusChem* **6**, 268–274 (2013).
[3] J.H. Park, J.J. Park, O.O. Park, J.H. Yang, *ChemSusChem* **9**, 3181–3187 (2016).
[4] C. Petchsingh, N. Quill, J.T. Joyce, N. Deirdre, D. Oboroceanu, C. Lenihan, X. Gao, R.P. Lynch, D.N. Buckley, *J. Electrochem. Soc.* **163**, 5068–5083 (2016).

SCIENTIFIC ACHIEVEMENTS 2016

Electrocatalysis & Interfaces

Unravelling the influence of crystallinity, particle size, and microstructure on the oxygen evolution activity of IrO_2

D. Abbott, D. Lebedev[1], K. Waltar[2], M. Povia[1], M. Nachtegaal, E. Fabbri, C. Copéret[1], T.J. Schmidt
phone: +41 56 310 4323, e-mail: daniel.abbott@psi.ch

A current challenge faced in water electrolysis is the development of structure–activity relationships for understanding and improving IrO_x-based catalysts for the oxygen evolution reaction (OER). We report a simple and scalable modified Adams fusion method for preparing highly OER active, chlorine-free iridium oxide nanoparticles of various size and shape [1]. The applied approach allows for the effects of particle size, morphology, and the nature of the surface species on the OER activity of IrO_2 to be investigated.

Experimental

Iridium oxide materials were synthesized via modified chlorine-free Adams fusion method. Briefly, $Ir(acac)_3$ and $NaNO_3$ were homogenized by grinding in a mortar. The obtained powder was heated in a furnace at different temperatures and times: 350 °C / 30 min or 500 °C / 1 h to produce the samples IrO_2–150 and IrO_2–30, respectively. The sample IrO_2–30 was additionally calcined at 600 °C in air for 1 h. The samples are named according to their approximate BET surface area, e.g. IrO_2–150 ≈ 150 $m^2 g_{ox}^{-1}$.

Particle surface area and morphology are first evaluated using BET N_2 adsorption/desorption and HRTEM, respectively. The electrochemical activity was then measured in a standard 3-electrode cell using the rotating disk electrode (RDE) methodology. Chronoamperometric measurements are used to record the steady-state polarization of each catalyst within the range of 1.0 to 1.6 V vs. RHE in 0.1 M $HClO_4$. The current was recorded after allowing two minutes for stabilization.

X-ray photoelectron spectroscopy (XPS) measurements were performed on the dry catalyst samples using an Al Kα monochromatic source (15 kV/150 W, 500 µm beam diameter) and a magnetic lens system. The binding energies of the acquired spectra were referenced to the C 1s line at 284.6 eV.

X-ray absorption spectra (Ir-L_{III} edge) were measured in transmission mode at the SuperXAS beamline at the Swiss Light Source (SLS). The beamline energy was calibrated with Pt reference foil to the Pt L_{III}-edge position at 11564 eV. The extended X-ray absorption fine structure (EXAFS) data were converted to the photoelectron wave vector *k* by assigning the photoelectron energy origin, E_0, corresponding to $k = 0$, to the first inflection point. The resulting $\chi(k)$ functions were weighted with k^2 to compensate for the dampening of the XAFS amplitude with increasing *k*. These $\chi(k)$ functions were Fourier transformed over 3–14 $Å^{-1}$ for sample IrO_2–30 and 3–10 $Å^{-1}$ for IrO_2–150. The theoretical model used for the EXAFS fitting was generated from the rutile-type IrO_2 structure.

Results

Chlorine-free iridium oxide electrocatalysts were prepared by a modified Adams Fusion method. Varying the synthesis conditions allowed for control over the particle size and morphology, which range from small, spherical particles (d = 1.7 nm) with high surface area (IrO_2–150; 150 $m^2 g^{-1}$) to larger, rod-shaped particles with well-defined crystal facets (IrO_2–30; 30 $m^2 g^{-1}$).

The electrochemical activities of the IrO_2 materials were evaluated in 0.1 M $HClO_4$. Figure 1 shows the mass-based OER activity (current density) measured at 1.525 V along with the integrated surface charge (extracted from cyclic voltammograms measured between 1.0 and 1.4 V_{RHE}), which can be considered as a relative measure of the electrochemically active surface area (ECSA). We observe that IrO_2–150 displays nearly a 10-fold increase in the measured activity versus IrO_2–30 despite having a BET surface area that is only 5 times higher. Furthermore, the measured surface charge (i.e. ECSA) of IrO_2–150 is only about 3.5-fold higher than IrO_2–30. The result is that the OER activity of IrO_2–150 is much higher than IrO_2–30 given the difference in surface area (both BET and ECSA-based). Although some of the discrepancies between the surface area and measured activity could be accounted for by differences in the exposed crystal facets or mesoporous features of the material [1], the large difference ultimately indicates that the distinct nature of the catalyst surface likely plays an important role in the OER activity.

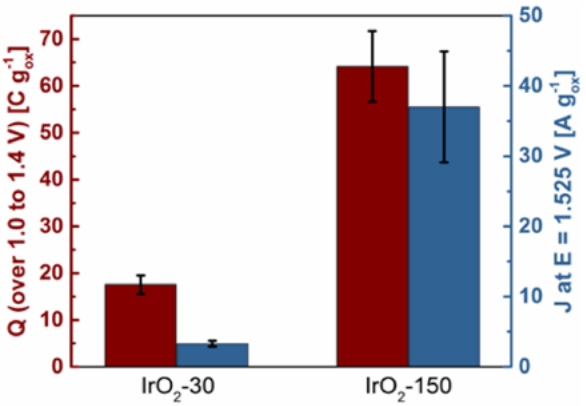

Figure 1. *Electrochemical activity of IrO_2–30 and IrO_2–150.*

In order to investigate the nature of the catalyst surface, X-ray photoelectron spectroscopy (XPS) was used to identify the surface oxygen functionalities. The resulting XPS spectra for the O1s level are shown in Figure 2. We observe two main peaks at a binding energy of ca. 530 eV and at 531 eV, which correspond to the binding of oxo and hydroxo species, respectively. We observe that IrO_2–150 displays a significantly higher signal for the binding of surface hydroxo species, indicating that the IrO_2–150 particle surface contains a much higher fraction of surface hydroxide species which may be important in catalyzing the OER.

The nature of the surface was further probed using operando X-ray absorption spectroscopy (XAS). Details on the *in situ* electrochemical cell can be found in reference [2]. Changes in the oxidation state and catalyst structure were monitored as a function of potential (2 min potential steps from 1.0 to

[1] Department of Chemistry and Applied Biosciences, ETHZ
[2] Surface Physics, Department of Physics, University of Zürich

1.5 V_{RHE}) while recording the XAS signal continuously during the last minute of each potential hold. Figure 3 a presents the 2nd derivative of the normalized X-ray absorption near edge structure (XANES) spectra of the iridium oxide catalysts. Given that the Ir-L_{III} absorption edge is highly sensitive to changes in the oxidation state, from Figure 3 a we can infer that IrO_2–150 shifts to a higher oxidation state upon anodic polarization and is then returned to the initial oxidation state when polarized cathodically at 1.00 V_{RHE}. This shift, however, is not observed for IrO_2–30. Since XAS is typically a bulk technique, however, this could be due to a lack of surface sensitivity that results from the larger size of the particles. The fact that IrO_2–30 is more representative of a bulk iridium oxide (i.e. Ir is in a 4+ oxidation state) then suggests that IrO_2–150 transitions from a mixed $Ir^{3+/4+}$ state to a state more heavily populated by Ir^{4+} upon anodic polarization. This is indicative of a transition from a hydroxo covered surface to an oxo covered surface and further supports the XPS results suggesting the initial presence of a hydroxo surface layer on the IrO_2–150 material.

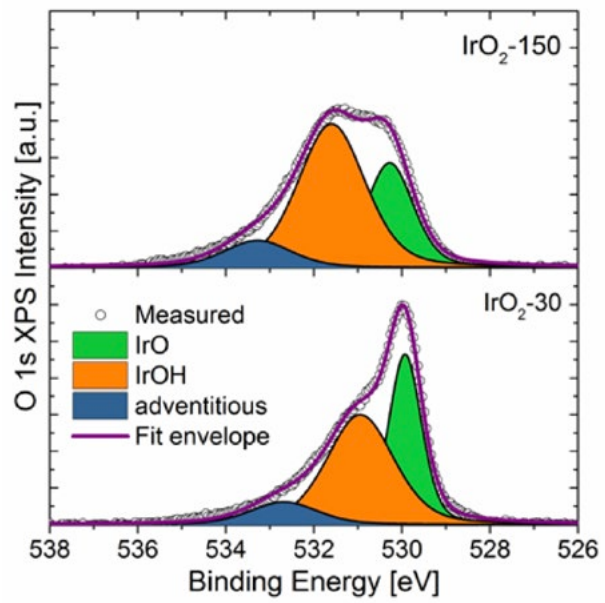

Figure 2. *O1s XPS spectra of IrO_2–30 and IrO_2–150.*

Complementary information can be further extracted from the Fourier transformed extended X-ray absorption fine structure (EXAFS) spectra by fitting the peak at ca. 1–2 Å, which corresponds to the 6 nearest neighbouring oxygen atoms forming the distorted octahedron, to a rutile structural model (Figure 3 b). The EXAFS-determined Ir–O bonding distance is then plotted in Figure 3 c as a function of the applied electrode potential. We observe that as the potential is increased, the Ir–O bonding distance in IrO_2–150 contracts from approxi-mately 2.02 Å, which is close to the expected bonding distance for Ir^{3+}–O (i.e. Ir–OH), to a bonding distance more representative of the Ir^{4+}–O bond in a bulk iridium oxide (1.98 Å) [3]. This shortening in the Ir–O bonding distance within the octahedron can therefore be interpreted as a transition of the IrO_2–150 from a lower oxidation state, i.e. a mixed $Ir^{3+/4+}$ state, to a structure more heavily populated by Ir^{4+}, adding further support to the XANES data. There is no detectable development in the structure of IrO_2–30 with the applied potential, however. This is also consistent with the observed XANES signal, which again may be due to the larger size of the IrO_2–30 particles.

In conclusion, we show that IrO_2–150 and IrO_2–30 display large differences in the OER activity that cannot simply be accounted for by differences in the measured surface area. Although XAS analysis provided little information regarding the nature of IrO_2–30 surface due to the larger size of the particles, valuable insight was gained regarding the surface of IrO_2–150. Combined with XPS, the results suggest that small IrO_2 nanoparticles with an initial hydroxide surface layer are particularly efficient OER catalysts.

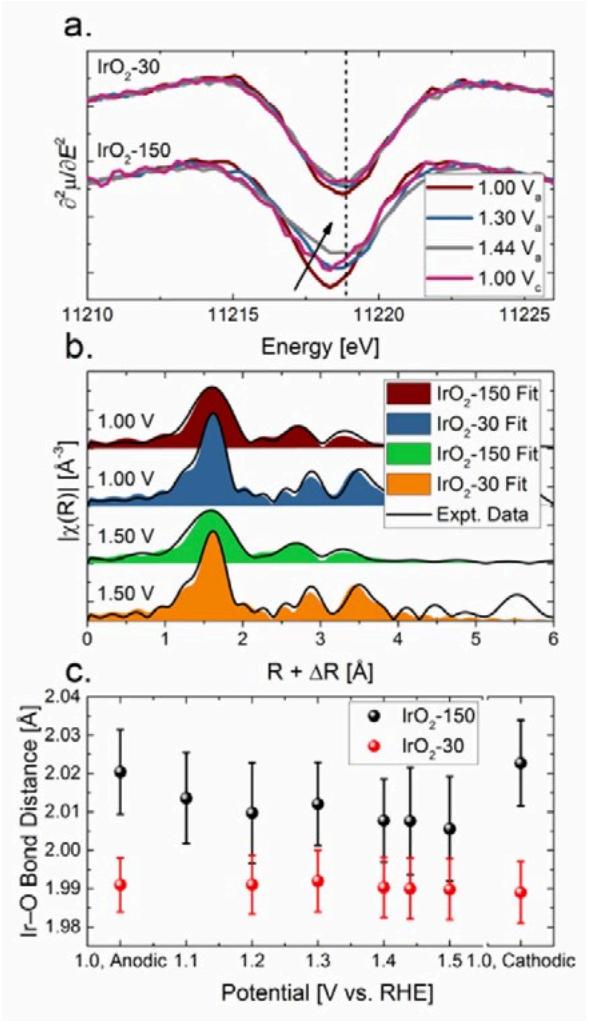

Figure 3. *a) 2nd derivative of normalized XANES spectra for IrO_2–150 and IrO_2–30 recorded at different electrode potentials; b) Typical example of FT-EXAFS fitting; c) EXAFS-determined Ir–O bond distance shown over the range of applied potentials.*

Acknowledgement

The authors would like to acknowledge and thank the Competence Center Energy & Mobility (CCEM-CH, Project Renerg²), the Commission for Technology & Innovation Switzerland (CTI) and the Swiss Competence Center for Energy Research (SCCER) Heat & Electricity Storage for their financial support.

References

[1] D.F. Abbott, D. Lebedev, K. Waltar, M. Povia, M. Nachtegaal, E. Fabbri, C. Copéret, T.J. Schmidt, *Chem. Mater.* **28**, 6591–6604 (2016).

[2] T. Binninger, E. Fabbri, A. Pătru, M. Garganourakis, J. Han, D.F. Abbott, O. Sereda, R. Kötz, A. Menzel, M. Nachtegaal, T.J. Schmidt, *J. Electrochem. Soc.* **163**, H906–H912 (2016).

[3] T. Pauporté, D. Aberdam, J.L. Hazemann, R. Faure, R. Durand, *J. Electroanal. Chem* **465**, 88–95 (1999).

Perovskite catalysts for the electrochemical splitting of water

E. Fabbri, F. Bozza, X. Cheng, B.-J. Kim, T.J. Schmidt
phone: +41 56 310 2795, e-mail: emiliana.fabbri@psi.ch

Water electrolyzers are electrochemical energy conversion devices that can produce hydrogen and oxygen from intermittent energy sources. Stored hydrogen and oxygen can be consequently reconverted to electricity by a fuel cell, representing overall an electricity storage system alternative to batteries. One of the main challenges towards electrolyzer widespread commercialization is the development of oxygen electrodes showing a high catalytic activity towards the oxygen evolution reaction (OER) and good stability under operative condition. While only few materials, mostly noble metals, present adequate chemical stability in contact with an acidic electrolyte, several transition metals possess good chemical stability in alkaline environment. [1]

Perovskite oxides have recently shown outstanding activities for the OER in alkaline environment. Particularly, composite electrodes made of perovskites and carbon have shown the most promising OER performance compared to electrodes made of only perovskite powder. We have previously shown by using X-ray absorption near edge structure spectroscopy (XANES) that changes in the perovskite local electronic induced by processing the perovskite with carbon black can boost the OER activity. [2] Particularly, it was found that carbon acts as reducing agent for $Ba_{0.5}Sr_{0.5}Co_{0.8}Fe_{0.2}O_{3-\delta}$ (BSCF) perovskite, reducing Co cations from 3^+ to 2^+ valence state, hence creating oxygen vacancies. [2] This finding provided a novel understanding of perovskite/carbon composite electrodes, addressing new perspectives for tailoring more active perovskite-based OER catalysts. The main drawbacks of the developed BSCF/carbon composite electrodes are

(i) carbon corrosion at the typical OER potentials and
(ii) the low surface area of BSCF perovskite synthesized by sol gel method.

In this study, BSCF synthesized by flame spray method shows a reduced Co oxidation state without the necessity to form a composite electrode with carbon and high surface area. BSCF produced by flame spray method displays outstanding performance proving that perovskite catalysts with tailored electronic structure and microstructure are truly viable oxygen electrodes for alkaline electrolyzers.

Experimental

BSCF was synthesized by flame spray method using the apparatus described in ref. [3] and preparing a precursor solution made of stoichiometric amounts $BaCO_3$ (99.0 %, Sigma Aldrich), $Sr(NO_3)_2$ (98 %, Sigma Aldrich), $Co(NO_3)_2 \cdot 6H_2O$ (99.9 %, Auer Remy) and $Fe(NO_3)_3 \cdot 9H_2O$ (98 %, Sigma Aldrich) in a solution of deionized water and acetic acid (99.0 %, Fluka). The combustion gas for the synthesis consists in a mixed gas flow of acetylene (99.6 %) and oxygen (99.5 %) from Carbagas, Switzerland. BSCF was also synthesized by the sol-gel method, using the same precursors mentioned above. The full synthesis procedure is described in ref. [2]. IrO_2-TiO_2 benchmark catalyst was provided by Umicore AG & Co KG. [4] The electrochemical protocol for the OER activity evaluation is fully described in reference [2]. XANES measurements at the Co K-edge have been performed at the SuperXas beamline at the Paul Scherrer Institut. [2]

Results

The OER activity of BSCF synthesized by flame spray and sol-gel method has been evaluated by chronoamperometric measurements in 0.1 M KOH and the obtained Tafel plots are reported in Figure 1. Compared to the same nominal composition synthesized by sol-gel, BSCF made by flame spray shows an improvement in mass current density of about 55 times despite the increase in surface area is only a factor of ~ 6 (from 4 m^2g^{-1} for the sol-gel sample to 25 m^2g^{-1} for the flame spray sample). This can be rationalized by XANES measurements at the Co K-edge (inset Figure 1), which show that, compared to the sol-gel sample, BSCF prepared by flame spray presents Co cations in a reduced oxidation state. It has been previously demonstrated that this particular electronic configuration for the BSCF perovskite boosts the OER activity. [2] Furthermore, BSCF prepared by flame spray method shows higher mass activity compared to IrO_2-TiO_2 (Figure 1), a commercial state-of-the-art OER catalyst with comparable surface area. [4]

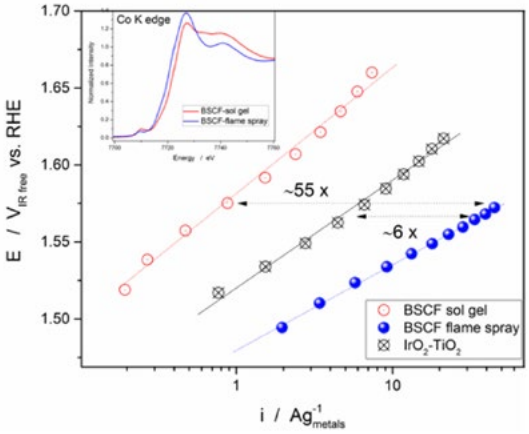

Figure 1. *Tafel plots for BSCF made by sol-gel and flame spray method and for IrO_2-TiO_2 in 0.1 M KOH. In the inset: XANES spectra at Co K-edge for BSCF prepared by sol-gel and flame spray method.*

Acknowledgement

The authors gratefully acknowledge the Ambizione Program of the Swiss National Science Foundation for financial contributions and Thomas Graule for the access to the flame spray apparatus.

References

[1] E. Fabbri, A. Habereder, K. Waltar, R. Kötz, T.J. Schmidt, *Catal. Sci. Technol.* **4**, 3800–3821 (2014).
[2] E. Fabbri, M. Nachtegaal, X. Cheng, T.J. Schmidt, *Adv. Energy Mater.* **5**, (2015).
[3] A. Heel, P. Holtappels, P. Hug, T. Graule, *Fuel Cells* **10**, 419–432 (2010).
[4] T. Binninger, E. Fabbri, A. Pătru, M. Garganourakis, J. Han, D.F. Abbott, O. Sereda, R. Kötz, A. Menzel, M. Nachtegaal, T.J. Schmidt, *J. Electrochem. Soc.* **163**, H906–H912 (2016).

Effect of material processing on the electrocatalytic activity of $Ba_{0.5}Sr_{0.5}Co_{0.8}Fe_{0.2}O_3$ towards the oxygen evolution reaction

X. Cheng, E. Fabbri, B. Kim, M. Nachtegaal, T.J. Schmidt
phone: +41 56 310 5937, e-mail: xi.cheng@psi.ch

Perovskite oxides (ABO_3) have shown the potentials of being efficient oxygen-electrode catalysts in alkaline solutions [1]. Numerous studies have been performed to find descriptors which are able to identify the most active oxides among the many different families of perovskites [2–5]. Certainly, the descriptor-based analysis could provide a promising approach to predict and identify the most active materials, but it is also important to consider that material processing might strongly modify the perovskite physico-chemical properties, leading to a different OER activity than the predicted one. Thus, in the present work, we carefully investigate the effect of material processing on the physico-chemical properties as well as the OER performance of BSCF perovskite. Our work demonstrates that there are at least two different methods to enhance the OER activity of BSCF:

(i) generating a surface layer with a short-range order and/or
(ii) modifying the BSCF electronic structure.

Further study shows that these two methods could be superimposed to furthermore improve the OER activity of BSCF. The processed BSCF delivers higher mass activity than benchmark commercial $IrTiO_2$ catalyst, ensuring the promising application of properly material process as preparing high OER active perovskite electrodes.

Experimental

$Ba_{0.5}Sr_{0.5}Co_{0.8}Fe_{0.2}O_3$ (BSCF) powders were synthesized using a modified sol-gel process. The detail of the synthesis is described in reference [6]. BSCF was mixed with functionalized acetylene black carbon (AB_f) in a 5 : 1 ratio in isopropanol and then ultrasonicating the suspension for 30 min. The BSCF/AB_f suspension was centrifuged at 1000 rpm for 1 min to remove the AB_f. The AB_f free BSCF/AB_f powder was then dried in air at 60 °C and noted as $(BSCF/AB_f)_{centrifuged}$. The $(BSCF/AB_f)_{centrifuged}$ powder was then ball milled in a stainless steel vial at 300 rpm under air atmosphere using a Fritsch Pulverisette 7 ball mill. The ball milling is switched on and off at intervals of 10 min to avoid overheating, the total ball milling process is 24 hours. The ball milled sample is noted as $(BSCF/AB_f)_{centrifuged\text{-}bm}$. X-ray diffraction (XRD), Brunauer-Emmett-Teller (BET) and the electrochemical protocol for the OER activity evaluation is fully described in reference [4]. The High-Resolution Transmission Electron Microscopy (HRTEM) was used to observe the morphology and surface structure. XANES measurements at the Co K-edge have been performed at the SuperXas beamline at the Paul Scherrer Institut. [4]

Results

The substantial removal of the carbon component from the BSCF/AB_f composite was confirmed by XRD analysis which did not show any signal related to an amorphous carbon phase in the XRD pattern of the $(BSCF/AB_f)_{centrifuged}$ powder (Figure 1a).

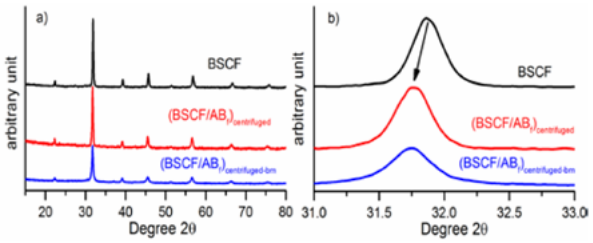

Figure 1. *a) XRD patterns for the BSCF, $(BSCF/AB_f)_{centrifuged}$ and $(BSCF/AB_f)_{centrifuged\text{-}bm}$ powders; b) (110) diffraction peak for the BSCF, $(BSCF/AB_f)_{centrifuged}$ and $(BSCF/AB_f)_{centrifuged\text{-}bm}$ powders.*

Figure 1 b shows a clear shift of the $(BSCF/AB_f)_{centrifuged}$ (110) diffraction peak towards lower angles compared to that of BSCF, corresponding to an increase of the lattice parameter from 3.97 to 4.01 Å, respectively. This increase can be ascribed to the reduction of the Co oxidation state in $(BSCF/AB_f)_{centrifuged}$ compared to that of BSCF. As discussed in our previous work, [7, 8] carbon can act as a reducing agent for the Co-sites within BSCF, with Co^{2+} having a larger ionic radius than Co^{3+} in the sixfold coordination. This point is confirmed with the XAS measurements (Figure 2). Concerning the ball milled sample, Figure 1 a shows that the ball milling procedure does not destroy the long-range order of BSCF. Nevertheless, the broadened diffraction peaks displayed by $(BSCF/AB_f)_{centrifuged\text{-}bm}$ powders indicate decreased crystallite sizes after ball milling. Figure 1 b shows that the $(BSCF/AB_f)_{centrifuged\text{-}bm}$ (110) diffraction peak retains the shift towards lower angles compared to that of BSCF. Figure 2 confirms the retaining of the reduction of the Co oxidation state in in $(BSCF/AB_f)_{centrifuged\text{-}bm}$ compared to that of BSCF.

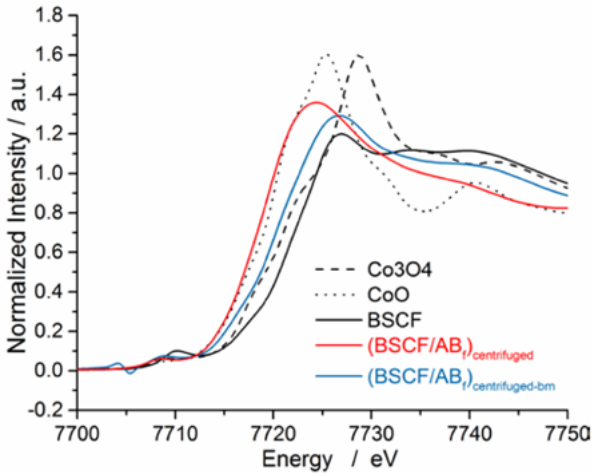

Figure 2. *XANES spectra at the Co K-edge for BSCF, $(BSCF/AB_f)_{centrifuged}$ and $(BSCF/AB_f)_{centrifuged\text{-}bm}$ at room temperature and compared with the XANES spectra at the Co K-edge for CoO and Co_3O_4 commercial metal oxide (Aldrich).*

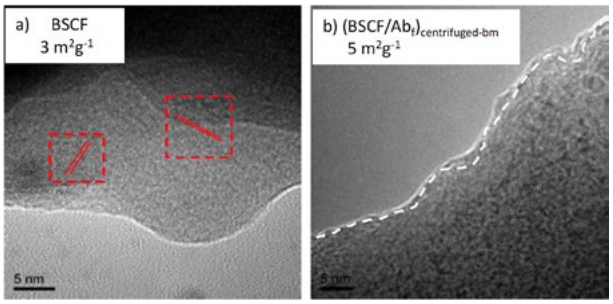

Figure 3. *BET surface area and high-resolution transmission electron microscopy (HRTEM) of (a) BSCF powders and (b) (BSCF/AB$_f$)$_{centrifuged\text{-}bm}$ powders. The red line serves as guide for the eyes for the atom column in crystalline BSCF sample, while the white line identifies the amorphous region in the (BSCF/AB$_f$)$_{centrifuged\text{-}bm}$ sample.*

Ball milling leads to a breaking of BSCF particle agglomerates resulting in higher BET surface area of (BSCF/AB$_f$)$_{centrifuged\text{-}bm}$ powders (Figure 3, 5 m^2g^{-1} vs. 3 m^2g^{-1}). From Figure 3, we can also observe that an amorphous layer on the surface was formed after ball milling.

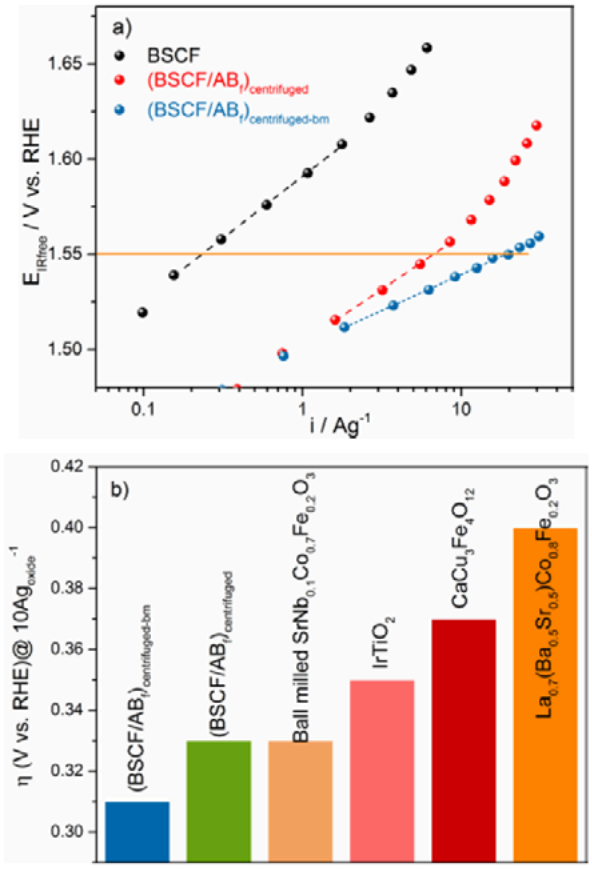

Figure 4. *a) OER Tafel slope obtained by chronoamperometry measurements for BSCF, (BSCF/AB$_f$)$_{centrifuged}$ and (BSCF/AB$_f$)$_{centrifuged\text{-}bm}$ electrode. b) iR-corrected overpotential (η) at 10 Ag_{oxide}^{-1} in 0.1 M KOH of this work is compared with noble metal catalyst such as IrTiO$_2$ (Umicore AG & Co. KG) and recently reported advanced perovskite catalysts with novel compositions (Ball milled $SrNb_{0.1}Co_{0.7}Fe_{0.2}O_3$, $IrTiO_2$, $CaCu_3Fe_4O_{12}$, $La_{0.7}(Ba_{0.5}Sr_{0.5})Co_{0.8}Fe_{0.2}O_3$).*

The OER measurement shows that the current density at 1.55 V vs. RHE of (BSCF/AB$_f$)$_{centrifuged}$ electrode is 30 times higher than that of BSCF electrode (Figure 4 a). As discussed in our previous report [7, 8] we proposed that the direct interaction between BSCF perovskite catalyst and AB$_f$ (Co oxidation state reduction) might account for the improved OER activity of composite electrodes compared to single perovskite catalysts. After ball milling, the current density at 1.55 V vs. RHE of (BSCF/AB$_f$)$_{centrifuged\text{-}bm}$ electrode is almost 3 times higher than that of (BSCF/AB$_f$)$_{centrifuged}$ electrode (Figure 4 a). Since the BET surface of (BSCF/AB$_f$)$_{centrifuged\text{-}bm}$ is only 1.7 times higher than that of BSCF. Thus, the significant improvement in the OER current cannot be fully explained by the particle agglomerate size reduction. We indeed deem that the OER activity improvement by the ball milling process is mostly due to the creation of a surface layer with a short-range order as shown in Figure 3. This result indicates that there are two different methods to enhance the OER activity of BSCF:

(i) generating a surface layer with a short-range order and
(ii) change the BSCF electronic structure.

Additionally, the Ohmic drop corrected overpotential (η) at 10 Ag_{oxide}^{-1} of (BSCF/AB$_f$)$_{centrifuged\text{-}bm}$ electrode is lower than those of recently reported advanced perovskite catalysts with novel compositions (Figure 4 b) and even lower than the OER benchmark noble metal catalyst IrTiO$_2$ (Umicore AG & Co. KG). [10] Therefore, the comprehension of the effect of physical/chemical treatments on the OER performance of perovskites and properly material processing ensure its promising application as preparing high OER active perovskite electrodes.

Acknowledgement

The authors gratefully acknowledge the Swiss National Science Foundation through its Ambizione Program, the Swiss Competence Center for Energy Research (SCCER) Heat & Electricity Storage and the Commission for Technology and Innovation (CTI) Switzerland as well as the Swiss National Science Foundation within NCCR Marvel and Paul Scherrer Institute for financial contributions to this work.

References

[1] E. Fabbri, A. Habereder, K. Waltar, R. Kötz, T.J. Schmidt, *Catal. Sci. Technol.* **4**, 3800–3821 (2014).
[2] J. Suntivich, K.J. May, H.A. Gasteiger, J.B. Goodenough, Y. Shao-Horn, *Science* **334**, 1383–1385 (2011).
[3] J.O. Bockris, T. Otagawa, *J. Electrochem. Soc.* **131**, 290–302 (1984).
[4] X. Cheng, E. Fabbri, M. Nachtegaal, I.E. Castelli, M. El Kazzi, R. Haumont, N. Marzari, T.J. Schmidt, *Chem. Mater.* **27**, 7662–7672 (2015).
[5] I.C. Man, H.Y. Su, F. Calle-Vallejo, H.A. Hansen, J.I. Martinez, N.G. Inoglu, J. Kitchin, T.F. Jaramillo, J.K. Norskov, J. Rossmeisl, *ChemCatChem* **3**, 1159–1165 (2011).
[6] E. Fabbri, R. Mohamed, P. Levecque, O. Conrad, R. Kötz, T.J. Schmidt, *ChemElectroChem* **1**, 338–342 (2014).
[7] E. Fabbri, X. Cheng, T.J. Schmidt, *ECS Transactions* **69**, 869–875 (2015).
[8] E. Fabbri, M. Nachtegaal, X. Cheng, T.J. Schmidt, *Adv. Energy Mater.* **5**, 17 (2015).

Study of thermodynamics, stability, and oxygen evolution activity of strontium ruthenium perovskite oxide – $SrRuO_3$

B. Kim, D.F. Abbott, X. Cheng, E. Fabbri, M. Nachtegaal, F. Bozza, I.E. Castelli[1], N. Marzari[1], T.J. Schmidt
phone: +41 56 310 4085, e-mail: joseph.kim@psi.ch

Extensive investigations in understanding the functional mechanisms of metal oxides behind oxygen evolution have been carried out since fuel cell technology has demonstrated promising possibilities as the alternative source of energy. In particular, perovskite oxides are reputable for outstanding activity towards oxygen evolution reaction (OER). We revisited the list of active perovskite oxides introduced by the first principle DFT calculations based on the theoretical oxygen binding energies of intermediates (O*, HO*, and HOO*) to the catalyst surface. Using these descriptors, $SrRuO_3$ (SRO) has been predicted as active perovskite to exhibit a particularly high OER activity. We report on the stability of this perovskite oxide prepared by a simple and scalable flame synthesis method. The material is evaluated for its electrochemical activity with a particular emphasis pointed towards chemical stability in both alkaline and acidic media. Through conjoining electrochemical methods, operando X-ray absorption spectroscopy (XAS) and theoretical calculations, we show that $SrRuO_3$ exhibits trivial activity towards OER that degrades promptly. On the basis of our findings, we prove the inadequacy of $SrRuO_3$ as OER catalysts, despite of the projection of their high oxygen evolution activities, owing to their unappealing stability in aqueous electrolyte solutions.

Experimental

The SRO was prepared through flame spray synthesis method using strontium nitrate and ruthenium nitrosyl-nitrate as precursors. [1] RuO_2 was prepared using one-pot Adams method using hydrated ruthenium chloride as the precursor. [2]

Phase analysis of the prepared material was performed using powder X-ray diffraction (XRD, Bruker D8 system in Bragg-Brentano geometry, CuKα radiation (λ = 0.15418 nm). Specific surface area was calculated by Brunauer-Emmett-Teller analysis of N_2 adsorption / desorption isotherms (AUROSORB-1, Quantachrome). Transmission electron microscopy (TEM) and energy dispersive X-ray spectroscopy (EDX) (TECNAI F30 operated at 300 kV) were used to study the surface morphology and composition of the prepared materials. For operando X-ray absorption near-edge structure (XANES) spectroscopy measurements, catalyst powders were dispersed in the mixture of isopropanol and Milli-Q water in the equal ratio sonicated for 60 min. The ink was then spray coated on Kapton film, which is fabricated into an operando XAS flow cell as described in our previous work [3]. XANES spectra at the Ru K-edge were recorded at the SuperXAS beamline of the Swiss Light Source (PSI, Villigen, Switzerland).

Electrochemical study was done using rotating disk electrode voltammetry. All the electrochemical measurements were performed at the standard room temperature using a reversible hydrogen electrode (RHE) and silver chloride electrode (Ag^+/AgCl) as the reference electrode in alkaline and acidic media, respectively.

Phase stabilities were studied by means of ab-initio quantum mechanics simulations in the framework of density-functional theory (DFT) using the Quantum ESPRESSO package [4] to fully relax the two perovskite structures as well as all the competing phases, as described in the Materials Project database [5].

Results

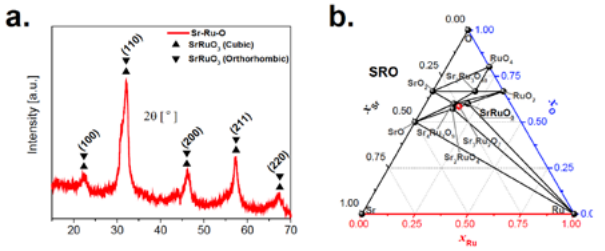

Figure 1. *X-ray diffraction analyses of (a) SRO (Miller indexes are given for the cubic structure [JCPDS PDF Card: 80-1529]), and (b) Sr, Ru, and O phases computed using DFT calculations. Black and red dots represent thermodynamically stable phases and unstable phases, respectively.*

The XRD pattern of SRO that is distinctively ascribable to its perovskite structure (Figure 1 a). The detection of SRO's perovskite phase (SRO-p) is thermodynamically validated based on its formation energy calculation (Figure 1 c).

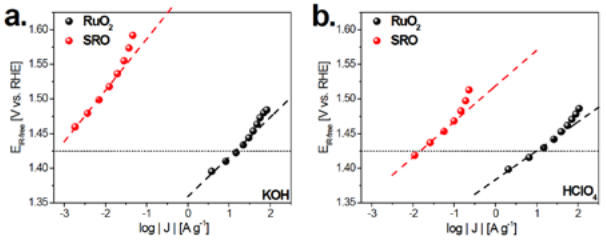

Figure 2. *Tafel plots for OER of SRO-p and RuO_2 calculated from the CA at increasing potentials (a) in KOH and (b) in $HClO_4$.*

SRO-p is compared against the state-of-the-art OER catalyst, RuO_2, in both alkaline and acidic electrolytes. Tafel plots of SRO-p in both electrolytes (Figure 2 a and b) reveal incomparably poorer activity than RuO_2, unlike its predicted high activity in the previous study [6]. The poor activities in both electrolytes suggest that SRO-p may be going under a different mechanism than speculated in the oxygen evolution potential domain regardless of the pH.

Operando XAS was carried out to examine changes in the oxidation state of the catalyst while conducting electrochemical study in a flow cell. Referring to Figure 3 a and b, SRO-p in both alkaline and acidic condition, respectively, shows severe

[1] EPFL : Theory and Simulation of Materials (THEOS), and National Centre for Computational Design and Discovery of Novel Materials (MARVEL)

decrease in absorption intensities during the anodic potential steps (~ 1.4 VRHE, Figure 3 c) from which precise estimation of its oxidation state was obstructed. The observed absorption intensity decrease suggests that the absorbing atom (i.e. Ru) is lost as the potential enters the oxygen evolution regime. This altogether indicates loss of material either through chemical dissolution and/or potential-induced dissolution.

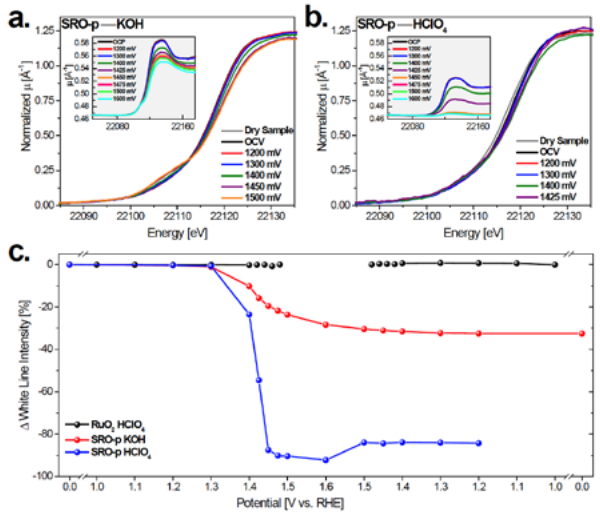

Figure 3. *Operando XAS results of the catalysts in flow cell. Normalized XANES spectra of SRO-p (a) in KOH, and (b) in $HClO_4$. The insets and (c) illustrate the loss in absorption edge-step intensity in the non-normalized XANES data.*

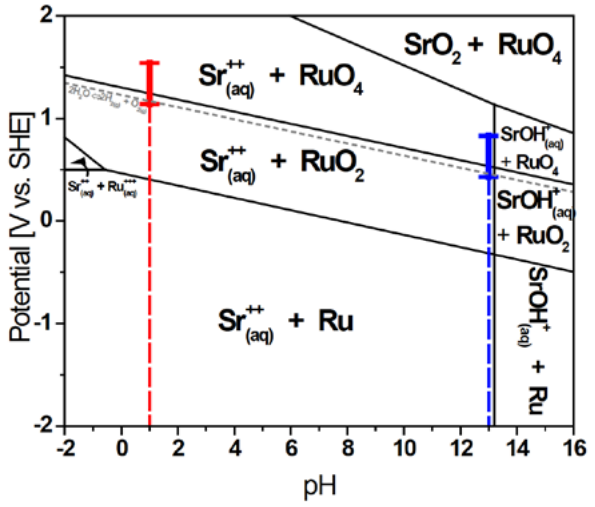

Figure 4. *Pourbaix diagram of SRO-p based on the DFT calculations. The vertical lines indicate the pH levels of the electrolytes that the materials were tested; and the marked show the potential range of the in situ flow cell testing.*

Interestingly, the potential (~ 1.4 V_{RHE}) at which the exponential drop in the absorption intensity was observed coincides with the RuO_4 dissolution potential.

This concurrent potential suggests that the material may be subjected to potential-induced dissolution.

In addition, the loss of SRO-p during the voltammetry in both electrolytes is discussed referring to the DFT calculated Pourbaix diagram (Figure 4). The Pourbaix diagram reveals that Sr cation would immediately dissolve out into the aqueous phase from its perovskite structure deteriorating its structural integrity. In addition to the operando XAS flow cell study, this result stresses that SRO-p is also subjected to chemical dissolution due to its thermodynamic instability in aqueous phase.

The above findings suggest that the activity of SRO-p is dependent on the thermodynamic nature under OER conditions, such that the dissolution of cation metals would play a key role. While Ru would be subjected to potential-induced dissolution at above 1.4 V_{RHE}, Sr would isolate from the perovskite structure into aqueous phase in both alkaline and acidic conditions disintegrating the perovskite oxide catalyst. Therefore, we can conclude that $SrRuO_3$ is an inadequate candidate for OER considering their thermodynamic instability under the operation condition. Therefore, it is critical to understand and address the origin of stability under a real operating condition in order to design an ideal oxygen activating catalyst.

Acknowledgement

The authors acknowledge SNSF through its Ambizione Program, CCEM (RENERG^2), Swiss Competence Center for Energy Research (SCCER) Heat & Electricity Storage, and SNSF-NCCR MARVEL, and Paul Scherrer Institute for financial contributions. The authors thank the Swiss Light Source for the beamtime at SuperXAS beamline. Addtionally, we thank Thomas Graule (Empa) and Christophe Copéret (ETHZ) for material syntheses.

References

[1] A. Heel, P. Holtappels, P. Hug, T. Graule, *Fuel Cells* **10** (3), 419–432 (2010).

[2] E. Oakton, D. Lebedev, A. Fedorov, F. Krumeich, J. Tittier, O. Sereda, T.J. Schmidt, C. Copéret, *New J. Chem.* **40** (2), 1834–1838 (2016).

[3] T. Binninger, E. Fabbri, A. Pătru, M. Garganourakis, J. Han, D.F. Abbott, O. Sereda, R. Kötz, A. Menzel, M. Nachtegaal, *J. Electrochem. Soc.* **163** (10), H906–H912 (2016).

[4] P. Giannozzi, S. Baroni, N. Bonini, M. Calandra, R. Car, C. Cavazzoni, D. Ceresoli, G.L. Chiarotti, M. Cococcioni, I. Dabo, A. Dal Corso, S. de Gironcoli, S. Fabris, G. Fratesi, R. Gebauer, U. Gerstmann, C. Gougoussis, A. Kokalj, M. Lazzeri, L. Martin-Samos, N. Marzari, F. Mauri, R. Mazzarello, S. Paolini, A. Pasquarello, L. Paulatto, C. Sbraccia, S. Scandolo, G. Sclauzero, A.P. Seitsonen, A. Smogunov, P. Umar, R.M. Wentzcovitch, *J. Phys. Condens. Matter.* **21** (39), (2009).

[5] A. Jain, S.P. Ong, G. Hautier, W. Chen, W.D. Richards, S. Dacek, S. Cholia, D. Gunter, D. Skinner, G. Ceder, K.A. Persson, *APL Mater.* **1** (1), 2013.

[6] I.C. Man, H.-Y. Su, F. Calle-Vallejo, H.A. Hansen, J.I. Martínez, N.G. Inoglu, J. Kitchin, T.F. Jaramillo, J.K. Nørskov, J. Rossmeisl, *ChemCatChem* **3** (7), 1159–1165 (2011).

Electrochemical cell configuration for CO_2 reduction in gas phase at low temperature

A. Pătru, T. Binninger, A.A. Permyakova, J. Herranz, T.J. Schmidt
phone: +41 56 310 2318, e-mail: alexandra.patru@psi.ch

The electrochemical production of chemical products like syngas, format, methane, ethylene, methanol or other transportation fuels starting from CO_2 reactant appears like a suitable technology to recycle and reduce this greenhouse gas. However a suitable process using only CO_2, water and renewable energy does not currently exist. Few models of co-electrolysis cells exist but they are limited by factors as energetic efficiency, reaction products selectivity and cost [1, 2]. So far only carbon monoxide and formate products appear to be economically interesting when produced by electrochemical CO_2 reduction compared to other well established chemical processes [3]. As the catalyst used for CO_2 reduction reaction (CO_2RR) is crucial for selectivity but also for the energetic efficiency of the whole process (i.e. kinetic overpotentials), a majority of the studies aim towards high-performance catalyst development [4, 5]. Product selectivity as a function of electrode material was established by Hori [6] and this is generally accepted by the scientific community. For example Au, Ag, Zn are widely known to be efficient for CO formation.

However, the overall efficiency of the process is not entirely dependent on the catalyst nature. Mass transport phenomena and pH conditions are equally crucial parameters for an optimal conversion process.

The present work is focused on the production of CO starting from CO_2 in the gas phase using typical membrane electrolyzer cells. Au electrodes were chosen for their selectivity against CO but also for their chemical stability in a broad pH range. Various cell configurations using solid polymer electrolyte are discussed.

Experimental

To produce CO with high selectivity the experiments were conducted in a membrane electrolyzer-like configuration setup. The cell consists of two metallic gold coated flow fields, two electrodes and different membranes. Au mesh (Goodfellow®) and Pt/C gas diffusion electrode were used as cathode and anode, respectively. The electrodes area was 0.5 cm^2. Various membranes were used as solid electrolyte: proton exchange membrane Nafion® XL 100 (30 µm thickness), anions exchange membrane Fumasep® AA (130 µm thickness) and bipolar membrane Fumasep® FBM (130 µm thickness). The anion exchange membrane was pretreated in 0.5 M $KHCO_3$ solution for 24 h before utilization.

For comparison a cell configuration containing a buffer layer between the cathode and the proton exchange membrane was tested [6]. The buffer layer was a Watman® paper impregnated in 0.5 M $KHCO_3$ solution in order to mimick a bipolar membrane architecture.

CO_2 was fed to the cathode side at 10 mL/min, whilst the anode side was fed with pure H_2 at 50 mL/min. Gas humidification was achieved by passing through a water-bubbling system; their temperature was set to yield 100 % humidification values. The cells were operated at 40 °C and ambient pressure.

Polarization curves were measured galvanostatically. For each data point, the cell current was stabilized for 5 minutes and the data were averaged from the last 3 minutes. The gas product from cathode was analyzed by mass spectroscopy (MS Prisma).

Results

Standard cell configurations – acidic vs alkaline system

When CO_2RR takes place at the gold cathode the principal electrochemical reactions are:

In alkaline environment (pH = 14)

$$CO_2 + H_2O + 2e^- \rightarrow CO + 2\,OH^- \qquad E = -0.932\ V/RHE \quad (1)$$
$$2\,H_2O + 2e^- \rightarrow H_2 + 2\,OH^- \qquad E = -0.828\ V/RHE \quad (2)$$

or in acidic environment (pH = 0)

$$CO_2 + 2H^+ + 2e^- \rightarrow CO + H_2O \qquad E = -0.104\ V/RHE \quad (3)$$
$$2\,H^+ + 2e^- \rightarrow H_2 \qquad E = 0.0\ V/RHE \quad (4)$$

Cation exchange membrane (CEM) and anionic exchange membrane (AEM) were used for CO_2 reduction from the gas phase. The polarization curves obtained under N_2 and CO_2 are shown in Figure 1. In the case of CEM configuration high current densities were obtained under CO_2 at low overpotential (–400 mA/cm^2 at –0.4V/RHE). Despite the good electrochemical performances achieved using a CEM cell configuration, H_2 was the majority reaction product obtained as shown by the MS results (Figure 2). In view of this result, it is likely that the acidity of the membrane shifts the cathode selectivity toward hydrogen evolution. Contrary, in the case of AEM configuration low current densities are obtained at high reaction overpotential. Moreover, an increase in membrane high frequency resistance (up to 15 Ωcm^2) and losses of membrane stability were observed. A product analysis was not possible under these conditions by MS.

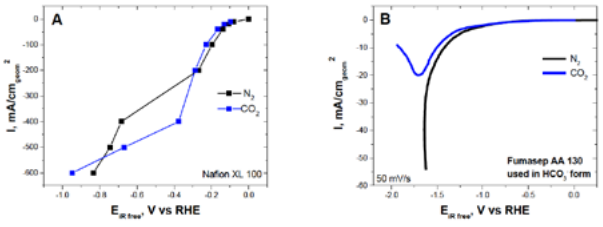

Figure 1. *Potential of the cathode obtained using CEM cell configuration (A) and AEM cell configuration (B). Cathode: Au mesh; flow 10 mL/min N_2/CO_2. Anode: Pt/C gas diffusion electrode; flow 50 mL/min H_2. T_{cell} 40°C, p ambient, full humidification.*

However, the use of AEM configuration can be interesting for CO_2 reduction from gas phase due to the pH increase, but membranes with improved stability, lower resistance and better affinities for carbonate and bicarbonate species must be found. Another possible limitation of this kind of system can

be the anode reaction when a complete co-electrolyser is used (i.e. oxygen evolution reaction at the anode side). In this case, HCO_3^-, CO_3^{2-} and OH^- are possible charge carriers and CO_2 can be produced at the anode side according to reactions 5 and 6. A considerable production of CO_2 at the anode side will obviously lead to an inefficiency of the system.

$$2\,HCO_3^- \rightarrow \tfrac{1}{2}\,O_2 + H_2O + 2\,e^- + 2\,CO_2 \quad E = -0.765\ V/RHE \quad (5)$$

$$CO_3^{2-} \rightarrow \tfrac{1}{2}\,O_2 + 2\,e^- + CO_2 \quad E = -0.692\ V/RHE \quad (6)$$

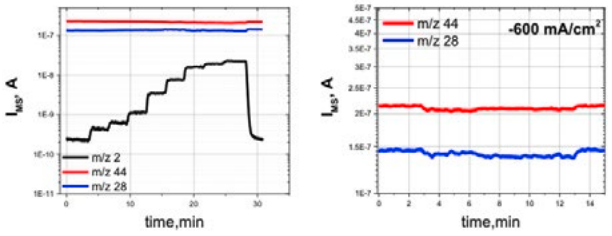

Figure 2. *Ion current recorded by MS for different mass fraction (m/z) showing the formation of H_2 (m/z = 2).*

Alternative cell configurations

A buffer-layer cell configuration was also used for CO_2 reduction in gas phase [6]. The polarization curves are shown in Figure 3 and the results are comparable with the available literature data [6]. With this cell configuration current densities > 200 mA/cm² were achieved with reasonable overpotentials. The consumption of CO_2 (m/z 44) was observed by MS (Figure 4). CO and H_2 were the only products obtained in this configuration using Au mesh electrodes. The CO selectivity calculated from the mass spectrometer signal and using Equation ① was ca. 35 % at –400 mA/cm².

$$selectivity = \frac{CO\ production\ rate}{CO\ production\ rate + H_2\ production\ rate} \quad ①$$

Currently, the buffer layer cell configuration is only a proof of concept, the cell stability being a major issue in this case. Therefore new stable layered cell configurations are needed.

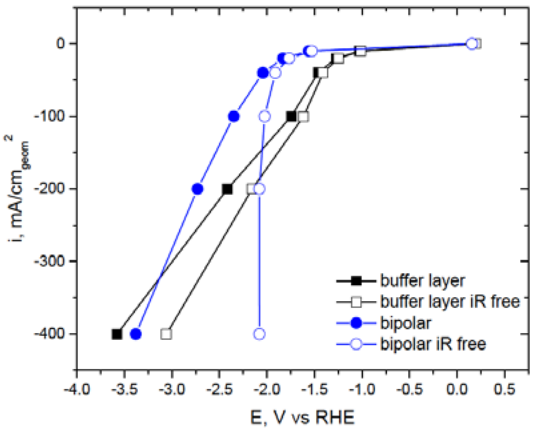

Figure 3. *Performances of alternative cell configurations: buffer-layer cell vs bipolar membrane cell. The raw data (full symbols) are compared with the iR corrected data (empty symbols). Same conditions for anode and cathode as in Figure 1.*

With this in mind, bipolar membranes were tested. The alkaline side was used at the cathode. The polarisation curves are compared against the buffer-layer cell configuration in Figure 3. Using this type of membrane high current densities were achieved, but with higher overpotentials (most probably due to the high membrane resistance, ca. 5 Ωcm²). The CO selectivity was 23 % at –400 mA/cm².

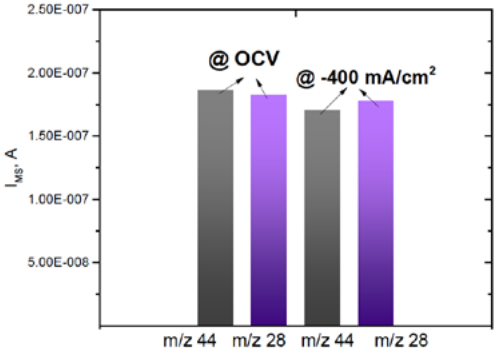

Figure 4. *Ion current recorded by MS for m/z 44 and m/z 28 recorded at open circuit voltage (OCV) and under cell operation at –400 mA/cm² proving the formation of CO.*

Conclusions

Various cell configurations for reduction of CO_2 in gas phase have been presented and their performances compared. For convenience, only Au mesh was used as cathode catalyst for CO_2 reduction to CO. A membrane electrolyzer-like configuration using CEM was shown to be unfavorable for CO_2 reduction, leading to H_2 evolution only. The same configuration using a commercially available AEM (Fumasep® AA 130) was not successful due to high membrane resistance and a loss of membrane stability. That said, we believe that this configuration can be improved by using different alkaline membranes.

Alternative cell configurations were also tested and it was proved that by using a bipolar membrane system (alkaline side used at the cathode) high current densities are achieved and the cathode selectivity to CO is enhanced. This first promising result shows the feasibility of using such a system for electrochemical CO_2 conversion from gas phase. However at this point the energetic efficiency is low and optimisation work must be carried out in order to reduce the high cathode overpotentials.

Acknowledgement

Financial support from the Swiss Competence Center for Energy Research (SCCER) is kindly acknowledged.

References

[1] D.T. Whipple, E.C. Finke, P.J.A. Kenis, *Electrochem. Solid-Sate Lett.* **13** (9), B109–B111 (2010).
[2] C. Delacourt, P.L. Ridgway, J.B. Kerr, J. Newman, *J. Electrochem. Soc.* **155** (1), B42–B49 (2008).
[3] J. Durst, A. Rudnev, A. Dutta, Y. Fu, J. Herranz, V.B.R. Kaliginedi, A. Kuzume, A.A. Permyakova, Y. Paratcha, P. Broekman, T.J. Schmidt, *Chimia* **69** (12), 1–8 (2015).
[4] J. Herranz, J. Durst, E. Fabrri, A. Patru, X. Cheng, A.A. Permyakova, T.J. Schmidt, *Nano Energy* **29**, 4–28 (2016).
[5] J. Rosen, G.S. Hutchings, Q. Li, S. Rivera, Y. Zhou, D.G. Vlachos, F. Jiao, *ACS Catal.* **5**, 4293–4299 (2015).
[6] Y. Hori, «*Electrochemical CO_2 reduction on metal electrodes. Modern aspects of electrochemistry*», Springer, 89–189 (2008).

CO_2 electroreduction to renewable fuels on Cu based thin films

A.A. Permyakova, A. Pătru, J. Herranz, T.J. Schmidt
phone: +41 56 310 2084, e-mail: anastasia.permyakova@psi.ch

In order to effectively address global warming issues, carbon dioxide emissions into the atmosphere must be reduced. Electrochemical reduction of carbon dioxide (CO_2RR) is an attractive way to utilise this greenhouse gas by converting it into useful carbon neutral fuel using renewable energy sources (wind and/or solar). That would allow not only to store excess energy, but also to eventually close the global carbon cycle [1, 2].

CO_2 combined with H_2O can be used as a feed in a co-electrolyser system and tuned to produce valuable chemical products, such as methanol and ethanol that can be used as a liquid fuel in direct methanol fuel cells (DMFCs) or in modified diesel engines. Offering promising advantages, this process has been widely studied in recent years. Despite the effort, the overall energy efficiencies and product selectivities still require improvement in order to make this process economically valuable [3]. One of the key challenges is the slow reaction kinetics that involves multiple proton-coupled electron transfer steps and is directly connected to the catalyst development. Most heavily investigated catalyst is Cu, since it can produce hydrocarbons with reasonable Faradaic efficiencies; however it is also relatively unselective and yields more than 16 different products. On the other hand, recent experimental studies on Cu electrodes have shown that higher CO_2 reduction efficiencies can be achieved by modifying these metallic electrodes [5, 6]. For example, Cu thin films prepared by electrochemical reduction of thermally grown Cu oxide (Cu_2O) layers exhibit dramatically improved selectivity and up to 50 % efficiency towards ethanol at –0.35 V [6].

The present contribution further examines the behaviour of modified Cu based thin film electrodes fabricated by reactive sputter deposition. Here, thin films are subsequently modified by heat treatment varying the temperature and exposure time. Electrochemical reduction of CO_2 is performed in 0.05 M Cs_2CO_3 using a custom made parallel plate electrochemical plate cell configuration [4]. Reaction products are analysed by gas and high-performance liquid chromatography. The crystal structure of pristine and modified electrodes is studied via grazing angle X-ray diffraction, whilst morphology by scanning electron microscopy.

Experimental

Caesium carbonate (≥ 99.999 % metals basis) from Sigma Aldrich was used without further purification. Electrolyte solution was prepared with 18.2 MΩ·cm deionized water from a Millipore system. 0.05 M Cs_2CO_3 solution was bubbled with CO_2 gas until 0.1 M $CsHCO_3$ electrolyte solution was prepared (a pH of 6.8 was achieved).

Electrochemical measurements were carried out using a Biologic SP-300 potentiostat. CO_2 electrolysis was performed at ambient pressure in a gas-tight custom-made cell made of PEEK and fitted with O-rings. The cell configuration is designed to ensure a uniform potential distribution across the surface of working electrode by placing counter electrode (platinum foil) parallel to the working electrode. The geometric surface area of both electrodes was 1.00 cm^2. To separate the anodic and cathodic compartments and to prevent the oxidation of reduced CO_2 products an anion exchange membrane (Selemion® AMV, AGC Inc.) was placed in between. Both anodic and cathodic compartments contained small electrolyte volumes (2 mL and 1.8 mL, respectively) to ensure high concentration of liquid products and, therefore, decrease the detection limits. A Ag/AgCl electrode (HARVARD APPARATUS GmbH) was used as the reference. Data were converted to a Reversible Hydrogen Electrode (RHE) scale by equation:
$E_{vs.\ RHE} = E_{vs.\ Ag/AgCl} + 0.197\ V + 0.0591 \times pH$ (6.8).
Before every electrolysis experiment, the solution resistance was first determined using electrochemical impedance spectroscopy by scanning from 1 MHz to 10 Hz. Before the cyclic voltammetry and chronoamperometry measurements Ohmic resistance was corrected by potentiostat set to compensate for 85 % of the measured IR drop.

The gas products analysis was carried out with a gas chromatograph (GC, SRI instruments) equipped with a packed HaySep D column and a packed MolSieve 5A column. A flame ionization detector (FID) with a methanizer was used to detect hydrocarbons with He as the carrier gas. A thermal conductivity detector (TCD) was used to detect hydrogen with nitrogen as the carrier gas. An online gaseous product analysis was carried every 20 min by the GC, after CO_2 passed through the cell directly into the gas sampling loop. For all experiments gas analysis was performed at 10, 30, 50, 70 and 90 min, during the 1.5 h of continuous electrolysis. Afterwards, obtained data were averaged to obtain the faradaic efficiencies of the various products.

The liquid products were analyzed by high-performance liquid chromatography (HPLC) with an UltiMate 3000 instrument from Thermo Scientific after 1.5 h of electrolysis. An Aminex HPX 87-H column (Bio-Rad) and diluted sulfuric acid (1 Mm) as the eluent were used. Both the cathode and anode electrolytes were analyzed.

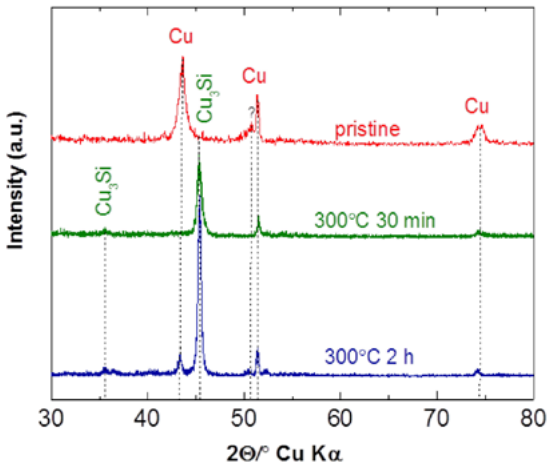

Figure 1. *X-ray diffraction on pristine (red) and heat treated at 300 °C for 30 min (green) and 2 h (blue) Cu thin films.*

Results

Cu thin films were sputter deposited on Si (100) substrate using PSI in-house sputtering system and were investigated for CO_2RR. During the first CO_2RR experiment Cu thin film (TF) appeared to be mechanically unstable. Therefore, Cu TFs were heat treated (HT) to increase thin film adhesion to the substrate. Heat treatment was done at 300 °C for 30 min and 2 hours. X-ray diffraction (XRD) (Figure 1) on as deposited (pristine) Cu TFs showed strictly crystalline structure, where is XRD after heat treatment of Cu thin films reveals presence of crystalline Cu and additional Cu silicide (Cu_3Si), which was formed in both heat treated samples. Formation of Cu_3Si alloy can be explained by mutual diffusion of Cu TFs into Si (100) substrate [7].

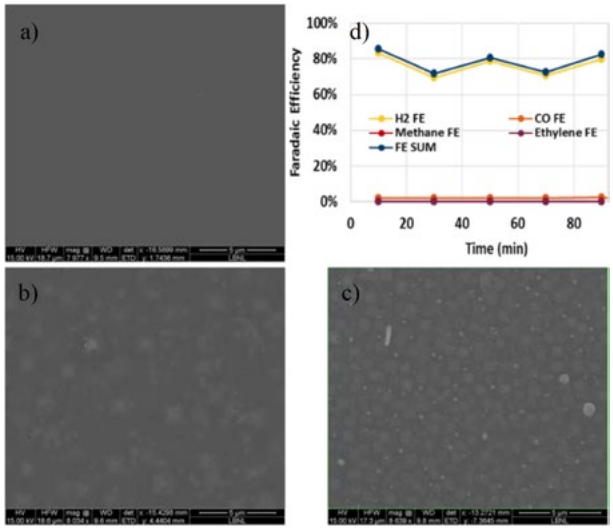

Figure 2. *Scanning electron microscopy images of a) pristine Cu TF, b) and c) Cu heat treated at 300 °C for 30 min and 2 h, respectively; d) Faradaic efficiency (%) of gas products detected by gas chromatography for Cu TF heat treated for 2 h at 300 °C.*

Scanning electron microscopy (SEM) showed changes in morphology of the samples (Figure 2 a, b, c), such as formation of Cu ‹islands› and Cu ‹cubes› in Cu TFs heat treated for 30 min and 2 hours at 300 °C, respectively. Notably, the heat treated samples, despite the morphology change exhibit significant stability improvement during the full course of the CO_2RR experiment. Cu TF heat treated for 2 hours turned to be the most stable catalyst, which can be seen from Figures 2 d), where the faradaic efficiency change is plotted against the time of chronoamperometry experiment (1.5 hours), collected at –1.05 V vs. RHE.

Together with improved stability of Cu thin film, the selectivity and efficiency were tuned after the heat treatment (Figure 3). Cu thin film heat treated at 300 °C for 30 min demonstrates product distributions comparable to the standard Cu foil with addition of increased efficiency towards methanol (~ 3.8 %). Whereas, Cu thin film heat treated at 300 °C for 2 hours produces selectively CO, formate, methanol and H_2, excluding the rest of expected products that are normally produced on metallic Cu. Remarkably, about 15 % of methanol is produced, compared to about 0.1 % that are reported on metallic Cu at the same potential range [4].

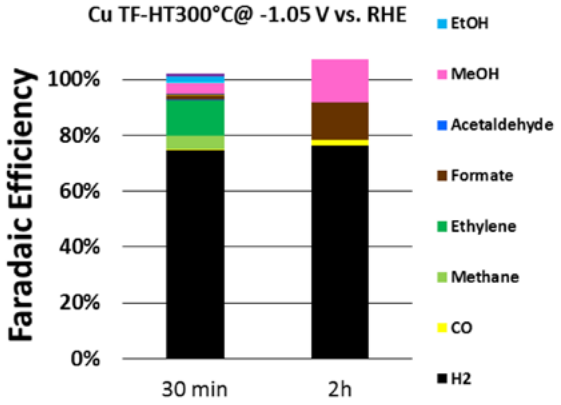

Figure 3. *Faradaic efficiencies of gas and liquid products (%) for Cu thin films heat treated at 300 °C for 30 min and 2 h at –1.05 V vs. RHE.*

Conclusions

Cu thin film catalysts were synthesised by sputter deposition and modified by heat treatment with further examination for CO_2 electroreduction in liquid electrolyte. As deposited (pristine) Cu thin film catalyst showed mechanically unstable behaviour during the CO_2 electroreduction experiment, making correct detection of products' yield/Faradaic efficiency impossible. On the other hand, heat treated Cu thin films showed improvement of mechanical stability. Cu thin film heat treated for 30 min at 300°C showed similar product distribution to Cu foil with additional methanol formation of about ~ 3.8 % FE; where the sample heat treated for 2 hours at 300 °C showed remarkable ~ 15 % FE for methanol and selective formation of CO, formate and H_2 at –1.05 V vs. RHE. Additionally to the crystalline copper, copper silicide was formed after heat treatment in both heat treated Cu thin films. Structural changes took place as well, forming Cu ‹islands› and Cu ‹cubes› like morphologies. These changes suggesting responsibility for the formation of methanol, however inquire further confirmation.

Acknowledgement

The authors gratefully acknowledge financial support from the Commission of Technology and Innovation Switzerland (CTI) and the Swiss Competence Center for Energy Research Heat and Electricity Storage.

References

[1] J. Herranz, J. Durst, E. Fabbri, A. Pătru, X. Cheng, A.A. Permyakova, T.J. Schmidt, *Nano Energy* **29**, 4–8 (2016).
[2] Y. Hori, «Electrochemical CO_2 reduction on metal electrodes. Modern aspects of electrochemistry», *Springer*, 89–189 (2008).
[3] J. Durst, A. Rudnev, A. Dutta, Y. Fu, J. Herranz, V. Kaliginedi, A. Kuzume, A.A. Permyakova, Y. Paratcha, P. Broekmann, T.J. Schmidt, *Chimia* **12**, 69 (2015).
[4] K.P. Kuhl, E.R. Cave, D.N. Abram, T.F. Jaramillo, *Energy Environ. Sci.* **5**, 7050–7059 (2012).
[5] Y. Chen, C.W. Li, M.W. Kanan, *J. Am. Chem. Soc.* **134**, 19969–19972 (2012).
[6] C.W. Li, J. Ciston, M.W. Kanan, *Nature* **508**, 504–507 (2014).
[7] N. Fréty, F. Bernard, J. Nazon, J. Sarradin, J.C. Tedenac, *J. Phase Eq. and Diff.* **27**, 6 (2006).

Understanding the influence of surface oxygen functionalities and carbon microstructure on the performance of carbon electrodes in the all-vanadium redox flow cell

S.M. Taylor, A. Pătru, E. Fabbri, T.J. Schmidt
phone: +41 563104340, e-mail: susan.taylor@psi.ch

The surface chemistry and structure of the carbon electrodes used in the all-vanadium redox flow cell have been found to play a key role in improving the kinetics of both the V(II) oxidation and V(V) reduction reactions [2–4].

Significant efforts have been made to understand and optimise the surface properties of the carbon electrodes [5,6]. A common approach to improving electrode performance has been the introduction of functional groups, in particular oxygen-containing groups onto the electrode surface. The observed improvements in electrode performance have been attributed to a wetting or surface area effect and/or a catalytic effect of these surface groups [1,7,8]. The exact role of surface oxygenated groups on the kinetics of both reactions is unclear and the limiting half-cell reaction is still a topic of debate. Recent studies have shown that the V(II) oxidation reaction limits the overall cell performance [5,7–15]. It has also been suggested that surface oxides could play a catalytic role in improving the kinetics of this reaction [8–10,15]. It is the purpose of this study to gain further insight into the influence of surface oxygen groups on the kinetics of the V(II) oxidation reaction. Modified glassy carbon electrodes were used to study V(II) oxidation reaction kinetics by Cyclic Voltammetry (CV) and Electrochemical Impedance Spectroscopy (EIS). Trends of reactivity vs. oxygen content determined by X-ray photo electron spectroscopy (XPS) were investigated.

Experimental

Glassy carbon (GC) disk electrodes were supplied by Hochtemperaturwerkstoffe GmbH (Sigradur® G, 5 mm OD x 4 mm thickness, mirror polished). The GC electrodes were treated oxidatively, by acid and electrochemical treatments and non-oxidatively by abrasive polishing on sandpaper (3MTM Grit size-600). A mixed treatment involving abrasive polishing followed by electrochemical oxidation was also carried out (see reference [6] for detailed experimental conditions).

Five GC electrode surfaces were investigated in this study using the following nomenclature as in our previous study on V(V) reduction [6]: pristine (GC-P), acid treated (GC-A), electrochemically treated (GC-EC), rough (GC-R) and mixed treatment (GC-R+EC). Electrochemical measurements were carried out using a standard three-electrode setup with a platinum-mesh counter electrode and a Hg/Hg_2SO_4 reference electrode (Gamry instruments Inc.®) at room temperature. Cyclic voltammograms (CVs) were recorded at 50 mV/s in an argon purged 1 M V(II) electrolyte and reported against the reversible hydrogen electrode (RHE). All CVs were corrected during data analysis for ohmic resistance. Electrochemical Impedance Spectroscopy (EIS) measurements were carried out at ~10 mV overpotential for V(II) oxidation with a voltage amplitude of 10 mV in the frequency range: 1 MHz – 50 mHz. X-ray photoelectron spectroscopy (XPS) measurements were performed using a VG ESCALAB 220iXL spectrometer (Thermo Fischer Scientific), spectra of the C1s and O1s peaks were used to determine the surface oxygen to carbon ratio (O/C ratio) for all electrode samples.

Results

Figure 1 below shows the CVs and Nyquist impedance plots for the modified GC electrodes measured in 1 M V(II) solution.

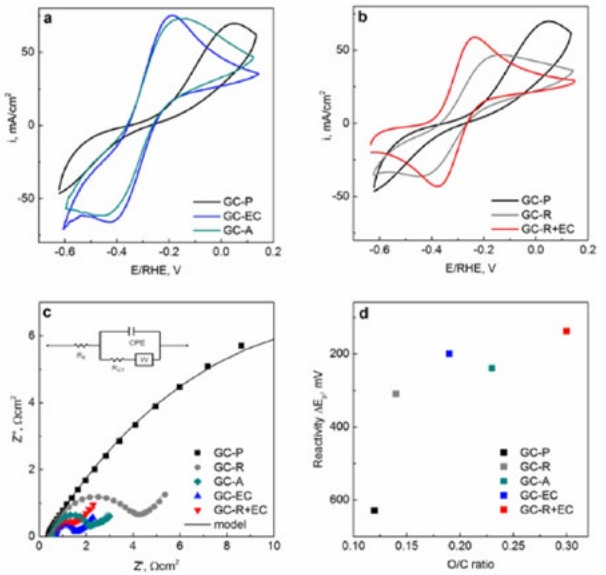

Figure 1. *CVs measured at 50 mV/s in 1 M V(II) / 2 M H_2SO_4 for GC electrodes subject to (a) oxidative treatments and (b) abrasive polishing and mixed treatment (c) Nyquist impedance plots for all GC electrodes (markers show experimental data, solid lines show the fitted data using the equivalent electrical circuit diagram shown in the inset), (d) reactivity (ΔE_p) versus O/C ratio determined by XPS for all GC electrodes.*

Electrode	O/C ratio	Reactivity ΔE_p, mV	Charge transfer resistance R_{CT} $\Omega.cm^2$
GC-R+EC	0.30	140	0.6
GC-EC	0.19	200	0.9
GC-A	0.23	240	1.7
GC-R	0.14	310	3.7
GC-P	0.12	630	28

Table 1. *Summary of CV, XPS and EIS data*

The GC-EC, GC-A and GC-R+EC electrodes showed the best reactivity towards V(II) oxidation. Analysis of the impedance data in Figure 1c revealed a decrease in the charge transfer resistance at these three surfaces. XPS analysis confirmed an increase in the oxygen content (O/C ratio) after treatment for these three surfaces (see Table 1.). It is notable that the roughened GC electrode with a low O/C ratio, showed a poor reactivity towards V(II) oxidation.

However, after electrochemical oxidation and a consequent increase in O/C ratio, a substantial improvement in reactivity was observed at the GC-R+EC surface. The effect of defect exposure by roughening the GC surface did not have the same positive effect on reactivity as was seen for the V(V) reduction reaction in our previous study [6]. Only after the introduction of surface oxygen groups a notable reactivity improvement was observed. A plot of oxygen content (O/C ratio) versus peak separation (ΔE_p) in Figure 1d indicates that the V(II) oxidation reaction is sensitive to the amount of oxygen present on the surface. Higher O/C ratios correspond to better reactivity and low R_{CT}. The observations made here are in line with several earlier and more recent studies involving V(II) oxidation at oxidised carbon surfaces [8, 9, 12, 16]. It was suggested previously that V(II) oxidation follows an inner-sphere reaction mechanism involving surface oxygen groups [16]. Thus the V(II) oxidation reaction appears to be sensitive to the presence of surface oxygen groups on the carbon electrode.

Conclusions

In this study we have shown that improvements in the V(II) oxidation reaction kinetics observed by EIS and CV correspond to an increase in the total surface oxygen content (O/C). This finding suggests that oxygen groups play a catalytic role in the oxidation of V(II) as has been suggested previously [16].

There is still much to be learned regarding the mechanism of V(II) oxidation and the catalytic role of surface oxygen groups. Further understanding of the reaction mechanism will help in optimising and developing more suitable and stable negative electrode materials for this reaction.

Acknowledgement

The authors thank The Swiss National Science Foundation (SNF) for their financial support within the REPCOOL Project (Grant No. 147 661).

References

[1] J. Maruyama, T. Hasegawa, S. Iwasaki, T. Fukuhara, M. Nogami, *J. Electrochem. Soc.* **160**, 8, A1293–A1298 (2013).
[2] J. Melke, P. Jakes, J. Langner, L. Riekehr, U. Kunz, Z. Zhao-Karger, A. Nefedov, H. Sezen, C. Wöll, H. Ehrenberg, C. Roth, *Carbon N. Y.* **78**, 220–230 (2014).
[3] J. Friedl, C.M. Bauer, A. Rinaldi, U. Stimming, *Carbon N. Y.* **63**, 228–239 (2013).
[4] L. Cao, M. Skyllas-Kazacos, D.-W. Wang, *J. Electrochem. Soc.* **163**, 7, A1164–A1174 (2016).
[5] E. Agar, C.R. Dennison, K.W. Knehr, E.C. Kumbur, *J. Power Sources* **225**, 89–94 (2013).
[6] S.M. Taylor, P. Alexandra, D. Streich, M. El Kazzi, E. Fabbri, T.J. Schmidt, *Carbon N. Y.* **109**, 472–478 (2016).
[7] A.M. Pezeshki, J.T. Clement, G.M. Veith, T.A. Zawodzinski, M.M. Mench, *J. Power Sources* **294**, 333–338 (2015).
[8] A. Bourke, M.A. Miller, R.P. Lynch, X. Gao, J. Landon, J.S. Wainright, R.F. Savinell, D.N. Buckley, *J. Electrochem. Soc.* **163**, 1, A5097–A5105 (2016).
[9] H. Fink, J. Friedl, U. Stimming, *J. Phys. Chem. C,* **120**, 29, 15893–15901 (2016).
[10] D. Dixon, D.J. Babu, J. Langner, M. Bruns, L. Pfaffmann, A. Bhaskar, J.J. Schneider, F. Scheiba, H. Ehrenberg, *J. Power Sources* **332**, 240–248 (2016).
[11] C.-N. Sun, F.M. Delnick, D.S. Aaron, A.B. Papandrew, M.M. Mench, T.A. Zawodzinski, *J. Electrochem. Soc.* **161**, 6, A981–A988 (2014).
[12] C.A. Mcdermott, K.R. Kneten, R.L. Mccreery, *J. Electrochem. Soc.* **140**, 9 (1993).
[13] D. Aaron, C.-N. Sun, M. Bright, A.B. Papandrew, M.M. Mench, T.A. Zawodzinski, *ECS Electrochem. Lett.* **2**, 3, A29–A31 (2013).
[14] J. Langner, M. Bruns, D. Dixon, A. Nefedov, C. Wöll, F. Scheiba, H. Ehrenberg, C. Roth, J. Melke, *J. Power Sources* **321**, 210–218 (2016).
[15] M.A. Miller, A. Bourke, N. Quill, J.S. Wainright, R.P. Lynch, D.N. Buckley, R.F. Savinell, *J. Electrochem. Soc.* **163**, 9, A2095–A2102 (2016).
[16] R.L. McCreery, K.K. Cline, C.A. McDermott, M.T. McDermott, *Colloids Surfaces A Physicochem. Eng. Asp.* **93**, C211–219 (1994).

Numerical model for comparison of Koutecký-Levich equations to theory

S.A. Tschupp, J. Herranz, T.J. Schmidt
phone: +41 56 310 2127, e-mail: simon.tschupp@psi.ch

Electrochemical flow cells (EFCs) have found widespread use as detectors in analytical research with high sensitivity and selectivity. Due to the ease of coupling to other analytical tools and the wide range of possible sample geometries, EFCs are also attracting increasing interest in electrocatalysis. However, due to the high importance of mass transport and non-trivial fluid dynamics, a fundamental understanding of the flow profile and electrode currents requires the use of several crude assumptions or numerical simulations. For channel and wall-jet flow cells, this development has led to Koutecký-Levich (K-L) type equations to separate kinetic and mass transport currents [1, 2].

In this contribution we use the finite element software COMSOL Multiphysics® to model current-voltage relations for an arbitrary model reaction and subsequently assess the accuracy of the K-L type equations for the two types of EFCs mentioned above. The geometry of the models corresponds to the experimental setups that were used to verify the description of the mass transport limited current for the K-L type equations mentioned above; see references [3] and [4] for the channel and wall-jet, respectively.

Experimental

A simplified cell layout of the two studied cells is shown in Figure 1. In order to decrease computational requirements, the model was solved in 2D, along a rotational axis and subsequently revolved before post-processing. Assuming the use of a highly conductive supporting electrolyte, the potential drop in the electrolyte can be neglected. Therefore, counter- and reference electrodes have been excluded from the modelled domain.

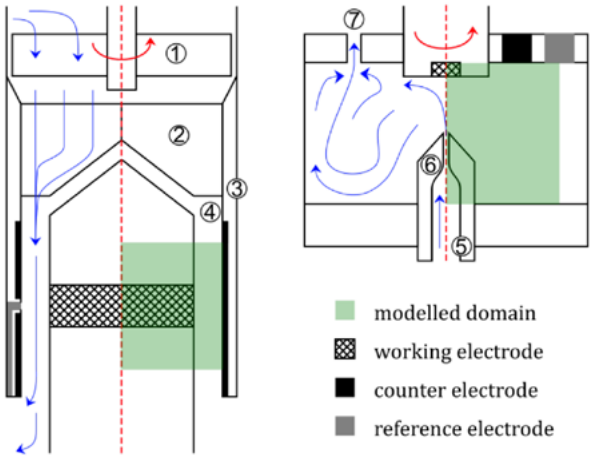

Figure 1. *Left: Cross-section of the channel EFC from reference [4] consisting of a rotating impeller ① and flow directing vanes ② in a steel tube ③ forming an annular flow channel ④. Right: cross-section of the wall-jet EFC from reference [5] with ⑤ inlet tube, ⑥ nozzle, and ⑦ outlet. Rotational axis, schematic flow profiles, and modelled domain are shown in red, blue, and green, respectively. Drawings are not to scale.*

The equations solved in the model have been outlined previously [5], in brief: The fluid velocity profile can be described by the incompressible Navier-Stokes equation for a steady-state problem, if the density of the electrolyte is constant across the domain:

$$\mu\nabla^2\mathbf{u} = \nabla p \qquad (1)$$

Where μ is the dynamic viscosity, u is the velocity tensor, and p is the pressure. Similarly, the steady-state mass transport can be described by the Nernst-Planck equation, neglecting the migration term due to the use of a supporting electrolyte:

$$\nabla\cdot(D\nabla c) = \mathbf{u}\cdot\nabla c \qquad (2)$$

Where D is the diffusion coefficient and c is the concentration of the reacting species. For this work, a first-order n-electron reaction was considered, with the electrode current i following a modified Butler-Volmer equation:

$$i = i_0\left[\frac{c_{ox,s}}{c_{ox,b}}\exp\left(\frac{\alpha n F}{RT}\eta\right) - \frac{c_{red,s}}{c_{red,b}}\exp\left(-\frac{\alpha n F}{RT}\eta\right)\right] \qquad (3)$$

Where i_0 is the exchange current density, c_s and c_b are the surface and bulk concentration of the reductant and oxidant, respectively, α is the transfer coefficient, n is the number of transferred electrons, η is the overpotential, T is the temperature, and F and R are the Faraday and ideal gas constants, respectively.

Results

In a first step, input parameters (see Table 1) were chosen to reflect experimental results obtained in the respective channel and wall-jet EFCs [3,4] for validation of the model. The values for i_0 and α have been taken from references [6] and [7], for the hydrogen oxidation and the ferricyanide reduction, respectively.

Parameter, abbreviation and unit	Hydrogen oxidation [4]	Ferricyanide reduction [5]
Temperature T [K]	298.15	298.15
Density ρ [g/cm^3]	0.997	0.997
Viscosity μ [Pa·s]	$8.92\cdot10^{-4}$	$8.91\cdot10^{-4}$
Concentration c_b [mol/cm^3]	$7.1\cdot10^{-7}$	$1.0\cdot10^{-7}$
Diffusion coefficient D [cm^2/s]	$4.8\cdot10^{-5}$	$0.76\cdot10^{-5}$
Exchange current density i_0 [mA/cm^2]	0.55	0.5
Transfer coefficient α	0.48	0.5
Transferred electrons n	2	1

Table 1. *Input parameters used for the different reactions modelled in this study.*

Figure 2 shows the limiting currents I_{lim} obtained at η = 0.5 V for different inlet electrolyte velocities. Close comparison with the experimental results in the channel (Table 1 and Figure 6 of reference [3]) and the wall-jet (Curve III in Figure 6 of refer-

ence [4]) EFCs reveals an excellent match of the limiting currents.

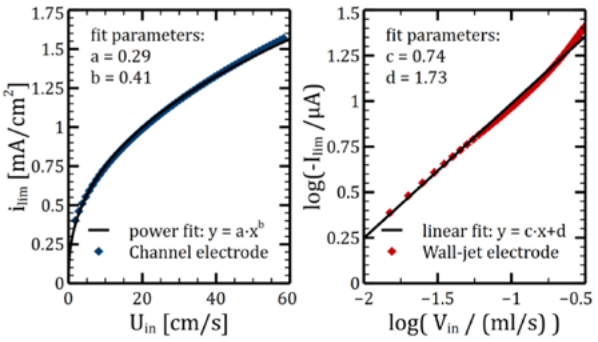

Figure 2. *Correlation of the calculated limiting current with the flow rate for the channel EFC (left) and the wall-jet EFC (right). Axis units have been chosen according to references [3] and [4] for ease of comparability.*

Both models describe the experimental results [3,4] adequately with the correlations between I_{lim} and U_{in} or V_{in} of 0.41 and 0.77 being close to the theoretical values of 0.33 and 0.75 for channel and wall-jet EFCs, respectively [1,2]. In order to assess the validity of the K-L type equations for these systems, polarization curves were calculated (Figure 3). However, exchange current densities i_0 were decreased by a factor of 108 for the hydrogen oxidation and 105 for the ferricyanide reduction, significantly decreasing the reversibility of the reactions, which is a necessary approximation for K-L type equations to be applicable.

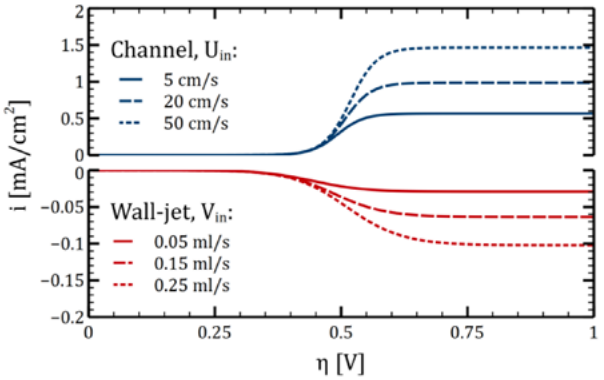

Figure 3. *Calculated polarization curves for channel (top) and wall-jet (bottom) EFCs at different electrolyte velocities or flow rates, respectively.*

The large difference in limiting current originates from the different values for c_b and n shown in Table 1, resulting in a factor of 14 before considering the difference in power of the convective source. In further step, the kinetic currents I_{kin} were obtained applying the K-L type equations summarized in Table 2:

Equation	Electrode	A	B	Reference
$\frac{1}{I} = \frac{A}{I_{kin}} + \frac{B}{I_{lim}}$	Channel	1	0.93	[1]
	Wall-jet	1.06	1	[2]
	Rotating disk	1	1	[8]

Table 2. *K-L type equations for different geometries.*

Plotting the kinetic current densities i_{kin} as function of overpotential η will yield the reactions' Tafel slope b as the slope of a linear fit, and the exchange current density i_0 as the y-axis intercept. However, as all K-L type equations are based on rigorous assumptions and do not hold in the mass transport limited regime, the accuracy of b and i_0 generally decreases upon consideration of mass transport limited currents for the linear fits. Figure 4 shows the difference between the values for b and i_0 obtained via the K-L analysis and those used as the model input.

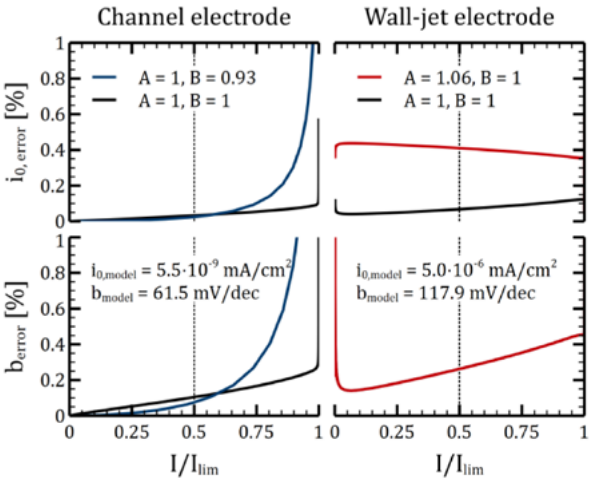

Figure 4. *Precision in % of the K-L analysis for both models using the K-L type equations shown in Table 2.*

From Figure 4 it is apparent that the K-L type equation for the channel will generally yield more accurate values for both i_0 and b, if applied to currents half the magnitude of the limiting current or less. At higher currents, the general K-L equation should be used. However, for the wall-jet, the general equation will yield more accurate values for i_0 and b regardless of current magnitude.

Conclusions

Modelling the experimental conditions of EFCs that have been used to verify the theoretical framework of the respective K-L type equations, we found that the general K-L equation works equally well. It should be noted that the errors on experimental currents surpass the equations' precision of 1 % by a large margin and the significance of i_0 and b are generally related to experimental procedures.

Acknowledgement

We would like to thank PSI Research Commission for financial support.

References

[1] D.A. Scherson, Y.V. Tolmachev, Z. Wang, J. Wang, A. Palencsar, *Electrochem. Solid-State Lett.* **11**, F1–F4 (2011).
[2] W.J. Albery, *J. Electroanal. Chem.* **191**, 1–13 (1985).
[3] D.D. Macdonald, J. Mankowski, M. Karaminezhaad-Ranjbar, Y.-H. Hu, *Corrosion* **44**, 186–192 (1988).
[4] J. Yamada, H. Matsuda, *J. Electroanal. Chem. Interfac. Electrochem.* **44**, 189–198 (1973).
[5] S.A. Tschupp, N. Poyatos-Salguero, S.E. Temmel, T.J. Schmidt, *PSI Electrochemistry Laboratory – Annual Report 2015*, 84–85, DOI: 10.3929/ethz-a-007047464 (2015).
[6] P.J. Rheinländer, J. Herranz, J. Durst, H.A. Gasteiger, *J. Electrochem. Soc.* **161**, F1448 (2014).
[7] D. Jahn, W. Vielstich, *J. Electrochem Soc.* **109**, 849 (1962).
[8] B. Levich, *Discuss. Faraday Soc.* **1**, 37 (1947).

A novel approach for the preparation of Fe-based, O_2-reduction catalysts for polymer electrolyte fuel cells

J. Herranz, T.J. Schmidt
phone: +41 56 310 5562, e-mail: juan.herranz@psi.ch

The commercialization of polymer electrolyte fuel cells (PEFCs) would be significantly enhanced if the Pt-based catalysts needed to catalyze the oxygen reduction reaction (ORR) at the cell's cathode were substituted with inexpensive materials based on abundant metals [1]. Such non-noble metal catalysts (NNMCs) have been studied since the 1960s, and the ongoing refinement of their syntheses has recently led to catalysts with ORR-activities and high-current performances commensurate with those observed for Pt catalysts [2, 3]. However, these qualities are accompanied by a poorly understood, fast deactivation that ultimately prevents NNMCs' device implementation. Since this instability is likely related to the catalysts' composition and porous structure [4], synthesis strategies allowing for a fine control of these properties are urgently needed in order to solve this problem [5]. With this motivation, we have developed a new method for the synthesis of highly-porous NNMCs. As it will be shown herein, the resulting materials are among the best-performing in their category (i.e., considering the absence of NH_3 in the heat-treatment step), but promptly deactivate upon PEFC-operation.

Experimental

All NNMCs were prepared with an initial iron-content of 0.1 %wt Fe (i.e., on the basis of the initial masses of all precursors). First, the amounts of Na_2CO_3 and PAN (set by the mass ratio of choice, cf. below) were dispersed separately in dimethylformamide (DMF) and left stirring overnight at 80 °C. In a separate container, the required mass of iron (in the form of Fe^{II}-acetate) was mixed with the amount of 1,10-phenantroline (phen) needed for a Fe : phen molar ratio of 1 : 5. Once this solution became deep-red in colour (indicating the formation of a Fe-phen complex), all three dispersions were mixed together and kept stirring for three hours at 80 °C. The volume was then reduced to ≈ 50 mL by heating the container at 120 °C, and the remaining solvent was evaporated overnight in a drying oven. Two grams of the resulting powder were ground and set in a ZrO_2 grinding bowl along with fifteen 7 mm diameter ZrO_2 balls. The powder was then submitted to eight ten-minute-long ball milling cycles at 300 rpm, with five-minute pauses in-between cycles. This milled powder was then heat-treated under N_2 (100 sccm) in a tubular quartz furnace; after three hours at 150 °C, the temperature was ramped (at 5 $K \cdot s^{-1}$) to 750 °C and held for 30 min. Once cooled down, ≈ 400 mg of the resulting powder were ultrasonically dispersed in ≈ 200 mL of 0.1 M $HClO_4$, and left stirring overnight. The acid-washed materials were recovered by vacuum-filtration and dried at 80 °C.

The catalysts' ORR-activity was evaluated by rotating disc electrode (RDE) voltammetry. Catalyst inks were prepared by dispersing a weighed amount of material in ultrapure water (18.2 MΩ·cm) and isopropanol (HPLC-grade), along with the amount of Nafion solution required for a catalyst-to-ionomer mass ratio of 0.3. The volume of the resulting inks required for an NNMC-loading of ≈ 500 $\mu g_{NNMC} \cdot cm_{geom}^{-2}$ was then pipetted atop a mirror-polished glassy carbon disc embedded in the RDE. The electrochemical glass cell included a shielded gold mesh and a house-made reversible hydrogen electrode (RHE) as the counter- and reference electrodes, respectively. All electrochemical measurements were performed in (O_2- or N_2-saturated) 0.1 M $HClO_4$. PEFC tests were performed at 80 °C and 1.5 kPa_{abs}, with 100 % humidified H_2 and O_2 and stoichiometries > 30.

N_2-physisorption measurements were performed on weighed amounts of NNMCs pre-outgassed overnight at 200 °C. Overall surface areas were derived from the Brunauer-Emmett-Teller equation within the range $0.05 \leq p/p_0 \leq 0.25$. Pore size distributions were estimated using the quenched solids density functional theory algorithm, assuming slit-like pores. The catalysts' surface speciation was determined by X-ray photoelectron spectroscopy (XPS), using an Al-K_α source (1,486.7 eV).

Results

Our synthesis efforts started by preparing NNMCs with a Na_2CO_3:PAN weight ratio of 3 : 1 and the amount of Fe-phen complex required for an initial metal content of 0.1 %wt Fe. The NNMC obtained after heat treatment at 750 °C and acid washing (cf. Experimental) displayed a relatively poor catalytic activity, requiring more than 650 mV of overpotential (η_{ORR}) to reach an ORR-current of 500 $\mu A \cdot cm_{geom}^{-2}$ (see Figures 1A and 1B).

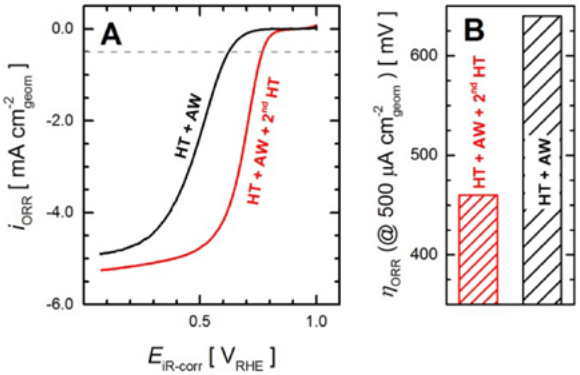

Figure 1. *Ohmically- and capacitively-corrected polarization curves (5 $mV \cdot s^{-1}$, 1,600 rpm) in O_2-saturated 0.1 M $HClO_4$ ('A'), for an NNMC prepared with an initial Na_2CO_3 : PAN ratio of 3 : 1, heat-treated and acid washed ("HT + AW") or additionally heat treated at 950 °C ("HT + AW + 2nd HT"). Average overpotentials at an ORR-current of 500 $\mu A \cdot cm_{geom}^{-2}$ (η_{ORR}, based on three independent measurements) for the same catalysts ('B').*

Considering that acid-washing can be detrimental to the ORR-activity [6], and that higher heat treatment temperatures typically improve NNMC-reactivity, the same catalyst was submitted to a second heat-treatment step at 950 °C (1 h, 5 % H_2 in Ar). As shown in Figure 1B, this resulted in a ≈ 170 mV decrease of η_{ORR} that translates into a three order of magnitude improvement of the catalyst's ORR-activity (assuming a Tafel slope of 60 $mV \cdot dec^{-1}$). Thus, all NNMCs discussed in the following were systematically submitted to this second heat treatment step at 950 °C.

Next, we proceeded to optimize the synthesis parameters by studying the effect of the Na_2CO_3:PAN ratio on the catalysts' ORR-activity, surface area/pore size distribution and surface chemistry. Figure 2A displays the relation between the initial amount of carbonate (i.e., on the sole basis of the Na_2CO_3 and PAN masses) and the ORR-activity, which reaches a maximum for carbonate contents between 50 and 67 % (corresponding to 1:1 and 2:1 ratios). Interestingly, the reactivity trend is not directly related to the surface N- or (micro-)porous contents (Figure 2B and 2C, respectively), which have been related to the NNMCs' ORR-activity [1]. Thus, the catalysts' performance may be determined by a combination of both of these variables, or by a third parameter like the materials' final Fe-content – a possibility that is currently under verification in our laboratory.

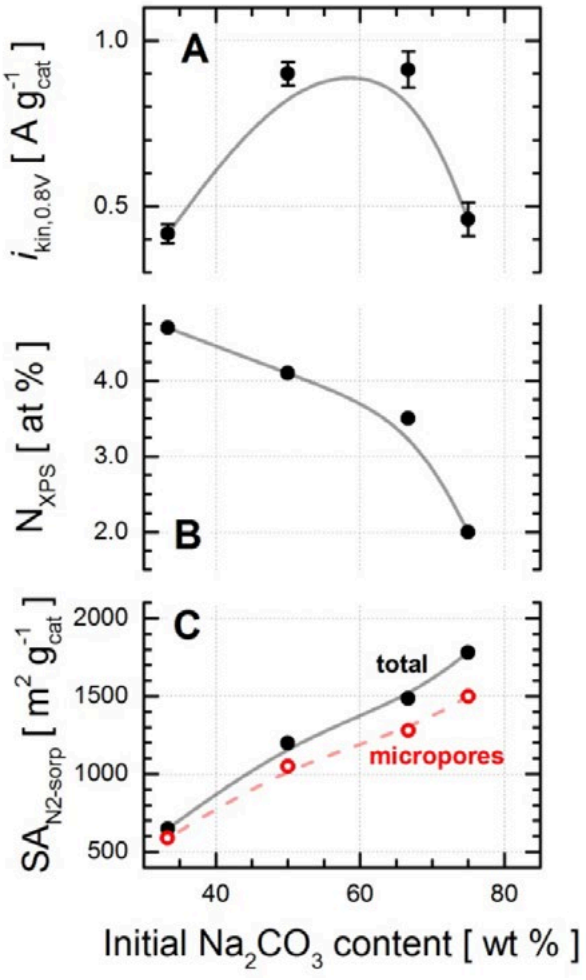

Figure 2. *Relation between NNMC-mass normalized ORR-activities (kinetic current at 0.8 V_{RHE}, $i_{kin0.8V}$, 'A'), XPS-determined surface N-contents (N_{XPS}, 'B') and total/microporous surface areas derived from N_2-sorption porosimetry ($SA_{N2\text{-}sorp}$, 'C'), for NNMCs with an initial Fe-content of 0.1 %wt Fe and different Na_2CO_3:PAN ratios (whereby the corresponding, initial Na_2CO_3-content is determined on the sole basis of carbonate and polyacrylonitrile masses).*

Encouraged by these results, we proceeded to evaluate the PEFC-performance of the catalyst prepared with an initial Na_2CO_3:PAN ratio of 2:1 (i.e., with 67 % carbonate, in Figure 2). The initial ORR-activity of ≈10 A·g_{NNMC}^{-1} at 0.8 V_{RHE} (cf. Figure 3A) is among the best reported in the literature for NNMCs prepared without using NH_3 in the heat treatment step [7]. However, the catalyst suffers from a fast deactivation upon potentiostatic operation at 0.5 V_{RHE}. Interestingly, the Tafel plot after this short stability test features a great resemblance with the one derived from the RDE measurement in an aqueous electrolyte, indirectly suggesting that the flooding of the catalyst's micropores with liquid water is the cause for its apparent instability [4].

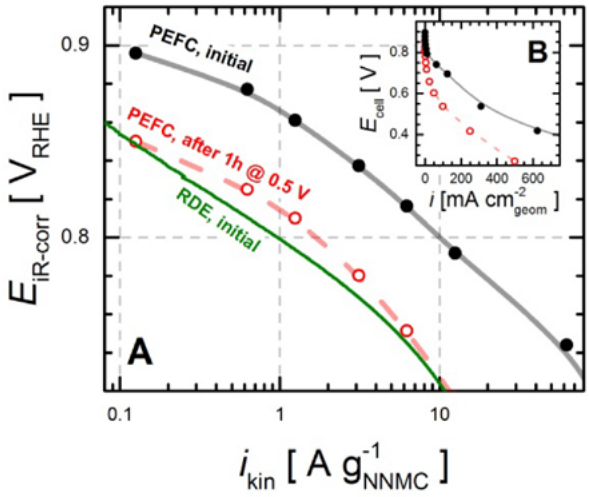

Figure 3. *Ohmically-corrected Tafel plots ('A') for the NNMC with an initial Na_2CO_3:PAN ratio of 2:1, recorded in the PEFC (800 $\mu g_{NNMC} \cdot cm_{geom}^{-2}$, 80 °C, 1.5 kPa_{abs}, 100 % RH) before and after one hour of potentiostatic operation at 0.5 V_{RHE}, or derived from the RDE-voltammetry in O_2-saturated, 0.1 M $HClO_4$ (≈20 °C, 500 $\mu g_{NNMC} \cdot cm_{geom}^{-2}$).Corresponding PEFC polarization curves before and after the potentiostatic test ('B').*

Conclusions

The newly developed NNMC-synthesis approach presented herein yields catalysts with ORR-activity values among the best reported in the literature for such materials. This behaviour is not solely governed by the catalysts' N- or porous-contents, suggesting that the amount of Fe in the final materials may be the decisive factor. Thus, our current efforts focus on the quantification of this parameter and the determination of iron's oxidation state and coordination environment, using state-of-the-art characterization tools like X-ray absorption and Mössbauer spectroscopies [5].

References

[1] F. Jaouen, E. Proietti, M. Lefèvre, R. Chenitz, J.-P. Dodelet, G. Wu, H.T. Chung, C.M. Johnston, P. Zelenay, *Energy Environ. Sci.* **4**, 114–130 (2011).
[2] J. Shui, C. Chen, L. Grabstanowicz, D. Zhao, D.-J. Liu, *Proc. Nat. Acc. Sci.* **112**, 10629–10634 (2015).
[3] E. Proietti, F. Jaouen, M. Lefèvre, N. Larouche, J. Tian, J. Herranz, J.-P. Dodelet, *Nat. Commun.* **2**, 416–424 (2011).
[4] D. Banham, S. Ye, K. Pei, J. Ozaki, T. Kishimito, Y. Imashiro, *J. Power Sources* **285**, 334–348 (2015).
[5] A. Zitolo, V. Goellner, V. Armel, M.-T. Sougrati, T. Minerva, L. Stievano, E. Fonda, F. Jaouen, *Nat. Mater.* **14**, 937–942 (2015).
[6] J. Herranz, F. Jaouen, M. Lefèvre, U.I. Kramm, E. Proietti, J.-P. Dodelet, P. Bogdanoff, S. Fiechter, I. Abs-Wurmbach, P. Bertrand, T. Arruda, S. Mukerjee, *J. Phys. Chem. C* **115**, 16087–16097 (2011).
[7] M.T. Sougrati, V. Goellner, A.K. Schuppert, L. Stievano, F. Jaouen, *Catal. Today* **262**, 110–120 (2016).

Modeling and structural analysis of Pt-based catalyst layers in PEFCs

H. Ishikawa[1], S. Henning, J. Herranz, T.J. Schmidt
e-mail: h.ishikawa23th@gmail.com, hiroshi.ishikawa@psi.ch

For more widespread commercial use of polymer electrolyte fuel cells (PEFCs), it is essential to reduce the catalyst costs and to guarantee long-term durability. Although carbon-supported platinum (Pt/C) catalysts are commonly used in the electrodes, there are some issues such as low ORR activity of Pt and low durability due to the carbon corrosion. As one approach to overcome these drawbacks, unsupported bimetallic Pt-Ni aerogels consisting of nanochains were developed [1]. They showed higher ORR activity and higher durability than commercial Pt/C in the RDE measurement. Thus, in the future we intend to prepare Pt-Ni catalyst layers (CL) and evaluate the performance in the actual cell. However, the structure of CLs from unsupported catalysts is completely different to that of commercial Pt/C due to the absence of carbon support and it typically requires a long time to optimize ink compositions and the fabrication processes. Thus in this study, by using structure modeling techniques [2, 3], CLs from unsupported catalysts were modelled for Pt-Ni aerogels and a Pt Black benchmark. The model CLs and their pore size distribution (PSD) were compared to the real CLs which were analyzed by TEM and FIB-SEM. From the results, the structural features of Pt-Ni aerogel CLs will be discussed.

Experimental

For the structure modelling of Pt-based CLs, virtual Pt aggregates and Pt agglomerates were designed by the following procedure. Pt aggregates were formed by connecting 25 primary particles, each 8 nm in diameter. Pt agglomerates were formed by connecting 50 aggregates. To control the aggregate structure, pseudo inter-particle forces were applied based on the algorithm from Inoue et al. [2]. By applying attractive and repulsive forces, ball and bar type aggregates were designed to simulate Pt Black and Pt-Ni aerogel structures. In the next step, 2 types of model CL were formed by arranging the aggregates and agglomerates randomly from bottom to top. The CL region was confined to 600 nm in width, 600 nm in depth and 1200 nm in height. The Pt volume ratio was set to 15.5 % which is a density equivalent to the 0.4 mg/cm^2 Pt-loadings in real CLs. The PSD of the CLs was analysed by the sphere packing method [3] and compared with that of the real CL which was obtained by FIB-SEM.

Results

Figure 1a shows ball type and bar type aggregates. The average sizes are around 30 nm and 80 nm, respectively. Figure 1b shows the ball type and bar type agglomerates. The average sizes are around 150 nm and 250 nm, respectively. The structures of agglomerates look similar to the TEM images of Pt Black and Pt-Ni aerogel CL, indicating that the real CL could consist of such agglomerates. The model CLs which consist of bar aggregates and bar agglomerates are shown in Figure 2a. The CL formed by aggregates showed smaller pores and lower thickness while the CL formed by agglomerates showed larger pores and higher thickness. It is assumed that large particles make larger pores due to the steric hindrance effect. Figure 2b shows the PSDs of the model CLs and real CL which was obtained by FIB-SEM. In the model CLs, the maximum pore size was observed around 10 nm which is probably present between the bar aggregates. PSD of the real CL was shifted to larger values compared to the model CLs. The real CL may consist of larger agglomerates and exhibit larger pores due to the higher steric hindrance effect.

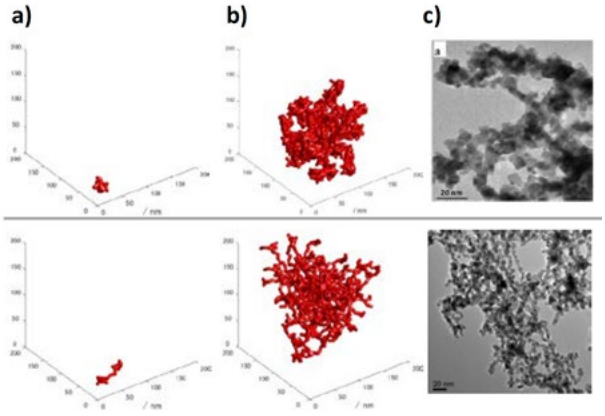

Figure 1. *a) b) Modeling aggregates and agglomerates of ball type (top) and bar type (bottom). c) TEM images of Pt Black (top) and Pt-Ni aerogels (bottom).*

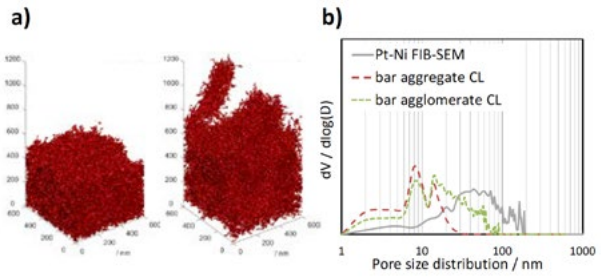

Figure 2. *a) Modeling CLs consisting of bar type aggregates (left) and bar type agglomerates (right). b) PSDs of the model CLs and the real CL consisting of Pt-Ni aerogels.*

Conclusions and outlook

Modeling techniques of CLs from unsupported catalysts were developed for the first time. By structural analysis, the catalyst shape and aggregation could be related to CL properties. Further improvement of the model to allow for accurate reconstruction and prediction of the real CLs will be the future focus.

References

[1] S. Henning, L. Kühn, J. Herranz, J. Durst, T. Binninger, M. Nachtegaal, M. Werheid, W. Liu, M. Adam, S. Kaskel, A. Eychmüller, T.J. Schmidt, *J. Electrochem. Soc.* **163**, F998–F1003 (2016) .
[2] G. Inoue, M. Kawase, *J. Power Sources* **327**, 1–10 (2016).
[3] G. Inoue, T. Yoshimoto, Y. Matsukuma, M. Minemoto, *J. Power Sources* **175**, 145–148 (2008).

[1] Fuel Cell Nanomaterials Center, University of Yamanashi, Kofu, Japan

Performance of Pt-Ni aerogel as cathode catalyst in differential fuel cells

S. Henning, H. Ishikawa[1], J. Herranz, T.J. Schmidt
phone: +41 56 310 2125, e-mail: sebastian.henning@psi.ch

State-of-the-art polymer electrolyte fuel cells (PEFCs) require large amounts of carbon-supported platinum nanoparticle (Pt/C) catalysts (up to 0.4 mg_{Pt}/cm^2_{MEA}) to account for the large overpotential of the oxygen reduction reaction (ORR). One approach to reduce this excessive Pt-loading relies on increasing the catalysts' ORR activity, e.g. by alloying platinum with other metals like Ni, Cu and Co, to form materials which show up to one order of magnitude higher specific activity than commercial Pt/C catalysts. [1] On the other hand, these carbon-supported materials suffer from significant carbon- and Pt-corrosion during the normal operation of PEFCs, gradually compromising their performance. [2]

To partially overcome these stability issues, unsupported bimetallic Pt-Ni aerogels consisting of nanochains with extended surface areas (~ 30 m^2_{ECSA}/g_{Pt}) were synthesized. [3] Those materials meet the US Department of Energy ORR activity target 2017 of 440 A/g_{Pt} at 0.9 V_{RHE} [4] when assessed by the rotating disk electrode technique. To evaluate the behaviour of these aerogels in a system closer to real PEFCs, the performance of Pt_3Ni aerogel was tested in a differential fuel cell [5] and compared to Pt/C and Pt black benchmarks, respectively.

Experimental

Bimetallic aerogels were synthesized at TU Dresden following the procedure described in Ref [3]. Pt/C (47 wt%, TEC10E50E) and Pt black (HiSPEC® 1000) benchmarks were purchased from Tanaka Kikinzoku Kogyo K.K. and Johnson Matthey PLC, respectively.

Catalyst inks were prepared by dispersing catalyst material in mixtures of ultrapure water, isopropanol and Nafion® 117 solution using a sonicator bath. Those inks were applied on the cathode side of a Nafion XL-100® membrane by spray coating until loadings of ~ 0.4 ± 0.1 $mgPt/cm^2$ were reached. Membrane electrode assemblies (MEAs) were prepared by hotpressing the catalyst coated membranes to GDLs (Sigracet® 25 BC) on the cathode side and commercial GDEs (0.4 $mgPt/cm^2$ HISPEC 9100 Pt/HAS on Sigracet® 25 BC) on the anode side applying pressures of 1 bar/cm^2 at 120 °C for 5 minutes.

After assembly of the differential fuel cell, MEA performance was assessed with an in-house built test bench in conjunction with a Biologic VSP-300 potentiostat equipped with a 10 A booster. All polarization curves were recorded at 80 °C, 100 % relative humidity (RH), 1.5 bar absolute pressure and high anodic/cathodic stoichiometries (λ > 30).

Results

As discernable from Figure 1, Pt_3Ni aerogel shows almost comparable performance to Pt/C and Pt black benchmark MEAs in H_2-O_2 polarization curves, but exhibits a potential drop at current densities > 1 A/cm^2_{MEA}.

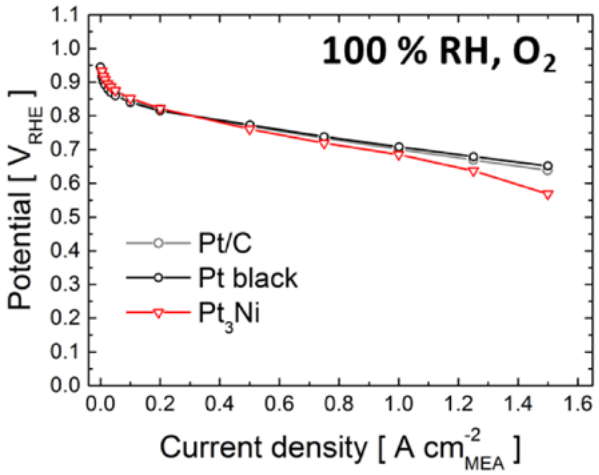

Figure 1. *H_2-O_2 polarization curves for Pt_3Ni, Pt/C and Pt black.*

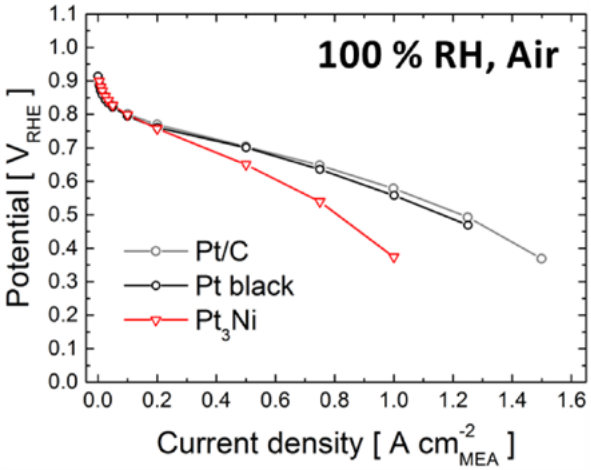

Figure 2. *H_2-air polarization curves for Pt_3Ni, Pt/C and Pt black.*

This performance difference becomes more pronounced, when the gas on the cathode side is replaced by air as shown in Figure 2. The lower cell potentials for Pt_3Ni can indicate that the diffusivity of reactive gases within Pt_3Ni catalyst layers is worse than within Pt/C and Pt black catalyst layers. To study the reasons for this presumed low diffusivity, the three dimensional (3D) structure of the Pt_3Ni catalyst layer was investigated by a combination of focused ion beam and scanning electron microscopy (FIB-SEM), during which the catalyst layer is removed by the ion beam and consecutive SEM images of the freshly exposed surfaces are taken.

In Figure 3 a representative SEM image of the Pt_3Ni catalyst layer cross section prepared by FIB cutting is shown.

[1] Fuel Cell Nanomaterials Center, University of Yamanashi, Kofu, Japan

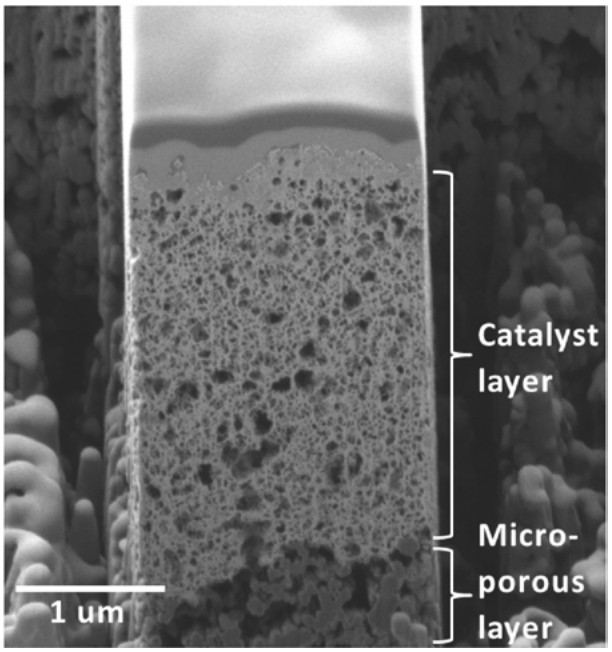

Figure 3. *SEM image of catalyst layer 'pillar' of Pt_3Ni aerogel on GDL substrate.*

Next, the 3D structure of 1 μm^3 of catalyst layer was obtained after registration and segmentation (de-noising, contrast enhancement, binarization) of 250 consecutive SEM images (c.f. Figure 3).

On the basis of this structure, the pore size distribution (PSD) was approximated by an algorithm that fills the porous network by spheres and maximises their diameters until the pore walls are reached. The resulting sphere diameters and quantities constitute the pore size distribution in Figure 4 which reveals that the majority of the pore volume is provided by micro- and mesopores (< 50 nm diameter). This PSD is in stark contrast to those reported for Pt/C catalyst layers [6] in which up to 50 % of the volume is provided by macropores (> 50 nm diameter).

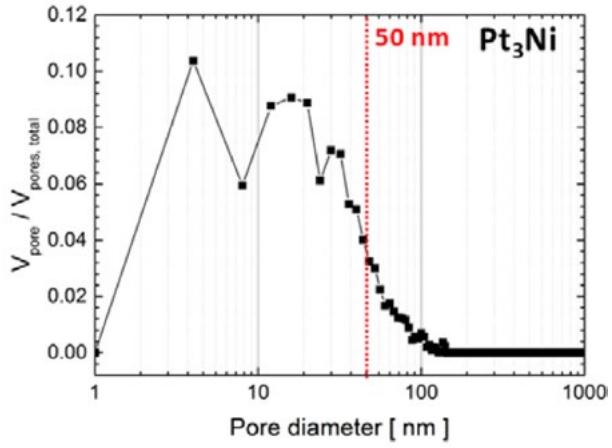

Figure 4. *Pore size distribution for Pt_3Ni catalyst layer based on 3D structure obtained from FIB-SEM experiment.*

Considering that pores < 30 nm, in which Knudsen diffusion vs. bulk diffusion becomes the predominant reactant transport mechanism [7], represent ~ 70 % of the Pt_3Ni catalyst layer porosity, can explain why gas diffusion and thus performance is significantly lower when compared to Pt/C MEAs.

Conclusions and outlook

First differential fuel cell experiments indicate that Pt-Ni aerogel materials could be incorporated successfully into PEFCs. Presently, the MEAs exhibit low performance at high current densities in H_2-air curves, presumably caused by poor diffusion characteristics of the aerogel catalyst layers. Future work will thus focus on optimizing the structure of the latter.

Acknowledgement

The authors thank Laura Kühn from the Chair of Physical Chemistry, Technische Universität Dresden for synthesis of the Pt_3Ni aerogel catalyst that was used in this study. We are grateful to Dr. Elisabeth Müller for assistance with the FIB-SEM experiment. Financial support from SNF (20001E_151122/1) and DFG (EY 16/18-1) is greatly acknowledged.

References

[1] H.H. Wang, Z.Y. Zhou, Q. Yuan, N. Tian, S.G. Sun, *Chem. Commun.* **47**, 3407–3409 (2011).
[2] A. Rabis, P. Rodriguez, T.J. Schmidt, *ACS Catal.* **2**, 864–890 (2012).
[3] S. Henning, L. Kühn, J. Herranz, J. Durst, T. Binninger, M. Nachtegaal, M. Werheid, W. Liu, M. Adam, S. Kaskel, A. Eychmüller, T.J. Schmidt, *J. Electrochem. Soc.* **163**, F998–F1003 (2016).
[4] O. Gröger, H.A. Gasteiger, J.P. Suchsland, *J. Electrochem. Soc.* **162**, A2605–A2622 (2015).
[5] P. Oberholzer, P. Boillat, R. Siegrist, A. Kästner, E.H. Lehmann, G.G. Scherer, A. Wokaun, *Electrochem. Comm.* **20**, 67–70 (2012).
[6] S. Thiele, R. Zengerle, C. Ziegler, *Nano Res.* **4**, 849–860 (2011).
[7] N. Nonoyama, S. Okazaki, A.Z. Weber, Y. Ikogi, T. Yoshida, *J. Electrochem. Soc.* **158**, B416 (2011).

Potential-dependent conductivity switching of metal oxide supports for electrocatalyst nanoparticles

T. Binninger, R. Mohamed[1], A. Pătru, E. Fabbri, A. Hoell[2], T.J. Schmidt
phone: +41 56 310 5728, e-mail: tobias.binninger@psi.ch

Whereas the use of metal oxides as support material for metal catalyst nanoparticles is very common in the field of heterogeneous catalysis, this concept is relatively new in electrocatalysis, where up to now the mostly and almost exclusively used supports consist of high-surface area carbon materials, a fact that can be explained with the strong focus of electrocatalysis research on the properties of the metal catalyst particles and not on the properties and interactions with the support material during the past decades.

However, it is well known from heterogeneous catalysis research that the support material can strongly influence the properties of the catalyst, not only in terms of activity but also in terms of stability. The latter aspect has brought metal oxide supports to the attention of research on electrocatalysts for the oxygen reduction reaction at the cathode of polymer electrolyte fuel cells (PEFC). The harsh, oxidizing conditions at the PEFC cathode make it difficult for conventional Pt/C catalysts to meet PEFC durability requirements. Metal oxide supports offer an alternative with possibly superior thermodynamic stability at high PEFC cathode potentials compared to carbon support.

In contrast to applications in heterogeneous catalysis, metal oxides as electrocatalyst support must provide sufficient electronic conductivity in order to sustain the electric current generated by electrochemical reactions that occur at the supported catalyst nanoparticles. This requirement severely restricts the selection of suitable metal oxide materials. Apart from exceptions, such as IrO_2 with metallic conductivity, most metal oxides are wide-band gap insulators. However, with the use of appropriate extrinsic dopants, semiconducting metal oxides, such as Sb-doped SnO_2, can be produced that have attracted considerable attention as possible electrocatalyst support materials in recent years.

The overall apparent conductivity of doped metal oxide high-surface area supports is a highly intricate quantity since it emerges from an interplay not only between chemical composition and solid state physical aspects, but also between metal oxide surface and bulk properties. It is understood that a homogeneous distribution of the dopant inside the host oxide lattice is highly desirable [1]. In this context, not only the as-synthesized metal oxide must be considered, but also the possible irreversible leaching of the dopant out of the host lattice in an electrochemical environment, which can lead to the formation of an insulating surface layer of the metal oxide particles.

There is, however, an exception where an inhomogeneous distribution of the dopant could be beneficial for the conductivity properties of the catalyst: The contact resistance between metal catalyst nanoparticles and metal oxide support can be influenced by the presence of segregated dopant species at the metal catalyst–oxide support interface [2].

Metal oxide conductivity can be furthermore influenced *in situ* due to electrochemical bulk redox processes. It is well known that metal oxides can be electrochemically bulk-reduced at low potentials by incorporation of H^+ from the electrolyte. Incorporated H species can act as electron donors with the effect of highly increased conductivity at low electrode potentials, e.g. in the case of WO_3 [3].

In addition to bulk effects, the conductivity of high-surface area metal oxide powders is strongly influenced by the formation of a surface space charge layer. Such a charge carrier accumulation / depletion layer can result from the electronic equilibration of the bulk of the metal oxide particles with surface states from adsorbed oxygen species [4]. The presence of Pt nanoparticles on the metal oxide surface can increase the metal oxide support conductivity by donation of electrons into the metal oxide surface depletion layer. This process can be furthermore influenced in an electrochemical environment by the potential-dependent oxidation state of Pt nano-particles with implication for their electron donation capability [5].

However, the space charge properties of a metal oxide surface in contact with an electrolyte are not only influenced by surface states from adsorbed species or by the presence of metal catalyst nanoparticles. It is well-known that the fundamental electrochemical behaviour of semiconductor electrodes is governed by the formation of a potential-dependent space charge layer even in absence of electrochemical bulk or surface redox processes. The transition from charge carrier accumulation to depletion occurs at the flat-band potential, which is equivalent to the potential of zero charge of the semiconductor electrode. For n-type conductivity, the electrode switches to depletion mode at potentials larger than the corresponding flat-band potential. At such potentials, the resistance of a high-surface area metal oxide electrode must strongly increase due to the reduced concentration of mobile charge carriers along the tortuous current paths connecting the supported catalyst particles. This behaviour of potential-dependent conductivity switching can be seen in direct analogy to the principle of a field-effect transistor.

Results and Discussion

The fundamental electrochemical field-effect transistor property of semiconducting metal oxides has strong implications for their use as electrocatalyst support: Only those metal oxide materials are suitable for a given electrocatalytic application that are in charge carrier accumulation at operando potentials. For instance, an n-type semiconducting metal oxide support for Pt catalyst at the PEFC cathode must possess a flat-band potential close to 1.0 V vs. RHE (reversible hydrogen electrode) in order to provide high electronic conductivity at PEFC cathode operation potentials below that value.

In fact, the strongly reduced electrode conductivity above the flat-band potential of the metal oxide support can be beneficially used to enhance the stability of the supported electrocatalyst beyond the improved corrosion resistance of the oxide support itself. This stabilization effect has been explored

[1] HySA/Catalysis, University of Cape Town, Rondebosch, South Africa
[2] Institut für Nanospektroskopie, Helmholtz-Zentrum für Materialien und Energie, Berlin, Germany

in an *in situ* anomalous small-angle X-ray scattering (ASAXS) study about the degradation properties of Pt/Sb-SnO_2 catalyst in comparison to Pt/C catalyst [6]. The degradation protocol consisted of 1000 potential cycles between 0.5 V and 1.5 V vs. RHE in 0.1 M $HClO_4$ electrolyte and mimicked the extremely corrosive conditions at PEFC cathodes during start/stop events.

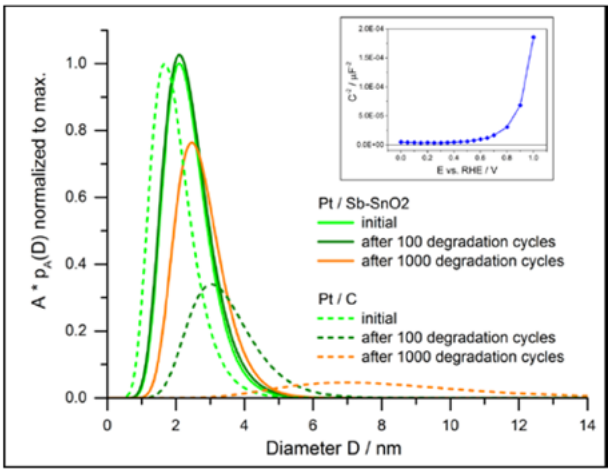

Figure 1. *Normalized Pt particle size distributions from ASAXS analysis of Pt/Sb-SnO_2 in comparison to Pt/C at different stages of the degradation protocol. Inset: Mott-Schottky plot for the Sb-SnO_2 support material.*

Figure 1 plots the normalized Pt particle size distributions at the beginning, after 100, and after 1000 degradation cycles for the Pt/Sb-SnO_2 in comparison to the Pt/C catalyst. Although initial size distributions are very similar, the one of Pt/C quickly shifts towards larger Pt particle diameters as a function of potential cycling. This growth of nanoparticles is known as electrochemical Ostwald ripening, and it results from Pt dissolution/redeposition cycles, in the course of which larger Pt particles grow at the expense of the smaller ones.

However, this process appears to be strongly suppressed on the Sb-SnO_2 support, a fact that cannot be explained merely by an improved support corrosion resistance. Instead, as described above, the electrochemical field-effect transistor switching of the Sb-SnO_2 conductivity leads to a strongly increased electrode resistance at high potentials, thereby protecting the Pt nanoparticles from electrochemical dissolution, and thus inhibiting the electrochemical Ostwald ripening process.

A confirmation of the effectiveness of the electrochemical field-effect transistor property in the Sb-SnO_2 support material is shown in a Mott-Schottky plot in the inset in Figure 1. The inverse square of the space charge capacitance of the oxide support alone is plotted vs. electrode potential. The strong increase at potentials above approx. 0.8 V vs. RHE corresponds to a strongly decreased space charge capacitance due to the formation of a charge carrier depletion layer in the oxide particle surfaces, which, in turn, leads to a strongly increased resistance along the tortuous current paths inside the high-surface area support structure.

Conclusions

The conductivity properties of metal oxides used as electrocatalyst support are influenced by different factors not only *ex situ* but also in an electrochemical environment. On the one hand, electrochemical bulk or surface redox processes of the metal oxide can lead to a potential-dependent *in situ* conductivity. On the other hand, even in absence of (electro)chemical redox processes, the intrinsic electrochemical behaviour of a semiconducting support material leads to a potential-dependent conductivity response that corresponds to an electrochemical field-effect transistor. The strongly reduced conductivity of an n-type support oxide at high potentials can protect supported catalyst nanoparticles from electrochemical degradation such as dissolution and Ostwald ripening.

Acknowledgement

This work was supported by CCEM Switzerland and Umicore AG & Co KG within the project DuraCat. The authors thank the BESSY II synchrotron at Helmholtz-Zentrum Berlin, Germany, for providing beamtime at the 7T MPW SAXS beamline.

References

[1] E. Fabbri, A. Rabis, R. Kötz, T.J. Schmidt, *Phys. Chem. Chem. Phys.* **16**, 13672–13681 (2014).
[2] Q. Fu, L.C.C. Rausseo, U. Martinez, P.I. Dahl, J.M.G. Lastra, P.E. Vullum, I.-H. Svenum, T. Vegge, *ACS Appl. Mater. Interfaces* **7**, 27782–27795 (2015).
[3] M.J. Natan, T.E. Mallouk, M.S. Wrighton, *J. Phys. Chem.* **91**, 648–654 (1987).
[4] H. Shintani, Y. Kojima, K. Kakinuma, M. Watanabe, M. Uchida, *J. Power Sources* **294**, 292–298 (2015).
[5] Y. Chino, K. Kakinuma, D.A. Tryk, M. Watanabe, M. Uchida, *J. Electrochem. Soc.* **163**, F97–F105 (2016).
[6] T. Binninger, R. Mohamed, A. Pătru, K. Waltar, E. Gericke, X. Tuaev, E. Fabbri, P. Levecque, A. Hoell, T.J. Schmidt, *Chem. Mater.* **29** (7), 2831–2843 (2017).

Electrochemical characterization of pyrochlore materials for the oxygen evolution reaction

M. Povia, D. Lebedev[1], E. Fabbri, C. Copéret[1], T.J. Schmidt
phone: +41 56 310 2535, e-mail: mauro.povia@psi.ch

Within a future economy mostly based on renewable energies, the surplus of electricity produced by intermittent renewable sources, like photovoltaic and wind power, must be stored and made readily available in times of high demand. Hydrogen as energy vector is one of the options to store large amounts of excess of renewable energy, since it can be efficiently re-electrified by fuel cells. [1] Water electrolyzers are electrochemical energy conversion devices that split water into its constituent parts, hydrogen and oxygen, which can be stored in common tanks and re-used in fuel cells where and when electricity is needed.

The limiting electrochemical process in a water electrolyzer is the oxygen evolution reaction (OER) occurring at the anodic electrode:

$$H_2O \rightarrow \tfrac{1}{2} O_2 + 2\,H^+ + 2\,e^-$$

State-of-the-art OER catalysts for polymer electrolyte membrane water electrolyzers (PEMWEs) consist of noble metal oxides, predominantly IrO_2 or RuO_2 with catalyst loadings in the range of 2 to 3 mg/cm^2.

The high cost and the scarcity of noble metal catalysts are, however, an obstacle for future widespread commercialization of PEMWEs. In order to make this technology suitable for a large scale market, it is mandatory to reduce the quantity of noble metals in the anodic electrode while keeping high performance. Possible strategies are:

1. Development of noble metal free catalysts;
2. Reducing the catalyst nano-particle (NP) sizes in order to maximize its specific surface area;
3. Dilution of the noble metal in a more complex metal oxide.

Concerning the strategy No. 1, recently several papers have shown the possibility to achieve high OER activity using noble metal-free catalysts with perovskite crystal structure. This approach, however, is mainly limited to alkaline electrolytes and appears not to be suitable for improving the OER in acidic environment due to catalyst stability reasons. [2] The strategy No. 2 consists of reducing the size of the catalyst NPs. This can be achieved by synthetizing smaller NPs [3] or by diluting very small NPs (1–3 nm diameter) on an inert and inexpensive support e.g., IrO_2 or TiO_2. Strategy No. 3 can be fulfilled by the development of Ir-based materials with a pyrochlore crystal structure. The molar weight fraction of Ir can be drastically reduced from 85 %, as in pure IrO_2, to 42 %–57 % in a pyrochlore structure.

Pyrochlores have a formal chemical composition $A_2B_2O_7$ and space group Fd-3m. Iridium occupies the B-site of the pyrochlore structure, coordinating oxygen ions in an octahedral configuration. The A-site metal is located in the interstitial space between the octahedrals.

Within this study, Ir-based pyrochlore catalysts with Yttrium, Bismuth and Lead as A-site have been synthetized at ETH Zurich by the group of Prof. C. Copéret using a modified Adams fusion method. Six pyrochlore compositions have been synthesized as single phase materials and further characterized: $Bi_2Ir_2O_7$ (Bi-Ir), $Pb_2Ir_2O_7$ (Pb-Ir), $Y_2Ir_2O_7$ (Y-Ir), $BiPbIr_2O_7$ (Bi-Pb-Ir), $BiYIr_2O_7$ (Bi-Pb-Ir), $YPbIr_2O_7$ (Y-Pb-Ir).

Experimental

$A_2B_2O_7$ pyrochlore materials were synthesized via a modified Adams fusion method according to the following procedure: Sample precursors ($IrCl_3 \cdot x\,H_2O$, $Y(NO_3)_3 \cdot 6\,H_2O$, $BiONO_3$, $Pb(NO_3)_2$, $Y(NO_3)_3 \cdot 6\,H_2O$) and $NaNO_3$ were dissolved in 100 mL of deionized H_2O, stirred for 10 min with sonication and then dried under ca. 15 mbar to give a black powder. The powder was transferred into a porcelain crucible and heated in a muffle furnace at 550 °C for 2 h (heating program: 2 °C min^{-1} to 150 °C, 30 min at 150 °C, ramp to the target reaction temperature for 2 h). The obtained samples were washed with deionized water and dried at 150 °C overnight under ca. 2 mbar to give the pyrochlore as a black powder. The BET surface area of the samples ranges between 11 and 38 m^2/g.

Catalyst inks were prepared diluting 10 mg of catalyst powder in 1 ml of water and 4 ml of isopropanol and 0.02 ml of 5 %wt Nafion solution. The inks were sonicated for 15 min before used. 10 µl of ink were spread on a standard 0.196 cm^2 glassy carbon electrode by dry spinning rotation method (rotation speed = 50 rpm). The electrochemical characterization was performed in a standard glass cell using a 0.1 M $HClO_4$ (saturated with synthetic air) as electrolyte, a platinum mash as counter electrode, and a standard $Hg/HgSO_4$ reference electrode. Tafel plots were obtained by chronoamperometric measurements. Those measurements were performed stepping the potential from 1.2 to 1.4 V vs. RHE and holding each potential for 60 sec. We elaborated the following protocol in order to test the long time stability of the electrode performance: the electrode potential was switched between 1.0 and 1.6 V vs. RHE with a holding time of 10 sec at each potential for 500 times (cycles). Each sample was characterized three times in order to check the data reproducibility and to have statistic values to analyse.

Results

The Figure 1 shows the Tafel plots of the studied electrocatalysts. The x-axis of the Tafel plot represents the current value normalized for the Iridium mass in the samples as determined by X-ray photoelectron spectroscopy (XPS) measurements, while the y-axis is the potential value corrected for the electrolyte ohmic drop. The Tafel slopes reported in Table 1 are almost similar for all the samples indicating that a similar oxygen evolution reaction mechanism takes place on the surface of the pyrochlore catalysts. Regarding the sample activity, the Y-Ir pyrochlore electrode shows the lowest overpotential at 10 A/g$_{Ir}$ and also the highest activity at 1.525 V vs. RHE. According to the data reported in Table 1, the least performing pyrochlore electrode is Pb-Ir.

[1] ETH Zürich, Department of Chemistry and Applied Biosciences, Zürich

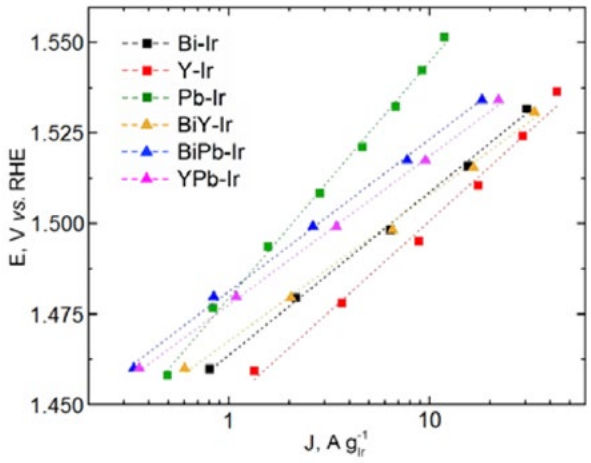

Figure 1. *Tafel plots for the pyrochlore electrocatalysts measured in 0.1 M $HClO_4$ by chronoamperometric measurements.*

Sample	Tafel slope [mVdec^{-1}]	E @ 10 Ag$_{Ir}^{-1}$ [V]	i @ 1.525 V [Ag$_{Ir}^{-1}$]
Bi-Ir	44.68 ± 1.2	1.5 ± 0.01	21.42 ± 4.7
Pb-Ir	65.18 ± 1.3	1.53 ± 0.01	9.84 ± 6.3
Y-Ir	50.41 ± 2.3	1.49 ± 0.007	38.37 ± 13.8
BiY-Ir	40.26 ± 1.4	1.5 ± 0.004	23.24 ± 5.4
BiPb-Ir	41.96 ± 1.0	1.51 ± 0.01	17.36 ± 6.7
YPb-Ir	41.13 ± 0.6	1.51 ± 7E-4	15.59 ± 0.5

Table 1. *Summary of the Tafel slope, potential (E) at 10 A/g$_{Ir}$, and the current density [A/g$_{Ir}$] at 1.525 V for all the investigated samples.*

Figure 2 shows the stability measurements for the pyrochlore samples. After 500 cycles all the pyrochlore electrodes show rather good stability. The most marked degradation is observed for the Pb-Ir sample, while the Y-Ir sample even show an initial increase in current density, followed by a slight decrease after 100–200 cycles. Also the mixed BiPb–Ir pyrochlore shows an initial slight increase in the current density reaching a plateau after ca. 300 cycles.

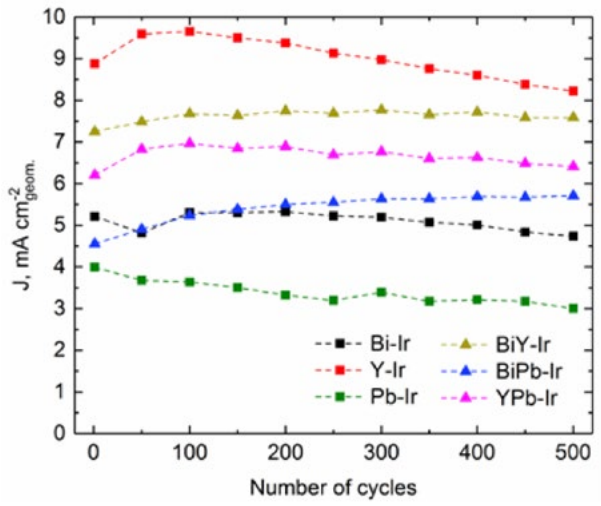

Figure 2. *Stability measurements for the pyrochlore samples.*

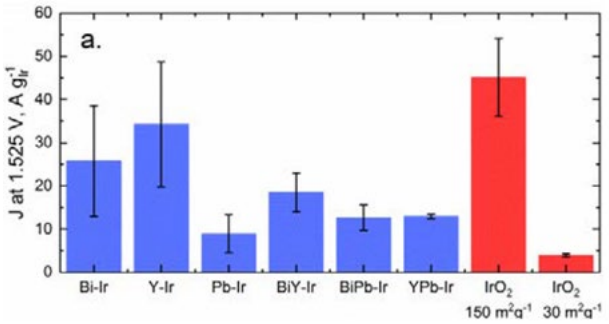

Figure 3. *OER activities of the pyrochlores and IrO_2 samples: mass-normalized current densities at 1.525 V vs. RHE.*

Conclusions

To summarize, considering both the OER activity and the current density under the applied stability test, the most promising pyrochlore catalyst appears to be the Y-Ir one. Furthermore, comparing the activity of the pyrochlore samples at 10 A/g to that of IrO_2 electrodes with comparable or higher surface area (see Figure 3), one can see that Y-Ir shows an significant higher mass current density to that of IrO_2 with a surface area of 30 m^2/g and comparable current density to that of IrO_2 with a much high surface area (150 m^2/g).

Acknowledgement

The authors want to acknowledge the financial support from CCEM (Renerg^2 project), the Swiss Competence Center for Energy Research Heat & Electricity Storage, the Swiss Federal Office of Energy and Swiss Electric Research.

References

[1] F.N. Büchi, M. Hofer, C. Peter, U.D. Cabalzar, J. Bernard, U. Hannesen, T.J. Schmidt, A. Closset, P. Dietrich, *RSC Adv.* **4**, 56139–56146 (2014).
[2] J. Herranz, J. Durst, E. Fabbri, A. Pătru, X. Cheng, A.A. Permyakova, T.J. Schmidt, *Nano Energy* **29**, 4–28 (2016).
[3] D.F. Abbott, D. Lebedev, K. Waltar, M. Povia, M. Nachtegaal, E. Fabbri, C. Copéret, T.J. Schmidt, *Chem. Mat.* **28**, 6591–6604 (2016).

THE ELECTROCHEMISTRY LABORATORY

Facts & Figures

STRUCTURE 2016

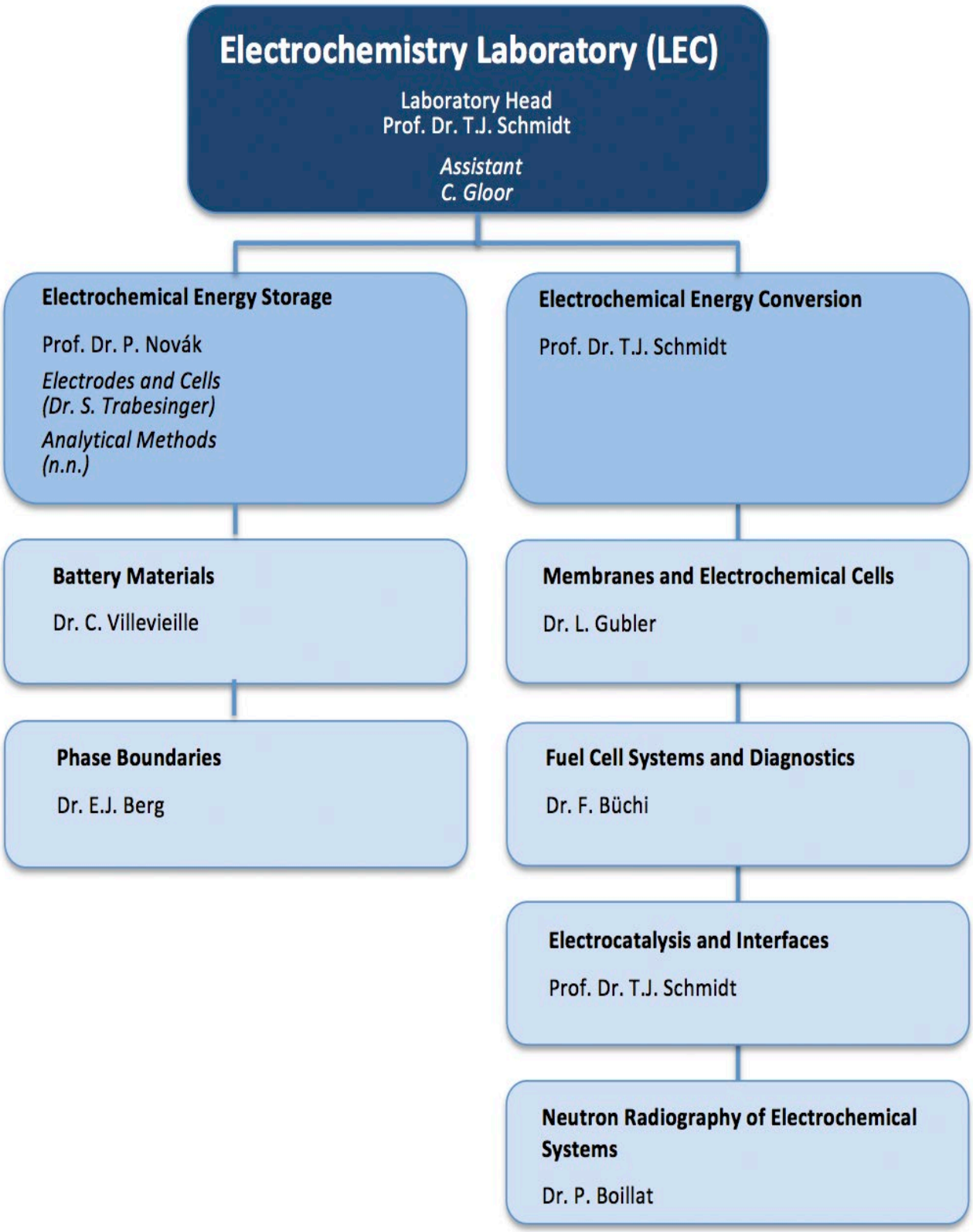

PERSONNEL 2016

Staff

Dr. Daniel ABBOTT (Post Doctoral Researcher)
Martin AMMANN (Technician)
Dr. Erik J. BERG (Group Leader)
Dr. Juliette BILLAUD (Post Doctoral Researcher)
Dr. Pierre BOILLAT (Group Leader)
Dr. Christoph BOLLI (Post Doctoral Researcher)
Lukas BONORAND (Engineer)
Dr. Felix BÜCHI (Group Leader)
Kira BUZDIN (Technician)
Dr. Xi CHENG (Post Doctoral Researcher)
Dr. Magali COCHET (Scientist)
Dr. Benjamin DECOOPMAN (Postdoc)
Dr. Mario EL KAZZI (Scientist)
Dr. Jens ELLER (Scientist)
Dr. Emiliana FABBRI (Scientist)
Cordelia GLOOR (Assistant)
Thomas GLOOR (Technician)
Dr. Lorenz GUBLER (Group Leader)
Dr. Aurélie GUÉGUEN (Scientist)
Dr. Juan HERRANZ SALANER (Post Doctoral Researcher)
Christoph JUNKER (Technician)
Hermann KAISER (Technician)
Sreeyuth LAL (Post Doctoral Researcher)
Dr. Adrien LAMIBRAC (Post Doctoral Researcher)
Michelle LOCHER (Technician)
Dr. Elena MARELLI (Scientist)
Dr. Cyril MARINO (Scientist)
Christian MARMY (Technician)
Dario MEIER (Technician)
Prof. Dr. Petr NOVÁK (Section Head)
Dr. Anastasia A. PERMYAKOVA (Post Doctoral Researcher)
Dr. Alexandra PĂTRU (Scientist)
Christian PETER (Engineer)
Dr. Rosa ROBERT SANCHEZ (Scientist)
Florian RUNTSCH (Engineer)
Dr. Sébastien SALLARD (Scientist)
Dirk SCHEUBLE (Engineer)
Prof. Dr. Thomas J. SCHMIDT (Laboratory Head)
Dr. Tiphaine SCHOTT-POUX (Post Doctoral Researcher)
Dr. Daniel STREICH (Post Doctoral Researcher)
Dr. Sigita TRABESINGER-URBONAITE (Scientist)
Dr. Bing SUN (Post Doctoral Researcher)
Dr. Claire VILLEVIEILLE (Group Leader)

PhD Students

Albert ALBERT
Ugljesa BABIC
Tobias BINNINGER
Johannes BIESDORF
Lucien BOULET-ROBLIN
Joel CABANERO JR.
Joanna CONDER
Sebastian EBERHARDT
Giulio FERRARESI
Eibar Joel FLORES CEDEÑO
Antoni FORNER-CUENCA
Jonathan HALTER
Minglong HE
Sebastian HENNING
Baejung KIM
Paul KITZ
Daniela LEANZA
Maria Victoria MANZI OREZZOLI
Marta MIROLO
Olga NIBEL
Fabio OLDENBURG
Yohan PARATCHA
Hai-Jung PENG
Mauro POVIA
Martin REICHARDT
Tomasz ROJEK
Sebastian SCHMIDT
Tobias SCHULER
Jakub SEWERYN
Muriel SIEGWART
Véronique SPROLL
Michel SUERMANN
Susan TAYLOR
Sandra TEMMEL
Simon TSCHUPP
Leonie VOGT
Xiaohan WU
Hong XU
Mateusz ZLOBINSKI

The Electrochemistry Laboratory, December 2016.

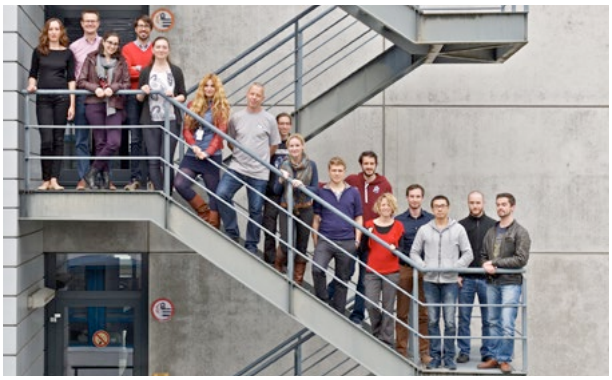

Electrocatalysis and Interfaces Group, May 2015

Energy Storage Section, December 2015.

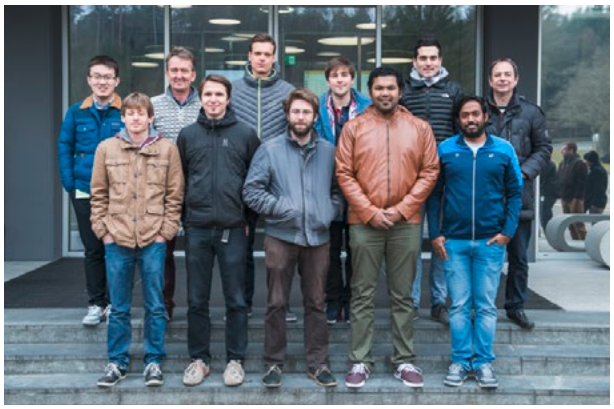

Fuel Cells Systems and Diagnostics Group, December 2016.

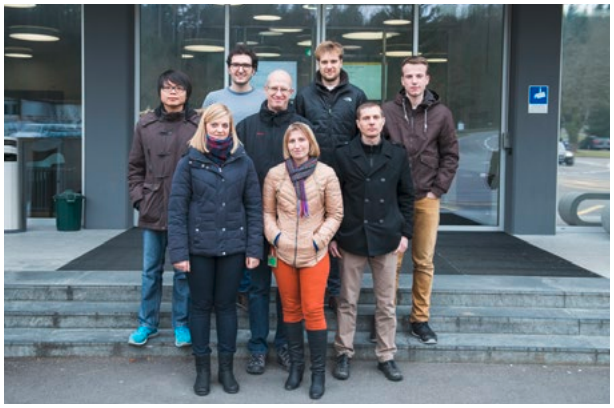

Membranes and Electrochemical Cells Group, December 2016.

Neutron Radiography of Electrochemical Systems Group, December 2016.

DISSERTATIONS 2016

Johannes Biesdorf

Neutron radiography of polymer electrolyte fuel cells: From conventional towards energy selective neutron imaging

Ph.D. Thesis No. 23308, ETH Zürich, Februar 2016.

Examiners: Prof. Dr. T.J. Schmidt, PSI Villigen/ETH Zürich
Prof. Dr. A. Wokaun, PSI Villigen/ETH Zürich
Dr. P. Boillat, PSI Villigen

Sebastian Eberhardt

Phosphoric acid electrolyte redistribution and loss in high temperature polymer electrolyte fuel cells

Ph.D. Thesis No. 23466, ETH Zürich, April 2016.

Examiners: Prof. Dr. T.J. Schmidt, PSI Villigen/ETH Zürich
Prof. Dr. M. Stampanoni, PSI Villigen/ETH Zürich
Prof. Dr. A. Wokaun, PSI Villigen/ETH Zürich
Dr. F.N. Büchi, PSI Villigen

Tobias Binninger

The interplay between Pt electrocatalyst nanoparticles and metal oxide support materials: A perspective on electrocatalytic properties, degradation, and X-ray scattering

Ph.D. Thesis No. 23685, ETH Zürich, Juli 2016.

Examiners: Prof. Dr. T.J. Schmidt, PSI Villigen/ETH Zürich
Prof. Dr. J.A. van Bokhoven, PSI Villigen/ETH Zürich
Dr. E. Fabbri, PSI Villigen

Sandra Elisabeth Temmel

Design and characterization of strained epitaxial thin film model catalysts: A combined physical and electrochemical study

Ph.D. Thesis No. 23680, ETH Zürich, Juli 2016.

Examiners: Prof. Dr. T.J. Schmidt, PSI Villigen/ETH Zürich
Prof. Dr. T. Lippert, PSI Villigen/ETH Zürich
Dr. E. Fabbri, PSI Villigen

Leonie O. Vogt

Reaction mechanism of Sn-based negative electrodes for Na-ion batteries

Ph.D. Thesis No. 23775, ETH Zürich, September 2016.

Examiners: Prof. Dr. P. Novák, PSI Villigen/ETH Zürich
Prof. Dr. M. Kovalenko, ETH Zürich
Dr. C. Villevieille, PSI Villigen

Joanna Maria Conder

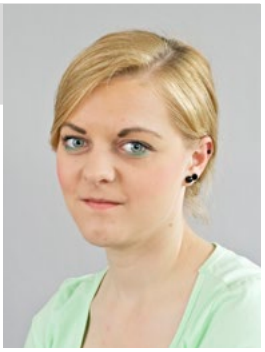

Asymmetrically functionalized separator for lithium–sulfur battery with polysulfide barrier properties

Ph.D. Thesis No. 23786, ETH Zürich, September 2016.

Examiners: Prof. Dr. P. Novák, PSI Villigen/ETH Zürich
Prof. Dr. M. Kovalenko, ETH Zürich
Dr. S. Trabesinger, PSI Villigen
Dr. L. Gubler, PSI Villigen

Hai-Jung Peng

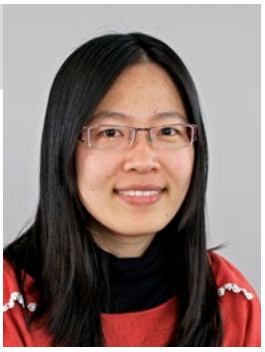

Unravelling the cell ageing phenomena in aprotic lithium-nickel-cobalt-manganese-oxide batteries

Ph.D. Thesis No. 23873, ETH Zürich, Oktober 2016.

Examiners: Prof. Dr. P. Novák, PSI Villigen/ETH Zürich
Prof. Dr. M. Kovalenko, ETH Zürich
Dr. S. Trabesinger, PSI Villigen
Dr. C. Villevieille, PSI Villigen
Dr. K. Leitner, ETH Zürich

Lucien Boulet Roblin

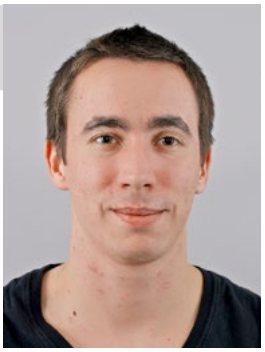

From bulk to near-surface investigations of 5 V lithium ion $LiNi_{0.5}Mn_{1.5}O_4$ vs graphite cells using operando techniques

Ph.D. Thesis No. 23906, ETH Zürich, November 2016.

Examiners: Prof. Dr. P. Novák, PSI Villigen/ETH Zürich
Prof. Dr. M. Kovalenko, ETH Zürich
Dr. C. Villevieille, PSI Villigen

Minglong He

Elucidating interface reactions in Li-ion batteries and supercapacitors by in situ gas analysis

Ph.D. Thesis No. 23920, ETH Zürich, November 2016.

Examiners: Prof. Dr. P. Novák, PSI Villigen/ETH Zürich
Prof. T.J. Schmidt, PSI Villigen/ETH Zürich
Dr. E. Jämstorp-Berg, PSI Villigen

Antoni Forner-Cuenca

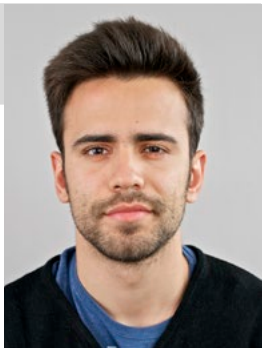

Novel gas diffusion layers with patterned wettability for advanced water management strategies in polymer electrolyte fuel cells

Ph.D. Thesis No. 23941, ETH Zürich, November 2016.

Examiners: Prof. Dr. T.J. Schmidt, PSI Villigen/ETH Zürich
Prof. Dr. A. Wokaun, PSI Villigen/ETH Zürich
Dr. P. Boillat, PSI Villigen

Sebastian Andreas Schmidt

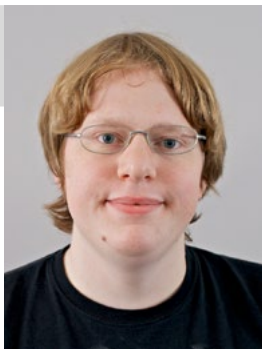

Transition metal diphosphonates, organic-inorganic hybrid electrode materials for Li-ion batteries

Ph.D. Thesis No. 23951, ETH Zürich, November 2016.

Examiners: Prof. Dr. P. Novák, PSI Villigen/ETH Zürich
Prof. Dr. M. Niederberger, ETH Zürich
Dr. C. Villevieille, PSI Villigen
Dr. S. Sallard, PSI Villigen

Albert Albert

Radiation-grafted polymer electrolyte membranes for water electrolysis

Ph.D. Thesis No. 24058, ETH Zürich, December 2016.

Examiners: Prof. Dr. T.J. Schmidt, PSI Villigen/ETH Zürich
Prof. Dr. G. Storti, ETH Zürich
Dr. L. Gubler, PSI Villigen

Véronique Sproll

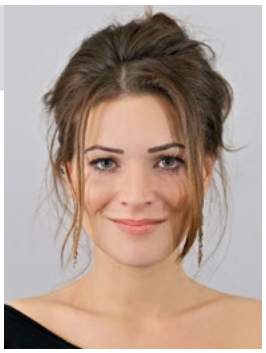

Structure-property correlations in radiation-grafted fuel cell membranes investigated on a polystyrene based model system

Ph.D. Thesis No. 24049, ETH Zürich, December 2016.

Examiners: Prof. Dr. T.J. Schmidt, PSI Villigen/ETH Zürich
Prof. Dr. W.R. Caseri, ETH Zürich
Dr. L. Gubler, PSI Villigen

EXCHANGE STUDENTS, DIPLOMA THESES, SUMMER STUDENTS, GUEST SCIENTISTS

Benjamin Hildebrandt
ETH Zürich

Cell monitoring for lithium-ion batteries using powerline communication
February – June 2016
November 2015 – March 2016 (Electrocatalysis & Interfaces).

Karin Blum
ETH Zürich

Performance analysis on a proton exchange membrane hydrogen pump
February – June 2016
(Membranes and Electrochemical Cells).

Adrian Heinritz
ETH Zürich

Onion-like-carbons and antimony-doped-tinoxide as catalyst support for low-temperature fuel cells
February – July 2016
(Electrocatalysis and Interfaces).

Experimental conditions for reproducible kinetic studies on gold electrodes for the Ce(III)/Ce(IV) redox-couple
September – December 2016
(Electrocatalysis and Interfaces).

Markus Gehring
RWTH Aachen University, Aachen, Germany

Determining factors for the cycling performance of lithium polysulphide battery cells
March – Mai 2016
(Electrochemical Energy Storage).

Ryo Asakura
ETH Zürich

Synthesis and electrochemical performance of Li_3VO_4
April – Mai 2016
(Electrochemical Energy Storage).

Characterization of nano-$LiNi_{0.80}Co_{0.15}Al_{0.05}O_2$ prepared and surface-coated by colloidal synthesis
September 2016 – January 2017
(Electrochemical Energy Storage).

Sophia Koch
Ostbayerische Technische Hochschule, Amberg-Weiden, Germany

Degradation of catalyst coated membranes in a membrane water electrolyzer
April – September 2016
(Membranes and Electrochemical Cells).

Harlin Brandvold
University of British Columbia, Vancouver, Canada

Pore network modelling of fuel cells: Modelling patterned wettability in gas diffusion layers
May – July 2016
(Neutron Radiography of Electrochemical Systems).

Hiroshi Ishikawa
University of Yamanashi, Yamanashi, Japan

Modeling and structural analysis of Pt-based catalyst layers in PEFCs
May – November 2016
(Electrocatalysis and Interfaces).

Marlène Demicheli
Grenoble INP Phelma, Grenoble, France

Research on non-noble metal catalysts for the reduction of oxygen
May – August 2016
(Electrocatalysis and Interfaces).

Simon Labbé
Grenoble INP Phelma, Grenoble, France

Numerical simulations of electrochemical flow cells with COMSOL Multiphysics
May – August 2016
(Electrocatalysis and Interfaces).

Victor Oliveros Colón Université de Rennes, Rennes, France	*Nano-architecturation of Cu nanopillars and deposition of Mn_xO_y as anodes for Li-ion batteries* May – August 2016 (Electrochemical Energy Storage).
Ahuja Navanshu ETH Zürich	*Image filtering of operando XTM data of PEFC* June – September 2016 (Fuel Cell Systems and Diagnostics).
Sunkyu Park University of Jules Verne Picardie, Amiens, France	*Optimization of the material P2-$Na_{0.67}Mn_xFe_yCo_jAl_zO_2$ as cathode for Na-ion batteries* July – September 2016 (Electrochemical Energy Storage).
Teng Ian Chan University of Macau, Macau, China	*Numerical optimization of an electrochemical wall-jet flow cell in 2D and 3D* September – November 2016 (Electrocatalysis and Interfaces).
Sobi Thomas Aalborg University, Aalborg, Denmark	*Limiting current analysis of HT-PEFC anodes* September 2016 – January 2017 (Fuel Cell Systems and Diagnostics).
Leslie Castillo Iracheta Istituto Tecnológico de Ciudad Madero, Madero, Mexico	*Switching to insertion of Li in $Li_{1+x}V_{1-y}Mn_yO_2$ anodes for Li-ion Batteries* September – December 2016 (Electrochemical Energy Storage).
Jan Dundalek University of Chemistry and Technology, Prague, Czech Republic	*Understanding the role of carbon properties for enhanced Li–S battery performance* September – December 2016 (Electrochemical Energy Storage).
Mathilde Fievez Chimie ParisTech, Paris, France	*2D and 3D nano-architectured electrodes for Li-ion batteries* September – December 2016 (Electrochemical Energy Storage).

.

SEMINAR, INVITED SPEAKERS

Cécile Tessier and Philippe Borel Saft SA, Bordeaux, France	*Research at Saft: advanced materials and processes for next generation Li (and Na)-ion batteries* January 13, 2016.
Gareth Hinds National Physical Laboratory (NPL), Electrochemistry Group, Teddington, Middlesex, UK	*Fuel cell reference electrode development at NPL* February 3, 2016.
Dr. Chih-Long Tsai Forschungszentrum Jülich, Jülich, Germany	*The development of all-solid-state Li batteries in IEK-1 at Forschungszentrum Jülich* February 24, 2016.
Prof. Clare P. Grey Department of Chemistry, University of Cambridge, UK	*Following function in real time: structure and dynamics in batteries and supercapacitors* March 7, 2016.
Prof. Philippe Sautet CNRS Lyon, France (Editor of ACS Catalysis)	*Theoretical aspects of materials and reactions related to catalysis and electrocatalysis* March 29, 2016.
ENE-Seminar / 2nd PSI Catalysis Symposium: **Prof. Marc Koper** Leiden University, Leiden, The Netherlands	*Electrocatalysis for fuel production: a tale of electrons, protons, and volcanoes* April 6, 2016.
Prof. Shinichi Komaba Tokyo University of Science, Shinjuku, Tokyo, Japan	*Binder chemistry for highly energetic Li-ion battery* May 12, 2016.
ECL / SCCER Heat and Electricity Storage Lecture: **Dr. Donat Adams Heer** Reliability Science and Technology Laboratory, Empa, Dübendorf	*Ab initio calculations on intercalation materials for Li-ion batteries* May 25, 2016.
Debora Pierucci CNRS – Laboratoire de Photonique et de Nanostructures, Paris, France	*2D materials: to graphene and beyond* June 8, 2016.
ECL / SCCER Heat and Electricity Storage Lecture: **Prof. Raffaella Buonsanti** Department of Chemical Sciences and Engineering, EPFL Lausanne, Sion	*Colloidal chemistry to advance every conversion studies* June 15, 2016.

ENE-Seminar / 3rd PSI Catalysis Symposium:

Dr.Ir. Alfons Molenbroek
Haldor Topsoe A/S, Lyngby, Denmark

In situ studies in industrial heterogeneous catalysis
June 23, 2016.

ENE-Seminar / 4th PSI Catalysis Symposium:

Prof. Alessandro Trovarelli
University of Udine, Department of Chemistry, Physics and the Environment, Udine, Italy

Forty years of catalysis by ceria: a success story
September 29, 2016.

Dr. Laurence Croguennec
ICMBC Laboratory, Bordeaux, France

High energy density positive electrode materials for Li and Na-ion batteries
October 26, 2016.

AWARDS

Claire Villevieille

ISE Prize for Electrochemical Materials Science
C. Villevieille
In recognition of her contributions to synthesis and characterization of electroactive materials for energy storage application.

67th Annual Meeting of the International Society of Electrochemistry, The Hague, the Netherlands, August 21–26, 2016.

Young Energy Storage Scientist Award (YESS) 2016
C. Villevieille
RS2E research network on electrochemical energy storage, led by Prof. Jean-Marie Tarascon of Collège de France, Paris. The jury was unanimous about the innovative quality of her project using improved neutron diffraction as a way to study batteries.

Batteries Event 2016, Nice, France, September 28, 2016.

Antoni Forner-Cuenca

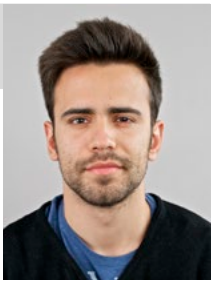

Energy Technology Division Graduate Student Award 2017
A. Forner-Cuenca
For his PhD thesis work «Novel gas diffusion layers with patterned wettability for advanced water management strategies in polymer electrolyte fuel cells».

The Electrochemical Society (ECS), New Orleans, May 2017.

ETH Medaille 2017
A. Forner-Cuenca
For his excellent PhD thesis «Novel gas diffusion layers with patterned wettability for advanced water management strategies in polymer electrolyte fuel cells».

Zürich, April 12, 2017.

CONFERENCES – SYMPOSIA

32nd PSI Electrochemistry Symposium April 27, 2016.

Electrolytes – The Underestimated Player in Electrochemical Processes

Organizers:
Thomas J. Schmidt, Cordelia Gloor, Electrochemistry Laboratory

Contributions from (in order of appearance):
Truls Norby, University of Oslo, Oslo, Norway
Klaus-Dieter Kreuer, Max-Planck-Institut für Festkörperforschung, Stuttgart, Germany
Wladyslaw Wieczorek, Politechnika Warszawska, Warszawa, Poland
Takeshi Abe, Kyoto University, Kyoto, Japan
Thomas A. Zawodzinski, University of Tennessee, Knoxville, USA

From left to right: *Takeshi Abe, Petr Novák, Claire Villevieille, Truls Norby, Wladyslaw Wieczorek, Lorenz Gubler, Thomas A. Zawodzinski, Thomas J. Schmidt, Klaus-Dieter Kreuer, Felix N. Büchi, Cordelia Gloor, Erik J. Berg.*

Registration, talks, poster session, lunch and discussions…

REVIEW ACTIVITIES OF THE LABORATORY

Journals

A ACS Applied Materials & Interfaces ♦ Advanced Energy Materials ♦ Advanced Functional Materials ♦ Advanced Materials ♦ Angewandte Chemie International Edition ♦ Applied Surface Science

C Carbon ♦ Chemical Science ♦ Chemical Reviews ♦ Chemistry of Materials ♦ ChemSusChem

E ECS Electrochemistry Letters ♦ Electrochemistry Communications ♦ Electrochimica Acta ♦ Energy and Environmental Science

F Fuel Cells

I International Journal of Hydrogen Energy

J Journal of the American Chemical Society ♦ Journal of the Electrochemical Society ♦ Journal of Fuel Cell Science and Technology ♦ Journal of Materials Chemistry A ♦ Journal of Membrane Science ♦ Journal of Physical Chemistry ♦ Journal of Power Sources ♦ Journal of Solid State Electrochemistry ♦ Journal of Synchrotron Radiation

N Nature ♦ Nature Chemistry ♦ Nature Communications ♦ Nature Energy ♦ Nature Materials ♦ Nature Scientific Reports

P Physical Chemistry Chemical Physics

R Radiation Physics and Chemistry ♦ RSC Advances

S Science ♦ Solid State Ionics

Organisations

A Agence National de Recherche, France ♦ Alexander von Humboldt-Stiftung, Germany

D Danish Council of Strategic Research ♦ Deutsche Forschungsgemeinschaft

E ETH Zürich Research Commission ♦ European Commission Research Executive Agency ♦ European Research Council

F FFG Österreichische Forschungsförderungsgesellschaft

G Gordon Research Conferences

N National Sciences and Engineering Research Council of Canada ♦ National Science Foundation, USA ♦ Netherlands Organisation for Scientific Research NWO

S SNF (Schweizerischer Nationalfonds) ♦ Society in Science

T The Research Council of Norway ♦ The Royal Swedish Academy of Scienes

Q Qatar National Research Fund

External Dissertations: Review Activities

Thomas J. Schmidt:

- Emma Oakton, ETH Zürich
- Yujia Deng, University of Copenhagen, Denmark
- Sebastian Helmly, University of Stuttgart, Germany
- Brian Knudsen, Technical University of Denmark Lyngby, Denmark

Petr Novák:

- Guobo Zeng, D-MATL, ETH Zürich
- Fabrizio Murgia, Université de Montpellier, France

INDUSTRIAL PARTNERS

Collaborations with Industrial Partners

The Laboratory had the pleasure to collaborate with the following industrial partners during the year 2016:

B BASF SE, Ludwigshafen, Germany

C Cellera, Caesarea, Israel

E ElringKlinger, Dettingen, Germany

H Heraeus Detschland GmbH & Co KG, Hanau, Germany

I IBM Zürich Research Laboratory, Rüschlikon ♦ IMERYS Graphite & Carbon, Bodio

O Osmotex AG, Thalwil

P Proton OnSite, Wallingford, CT, USA

S Saft SA, Bordeaux, France ♦ Siemens AG, Erlangen, Germany ♦ Swiss Hydrogen SA, Fribourg

T Toyota Motor Europe, Zaventem, Belgium

U UMICORE AG & Co. KG, Hanau, Germany

DOCUMENTATION

Project Collaborations with External Partners

BFE

P. Boillat Project leader	*In situ study of water transport processes in polymer electrolyte electrolysers with neutron imaging*
F.N. Büchi Project leader	*High Pressure Polymer Electrolyte Electrolysis* with Belenos Clean Power AG, Biel/Bienne
L. Gubler Project leader	*EL YDEG – Understanding of degradation signatures in water electrolyzers operated with variable input*
L. Gubler Project leader	*RFBmem – Chemistry and stability of grafted membranes for redox flow batteries*
T.J. Schmidt Project leader	*RENERG^2 (Renewable Energies in Future Energy Supply)*

CCEM

C. Bach, T.J. Schmidt Project leaders	*RENERG^2 (Renewable Energies in Future Energy Supply)* with ETH Zürich, Empa Dübendorf, EPF Lausanne, ZAHW Winterthur
F.N. Büchi Project leader	*ADMIST (Advanced Understanding of Micro Structures in Fuel Cells and Batteries through X-ray Imaging)* with Laboratory for Nanoelectronics ETH Zürich
L. Gubler Co-project leader	*Hy-Form: Formic acid – chemical storage of electrical energy and on-site hydrogen production for use in PEM fuel cells* with EPF Lausanne, Granit Technologies SA, ZHAW Winterthur
T.J. Schmidt Project leader	*From tailored CO_2-sorbent to optimized CO_2 electrochemical reduction catalyst: building tools for converting waste CO_2 to valuable chemicals* with ETH Zürich
C. Villevieille Project leader	*SLIB (All- Li-ion- Solid State Batteries* with ETH Zürich, Empa Dübendorf

EU

F.N. Büchi Project leader	*Auto-Stack CORE (Automotive Fuel Cell Stack Cluster Initiative for Europe)*
L. Gubler Project leader	*NOVEL (Novel materials and system designs for low cost, efficient and durable PEM electrolysers)*

KTI

F.N. Büchi Co-Leader Capacity Area 2	*SCCER Mobility: Efficient Technologies and Systems for Mobility*
F.N. Büchi , P. Boillat Co-Project leaders	*SCCER Mobility: Thermo-neutral fuel cells*
P. Novák Work package leader	*SCCER Heat & electricity storage: Materials, systems, and modelling*
T.J. Schmidt Director	*Swiss Competence Center for Energy Research – Heat & Electricity Storage*
T.J. Schmidt Work package leader	*SCCER Heat & Electricity Storage: Catalytic and Electrocatalytic CO_2 Reduction*

PSI Research Commission

T.J. Schmidt Co-Project leader	*Improved Insight into Catalysis Mechanisms via Nanopatterned Metal Structures (Nanocat)* Cross Initiative with Prof. J. Gobrecht; Prof. J.A. van Bokhoeven

SNSF

E.J. Berg Project leader	*Interphase formation on high voltage and energy Li-ion cathodes* Ambizione Energy
P. Boillat Project leader	*Synthesis and characterization of porous materials with patterned wettability for advanced fuel cell water management strategies*
F.N. Büchi Project leader	*Sub-second dynamics of liquid water transport in polymer electrolyte fuel cells revealed by 4D X-ray Tomographic Microscopy*
F.N. Büchi Co-project leader	*NFP70: Designing multifunctional materials for proton exchange membrane fuel cells* with Institute for Computational Physics, ZHAW Winterthur
E. Fabbri Project leader	*Designing novel electrocatalysts for fuel cells and electrolyzers by tailoring perovskite surface properties* SNSF Ambizione project
L. Gubler Project leader	*Radiation grafted proton conducting membranes for high-temperature polymer electrolyte fuel cells*
L. Gubler/S. Trabesinger Project leader/Co-project leader	*Lithium conducting polymer electrolytes with polysulphide barrier properties*
P. Novák Project leader	*New oxyphosphates as high specific charge electrode materials for lithium-ion batteries*
P. Novák Project leader	*In situ research on new generation of electrochemical capacitors* (Polish-Swiss research programme)
S. Sallard Project leader	*Hybrid organic-inorganic lithium metal diphosphonates and derivatives, new insertion materials for Li-ion batteries*

T.J. Schmidt Project leader	*Designing nano-extended multimetallic aerogel fuel cell catalysts for oxygen reduction reaction* with TU Dresden, Germany
T.J. Schmidt Experimental project leader	*NCCR Marvel Experimental Platform Project* Development of advanced electrocatalysts for water splitting: Correlation between electronic structure, surface properties and electrochemical activity.
C. Villevieille Project leader	*Surface and interface investigations of high density energy electrodes for sodium-ion batteries*

Industry

L Gubler Project leader	*Synthesis of custom polyelectrolytes* Osmotex AG, Thalwil
M. El Kazzi Project leader	*Analyses of lithium-ion battery electrodes* Toyota Motor Europe NV/SA, Brussels, Belgium
P. Novák Project leader	*Forschungsnetzwerk «Elektrochemie und Batterien»* BASF SE, Ludwigshafen, Germany
T.J. Schmidt Project leader	*Advanced degradation studies on PBI/H_3PO_4 based MEAs for high temperature PEFCs* BASF SE, Ludwigshafen, Germany
S. Trabesinger Project leader	*Graphite für Lithiumionen-Batterien* Imerys Graphite & Carbon, Bodio
C. Villevieille Project leader	*Operando X-ray tomography applied to all-solid-state-batteries* Toyota Europe, Belgium
C. Villevieille Project leader	*Study of full cell reaction mechanism of lithium-ion batteries using 5 V spinel materials* Saft SA, Bordeaux, France

Teaching Activities

University Level Teaching

Prof. Dr. P. Novák	*Elektrochemie* ETH Zürich, HS 2016.
Prof. Dr. P. Novák	*Basics of Battery Electrochemistry* SCCER Energy Storage in Batteries: Materials, Systems, and Manufacturing 2016 Summer School ETH Zürich, Möschberg, July 11–15, 2016.
Prof. Dr. T.J. Schmidt	*Renewable Energy Technologies 2* ETH Zürich, FS 2016.
Prof. Dr. T.J. Schmidt	*Physical Electrochemistry & Electrocatalysis* ETH Zürich, FS 2016.
C. Villevieille	*Characterizations of cell components* SCCER Energy Storage in Batteries: Materials, Systems, and Manufacturing 2016 Summer School ETH Zürich, Möschberg, July 11–15, 2016.

Lecture Courses at other Schools

P. Boillat	*Neutron Imaging of Fuel Cells: Retrospective and Future Work* Tsinghua University, Beijing, China, November 3, 2016.

Contributions to Courses at Universities, FHL, and other Institutes

L. Gubler	*Renewable Energy Technologies 2* ETH Zürich, May 10, May 17, May 24, May 31, 2016.
L. Gubler	*Energy Storage Systems* Lucerne University of Applied Sciences and Arts, April 13, 2016.

Publications

Peer Reviewed Papers

D.F. Abbott, D. Lebedev, K. Waltar, M. Povia, M. Nachtegaal, E. Fabbri, C. Copéret, T.J. Schmidt
Iridium oxide for the oxygen evolution reaction: Correlation between particle size, morphology, and the surface hydroxo layer from operando XAS
doi : 10.1021/acs.chemmater.6b02625, Chem. Mater. **28** (18), 6591–6604 (2016).

T. Agaesse, A. Lamibrac, F.N. Büchi, J. Pauchet, M. Prat
Validation of pore network simulations of ex-situ water distributions in a gas diffusion layer of proton exchange membrane fuel cells with X-ray tomographic images
doi: 10.1016/j.jpowsour.2016.09.076, J. Power Sources **331**, 462–474 (2016).

A. Albert, T. Lochner, T.J. Schmidt, L. Gubler
Stability and degradation mechanisms of radiation-grafted polymer electrolyte membranes for water electrolysis
doi: 10.1021/acsami.6b03050, ACS Appl. Mater. Interfaces **8**, 15297–15306 (2016).

J. Biesdorf, A. Forner-Cuenca, M. Siegwart, T.J. Schmidt, P. Boillat
Statistical analysis of isothermal cold starts of PEFCs: Impact of gas diffusion layer properties
doi: 10.1149/2.1071610jes, J. Electrochem. Soc. **163**, F1258–F1266 (2016).

J. Billaud, F. Bouville, T. Magrini, C. Villevieille, A. Studard
Magnetically aligned graphite electrodes for high rate performance Li-ion batteries
doi: 10.1038/nenergy.2016.97, Nature Energy **1**, 16097 (2016).

T. Binninger, E. Fabbri, A. Patru, M. Garganourakis, J. Han, D.F. Abbott, O. Sereda, R. Kötz, A. Menzel, M. Nachtegaal, T.J. Schmidt
Electrochemical flow-cell setup for in situ X-ray investigations: I. Cell for SAXS and XAS at synchrotron facilities
doi:10.1149/2.0201610jes, J. Electrochem. Soc. **163** (10), H906–H912 (2016).

A. Borgschulte, R. Delmelle, R.B. Duarte, A. Heel, P. Boillat, E. Lehmann
Water distribution in a sorption enhanced methanation reactor by time resolved neutron imaging
doi: 10.1039/C5CP07686B, Physical Chemistry Chemical Physics **18**, 17217–17223 (2016).

L. Boulet-Roblin, P. Borel, D. Sheptyakov, C. Tessier, P. Novák, C. Villevieille
Operando neutron powder diffraction using cylindrical cell design: The case of $LiNi_{0.5}Mn_{1.5}O_4$ vs. graphite
doi: 10.1021/acs.jpcc.6b05777, J. Phys. Chem. C **120**, 17268–17273 (2016).

L. Boulet-Roblin, C. Villevieille, P. Borel, C. Tessier, P. Novák, M. Ben Yahia
Versatile approach combining theoretical and experimental aspects of Raman spectroscopy to investigate battery materials: The case of $LiNi_{0.5}Mn_{1.5}O_4$ spinel
doi: 10.1021/acs.jpcc.6b04155, J. Phys. Chem. C **120**, 16377–16382 (2016).

J. Conder, A. Forner-Cuenca, E. Müller-Gubler, L. Gubler, P. Novák, S. Trabesinger
Performance-enhancing asymmetric separator for lithium–sulfur batteries
doi: 10.1021/acsami.6b04662, ACS Appl. Mater. Interfaces **8**, 18822–18831 (2016).

E. Coz, J. Théry, P. Boillat, V. Faucheux, D. Alincant, P. Capron, G. Gébel
Water management in a planar air-breathing fuel cell array using operando neutron imaging
doi: 10.1016/j.jpowsour.2016.09.041, J. Power Sources **331**, 535–543 (2016).

S.H. Eberhardt, F. Marone, M. Stampanoni, F.N. Büchi, T.J. Schmidt
Operando X-ray tomographic microscopy imaging of HT-PEFC: A comparative study of phosphoric acid electrolyte migration
doi: 10.1149/2.0801608jes], J. Electrochem. Soc. **163**, F842–F847 (2016).

M. El Kazzi, I. Czekaj, E.J. Berg, P. Novák, M.A. Brown
Investigation of Li-ion solvation in carbonate based electrolytes using near ambient Pressure Photoemission
doi: 10.1007/s11244-015-0518-2, Top. Catal. **59**, 628–634 (2016).

T. Engl, L. Gubler, T.J. Schmidt	*Fuel electrode carbon corrosion in high temperature polymer electrolyte fuel cells – crucial or irrelevant ?* doi: 10.1002/ente.201500217, Energy Technol. **4**, 65–74 (2016).
G. Ferraresi, L. Czornomaz, C. Villevieille, P. Novák, M. El Kazzi	*Mechanism of the carbonate-based-electrolyte degradation and its effects on the electrochemical performance of $Li_{1+x}(Ni_aCo_bMn_{1-a-b})_{1-x}O_2$ cells* doi: 10.1016/j.jpowsour.2016.10.031, J. Power Sources **335**, 91–97 (2016).
A. Forner-Cuenca, V. Manzi-Orezzoli, J. Biesdorf, M.E. Kazzi, D. Streich, L. Gubler, T.J. Schmidt, P. Boillat	*Advanced water management in PEFCs: Diffusion layers with patterned wettability: I. Synthetic routes, wettability tuning and thermal stability* doi: 10.1149/2.0271608jes, J. Electrochem. Soc. **163**, F788–F801 (2016).
A. Forner-Cuenca, J. Biesdorf, A. Lamibrac, V. Manzi-Orezzoli, F.N. Büchi, L. Gubler, T.J. Schmidt, P. Boillat	*Advanced water management in PEFCs: Diffusion layers with patterned wettability: II. Measurement of capillary pressure characteristic with neutron and synchrotron imaging* doi: 10.1149/2.0511609jes, J. Electrochem. Soc. **163**, F1038–F1048 (2016).
A. Forner-Cuenca, J. Biesdorf, V. Manzi-Orezzoli, L. Gubler, T.J. Schmidt, P. Boillat	*Advanced water management in PEFCs: Diffusion layers with patterned wettability: III. Operando characterization with neutron imaging* doi: 10.1149/2.0891613jes, J. Electrochem. Soc. **163**, F1389–F1398 (2016).
J.L. Gómez-Cámer, C. Bünzli, M.M. Hantel, T. Poux, P. Novák	*On the correlation between electrode expansion and cycling stability of graphite/Si electrodes for Li-ion batteries* doi: 10.1016/j.carbon.2016.04.022, Carbon **105**, 42–51 (2016).
A. Guéguen, P. Novák, E.J. Berg	*XPS study of the interface evolution of carbonaceous electrodes for Li-O_2 batteries during the 1st cycle* doi: 10.1149/2.0351613jes, J. Electrochem. Soc. **163**, A2545–A2550 (2016).
A. Guéguen, D. Streich, M. He, M. Mendez, F.F. Chesneau, P. Novák, E.J. Berg	*Decomposition of $LiPF_6$ in high energy lithium-ion batteries studied with online electrochemical mass spectrometry* doi: 10.1149/2.0981606jes, J. Electrochem. Soc. **163**, A1095–A1100 (2016).
M. He, L. Boulet-Roblin, P. Borel, C. Tessier, P. Novák, C. Villevieille, E.J. Berg	*Effects of solvent, lithium salt, and temperature on stability of carbonate-based electrolytes for 5.0 V $LiNi_{0.5}Mn_{1.5}O_4$ electrodes* doi: 10.1149/2.0201602jes, J. Electrochem. Soc. **163**, A83–A89 (2016).
M. He, K. Fic, E. Frąckowiak, P. Novák, E.J. Berg	*Influence of aqueous electrolyte concentration on parasitic reactions in high-voltage electrochemical capacitors* doi: 10.1016/j.ensm.2016.06.001, Energy Storage Materials **5**, 111–115 (2016).
M. He, K. Fic, E. Frąckowiak, P. Novák, E.J. Berg	*Ageing phenomena in high-voltage aqueous supercapacitors investigated by in situ gas analysis* doi: 10.1039/C5EE02875B, Energy Environ. Sci. **9**, 623–633 (2016).
J. Herranz, J. Durst, E. Fabbri, A. Patru, X. Cheng, A.A. Permyakova, T.J. Schmidt	*Interfacial effects on the catalysis of the hydrogen evolution, oxygen evolution and CO_2-reduction reactions for (co-)electrolyzer development* doi: 10.1016/j.nanoen.2016.01.027, Nano Energy **29**, 4–28 (2016).
S. Henning, L. Kühn, J. Herranz, J. Durst, T. Binninger, M. Nachtegaal, M. Werheid, W. Liu, M. Adam, S. Kaskel, A. Eychmüller, T.J. Schmidt	*Pt-Ni Aerogels as unsupported electrocatalysts for the oxygen reduction reaction* doi: 10.1149/2.0251609.jes, J. Electrochem. Soc. **163**, F1–F6 (2016).

A. Iranzo, J. Biesdorf, M. Cochet, A. Salva, P. Boillat, F. Rosa	*Effect of serpentine multi-pass flow field channel orientation in the liquid water distributions and cell performance* doi: 10.1002/fuce.201600096, Fuel Cells **16**, 777–783 (2016).
A. Iranzo, P. Boillat, A. Salva, J. Biesdorf	*PEM fuel cell operation under air and O_2 feed: Analysis of cell performance and liquid water distributions* doi: 10.1002/fuce.201500145, Fuel Cells **16**, 463–468 (2016).
L. Kühn, A.-K. Herrmann, B. Rutkowski, M. Oezaslan, M. Nachtegaal, M. Klose, L. Giebeler, N. Gaponik, J. Eckert, T.J. Schmidt, A. Czyrska-Filemonowicz, A. Eychmüller	*Alloying behavior of self-assembled noble metal nanoparticles* doi: 10.1002/chem.201602487, Chem. Eur. J. **22**, 13446–13450 (2016).
A. Lamibrac, J. Roth, M. Toulec, F. Marone, M. Stampanoni, F.N. Büchi	*Characterization of liquid water saturation in gas diffusion layers by X-ray tomographic microscopy* doi: 10.1149/2.0401603jes, J. Electrochem. Soc. **163** (3), F202–F209 (2016).
T. Lippert, T.J. Schmidt	*Investigating the role of strain towards the oxygen reduction activity on model thin film Pt catalysts* doi: 10.1021/acscatal.6b01836, ACS Catalysis **6**, 7566–7576 (2016).
Q. Meyer, S. Ashton, P. Boillat, M. Cochet, E. Engebretsen, D.P. Finegan, X. Lu, J.J. Bailey, N. Mansor, R. Abdulaziz, O.O. Taiwo, R. Jervis, S. Torija, P. Benson, S. Foster, P. Adcock, P.R. Shearing, D.J.L. Brett	*Effect of gas diffusion layer properties on water distribution across air-cooled, open-cathode polymer electrolyte fuel cells: A combined ex-situ X-ray tomography and in-operando neutron imaging study* doi: 10.1016/j.electacta.2016.06.068, Electrochim. Acta **211**, 478–487 (2016).
Q. Meyer, S. Ashton, S. Torija, C. Gurney, P. Boillat, M. Cochet, E. Engebretsen, D.P. Finegan, P. Adcock, P.R. Shearing, D.J.L. Brett	*Nitrogen blanketing and hydrogen starvation in dead-ended-anode polymer electrolyte fuel cells revealed by hydro-electro-thermal analysis* doi: 10.1016/j.electacta.2016.04.018, Electrochim. Acta **203**, 198–205 (2016).
O. Nibel, T.J. Schmidt, L. Gubler	*Bi-functional ion-conducting polymer electrolyte for the vanadium redox flow battery with high selectivity* doi: 10.1149/2.0441613jes, J. Electrochem. Soc. **163** (13), A2563–A2570 (2016).
E. Oakton, D. Lebedev, A. Fedorov, F. Krumeich, J. Tillier, O. Sereda, T.J. Schmidt, C. Coperet	*A simple one-pot Adams method route to conductive high-surface area IrO_2-TiO_2 materials* doi: 10.1039/C5NJ02400E, New J. Chem. **40**, 1834–1838 (2016).
M. Oezaslan, W. Liu, M. Nachtegaal, A.I. Frenkel, B. Rutkowski, M. Werheid, A.-K. Herrmann, C. Laugier-Bonnaud, H.-C. Yilmaz, N. Gaponik, A. Czyrska-Filemonowicz, A. Eychmüller, T.J. Schmidt	*Homogeneity and elemental distribution in self-assembled bimetallic Pd-Pt aerogels prepared by a spontaneous one-step gelation process* doi: 10.1039/c6cp03527b, Phys. Chem. Chem. Phys. **18**, 20640–20650 (2016).
A. Patru, A. Rabis, S. Temmel, R. Kötz, T.J. Schmidt	*Pt/IrO_2-TiO_2 cathode catalyst for low temperature polymer electrolyte fuel cells – application in MEAs, performance and stability issues* doi: 10.1016/j.cattod.2015.09.009, Catalysis Today **262**, 161–169 (2016).

A. Perez, D. Batuk, M. Saubanère, G. Rousse, D. Foix, E. McCalla, E.J. Berg, R. Dugas, K.H.W. van den Bos, M.L. Doublet, De Gonbeau, A.M. Abakumov, G. Van Tendeloo, J.M. Tarascon	*Strong oxygen participation in the redox governing the structural and electrochemical properties of Na-rich layered oxide Na_2IrO_3* doi: 10.1021/acs.chemmater.6b03338, Chemistry of Materials **28**, 8278–8288 (2016).
T. Poux, P. Novák, S. Trabesinger	*Pitfalls in Li-S rate-capability evaluation* doi: 10.1149/2.0181607jes, J. Electrochem. Soc. **163**, A1139–A1145 (2016).
J. Seweryn, J. Biesdorf, T.J. Schmidt, P. Boillat	*Neutron radiography of the water/gas distribution in the porous layers of an operating electrolyser* doi: 10.1149/2.0641607jes, J. Electrochem. Soc. **163**, F3009–F3011 (2016).
V. Sproll, G. Nagy, U. Gasser, J. Embs, M. Obiols-Rabasa, T.J. Schmidt, L. Gubler, S. Balog	*Radiation grafted ion-conducting membranes: the influence of variations in base film nanostructure* doi: 10.1021/acs.macromol.6b00180, Macromolecules **49**, 4253–4264 (2016).
V. Sproll, G. Nagy, U. Gasser, S. Balog, S. Gustavsson, T.J. Schmidt, L. Gubler	*Structure-property correlations of ion-containing polymers for fuel cell applications* doi: 10.1016/j.radphyschem.2015.01.036, Radiat. Phys. Chem. **118**, 120–123 (2016).
V. Sproll, T.J. Schmidt, L. Gubler	*Grafting design: a strategy to increase the performance of radiation grafted membranes* doi: 10.1002/pi.5041, Polym. Int. **65**, 174–180 (2016).
P. Stahl, J. Biesdorf, P. Boillat, K.A. Friedrich	*An investigation of PEFC sub-zero startup: Evidence of local freezing effects* doi: 10.1149/2.0771614jes, J. Electrochem. Soc. **163**, F1535–F1542 (2016).
D. Streich, A. Guéguen, M. Mendez, F. Chesneau, P. Novák, E.J. Berg	*Online electrochemical mass spectrometry of high energy lithium nickel cobalt manganese oxide / graphite half- and full-cells with ethylene carbonate and fluoroethylene carbonate based electrolytes* doi: 10.1149/2.0801606jes, J. Electrochem. Soc. **163**, A964–A970 (2016).
D. Streich, P. Novák	*Electrode-electrolyte interface characterization of carbon electrodes in Li-O_2 batteries: Capabilities and limitations of infrared spectroscopy* doi: 10.1016/j.electacta.2015.12.061, Electrochim. Acta **190**, 753–757 (2016).
M. Suermann, T.J. Schmidt, F.N. Büchi	*Cell performance determining parameters in high pressure water electrolysis* doi: 10.1016/j.electacta.2016.06.120, Electrochim. Acta **211**, 989–997 (2016).
S. Taylor, E. Fabbri, P. Levecque, T.J. Schmidt, O. Conrad	*The effect of platinum loading and surface morphology on oxygen reduction activity* doi: 10.1007/s12678-016-0304-3, Electrocatalysis **7** (4), 287–296 (2016).
S.M. Taylor, A. Patru, D. Streich, M. El Kazzi, E. Fabbri, T.J. Schmidt	*Vanadium (V) reduction reaction on modified glassy carbon electrodes – role of oxygen functionalities and microstructure* doi: 10.1016/j.carbon.2016.08.044, Carbon **109**, 472–478 (2016).
S.E. Temmel, E. Fabbri, D. Pergolesi, T. Lippert, T.J. Schmidt	*Tuning the surface electrochemistry by strained epitaxial Pt thin film model electrodes prepared by pulsed laser deposition* doi: 10.1002/admi.201600222, Adv. Mater. Interfaces 1600222 (2016).
S.E. Temmel, E. Fabbri, D. Pergolesi, T. Lippert, T.J. Schmidt	*Investigating the role of strain towards the oxygen reduction activity on model thin film Pt catalysts* doi: 10.1021/acscatal.6b01836, ACS Catal. **6**, 7566–7576 (2016).
S.E. Temmel, S.A. Tschupp, T.J. Schmidt	*A highly flexible electrochemical flow cell designed for the use of model electrode materials on non-conventional substrates* doi: 10.1063/1.4947459, Rev. Sci. Instrum. **87**, 045115 (2016).

J. Tillier, T. Binninger, M. Garganourakis, A. Patru, E. Fabbri, T.J. Schmidt, O. Sereda
Electrochemical flow-cell setup for in situ X-ray investigations: II. Cell for SAXS on a multi-purpose laboratory diffractometer
doi: 10.1149/2.0211610jes, J. Electrochem. Soc. **163** (10), H913–H920 (2016).

A.S. Tremsin, M.G. Makowska, D. Perrodin, T. Shalapska, I.V. Khodyuk, P. Trtik, P. Boillat, S.C. Vogel, A.S. Losko, M. Strobl, L.T. Kuhn, G.A. Bizarri, E.D. Bourret-Courchesne
In situ diagnostics of the crystal-growth process through neutron imaging: Application to scintillators
doi: 10.1107/S1600576716004350, J. Appl. Cryst. **49**, 743–755 (2016).

L.O. Vogt, C. Villevieille
$MnSn_2$ negative electrode for Na-ion batteries: A conversion-based reaction dissected
doi: 10.1039/C6TA07788A, J. Mater. Chem. A **4**, 19116–19122 (2016).

L.O. Vogt, C. Villevieille
$FeSn_2$ and $CoSn_2$ electrode materials for Na-Ion batteries
doi: 10.1149/2.0791607jes, J. Electrochem. Soc. **163**, A1306–A1310 (2016).

I.V. Zenyuk, A. Lamibrac, J.J. Eller, D.Y. Parkinson, F. Marone, F.N. Büchi, A.Z. Weber
Investigating evaporation in gas diffusion layers for fuel cells with X-ray computed tomography
doi: 10.1021/acs.jpcc.6b10658, J. Phys. Chem. C **120** (50), 28701–28711 (2016).

Talks

Invited Talks

E.J. Berg
Electrode/electrolyte stability in Li-ion batteries: Operando gas analysis
Japanese Swiss Energy Materials Workshop, Tokyo, Japan, October 5, 2016.

E.J. Berg
Development and application of operando gas analysis for lithium based rechargeable batteries
Battery-Monday-seminar, Chair of Structural Chemistry, University of Uppsala, Uppsala, Sweden, September 26, 2016.

E.J. Berg
Development and application of online electrochemical mass spectrometry (OEMS)
Seminar, Chair of Energy Materials, Collège de France, Paris, France, May13, 2016.

P. Boillat
Novel fuel cell gas diffusion layers with patterned wettability: An in situ study with neutron imaging
Zing Functional Energy Materials Conference, Dubrovnik, Croatia, September 28 – October 1, 2016.

P. Boillat
Neutron imaging of polymer electrolyte fuel cells (PEFCs)
MLZ Conference: Neutrons for Energy, Bad Reichenhall, Germany, July 18–22, 2016.

F.N. Büchi
Trends und Potentiale der Brennstoffzellen-Entwicklung
Workshop: Brennstoffzellen in automobilen Anwendungen – sicher und nachhaltig? EMPA Dübendorf, January 26, 2016.

F.N. Büchi
Analysis of voltage losses in polymer electrolyte electrolysis cells
Second International Workshop: Durability and Degradation Issues in PEM Electrolysis Cells and its Components, Freiburg, Germany, February 16, 2016.

F.N. Büchi	*X-ray imaging of polymer Electrolyte fuel cells* Fuel Cells Science and Technology 2016, Glasgow, United Kingdom, April 13, 2016.
F.N. Büchi	*Imaging as a diagnostic tool for PEFC – membrane degradation by pinholes* Summer School FCT2016, University of Technology of Belfort-Montbéliard, Belfort, France, July 5, 2016.
F.N. Büchi	*X-ray imaging of water in polymer electrolyte fuel cells* 11th European Fluid Mechanics Conference, EFMC11, Sevilla, Spain, September 13, 2016.
F.N. Büchi	*X-ray imaging of liquid water in PEFC* 57th Battery Symposium, Makuhari Messe, Chiba, Japan, November 28, 2016.
F.N. Büchi	*X-ray imaging: Powerful tool for fuel cell development* Fuel Cell Nanomaterials Center, University of Yamanashi, Kofu, Japan, December 1, 2016.
E. Fabbri	*Oxide electrocatalysts for application in fuel cells and electrolyzers* 3rd European-Korean Workshop on Advanced Materials for Energy, Warsaw, Poland, September 22, 2016.
E. Fabbri	*Insights into perovskite catalysts for the electrochemical splitting of water* EMRS Fall Meeting, Warsaw, Poland, September 19–22, 2016.
L. Gubler	*Membranes for water electrolysis – target-oriented choice and design of materials* Second International Workshop on Durability and Degradation Issues in PEM Electrolysis Cells and its Components, Fraunhofer ISE, Freiburg, Germany, February 16–17, 2016.
P. Novák	*Materialforschung für Batterien: Realität vs. Wunschdenken* KLiB Meeting, Frankfurt/Main, Germany, September 22, 2016.
P. Novák	*A reality check on battery materials development* Plenary Presentation at the 17th International Meeting on Lithium Batteries, Chicago, IL, USA, June 20, 2016.
P. Novák	*From bulk to near-surface investigations of $LiNi_{0.5}Mn_{1.5}O_4$ using operando techniques (neutron/X-ray/Raman/OEMS)* Keynote Presentation at the IBA 2016 – International Battery Association Meeting, Nantes, France, March 22, 2016.
T.J. Schmidt	*Elektrochemie: Lösungen für die Langzeitspeicherung* Symposium Die Zukunft der Energiespeicher – Trends und offene Fragen, Zürich, December 14, 2016.
T.J. Schmidt	*Oxygen evolution: The key for efficient water splitting* University of Birmingham School of Chemistry, Birmingham, UK, December 2, 2016.
T.J. Schmidt	*Polymer electrolyte water electrolysis: Technical gaps and challenges* UK Energy Storage Conference 2016, Birmingham, UK, November 30 – December 2, 2016.
T.J. Schmidt	*Durability challenges for PEM fuel cells* International Workshop Fuel to Electricity, Cape Town, South Africa, October 26–27, 2016.

T.J. Schmidt	*Technologien für Dezentrale Speicherlösungen – Eine Übersicht* Energiespeichersysteme – Dezentrale Batteriespeicherlösungen, Hightech Zentrum Aarau AG, Brugg, October 18, 2016.
T.J. Schmidt	*Hydrogen and fuel cell research @ PSI* IEA Advanced Fuel Cells Implementing Agreement, Annex 33 Stationary Fuel Cells, Villigen, October 12–13, 2015.
T.J. Schmidt	*Materials for PEM water electrolysis* EMRS Fall Meeting, Warsaw, Poland, September 19–22, 2016.
T.J. Schmidt	*Oxygen evolution on nano-sized non-noble metal catalysts* International Conference on Advances in Semiconductors and Catalysts for Photo-electrochemical Fuel Production, Berlin, Germany, September 5–6, 2016.
T.J. Schmidt	*Water electrolysis: Gaps for new innovations* Workshop Breakthrough Innovations, Park InnovAare, Villigen, August 23, 2016.
T.J. Schmidt	*Water electrolysis: From materials to systems* Seminar at DTU Physics, Lyngby, Denmark, August 18, 2016.
T.J. Schmidt	*Power-to-hydrogen-to-power* Open Workshop *Energy Storage in the Electricity Grid*, Dublin, Ireland, March 23, 2016.
T.J. Schmidt	*Insights into oxygen evolution electrocatalysis on perovskites* 80. Jahrestagung der DPG und DPG Frühjahrstagung 2016, Regensburg, Germany, March 6–11, 2016.
T.J. Schmidt	*Technische Optionen der Energiespeicherung* Technische Gesellschaft Zürich, Zürich, March 7, 2016.
T.J. Schmidt	*Development of advanced water splitting electrocatalysts* NCCR Marvel Workshop, Villigen, March 3, 2016.
T.J. Schmidt	*Oxygen evolution on non-noble metal electrocatalysts* Workshop Munich ECS Student Chapter, Munich, Germany, February 15, 2016.
T.J. Schmidt	*H_2 production by electrolysis* Workshop on Electrolysis, Aalborg University, Kopenhagen, Denmark, February 9, 2016.
V. Sproll	*Radiation grafted membranes for fuel cells: Understanding and improving polymer architecture* University of Applied Sciences Esslingen, Esslingen, Germany, October 5, 2016.
S. Trabesinger	*Comparative Commercial-Viability Evaluation of Rechargeable-Battery Chemistries* MRS Spring Meeting, Phoenix, USA, March 30, 2016.
S. Trabesinger	*Comparative evaluation of battery chemistries* INESS 2016, Almaty, Kazakhstan, August 12, 2016.
S. Trabesinger	*Comparative evaluation of battery chemistries* HIU, Ulm, Germany, October 18, 2016.
C. Villevieille	*Advances in operando neutron diffraction measurements applied to batteries* SENS workshop, Bordeaux, France, May 29, 2016.

C. Villevieille	*Designing, synthesizing, and understanding of host materials for battery electrodes* University of Grenoble, France, May 18, 2016.
C. Villevieille	*Operando techniques to probe battery materials* Nanosa15 – Nanoscale Assemblies of Semiconductor Nanocrystals, Metal Nanoparticles and Single Molecules: Theory, ExpIMLB, Chicago, USA, June 22, 2016.
C. Villevieille	*Recent development in the field of Na-ion batteries* SCCER Symposium, Lucerne, October 24, 2016.
C. Villevieille	*From bulk to surface analyses of 5 V cathode materials* MRS Fall Meeting, Boston, USA, November 29, 2016.
C. Villevieille	*Pushing the limits of operando techniques* EMPA Swiss-Japanese Symposium, Dübendorf, March 8, 2016.
C. Villevieille	*Pushing the limits of operando techniques* IBA, Nantes, France, March 24, 2016.

Contributed Talks

L. Boulet, J. Conder, C. Villevieille	*Operando techniques to probe battery materials* International Battery Association (IBA), Nantes, France, March 20–25, 2016.
L. Boulet, J. Conder, S. Sallard, C. Villevieille	*Operando techniques to probe battery materials* 18th Internat. Meeting on Lithium Batteries (IMLB), Chicago, USA, June 19–24, 2016.
F.N. Büchi, S. H. Eberhardt, J. Halter, T.J. Schmidt	*Imaging phosphoric acid in HT-PEFC: What has been learnt so far?* PRiME 2016 / 230th ECS Meeting, Symposium on Polymer Electrolyte Fuel Cells 16, Honolulu, HI, USA, October 2–7, 2016.
M. Cochet, P. Groeninger, A. Forner-Cuenca, D. Scheuble, P. Boillat	*Neutron imaging characterization for optimization of an evaporation cooled polymer electrolyte fuel cell (PEFC)* 67th ISE Annual Meeting, The Hague, The Netherlands, August 21–26, 2016.
J. Eller, F.N. Büchi	*Operando water cluster connectivity and liquid permeability in PEFC gas diffusion layers* 13th Symposium on Fuel Cell and Battery Modelling and Experimental Validation – ModVal 13, Lausanne, March 22–23, 2016.
J. Eller, F.N. Büchi	*Characterization of water cluster connectivity and fluid transport in PEFC gas diffusion layers* PRiME 2016 / 230th ECS Meeting, Symposium on Polymer Electrolyte Fuel Cells 16, Honolulu, HI, USA, October 2–7, 2016.
J. Eller, A. Lamibrac, F. Marone, F.N. Büchi	*Influence of binder porosity on GDL gas phase transport* PRiME 2016 / 230th ECS Meeting, Symposium on Polymer Electrolyte Fuel Cells 16, Honolulu, HI, USA, October 2–7, 2016.
A. Forner-Cuenca, J. Biesdorf, L. Gubler, T.J. Schmidt, P. Boillat	*Capillary pressure characteristic of GDLs with patterned wettability* 13th Symposium on Fuel Cell and Battery Modelling and Experimental Validation – ModVal 13, Lausanne, March 22–23, 2016.
A. Forner-Cuenca, J. Biesdorf, L. Gubler, T.J. Schmidt, P. Boillat	*Engineered water highways in fuel cells: an in-situ study combining electrochemical characterization with neutron imaging* 21st World Hydrogen Energy Conference (WHEC), Zaragoza, Spain, June 13–16, 2016.

A. Forner-Cuenca, V. Manzi-Orezzoli, J. Biesdorf, L. Gubler, T.J. Schmidt, P. Boillat	*In situ characterization of novel gas diffusion layers for advanced water management in fuel cell* 229th Meeting of The Electrochemical Society (ECS), San Diego, USA, May 29 – June 2, 2016.
A. Forner-Cuenca, V. Manzi-Orezzoli, J. Biesdorf, A. Lamibrac, F.N. Büchi, L. Gubler, T.J. Schmidt, P. Boillat	*Novel diffusion layers with patterned wettability: Measurement of capillary pressure characteristic with neutron and synchrotron imaging* 229th Meeting of The Electrochemical Society (ECS), San Diego, USA, May 29 – June 2, 2016.
L. Gubler, O. Nibel, T.J. Schmidt	*Ion-conducting membranes with vanadium barrier motif for redox flow battery applications* 15th International Symposium on Polymer Electrolytes (ISPE-XV), Uppsala, Sweden, August 15–19, 2016.
L. Gubler	*Fluoropolymer based radiation grafted ion-conducting membranes for electrochemical energy devices* Fluoropolymer 2016, ACS Division of Polymer Chemistry, New Orleans, USA, October 2–5, 2016.
A. Guéguen, D. Streich, M. He, P. Novák, E. Berg	*Decomposition of $LiPF_6$ in high energy lithium-ion batteries studied with online electrochemical mass spectrometry* 67th ISE Annual Meeting, The Hague, The Netherlands, August 21–26, 2016.
M. He, K. Fic, E. Frąckowiak, P. Novák, E.J. Berg	*Ageing phenomena in high-voltage aqueous supercapacitors investigated by in situ gas analysis* 67th ISE Annual Meeting, The Hague, The Netherlands, August 21–26, 2016.
M. He, K. Fic, P. Novák, E.J. Berg, E. Frąckowiak	*In situ gas analysis of carbon based supercapacitor operating in aqueous electrolyte* PRiME 2016 / 230th ECS Meeting, Symposium on Polymer Electrolyte Fuel Cells 16, Honolulu, HI, USA, October 2–7, 2016.
M. He, K. Fic, E. Frąckowiak, P. Novák, E.J. Berg	*Chemistry of aging phenomena in high-voltage carbon-based supercapacitors investigated by in situ gas analysis* MRS Spring Meeting 2016, Phoenix, AZ, USA, March 28 – April 1, 2016.
A. Lamibrac, F.N. Büchi	*Improvements of gas transport characterization in GDL based on XTM imaging* ECS Conference on Electrochemical Energy Conversion & Storage with SOFC-XIV, Modval 13, Lausanne, March 22–23, 2016.
D. Leanza, C.A.F. Vaz, P. Novák, M. El Kazzi	*Nanoscale PEEM spectroscopy combined with XPS to elucidate the surface mechanism of cycled electrodes* Giornate dell'Elettrochimica Italiana (GEI 2016), Gargnano, Italy, September 11–14, 2016.
D. Leanza, C.A.F. Vaz, P. Novák, M. El Kazzi	*Nanoscale PEEM spectroscopy combined with XPS to elucidate the surface reaction mechanism of cycled battery electrodes* PRiME 2016 / 230th ECS Meeting, Symposium on Polymer Electrolyte Fuel Cells 16, Honolulu, HI, USA, October 2–7, 2016.
D. Leanza, C.A.F. Vaz, P. Novák, M. El Kazzi	*PEEM spectroscopy a promising technique to study the surface of commercial-like battery electrodes at the nanoscale level* SOLEIL Synchrotron Hi-SPEAR Users Meeting, Paris, France, January 19–20, 2016.

G. Nagy, V. Sproll, U. Gasser, J.P. Embs, M. Obiols-Rabasa, S. Gustavsson, T.J. Schmidt, L. Gubler, S. Balog	*Correlation between nano-structure proton-dynamics and performance-related properties of radiation grafted proton-conducting membranes* 15th International Conference on Sustainable Energy Technologies, Singapore, July 19–22, 2016.
M. Reichardt, S. Sallard, P. Novák, C. Villevieille	*$Li_3Cr_2(PO_4)_3$ as cathode material for Li-ion batteries* 229th ECS Meeting, San Diego, CA, USA, May 29 – June 2, 2016.
R. Robert, P. Novák	*Li-ion (de-)insertion mechanism of a $LiNi_{0.8}Co_{0.15}Al0_{.05}O_2$ electrode: Insights into the first charge activation mechanism and its impact on the irreversible charge «loss»* 67th ISE Annual Meeting, The Hague, The Netherlands, August 21–26, 2016.
M. Siegwart, J. Biesdorf, A. Kaestner, P. Vontobel, E.H. Lehmann, T.J. Schmidt, P. Boillat	*Energy selective neutron imaging for distinction of ice and liquid water* 8th Workshop on NEUtron WAVElength Dependent Imaging (NEUWAVE-8), Abingdon, UK, June 12–15, 2016.
M. Suermann, T.J. Schmidt, F.N. Büchi	*Overpotential analysis in high pressure water electrolysis* PRiME 2016, Honolulu, HI, USA, October 2, 2016.
S. Schmidt, S. Sallard, P. Novák, C. Villevieille	*Lithium iron methylene diphosphonate, and organic-inorganic hybrid material for positive and negative Li-ion battery electrodes* 67th ISE Annual Meeting, The Hague, The Netherlands, August 21–26, 2016.
C.A.F. Vaz, D. Leanza, P. Novák, M. El Kazzi	*Investigating electrolyte-electrode interface layer formation in Li-ion batteries using X-ray spectromicroscopy* The 10th LEEM/PEEM Workshop, Monterey, CA, USA, September 11–15, 2016 (Abstracts, p. 20).

Posters

E.J. Berg, C. Bolli, A. Guéguen, M. He, D. Streich, P. Novák	*In situ gas analysis of Li-ion $Ni_xCo_yMn_z$ cathode interface reactivity* 18th Int. Meeting on Lithium Batteries, Chicago, IL, USA, June 19–24, 2016.
J. Billaud, S. Sallard, P. Novák, C. Villevieille	*Influence of dopants on the stability of high energy NCM $Li_x(Ni_aCo_bMn_c)O_2$* IBA 2016 – International Battery Association Meeting, Nantes, France, March 20–25, 2016.
J. Conder, L. Gubler, P. Novák, S. Trabesinger	*Polysulphides confined! New design of the separator for better Li–S cell performance* IBA 2016 – International Battery Association Meeting, Nantes, France, March 20–25, 2016.
J. Conder, L. Gubler, P. Novák, S. Trabesinger	*Li–S cell performance* IBA 2016 – International Battery Association Meeting, Nantes, France, March 20–25, 2016.
M. El Kazzi, I. Czekaj, E.J. Berg, P. Novák, M.A. Brown	*Investigation of Li-ion solvation in carbonate based electrolytes using high pressure XPS equipped with liquid jet* 32nd PSI Electrochemistry Symposium, Villigen, April 27, 2016.
G. Ferraresi, L. Czornomaz, P. Novák, C. Villevieille, M. El Kazzi	*Surface investigation of amorphous Si thin films cycled as anodes for Li-ion batteries* IBA 2016 – International Battery Association Meeting, Nantes, France, March 20–25, 2016.

E. Flores, R. Robert, P. Novák, E.J. Berg	*Interface stability of the Li-ion cathode $LiNi_{0.8}Co_{0.15}Al_{0.05}O_2$ during overcharge and discharge conditions* 67th ISE Annual Meeting, The Hague, The Netherlands, August 21–26, 2016.
J. Halter, A. Lamibrac, F.N. Büchi	*Characterization of phosphoric acid invasion/withdrawal in GDLs using X-ray tomographic microscopy* Modval 13, Lausanne, March 22–23, 2016.
J. Halter, A. Lamibrac, T.J. Schmidt, F.N. Büchi	*Characterization of phosphoric acid invasion in GDLs using X-ray tomographic microscopy* Materials Challenges for Fuel Cells and Hydrogen Technologies, Grenoble, France, September 19–21, 2016.
J. Halter, A. Lamibrac, T.J. Schmidt, F.N. Büchi	*Characterization of phosphoric acid invasion in GDLs using X-ray tomographic microscopy* Interdisciplinary Symposium on 3D Microscopy, Les Diablerets, October 18–21, 2016.
M. He, L. Boulet-Roblin, P. Borel, C. Tessier, P. Novák, C. Villevieille, E.J. Berg	*Solvent, lithium salt, and temperature influence on stability of carbonate based electrolytes for 5 V $LiNi_{0.5}Mn_{1.5}O_4$* 18th International Meeting on Lithium Batteries, Chicago, IL, USA, June 19–24, 2016. (Abstract No. P1 0715).
A. Lamibrac, F.N. Büchi	*X-ray tomography of dynamic processes in PEFC* Gordon Research Conference on Fuel Cells, Stonehill College Easton, MA, USA, August 7–12, 2016.
A. Lamibrac, F.N. Büchi	*Segmentation of low quality gas diffusion layer X-ray tomographic microscopy images* 8th International Conference on Porous Media & Annual Meeting, Cincinnati, OH, USA, May 9–12, 2016.
D. Leanza, C.A.F. Vaz, A. Gillen, P. Novák, M. El Kazzi	*Nanoscale PEEM spectroscopy combined with XPS to elucidate the surface mechanism of cycled electrodes* IBA 2016 – International Battery Association Meeting, Nantes, France, March 20–25, 2016.
D. Leanza, C.A.F. Vaz, P. Novák, M. El Kazzi	*Nanoscale PEEM spectroscopy combined with XPS to elucidate the surface mechanism of cycled electrodes* 39th International Conference on Vacuum Ultraviolet and X-ray Physics (VUVX 2016), Zürich, July 3–8, 2016.
P. Marmet, J.Dujc, L. Holzer, J.O. Schumacher, A. Lamibrac, F.N. Büchi	*Multi-scale modeling of PEFCs* SCCER Mobility 3rd Annual Conference, Zürich, September 16, 2016.
O. Nibel, T.J. Schmidt, L. Gubler	*Ion-exchange membranes with designed bifunctionality for vanadium redox flow batteries* The International Flow Battery Forum, Karlsruhe, Germany, June 7–9, 2016.
H. J. Peng, S. Trabesinger, C. Villevieille, H. Wolf, K. Leitner, P. Novák	*Transition metal dissolution in the $Li_{1+x}(Ni_aCo_bMn_{1-a-b})_{1-x}O_2$ / graphite full-cell* IBA 2016 – International Battery Association Meeting, Nantes, France, March 20–25, 2016.
T. Poux, S. Trabesinger, J.L. Gómez-Cámer, D. Cericola, T. Hucke, M.E. Spahr, P. Novák	*Si/C composite as additive to graphite for high-energy Li-ion batteries* Advanced Battery Power Conference, Münster, Germany, April 26–27, 2016.
T. Poux, P. Novák, S. Trabesinger	*Pitfalls in Li–S rate capability tests* Advanced Battery Power Conference, Münster, Germany, April 26–27, 2016.

T. Rojek, T.J. Schmidt, L. Gubler	*Radiation grafted membranes for high temperature hydrogen pumping* Ion Exchange Membranes for Energy Applications – EMEA2016, Bad Zwischenahn, Germany, June 27–29, 2016.
S. Sallard, S. Schmidt, D. Sheptyakov, P. Novák, C. Villevieille	*Lithium iron methylene diphosphonate, a new organic-inorganic hybrid material for Li-ion batteries* IBA 2016 – International Battery Association Meeting, Nantes, France, March 20–25, 2016.
V. Sproll, G. Nagy, U. Gasser, S. Balog, T.J. Schmidt, L. Gubler	*Grafting design: Structural impact on the performance of proton exchange membranes* E-MRS 2016, Lille, France, May 2–6, 2016.
V. Sproll, G. Nagy, U. Gasser, S. Balog, T.J. Schmidt, L. Gubler	*Grafting design: A way to the optimized proton exchange membrane ?* Fluoropolymer 2016, ACS Division of Polymer Chemistry, New Orleans, USA, October 2–5, 2016.
D. Streich, A. Guéguen, M. He, P. Novák, E.J. Berg	*Impact of Ni content on interface reactions at NCM electrodes* Gordon Research Conference – Batteries: Fundamental Tools for Designing the Next Generation of Electrochemical Energy Storage, Ventura, CA, USA, February 21–26, 2016.

Conferences & Workshops Organizations

F.N. Büchi, T.J. Schmidt	*16th Symposium on Polymer Electrolyte Fuel Cells PEFC 16* 230th ECS Meeting, Honolulu, HI, USA, October 2–7, 2016. Members of organizing committee
P. Novák, A. Vezzini	*Summer School «Energy Storage in Batteries: Materials, Systems, and Manufacturing»* Möschberg, July 11–15, 2016. Organizers
T.J. Schmidt	*Swiss-Japanese Workshop Hydrogen Technology and Energy Storage* Tokyo, Japan, October 05–06, 2016.
T.J. Schmidt	*International Summer School on CO_2 Conversion: From Fundamentals towards Applications* Villars-sur-Ollon, August 29 – September 2, 2016.
T.J. Schmidt	*32nd PSI Electrochemistry Symposium: Electrolytes – The Underestimated Player in Electrochemical Processes* Paul Scherrer Institut, Villigen, April 27, 2016.

Members in External Committees

P. Novák	*International Meetings on Lithium Batteries LLC* Director
P. Novák	*CIC Energigune, Vitoria, Spain* Member of Scientific Committee

P. Novák	*IMLB-2016* Member of the Organizing and Scientific Committee
P. Novák	*Graz Battery Days 2016* Member of the Scientific Committee
P. Novák	*Symposium Series «Advanced Battery Power Conference»* Member of Scientific Advisory Board
T.J. Schmidt	*The Journal of the Electrochemical Society* Associate Editor
T.J. Schmidt	*Kopernikus Project Power-to-X* Member of Scientific Council
T.J. Schmidt	*Swiss Hydrogen SA, Fribourg* Board of Directors
T.J. Schmidt	*European Academy of Sciences Advisory Council* Working Group Member *Dedicated Energy Storage (Task: Filing of Advisory Document for European Commission)*
T.J. Schmidt	*The Electrochemical Society* Individual Membership Committee
T.J. Schmidt	*Competence Center Energy & Mobility Switzerland* Member of Steering Board
T.J. Schmidt	*Technical University of Denmark, Lyngby* *4M Centre – Mechanisms, Materials, Manufacturing and Management – Interdisciplinary Fundamental Research to Promote Commercialization of HT-PEMFC* Member of Technical Steering Committee
T.J. Schmidt	*University of Cape Town (South Africa)* Member of Technical Steering Committee *HySA/Catalysis*
S. Trabesinger	*The Research Council of Norway (RCN)* Member of Peer Review Panel/Expert Evaluator
S. Trabesinger	*4Qatar National Research Fund (QNRF)* Expert Evaluator
S. Trabesinger	*European Commission* Member of Peer Review Panel / Expert Evaluator
C. Villevieille	*Agence Nationale pour la Recherche (ANR)* Expert Evaluator
C. Villevieille	*PSI Forschungskommission (FOKO)*

Editorial Work

D.J. Jones, H. Uchida, H.A. Gasteiger, K. Swider-Lyons, F.N. Büchi, P.N. Pintauro, B.S. Pivovar, K.E. Ayers, K.A. Perry, P. Shirvanian, A.Z. Weber, V.K. Ramani, P. Strasser, R.A. Mantz, K. Shinohara, S. Mitsushima, C. Coutanceau, J.M. Fenton, T.J. Schmidt, T.F. Fuller, S.R. Narayanan, Y.T. Kim, L. Zhuang, S.G. Sun	*Polymer Electrolyte Fuel Cells 16* ECS Transactions **75** (14), The Electrochemical Society, Pennington, NJ, (2016).
C. Gloor, L. Gubler, T.J. Schmidt	*PSI Electrochemistry Laboratory Annual Report 2015* doi.10.3929/ethz-a-007047464, ISSN 1661-5379

Paul Scherrer Institut :: 5232 Villigen PSI :: Switzerland :: Tel. +41 56 310 21 11 :: Fax +41 56 310 21 99 :: www.psi.ch